Potential of Micro-scale Optical Spectroscopy for Environmental sensing : Focus on Gas and Air Quality

Alaaeldeen Fathy Rezk Thabet Mohamed

To cite this version:

Alaaeldeen Fathy Rezk Thabet Mohamed. Potential of Micro-scale Optical Spectroscopy for Environmental sensing : Focus on Gas and Air Quality. Optics / Photonic. Université Paris-Est, 2020. English. NNT : 2020PESC2023 . tel-03920276

HAL Id: tel-03920276
https://theses.hal.science/tel-03920276
Submitted on 3 Jan 2023

HAL is a multi-disciplinary open access archive for the deposit and dissemination of scientific research documents, whether they are published or not. The documents may come from teaching and research institutions in France or abroad, or from public or private research centers.

L'archive ouverte pluridisciplinaire **HAL**, est destinée au dépôt et à la diffusion de documents scientifiques de niveau recherche, publiés ou non, émanant des établissements d'enseignement et de recherche français ou étrangers, des laboratoires publics ou privés.

UNIVERSITÉ PARIS-EST

Ecole Doctorale
Mathématiques, Sciences de l’Information et de la Communication (MSTIC)

THÈSE
pour obtenir le grade de
Docteur de l’Université Paris-Est

Spécialité : Electronique, Optronique et Systèmes

Présentée et soutenue publiquement le 19 Novembre 2020 par

ALAAELDEEN FATHY REZK THABET MOHAMED

Exploration du potentiel de la micro-spectrométrie optique pour l'analyse de l'environnement : Focus sur les gaz et la qualité de l'air

Potential of Micro-scale Optical Spectroscopy for Environmental sensing: Focus on Gas and Air Quality

Directeurs de thèse

Tarik Bourouina, et Yasser M. Sabry

Jury

Hans Zappe, Professeur, Freiburg University, Germany	Rapporteur
Sébastien Hentz, Directeur de Recherche, CEA-LETI, Université Grenoble Alpes,	Rapporteur
Ian Hunter, Professeur, Massachusetts Institute of Technology, USA	Examinateur
Alain Bosseboeuf, Directeur de Recherche, CNRS, Université Paris-Saclay	Examinateur
Diaa Khalil, Professeur, Ain-Shams University, Egypte	Examinateur
Martine Capo-chichi, Ingénieur de Recherche, Université Gustave Eiffel,	Examinateur
Tarik Bourouina, Professeur, ESIEE Paris, Université Gustave Eiffel,	Directeur
Yasser M. Sabry, Professeur Associé, Ain-Shams University, Egypte	Co-Directeur

© UPE

Acknowledgment

Praise is due to God, even if after his satisfaction. Glory for Allah who taught and guided me all good things. Whatever blessing has been received by me, it is from God alone with no partner.

Thanks to my mother and sister. My mother taught and encouraged me to superiority. Pray upon my father, he has a great credit for educating and encouraging me.

My sincere gratitude to Prof. Tarik for his humanity, good scientific guidance and advices. Thanks to Dr. Yasser Sabry for helping me in acquiring this Ph.D. grant and for the scientific guidance. Thanks to Prof. Diaa for his guidance. Thanks to them for helping me to accomplish this.

I would like to extend my deep gratitude to Si-ware Systems for sponsoring my Ph.D. (special thanks to Dr. Bassam Saadany) and the optical MEMS team (specially Momen Anwar, Amr Osama and Mariam Amr) for helping me during my Ph.D.

I would like to thank Fredric Marty for doing all the fabrication process of the designs.

I was happy to participate in the measurements of air purification which were performed by Mame Ousmane, Young Jai and Marie under the supervision of Prof. Yamin and Martine.

Finally, thanks to my friends Mazen Erfan and Ahmed Amr. Specially, Mazen helped me a lot during the Ph.D.

Table of Contents

List of Figures

List of Tables

Introduction

I. Motivation and Objectives

Air pollution is considered a big disaster that affects mankind. Air pollution mainly arises from man activities. The main anthropogenic sources of pollution are factories, agriculture, aircraft and automotive traffic, power plants, fires, and wars. The effects of the pollution on the environment include global warming, floods, and global sea levels rising. Regarding human health, air pollution can lead to stroke, heart diseases, chronic obstructive pulmonary disease, and acute respiratory infections[1]. Urban regions are also more exposed to air pollution. Low-income countries are more suffering from the highest exposure both indoor and outdoor. Thus, there is a strong need for mitigating air pollution. The more ability to monitor and map the pollution, the more we are going to map its diffuse, localize its sources, and the earlier detection before exceeding limits. Decision-makers then can take actions, the most popular to-date being traffic regulation. At the individual level, the knowledge about pollution status can be also used to trigger the emerging indoor air-purification systems either at home or in cars.

Gas sensing can be performed using different technologies where they differ in performance and cost. Examples for these technologies are metal oxide semiconductor (MOS), polymer, carbon-nanotubes, gas chromatography (GC), optical methods, acoustic detectors, and catalytic sensors. MOS is based on gas interaction with the surface of a metal oxide resulting in a change of carrier concentrations. This leads to a change in the resistivity which can be further measured [2]. It is featured by low cost and high sensitivity while its challenge is selectivity, long recovery time after exposure, and high power consumption due to high temperature operation [3], [4]. Polymer-based sensors are based on adsorption of the target gas on the polymer layer leading to change in the physical properties of the polymer. It is characterized by high sensitivity, shorter response time, and working at room temperature [5]. Its drawbacks are the low selectivity, long time instability in addition to irreversibility [3]. Carbon nanotubes CNT has the advantage of low weight and rather quick response. However, its disadvantage is the complicated and non-reproducible fabrication process and high cost [3], [6]. Gas Chromatography is based on the separation of gases in a long column followed by a gas detector (i.e. photoionization detector). It is usually used for organic chemicals. It has excellent separation performance, high sensitivity, and selectivity. Its disadvantage is the high cost and low speed; it is mainly limited for laboratories use.

Gas sensing by optical methods is usually straightforward and could achieve higher sensitivity, selectivity, and stability than non-optical methods with much longer lifetime and relatively short response time [3]. Its main advantage relies on the fact that there is no chemical contact between the optical sensor and the gas. It is based on remotely analyzing the optical power absorbed by the gas. The performance is not deteriorated by the changing environment or catalyst poisoning caused by specific gases. Examples for optical methods are non-dispersive infrared detectors NDIR, Fourier transform FT spectroscopy, and laser spectroscopy. NDIR is based on using white light source followed by gas cell (usually short) followed by a spectral filter (corresponds to the absorption band of the target gas) followed by the detector. Thus, each NDIR is specific for a certain gas. On the other side, Fourier transform spectroscopy is based on using optical interferometer which scans wide spectral range leading to multiple detection lines of different gases. For laser spectroscopy, a tunable laser is used to scan a spectral range relatively narrower than Fourier transform spectroscopy but with higher sensitivity. A summary of the performance of the different technologies can be found in Table 0-1.

Table 0-1 Performance between different gas sensing technologies

	Cost	Sensitivity	Selectivity	Response time	Operating temp.	Size
Optical methods	High	High	High	Fast	Normal	Big
Metal oxide semiconductor	Low	Relatively low	Low	Fast	High	Small
Polymer	Low	High	Low	Fast	Normal	Small
Carbon nanotube	High	High	Low	Fast	High	Small
Gas chromatography	High	High	High	Slow	high	Big

Gas sensors based on optical measurements are more compatible with the real-time/continuous measurements besides being stable, and highly accurate[3], [7]. To achieve such an effective and wide monitoring of pollution, low-cost miniaturized sensors of good performance are needed. This enables large scale deployment of sensors in cities, factories, and inside houses. Miniaturizing the sensors can be achieved using micro-electro-mechanical systems (MEMS) technology. Different miniaturized spectrometers, operating in the mid-infrared, are reported in the literature. Reported spectrometer can be based on linear variable optical filter LVOF, tunable Fabry-Pérot or Fourier transform spectrometer. The Fourier transform spectrometer can be implemented using Lamellar grating, Wishbone or Michelson interferometers. Comparison between these different spectrometers is shown in Table *0-2*.

Fourier transform MEMS based spectrometer was a proved a successful trial to have a handheld spectrometer of low cost [14], [15]. A spectrometer which covers the range from 1.5 μm to 4.9 μm is presented in the reference[13]. It is based on a Michelson interferometer whose optical components are monolithically integrated on the same chip leading to low cost and the ability to produce low-cost sensor with considerable performance. This MEMS solution motivates us for using the MEMS spectrometer in different gas sensing applications such as monitoring of volatile organic compounds VOCs, open-path measurements, monitoring air purification, etc...

Table 0-2 Review of different reported spectrometers operating in the mid-infrared.

Principle	Spectral range (μm)	Resolution	Ref.
LVOF	2.5 to 5	400 nm	[8]
LVOF	3 to 3.8	4 cm^{-1}	[9]
FPI using subwavelength grating reflector	2.9 to 3.5	50 nm	[10]
Lamellar grating-based FT	1.5 to 4.5	20 cm^{-1}	[11]
Wishbone-based FT	2.9 to 10	10.4 cm^{-1}	[12]
Michelson-based FT	1.5 to 4.9	33 cm^{-1}	[13]

Since gas cells are key components in sensors where light interaction occurs, integrating them with the MEMS spectrometer is an ultimate goal for having all the senor completely integrated on the same chip, leading to a more compact and lower cost sensor.

II. Main Contributions

The main contributions reported in the thesis can be summarized as the following:

1. A review was conducted on optical-based gas sensing technologies: Fourier transforms spectroscopy and laser spectroscopy. Each technology was reviewed in case of using it in direct absorption (DA) mode (transmitted light is detected by an optical detector) or in photoacoustic (PA) mode (amount of absorbed light is known by measuring the corresponding acoustic signal). A theoretical analysis was performed for different technologies. Figures of merit are derived to compare detection methods (DA or PA) given different system parameters (i.e. feasibility of using PA with MEMS spectrometer). Feasibility study of using the cavity enhancement techniques with MEMS FTIR spectrometer was also performed.

2. Exploring even more compact and more simple spectrometers, the new concept of differential spectrometer based on critical angle dispersion was presented. Theoretical analysis of the spectrometer was performed in the sense of the principle of operation, spectrometer resolution, and signal to noise ratio. Laser and reference materials were measured using the spectrometer as a proof of concept. System non-idealities faced in the measurements were studied and a signal processing was presented to reduce its effect on resolution. Another innovative concept, the parallel Fourier Transform spectrometer was evaluated for its potential to gas sensing, thanks to its better spectra resolution.
3. Open-path Fourier transforms spectroscopy using the mid-infrared MEMS spectrometer in Sense city (huge climate chamber of 20 meter characteristic dimension) was reported. An optical system compatible with the MEMS spectrometer was designed and built. Pollution stimulated by a car was monitored and compared to the measurements of localized reference analyzers. For localized gas sensing, toluene, as an example for the VOCs, was measured using a benchtop multi-pass gas cell coupled to the MEMS spectrometer. Ppb-level of toluene concentration, as a detection limit, was achieved.
4. A chip-scale multi-pass cell was designed and fabricated and this is the first of this kind to be reported based on silicon technologies, according to our

knowledge. Design considerations including the light guiding mechanism and mirrors design were studied. Fabrication of the cell and characterization using the MEMS spectrometer were performed. Different gases were measured such as acetylene, butane, carbon dioxide, and water vapor. In addition to that, integrated large throughput hollow waveguides are designed, fabricated, and characterized. This is a solution for localized sensing and enables the possibility of integration with the MEMS spectrometer on the same chip.

III. Thesis Outline

This thesis is organized in main four chapters as described hereafter; these are complemented by an introduction, a conclusion, and perspective section, as well as appendixes. The introduction presents the motivation and objectives of this work, our major contributions, and the overall organization of the thesis.

Chapter 1:

A review of using Fourier transform and laser spectroscopy in gas sensing. The review covers the two methods of detection (DA or PA) to be used in both technologies. The theoretical analysis of the detection limits was conducted.

Chapter 2:

Gas sensing measurements using the new concept of parallel MEMS spectrometer was presented. Another original spectrometer, the differential spectrometer, was proposed. It is based on the critical angle dispersion. This chapter includes theoretical analysis and measurements. Studying the effect of non-idealities of the optical component on the performance and a correction method are also presented.

Chapter 3:

Gas sensing on different scales and applications using the MEMS spectrometer are presented. In the first part, open path gas measurements using the Fourier transform MEMS spectrometer in a huge climate chamber (Sense city) is presented. Pollution from the car was monitored. In the second part, a setup for reaching the ppb-detection limit of VOCs is presented. In the third part, monitoring of air purification using ZnO nanowires are presented.

Chapter 4:

Integrated gas cells on the silicon are presented. This includes an integrated hollow waveguide and a multi-pass cell. Characterization and gas sensing using the MEMS spectrometer are presented. Theoretical background is given for further optimization, anticipating for technological advances in optical sources and photodetectors, that will contribute enhancing the lower-limit of detection, down the ppb-level, which will accommodate for a vast majority of the applications of spectral gas sensors.

Finally, the conclusion of this thesis is presented while introducing recommendations for future work.

CHAPTER 1: INTRODUCTION TO GAS SENSING TECHNOLOGIES

1.1 Introduction

Gas sensors are used extensively in the chemical and pharmaceutical industry, oil refineries, and material science in addition to environmental monitoring. They are also used in the early detection of fires. They are crucial for the measurements of air pollution such as indoor air quality control, monitoring outdoor pollution, and the study of greenhouse gas emission and their dispersion. Consequently, they can be used as an alarm for exceeding pollution limits or for triggering a process for controlling gas emission or air purification. The workspace exposure limit of hazardous gases ranges from part per million (*ppm*) down to part per billion (*ppb*) [16]. Such low concentration levels require sensors with very small lower-limit of detection (LLOD). The corresponding high sensitivity levels are also required in some outdoor environments, such as monitoring the dispersion of atmospheric pollutants, including greenhouse gases that contribute to global warming [17] or for early-stage detection and localization of gas leakages around hazardous gas plants. Detection limits of ppb concentration levels of Volatile Organic Compounds (VOCs) are often required for addressing possible health consequences. Consequently. sensors should be able to detect levels smaller than such the limits to enable providing an early alarm.

Gas measurement can be conducted using electrochemical sensors, metal oxide semiconductors, gas chromatographs, mass spectrometers, or optical spectrometers [3]. The optical methods are more compatible with real-time/continuous measurements as compared to gas chromatography for example which require typically tens of minutes to finalize a measurement [18]. More importantly, optical measurements are the only way to achieve measurements without any chemical contact between the sensor and the gas. This capability not only offers the advantage of remote sensing but it also avoids irreversible effects such as sensor fouling and related induced metrological drawbacks such as hysteresis in addition to reduced lifetime and reliability and robustness to harsh environments. Among the different optical techniques, optical spectroscopy is in the class of analytical chemistry devices, meaning that it allows measuring multiple gases simultaneously, through their specific spectral responses which can be recorded and analyzed from a single spectrum.

1.2 Optical spectroscopy for gas sensing

The different forms of optical spectroscopy include atomic emission spectroscopy (AES), Raman spectroscopy, and fluorescence spectroscopy, but these are not considered in this work. Absorption spectroscopy is the most widespread technique used for gas analysis and probably the most suitable. Within this, the main techniques used include non-dispersive infrared spectroscopy, tunable laser spectroscopy (TLS) and Fourier transform infra-red (FTIR) spectroscopy. Among the different detection methods, TLS is characterized by its high sensitivity and excellent spectral resolution. FTIR is characterized by its wide infra-red spectral range covering the absorption molecular spectrum of a broad variety of gases. The focus in the next discussion will be on the TLS and FTIR due to their superior performance compared to other technologies besides high-temperature stability, insensitivity to environmental change, and long lifetime [3]. Measurement of the amount of light absorbed by gas can be conducted using either an optical detector or a photoacoustic cell. In the former case, we refer to direct absorption spectroscopy DAS whereas in the latter case, we refer to photoacoustic spectroscopy PAS.

Within the DAS category, TLS is used to identify systems that use a tunable laser followed by a gas cell and then an optical detector, as depicted in Figure 1-1(a). The transmitted light after gas absorption is the detected signal. Laser spectroscopy is distinguished by its high power and excellent spectral resolution, which enables excellent gas selectivity; however, it has a limited tunability, in the order of 50-200 nm, hence restricting the spectral range as compared to FTIR spectrometers, whose spectral range is in the order of 2,000-20,000 nm. TLS has a tremendous range of applications. This high sensitivity of TLS has led to detection limits in the order of parts per trillion (ppt) using MP cells. For example, a detection limit of ammonia (NH_3) of 200 ppt was achieved for a 1 s measurement time and a path length of 76 m, whereas for the same configuration it was 300 ppt for nitric oxide (NO) [19]. A detection limit of 20 ppb of methane (CH_4) was reported in [20] using a Herriot cell of path length 252 m and 2 s measurement time.

FTIR spectrometers use a broadband source instead of lasers narrowband widths, in conjunction with an interferometer, which is typically a Michelson configuration. FTIR spectrometers can simultaneously analyze multi-species within a wide range of infrared absorption spectra [21]. They also have a high spectral resolution, but it is lower than that of the TLS in addition to its lower spectral power density. FTIR spectrometers have better tolerance against different gases interferences by applying multivariate analysis [22], a kind of machine-learning approach. It has been used for many years for the detection of air pollutants. The detection limits of FTIR spectrometers can be enhanced using long path cells (up to hundreds of meters), which enables concentrations as low as the *ppb* range or even lower to be measured [23], [24]. Recently, miniaturized MEMS spectrometers have proven to be a good solution for air monitoring with sub-*ppm* range detection limits[25]. In general, FTIR-based DAS is applicable for studying gas reactions [26], [27], gas emission[28]–[30], measuring atmospheric trace gases and greenhouse gases flux [31], open path measurements [17], [32]–[36] and airborne measurements [37].

The PAS category has two configurations, similar to the TLS or FTIR in the DAS category. The first configuration is similar to TLS except that a modulator and a microphone are used instead of the optical detector. The output light from the laser is modulated using either an electrical or a mechanical modulator. The modulated light is absorbed by the gas. The gas absorption of such modulated light leads to the emission of an acoustic pressure wave which is detected by the microphone. The gas is contained in an acoustic cell which can be operated at resonance or not. The cell configurations include one-dimensional cylindrical resonators, Helmholtz resonators, or cavity resonators[38]. This is depicted in Figure 1-1(b). The second configuration exploits the modulated output from an interferometer, which is illuminated by a broad-band source, to pass through a gas. This modulated optical intensity is converted into an acoustic wave, which is then detected by a microphone. This system is depicted in Figure 1-1 (d). The photoacoustic-based system is characterized by its independence on the gas cell length, which allows the possibility of using small volume gas cells instead of the large ones used in the DAS scheme. However, this can be seen as a disadvantage, since the detection limit cannot be enhanced by increasing the path length. This leads to the DAS being superior when large gas cells are used. Another advantage is that the measured signal is directly related to the absorbed power, not the transmitted one as in TLS. The pioneering microphone type for TLS and FTIR is the one based on the cantilever, which has much higher sensitivity than conventional electret microphones. PAS has a tremendous range of applications such as in trace-gases monitoring [38], open-air measurements [39], smoke detectors [40], breath analysis [41], automotive emissions [42], radioactive components analysis [43], manned spaceships [44], biological and medical applications, microbiology [45] and even in the analysis of the status of power transformers [46]. Regarding its sensitivity, with lasers PAS shows good performance for small gas lengths (< 100 mm) [7]. As an example in [47], using a photoacoustic PA cell of 95 mm long and a laser of 0.95 W, a detection limit of 0.65 *ppt* of hydrogen fluoride (HF) was obtained in half an hour.

It is apparent that the PAS shows good performance for short cells (20 mm or less) while direct absorption spectroscopy TLS (Direct TLS) has better sensitivity for longer cells [7]. However, some questions remain; which detection scheme is more sensitive given certain laser power, given a particular gas cell length, the presence or not of an optical detector, the measurement time for it to be more sensitive than using a 20 mm long photoacoustic cell with a microphone. To answer these questions, a comparison is needed between the two detection systems in the case of TLS for a given power or in the case of FTIR for a given spectral resolution, throughput, and mirror velocity. This comparison was conducted by deriving the theoretical extreme detection limits of the different detection schemes. The related theoretical equations show the limiting parameters of each system alone compared with its respective technology. The figure of merit for this comparison is the normalized absorption coefficient defined as the minimum detectable absorption coefficient normalized for the measurement bandwidth $(cm^{-1}Hz^{-0.5})$. In addition, the normalized noise equivalent absorption coefficient NNEA $(cm^{-1}W.Hz^{-0.5})$, commonly used in PAS, is also employed for these comparisons for laser spectroscopy. A review of the literature was also conducted for TLS and FTIR approaches using photoacoustic PA or DAS. This was not only intended to show the latest advancements in these fields but also to summarize the real achieved detection limits and make further comparisons resulting from an analysis based on the proposed theoretical framework. This chapter is organized as follows: Section 1.2.1 reviews the technology of using TLS in both the DAS and PAS modes. The theoretical detection limits of both systems are derived and compared. Section 1.2.2 reviews technology of using FTIR in both the DAS and PAS modes. The corresponding theoretical detection limits are also derived. Finally, in conclusion, we summarize the main results of this critical review.

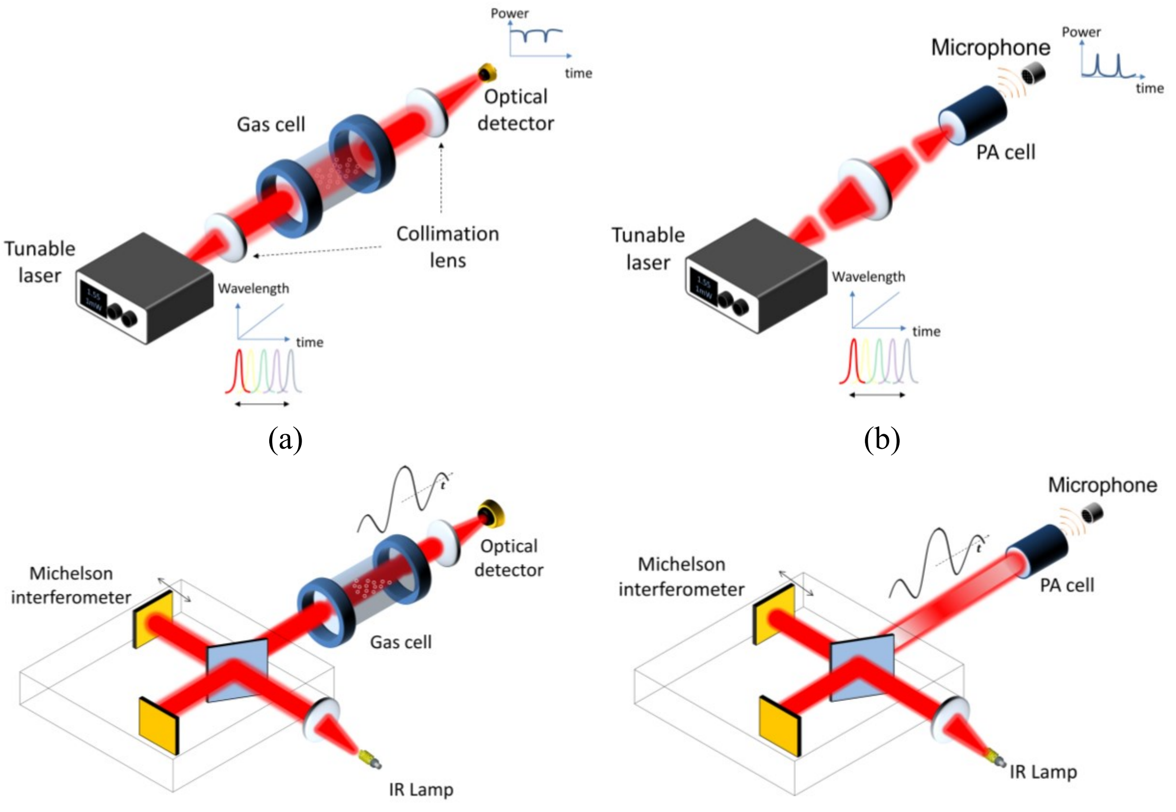

(a) (b)

(c) (d)

Figure 1-1 Different gas sensing techniques. (a) 3D view of direct absorption spectroscopy using a tunable diode laser. (b) 3D view of PAS systems using a modulated tunable diode laser. (c) DAS based FTIR spectrometer comprising a Michelson interferometer, a gas cell, and an optical detector. (d) PA-based FTIR spectrometer comprising a Michelson interferometer, a PA cell, a microphone (cantilever), and another interferometer (not shown) for the PA signal detection.

1.3 Laser spectroscopy

1.3.1 Direct absorption laser spectroscopy

The TLS system is depicted in Figure 1-1 (a), where the output power from the tunable laser source, at a given wavelength λ and power P_o, is coupled into a gas cell using collimation optics (e.g., a lens). The collimated light propagating in the gas cell interacts with its gaseous content. At the output from the gas cell, light is refocused onto the detector for conversion to an electrical signal. The laser's wavelength is selected at a given gas absorption line. To detect another absorption line or another gas the laser must be tuned to the respective wavelength. The linewidth of lasers can be as low as a few MHz or even less [48]–[52]. On the other hand, the linewidth of gases is a few GHz at atmospheric pressure, [7], [49], [53]–[55], while at reduced pressure linewidths can reach tenths of MHz [56], [57]. Thus, the laser linewidth is much smaller than the gas linewidth.

Theoretical detection limit

Shot noise, thermal noise, quantization noise, and flicker noise represent the different noise types in the optical detector-based systems. The shot noise represents the theoretical noise limit for such systems, and it is given by:

$$i_n = \sqrt{2qi\Delta f}, \tag{1.1}$$

where i is the total detector current, q is the elementary charge of an electron, and Δf is the noise bandwidth (single-sided). To compare different detectors of different areas, a figure of merit called the specific detectivity is used and is expressed as:

$$D^* = \frac{\sqrt{\mathrm{A_d}}}{NEP}, \tag{1.2}$$

where A_d is the detector area and NEP $(W.Hz^{0.5})$ represents the equivalent optical power of noise when the signal to noise ratio SNR is equal to 1 and is given by [58]:

$$NEP = \frac{i_n}{R_i\sqrt{\Delta f}}, \tag{1.3}$$

where i_n is the current noise and R_i is the detector current responsivity (A/W). The equivalent power of the detector signal at a given wavelength, λ, is given by $(\alpha l \ll 1)$:

$$P_{detector}(\lambda) = P_o(\lambda)\zeta(1-\alpha(\lambda)l) + NEP\sqrt{\Delta f}, \tag{1.4}$$

where l is the gas interaction length, $\alpha(\lambda)$ is the wavelength-dependent absorption, $P_o\zeta\alpha l$ represents the amount of power absorbed by the gas, $P_o(\lambda)$ is the laser power at a given wavelength and ζ is the coupling coefficient from the laser output to the detector. Thus, one can define the SNR as:

$$SNR(\lambda) = \frac{P_o\alpha(\lambda)l\zeta}{NEP\sqrt{\Delta f}}. \tag{1.5}$$

Thus, the minimum normalized absorption coefficient is given by:

$$\alpha_{min_{DAS}}(\lambda) = \frac{\alpha(\lambda)}{SNR(\lambda)\sqrt{\Delta f}} = \frac{NEP}{P_o(\lambda)l\zeta} \tag{1.6}$$

The total detector current, i , is the sum of the currents due to the laser power and background power:

$$i = P_o\zeta\, R_i(\lambda)\ + \int_0^{\lambda} B_{BG}(\lambda')\, TP_d R_i(\lambda')\ d\lambda', \tag{1.7}$$

where TP_d is the detector throughput in $Sr.m^2$ and B_{BG} represents the spectral radiance (per unit wavelength) of the black body source at temperature T_{BG} in $W.Sr^{-1}m^{-2}m^{-1}$. The first term represents the contribution from the output power from the laser (percentage absorbed by the gas is neglected), while the second term represents the contribution of the background power. The maximum limit of the integration in Equation(1.7) is the peak sensitivity of the detector and also the cutoff wavelength in semiconductor detectors[59]. The first term dominates the second term for the range of laser power used in gas sensing (few mW up to W). Also, the laser spot size is within a few micrometers, meaning that the detector area can be reduced significantly leading to small thermal and background noise. Thus, the second term can be neglected. In view of Equation(1.1),(1.3), (1.6) and (1.7)the corresponding α_{min} is obtained as follows:

$$\alpha_{min_{DAS}} = \frac{1}{l}\sqrt{\frac{2q\zeta}{R_i(\lambda)P_o}}. \tag{1.8}$$

As can be seen, the minimum absorption coefficient is inversely proportional to $\sqrt{P_o}$. The responsivity equation is given by $\frac{\eta q\lambda}{hc}$ $(\lambda\colon 0 \rightarrow \lambda_c)$, where η is the detector quantum efficiency, q is the electron charge, h is Plank's constant and λ_c is the cut off wavelength of the detector. Also, increasing the wavelength has a better detection limit, due to the increased number of photons (better responsivity).

Technologies used in laser spectroscopy

In TLS, the laser source can be a diode laser, inter-band cascade laser (ICL), or a quantum cascade laser (QCL). The physical mechanism of the laser diodes is characterized by the conversion efficiency of photons into electrons at fixed and stable wavelengths. Increasing the emission wavelength of a diode laser requires a smaller bandgap that is closer to the background thermal fluctuations [7]. In addition, more non-radiative losses are encountered due to increased Auger recombination[60], [61]. An example of such a laser operating in the mid-infrared MIR spectral range is the lead salt laser. It can operate over a large spectral range in the IR range (3.3 μm to 29 μm)[60], [62] but operated under cryogenic conditions and has low power emission of few mW [63]. Therefore, QCL and ICL are used for the MIR spectral range.

The QCL was first demonstrated in 1994 [64]. The QCL is based on a periodic structure of multiple quantum wells. Each quantum well introduces discrete electronic states within the band, where photon emission occurs in-between (intersub-band/intraband transition). The spacing between the states and, thus, the emission wavelength is determined by the thickness of the layers. After that, the electron tunnels to the next quantum well (intraband tunneling), emits a photon and so on. The multiple photons emission by a single electron raises the efficiency of such a laser. Over the last decade, there have been successful efforts in increasing the overall efficiency of QCL for both continuous and pulsed operation [50]. The QCL appears as a strong candidate for mid-infrared gas sensing from 4 μm to 15 μm and even in the terahertz range [7]. The idea of stacking different wavelength quantum cascade stages was exploited for covering a large spectral range from 5.9 to 10.9 μm using the same device with a peak power around 50 mW [65]. The main disadvantage of QCLs is the large threshold current, and thus the high power consumption [61], [66]. Also, the QCL performance is still limited for wavelengths less than 4 μm [48], [61]. The ICL, like the QCL, is based on cascading multiple layers and similar to laser diodes, where transitions occur between the conduction and the valence band (interband transitions). After photon emission, the electrons tunnel to the next layer through interband tunneling from the valence band to the conduction band of another layer and so on. The ICL is the choice for applications of low power consumptions.

In its simplest form, the feedback in the laser system is implemented using two mirrors forming a Fabry-Pérot cavity, which is characterized by its rather large bandwidth leading to multimode lasing. This can be mitigated with a narrowband feedback operation using a diffraction grating on the top of the active layer, described as a distributed feedback DFB laser. This method can be applied to laser diodes, QCL, and ICL. Another approach is to apply a multilayer Bragg reflector on the top and bottom of the active layer, where the laser beam is emitted vertically. Thus, it is called a vertical-cavity surface-emitting laser (VCSEL). It can also be applied to laser diodes, QCL [67], and ICL[68]. For a wider tuning range an external cavity is used to tune the wavelength using the laser active medium and for example, a grating as the wavelength selection component.

To achieve smaller detection limits, there is a need for multiplying the interaction length with the gas for a given volume. This can be accomplished using multi-pass gas cells, where the light bounces forth and back many times using high reflectivity mirrors.

Optical detectors in general can be classified into photon (quantum) detectors and thermal detectors. Quantum detectors can detect photons whose energy is greater than the bandgap energy of the semiconductor. This bandgap corresponds to the cut-off wavelength of the detector. In contrast, thermal detectors can detect light due to changes in temperature through the absorption of light [58]. They are characterized by a nearly flat and wide spectral response, although they suffer from higher noise and slower response time.

The specific detectivity D^* of the different detectors as a function of wavelength is depicted in Figure 1-2. The wavelength detectors such as InAs, InGaAs, and PbS are examples of quantum detectors while pyroelectric is an example for thermal detectors. The theoretical limits of D^* for all these detectors are represented by the dashed line. These limits correspond to the shot noise due to only the background thermal radiation, which is unavoidable.

In the case of near-infrared (NIR), for wavelengths ranging from 1 μm to 1.7 μm, indium gallium arsenide (InGaAs) (peak responsivity at 1.7 μm) at room temperature can be considered as a highly sensitive detector and a popular choice, although mercury cadmium telluride (MCT) has the same ultimate fundamental performance [69]. For the wavelength range from 1 μm to 2.5 μm, extended InGaAs (peak responsivity at 2.3 μm) or lead sulfide (PbS) at room temperature are preferred. For better sensitivity, the nitrogen cooled indium arsenide (InAs) can be used. In case of mid infrared MIR for the wavelength range of less than 5 μm, nitrogen cooled indium Antimonide (InSb) and nitrogen cooled MCT are the preferred choice. For the wavelength range from 7.7 μm to 14 μm, cooled MCT is the better choice[31], [69], [70]. MCT is likely to remain unchallenged for its high performance in long-wavelength infrared LWIR for the next few years [71].

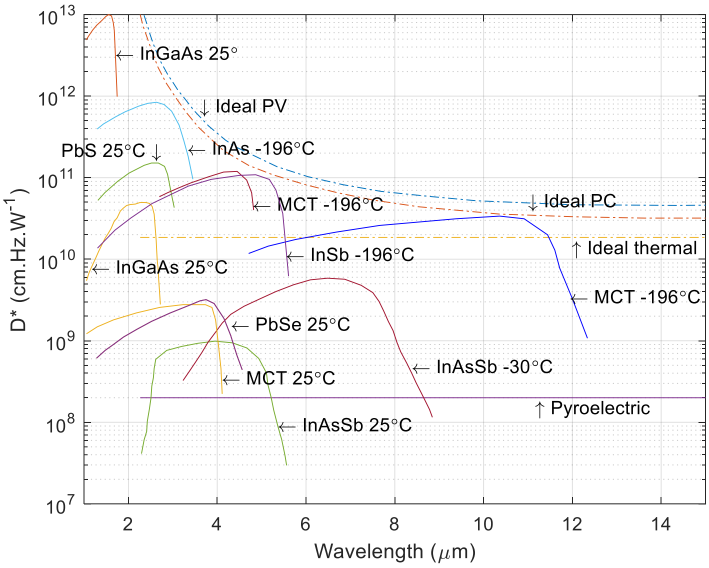

Figure 1-2 Specific detectivity of different detectors versus the wavelength of operation. PC denotes photoconductive and PV denotes photovoltaic. Data adapted from references [58], [70], [72], [73].

Theoretically, shot noise is the quantum limit of the sensitivity of optical detectors[74]. In practice, other noise sources are affecting these systems such as laser source noise and optical fringes. The effect of laser source noise can be reduced by 1) increasing the absorbed signal by increasing the interaction length L using a cavity or a multi-pass cell; 2) modulating the wavelength of the laser to operate away from the flicker noise due to laser power fluctuations [7]. TLS is also often limited by optical fringes rather than the theoretical detection limit of the detector [7]. These fringes arise from the parasitic Fabry-Pérot cavity introduced into the system by the different components such as the laser source, the detector, the optical windows, and the collimation optics. These fringes are the main contributors to background noise [75]. Various methods have been described in the literature for suppressing the fringes such as wedging of optical components [76], anti-reflective coating for suppressing the Fabry-Pérot effect, dithering/ mechanical vibration of optical components to vary the cavity length, double-tone modulation [75] and using neural algorithms [77]. TLS is also affected by light intensity fluctuations and baseline-fitting errors, which can also be minimized by modulation [78]. Modulation relies on imposing a sinusoidal current component at a high frequency f_m to the slower ramp laser current (ramp current is responsible for spectrum scanning). Thus, the laser wavenumber equation is given as [79], [80]:

$$\nu_l(t) = \bar{\nu}_l(t) + \nu_a \cos(2\pi f_m t), \tag{1.9}$$

where $\bar{\nu}_l(t)$ is the corresponding ramp wavenumber function and ν_a is the corresponding modulation wavenumber amplitude. Substituting the above equation in Beer Lambert's law for an interaction with a gas of small absorption ($\alpha(\nu)l \ll 1$), the transmitted power is given by:

$$\begin{aligned} P(t) &\sim P_o(t)(1-\alpha(\nu)l) \\ &= P_o(t)(1-\alpha(\bar{\nu}_l(t)+\nu_a\cos(2\pi f_m t))\,l), \end{aligned} \tag{1.10}$$

where P_o is the laser power. The imposed harmonic component leads to a periodic signal for the detected power, which can be further decomposed by the Fourier series into its harmonic components including the second harmonic $2f_m$ that is away from the flicker noise. Another advantage of this method is the ability to have a free calibration method independent of the laser power since the ratio between different harmonics is independent of the laser power and depends on the gas absorption [80].

The normalized noise equivalent absorption coefficient (NNEA) is a common figure of merit in the PAS. NNEA is the product of the normalized minimum absorption coefficient (absorption coefficient normalized with respect to the measurement time) and the laser power, so it is dependent only on the detector specifications. Thus, one can compare between different PA detectors. Trying to define such parameters in the DAS, in the case of a shot-noise limited system leads to a power-dependent NNEA, which cannot be used as a comparison figure of merit. However, in some circumstances, the detection limit in the DAS originates from the thermal noise of the detector instead of the shot noise, for example in an uncooled detector, large detector area, or small laser power. The thermal noise increases with the optical detector area A_d and can be related to the specific detectivity in Figure **1-2**. Returning to Equation (1.6) and knowing that $NEP=\sqrt{A_d}/D^*$ [58], the corresponding NNEA can be given by :

$$NNEA_{DAS}=\frac{\sqrt{A_d}}{Dl}. \tag{1.11}$$

In the above equation, the $NNEA$ is path length and area dependent while it is independent onf the optical power. The NNEA curves of the DAS of different detector types are plotted in Figure **1-3** using Equation (1.11)and the data in Figure **1-2**. The curves are for detectors of diameter of 1 mm and path length of 1 m with no propagation losses and assuming that the system is thermal noise limited. For different detector areas, one multiplies the NNEA of the different detectors by $\sqrt{A_d}$, where A_d is in $(mm)^2$. For such curves, the NNEA is independent of the laser power and increasing the source power directly enhances the sensitivity. The nitrogen cooled MCT detectors have the best sensitivity in the MIR range while the InGaAs detector has good performance in the NIR range (1.2 to 3 μm) in addition to the PbS. In the case of different path lengths, one could easily divide the curves by the new length in meters. These curves will be used later to compare DAS and PAS. Also, for different detector diameters, one directly multiplies the curves by $\sqrt{A_d}$ where A_d is in $(mm)^2$.

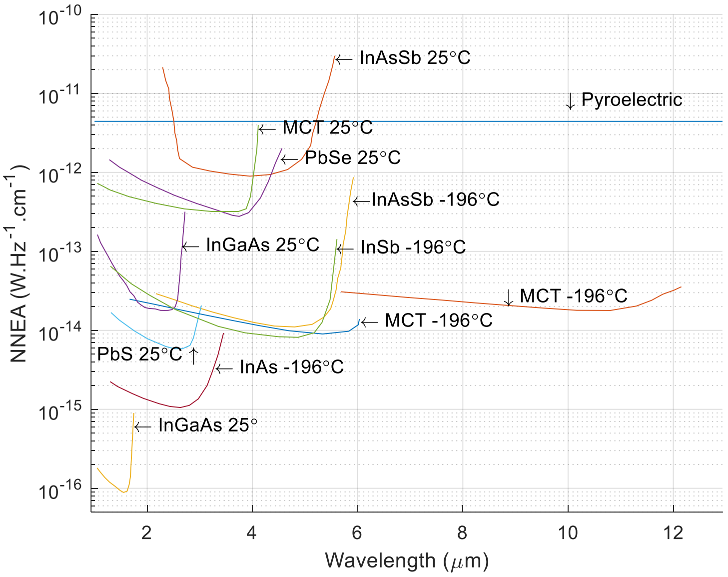

Figure 1-3 NNEA of DAS of different detectors (detector diameter 1 *mm* and path length 1 *m*

1.3.2 Photoacoustic laser spectroscopy

A simple illustration of the PAS mechanism is depicted in Figure 1-4. The system consists mainly of an excitation light source, which could be a laser, an LED, or even a white light source. The light is coupled into an acoustic cell containing a gas that has an absorption at a wavelength aligned with the excitation wavelength. Thus, the gas absorbs the optical energy and the molecules are excited to a higher energy level. After that, the molecules relax the energy in non-radiative in the form of kinetic or translational energy via inelastic collision. Such a process occurs within a time denoted as the relaxation time τ_R. This leads to a rise in the local temperature T, which corresponds directly to a rise in the local pressure P. The heat energy transfers to the walls of the cell within a response time τ_H. Introducing an amplitude modulation for the excitation light leads to variation in the pressure with the time that forms an acoustic wave. This wave propagates inside the PA cell and can be detected by a microphone. The sensitivity of the PA sensors strongly depends on the geometry of the PA cell and can be improved further by operating at its resonance frequency [81], [82]. Most of the cells described in the literature are used in conjunction with cantilevers that have a cylindrical form whose length and diameter typically range from 1 to 20 mm.

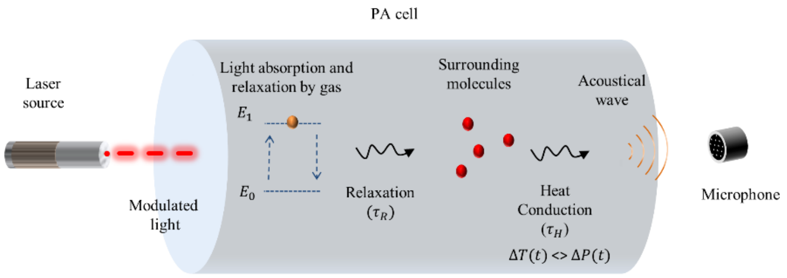

Figure 1-4 Illustration of PAS mechanisms including light absorption, vibrational relaxation, heat conduction, and propagation of acoustical waves.

Theoretical detection limit

In the PAS, a laser of a given wavelength λ and power P_o is modulated with a repetition rate $\omega = 2\pi f\ (rad./s)$. The modulated output from the laser is coupled into a photoacoustic cell of an illumination area A_{cell} and cell length l containing a gas of an absorption coefficient α. The PA cell comprises the cantilever for acoustic wave detection. The cantilever motion can be detected using an interferometer, for high dynamic range and sensitivity. The deflection of the cantilever x produces fringes at the interferometer output, which corresponds to the magnitude of beam deflection [83]. The cantilever dimensions are $b_b \times l_b \times t_b$ (width × length × thickness). Solving a set of equations, namely the gas law equation, heat transfer rate equation, first law of thermodynamics and cantilever second order differential equation, one can find a relation between the absorbed power $P_o \alpha l$ and the beam deflection x (for a non-resonant PA cell), a simplified relation can be found [84]:

$$x = \frac{b_b l_b (\kappa - 1)}{A_{cell} k \omega} \alpha P_o. \tag{1.12}$$

where ω_o, k and Q are the beam resonance angular frequency, stiffness, and quality factor, respectively, and κ is the ratio of the specific heat capacity at constant pressure to the specific heat capacity at a constant volume (for air, $\kappa = 1.4\ \ at\ T = 300\ K$ [85]).

Such an equation is valid when the cantilever is operated in the non-resonant mode of the cantilever ($\omega < 0.25\ \omega_o$) as the Brownian noise is amplified with the PA signal around the resonance and, thus, there is no enhancement in the signal to noise ratio [1][45]. Also, the non-resonance operation is similar to the operation of FTIR spectrometers where a wide range of modulation frequencies with a flat response is required. Second, the thermal response time increases dramatically with increasing the cell volume.

Note evident that the response is independent of the path length. An undesired photoacoustic signal is generated by the windows installed in the PA cell, which can be reduced by increasing the cell length so that the signal is spread over a larger volume[45]. One can define the gas cell constant, as the ratio of cantilever deflection to the product of the absorption coefficient and power. This is given by:

$$C = \frac{b_b l_b(\kappa - 1)}{A_{cell} k\omega} = \frac{(\kappa - 1)}{A_{cell}\rho_b t_b \omega_o^2 \omega}\ \ (m^2 W^{-1}). \tag{1.13}$$

Thus, a noisy PA signal is given by:

$$x = CP_o\alpha + \Delta x_n\sqrt{\Delta f}, \tag{1.14}$$

where Δx_n represents the noise normalized to the square root of the measurement bandwidth. Then the signal to noise ratio, SNR, is given by:

$$SNR = \frac{P_o\alpha C}{\Delta x_n\sqrt{\Delta f}}. \tag{1.15}$$

The minimum detectable absorption coefficient, defined as the detectable absorption coefficient, when SNR is unity, normalized to square root of measurement bandwidth, is given by:

$$\alpha_{min_{PA}} = \frac{\alpha}{SNR\sqrt{\Delta f}} = \frac{\Delta x_n}{P_o C}. \tag{1.16}$$

Then, the $NNEA$ is given by,

$$NNEA_{PAS} = \alpha_{min_{PA}} P_o = \frac{\Delta x_n}{C}. \tag{1.17}$$

It is clear that the $NNEA$ in the PAS is independent of the laser power and measurement time but depends on the cell response and noise. The encountered noise types are acoustical noise, Brownian noise, source fluctuation noise, vibrational (or acceleration) noise, light back-action on the cantilever (fluctuation in radiation pressure)[86], and thermal and shot noise due to the optical detector used in the beam deflection measurement. For an ideally sealed cell, the sum of dominated noises is given by:

$$\Delta x_n^2 = < x_{Bn}^2 > + < x_{Sn}^2 > + < x_{ban}^2 >, \tag{1.18}$$

where x_{Bn}, x_{Sn} and x_{ban} represent the Brownian noise, shot noise (laser source of cantilever detection interferometer), and back-action noise, respectively. The symbols $< >$ mean the statistical average. Increasing the laser power, P_b, leads to decreasing the shot noise but increasing the back-action noise. An optimum value of the power for non-resonant operation is given by [86]:

$$P_b = \frac{k_b c\lambda}{8\pi}, \tag{1.19}$$

where c is the speed of the light. In this case, the total displacement noise can be given by [86]:

$$\Delta x_n^2 = \left(\frac{4K_B T_{BG}}{\omega_o Q} + \frac{2h}{\pi}\right)\frac{\Delta f}{k}. \tag{1.20}$$

The Brownian noise term is the dominating term as long as $f_o Q \ll \frac{K_B T_{BG}}{h} \sim 6 \times 10^{12}$. This condition is practically satisfied even at high frequencies. The stiffness equation is given by [87]:

$$k = \frac{\lambda_n^4}{12}\frac{t_b^3}{l_b^3} b_b E, \tag{1.21}$$

where E is Young's modulus and λ_n is the mode Eigenvalue (for the first mode: $\lambda_1 = 1.875$). In the viscous regime (air pressure is in the vicinity of atmospheric pressure), by modeling the beam as a string of spherical beads, the quality factor can be given by [87]:

$$Q = \frac{\lambda_n^2 t_b^2 \sqrt{E\rho_b}}{12\sqrt{3}\pi\mu l_b\left(1 + b_b\sqrt{\frac{\rho_g \omega}{2\mu}}\right)}, \tag{1.22}$$

where μ is the viscosity of the surrounding fluid (For air: μ=18.6 $\mu Pa.s$ and for nitrogen: μ= 17.9 $\mu Pa.s$ at 300 K and 1 atm. [88]). In view of Equation(1.16), (1.20), (1.21), and (1.22), α_{min} is given by:

$$\alpha_{min_{PA}} = \frac{4\omega A_{cell}}{P_o(\kappa - 1)}\sqrt{\frac{3\sqrt{3}K_B T_{BG}\,\pi\mu\omega_o}{\lambda_n^2 t_b}\left(\frac{1}{b_b} + \sqrt{\frac{\rho_g \omega}{2\mu}}\right)\sqrt{\frac{\rho_b}{E}}}. \tag{1.23}$$

Fora beam diameter in the range of few mms or larger ($f b_b^2 \gg \frac{\mu}{\pi\rho_g} \sim 5.1\ (mm)^2.s^{-1}$), Equation 24 can be approximated by:

$$\alpha_{min_{PA}} = \frac{13.6}{P_o}\left(\frac{\omega}{\omega_o}\right)^{1.25}\omega_o^{1.75}\,\theta_{PA}\Gamma_g, \tag{1.24}$$

where θ_{PA} is frequency independent but depends on the cantilever and cell area. It is given by:

$$\theta_{PA} = A_{cell}\sqrt{\frac{1}{\lambda_n^2 t_b}\sqrt{\frac{\rho_b}{E}}}, \tag{1.25}$$

and

$$\Gamma_g = \frac{\sqrt{K_B T_{BG}\sqrt{\rho_g \mu}}}{(\kappa-1)}. \tag{1.26}$$

From the above equation, one can see that the detection limit depends on different parameters which correspond to different system components as follows: 1) ratio of the modulation frequency to the cantilever resonance frequency, cantilever resonance frequency, cantilever thickness, and cantilever specific stiffness E/ρ_b.,2) laser power, and 3) cell area and the density of the gas inside.

Decreasing the ratio of ω/ω_o by 10 dB enhances the detection limit by 12.5 dB. In addition, the detection limit is enhanced by decreasing cantilever resonance means worse the detection limit. Using typical values of the cell diameter, the modulation frequency and the cantilever thickness in the literature, one can draw a color plot of NNEA for different ω/ω_o and resonance frequencies f_o in the case of unity θ_{PA} as shown in Figure 1-5 (a). For different θ_{PA}, one simply multiplies the curves by the corresponding value.
Increasing the cantilever thickness enhances performance. However, increasing the thickness by 10 dB increases the stiffness by 30 dB according to Equation (1.21)(1.22), which increases the optimum laser power by 30 dB according to Equation (1.21). Thus, increasing the thickness is not practically applicable. The higher E/ρ_b is, the better the sensitivity. NNEA is also plotted Figure 1-5 (b) for different cantilever thicknesses and different E/ρ_b($f_o = 500\ Hz$, ω/ω_o= 0.2 and the cell diameter equals 5 mm). It is apparent from this figure that silicon has high specific strength compared to different metals and polymers.

The detection limit is enhanced linearly with the source power[43], which is an advantage compared to the DAS. Decreasing the cell area enhances the system's sensitivity unless it affects the flow of the gas into the cavity. Finally, it is apparent from Equation(1.24) that there is no dependence on the wavelength of operation as compared to the DAS.

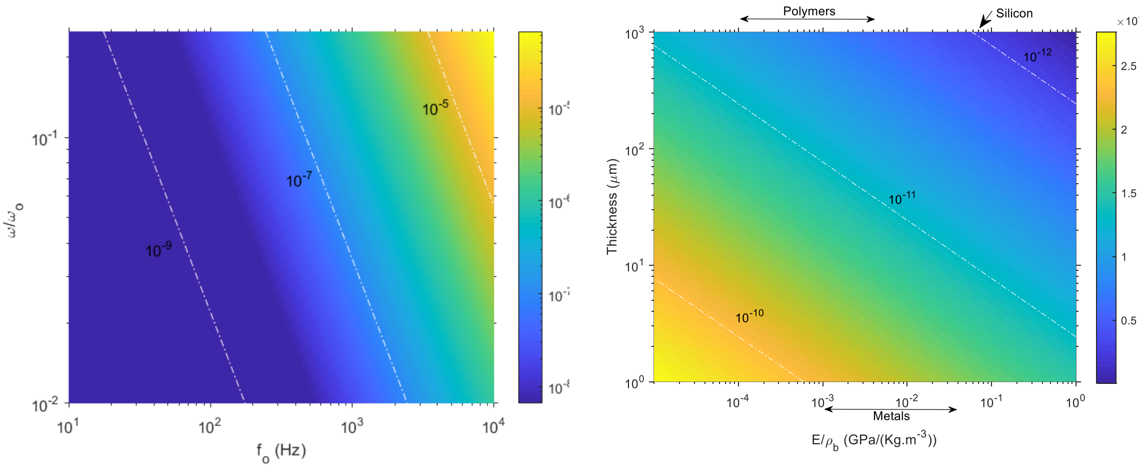

(a) (b)

Figure 1-5 (a) Color map of $NNEA$ versus ω/ω_o and resonance frequency f_o of the cantilever $(\theta_{PA} = 1)$. (b) Color plot of NNEA as function of stiffness and cantilever thickness (($f_o = 500\ Hz$, ω/ω_o= 0.2 and cell diameter = 5 mm).

Excitation sources

Erbium-doped ring lasers [89], DFB [90], [91], CO_2 lasers [92], visible LEDs [93], IR LEDs [94] and THz diodes [95] [96] are among the source types used with PA cells equipped with cantilevers. To enhance the sensitivity of such systems, optical amplifiers such as Erbium-doped fiber amplifiers have been used [89]. Another type of source is blackbody emitters followed by an IR filter at the corresponding absorption wavelength of the gas. This technique is characterized by its simplicity but lack of power and the slow response time limit its modulation frequency to less than 50 Hz [97]. Blackbody sources are either electrically amplitude modulated (EM) at low frequencies (20 Hz) [98] or modulated using a mechanical chopper [83]. In the case of the laser, it is more efficient to use wavelength modulation and detect the 2nd harmonic signal [89], [99]. When using wavelength modulation, the PA signal is dependent on wavelength-dependent losses, such as the absorption lines of the gases, not the losses introduced by the windows and the walls[47], [82]. Compared to conventional sinusoidal modulation, triangular-shaped and quasi-square waves enhance the photoacoustic signal by factors of 1.12, 1.42, and 1.57, respectively [100]. The modulation frequency is off-resonance for a flat response [90], [101], [102] or at resonance[99], [103]. For the 2nd harmonic detection, the modulation frequency should be half the 2nd harmonic frequency. For multiple component analysis at the same time, multiple laser sources can be combined using frequency division multiplexing (where each laser is WM modulated at a different frequency) and detected using the same PA detector[104].

Acoustic detector

Microphones used in the PAS can be capacitive (electret or condenser) [105], [106], piezoelectric, quartz tuning forks [107], cantilevers, polymer diaphragms [108], [109] and membranes. In recent years, cantilevers have appeared as a strong candidate for PA detection taking advantage of the intensive studies and optimizations of cantilevers in atomic force microscopes (AFM). The motion of the cantilever is characterized by its high linearity and large dynamic range, which is larger than that of conventional membranes [82]–[84], [92], [110], while the limited sensitivity of the membrane cannot be improved by further decreasing the gap [84]. An experimental comparison of an electret microphone, a differential microphone, and a cantilever shows the superiority of using cantilevers by two orders of magnitudes over the microphone [84], [111], [112]. NNEA in the order of $10^{-10} cm^{-1} W\ Hz^{-0.5}$ can be achieved without using a resonant PA cell [113]. These values can be attained using an electret microphone in the case of a resonant PA cell. For example, a differential Helmholtz resonator PA cell (resonance frequency is 320 Hz) equipped with electret microphones (sensitivity 100 mV/Pa) has an NNEA of about 2.4×10^{-10} [114].

An alternative is to use a quartz tuning fork as a resonant transducer. It is characterized by its high-quality factor (can reach 8000 or even 18,000 at low pressure [115]) and its immunity to acoustical noise due to its high resonance frequency (32.8 kHz) [84]. Acoustical resonance in conjunction with quartz can be used to improve sensitivity[82]. It can also be used in conjunction with a high finesse cavity [116] or multi-pass cell [117] to further improve the sensitivity. The obtained NNEA values are around $10^{-10}\ cm^{-1} W\ Hz^{-0.5}$ [115], [118], [119]. Better sensitivity is reached by measuring methanol (CH_3OH) using a THz quantum cascade laser at 3.93 THz. The NNEA achieved was $3.75 \times 10^{-11}\ cm^{-1} W\ Hz^{-0.5}$ [120]. However, using such a structure has a drawback in that precise adjustment of the modulation frequency is needed [121] and it is incompatible with blackbody sources, which cannot be modulated with such a high frequency [84]. Finally, it cannot be used with scanning FTIR spectrometers due its limited bandwidth. A detailed review of QEPAS was recently published [122]. Thus, the focus of this review is the cantilever-based PAS.

For the cantilever-based microphone, different materials are used such as silicon[83], mica for highly corrosive chemicals [123], stainless steel [124], silica, borosilicate [99] and polyvinylidene fluoride [125]. The process of fabricating such cantilevers made from silicon is discussed in [126].

The higher the length to thickness ratio, the less stiff the beam, and consequently, the higher the sensitivity. However, this makes the cantilever more fragile and easier to break [96]. In the case of a system dominated by Brownian noise, this means greater sensitivity to Brownian noise. With respect to cantilever gap, a large gap means more gas leakage and in the case of low pressure, the beam behaves as an undamped structure. The minimum gap that can be achieved is dependent on the minimum feature size of the lithography process [95] used in cantilever fabrication.

Different locations for the cantilever in the system have been described. These include: 1) the cantilever can be placed in the PA cell at one end of the cylinder while the excitation light is from the other end [99]; 2) both the excitation and readout fibers are on the same side[127], and 3) the cantilever can be placed at the side of the cell[102].

The detection of the cantilever's motion can be performed using a Michelson interferometer (MI) [128], [129], Fabry-Pérot cavity [130], or the piezo-electric effect[125]. The Fabry-Pérot configuration can be a white-light based Fabry-Pérot interferometer (WL-FPI) as in [130], where the fiber end and cantilever side constitute such a Fabry-Pérot configuration, or a laser-based Fabry-Pérot interferometer (L-FPI) [131]. Fabry-Pérot cavities are characterized by their high sensitivity, small size, and immunity to electromagnetic radiation [89]. Alternatively, Michelson interferometers can be used with a sensitivity down to a few picometers [83]. In the Michelson configuration, an iris can be placed in the path of the laser beam before impinging on the cantilever, which controls the size of the beam impinging on and reflecting off the cantilever In the path of[95]. Its disadvantages are cost and complexity [110], [132]. In its simplest form, the cantilever deflection can be measured using a laser impinged on the cantilever with a certain incidence angle, and the reflected light is detected using a quadrant detector [92], [103]. Instead of using the optical detection methods for detecting cantilever vibration, one could use a cantilever made of a material that has a piezoelectric effect. In this case, the output piezo-electric signal, due to the film vibration, can be related to the PA signal.

1.3.3 Comparison between photoacoustic and direct detection in TLS

A comparison between two systems using Equation (1.8) and Equation (1.24) can be carried out based on the ratio between the minimum absorption coefficients in the PAS system as compared to the optical detector system. This ratio is given by:

$$\gamma = \frac{\alpha_{min_{PA}}}{\alpha_{min_{DAS}}} = 9.6\sqrt{\frac{R_i(\lambda)}{q\zeta P_o}}\ \left(\frac{\omega}{\omega_o}\right)^{1.25} \omega_o^{1.75}\ \theta_{PA} l \Gamma_g. \tag{1.27}$$

From the above equation, one can conclude the following. The DAS using TLS outperforms in the case of lower laser power and longer path length, $\left(\frac{\omega}{\omega_o}\right)^{1.25}\omega_o^{1.75}\theta_{PA}l$. On the other hand, the PA system may be preferred when size is a limitation and there is a need for a compact gas cell since θ_{PA} is proportional to the cell area. The term $\left(\frac{\omega}{\omega_o}\right)^{1.25}\omega_o^{1.75}\theta_{PA}l$ is dependent on detector parameters DAS or the PA cell in the PAS. A general color plot of γ versus wavelength and source power is illustrated in Figure 1-6 (a) for the unity value of this term. The white contour line represents the trajectory of the unity ratio. For longer wavelengths and lower powers, the DAS outperforms the PAS. For a given laser power, modulation frequency, cell area, and cantilever thickness of the PAS compared to the DAS of a given path length l, one can check if the direct or the photoacoustic system has better sensitivity at the required wavelength of operation. For example, for the high-performance PA gas sensor mentioned in [47], [133] ($t_b = 10\ \mu m$, cell diameter equals to 4 mm), the respective θ_{PA} equals $2.2\ \times 10^{-5}\ (Pa^{-1}.kg.(mm)^3)^{-0.25}$. Then, in the case of $\omega/\omega_o = 0.25$ and $f_o = 480\ Hz$, one can evaluate the term $\left(\frac{\omega}{\omega_o}\right)^{1.25}\omega_o^{1.75}\theta_{PA}$ to be $5\ Hz^{1.75}(Pa^{-1}.kg.(mm)^3)^{-0.25}$. When comparing with a laser based DAS of path length 0.2 m, the term $\left(\frac{\omega}{\omega_o}\right)^{1.25}\omega_o^{1.75}\theta_{PA}l$ will be unity as assumed in Figure 1-6 (a). When the path length is 20 m, the unity contour line should be moved to the upper left corner of the plot and the DAS will best performer for a larger range of laser powers and wavelength ranges. Therefore, for lasers with the power of a few mWs the DA systems with path lengths greater than tens of mms should provide better sensitivity. Increasing the power to hundreds of mWs or even greater results in the PAS having better sensitivity as compared to the DAS with a path length smaller than hundreds of mms.

The NNEA for a DAS in a shot-noise limited system is inversely proportional to the square root of the input laser power when compared to the NNEA in the PAS which is independent of laser power. But as shown before, for a thermal noise limited DAS, the NNEA becomes independent of the laser power. Thus, one can plot the NNEA of the PAS in conjunction with the NNEA of the DAS which is depicted in Figure 1-3, to have a quantitative comparison between the two technologies. For the PAS (dash-dot curve), the parameters are $t_b = 10\ \mu m, f_o = 500\ Hz, \frac{\omega}{\omega_o} = 0.25$ and cell diameter = 5 mm. For the DAS, the diameter of the optical detector is 1 mm and path length is 1 m in Figure 1-6 (b) and 10 mm in Figure 1-6 (c). To compare the PAS and the DAS with path lengths of 1 m or longer, the theoretical detection limit of DAS is better, except for the InAsSb detector operating at room temperature. Using detectors cooled down to -196 ℃ enhances dramatically the detection limit when compared to the PAS (i.e. NNEA = $10^{-14}\ WHz^{-1}cm^{-1}$ using MCT cooled by nitrogen). However, if one is interested in applications involving small sampling volumes and short path lengths, the PAS becomes better than the DAS using thermal detectors or uncooled MCT or PbSe. However, InGaAs, PbS, and ultra-cooled detectors still have superior performance.

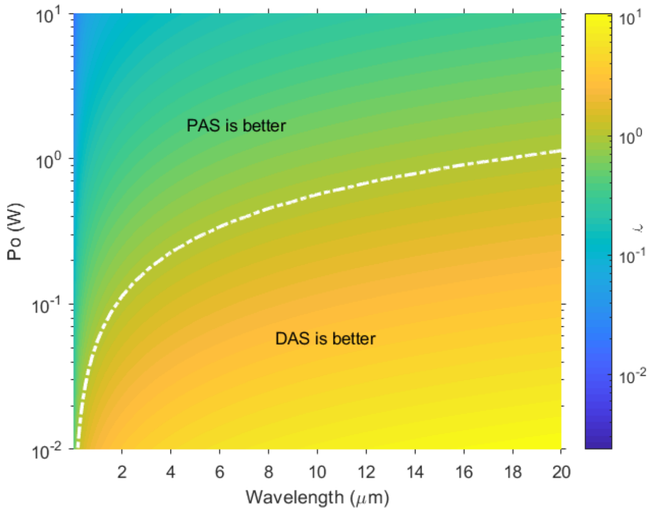

(a)

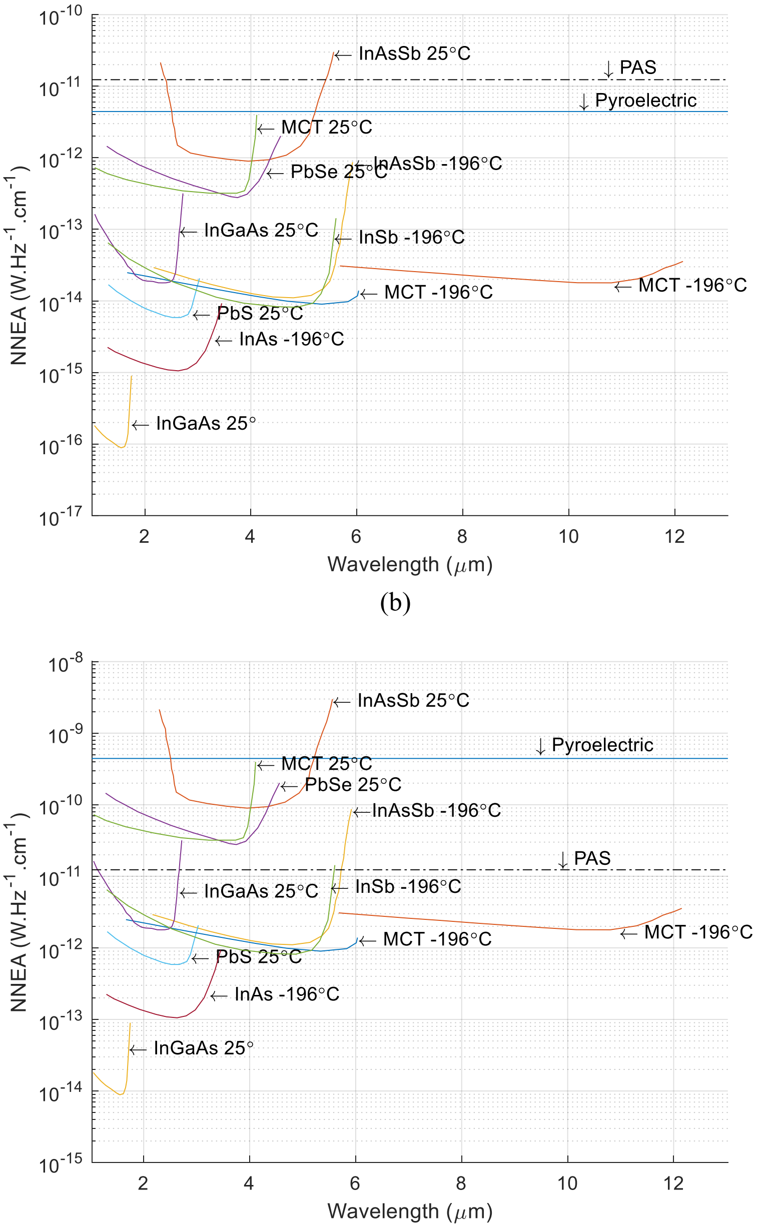

(b)

(c)

Figure 1-6 (a) Color plot of the ratio of the normalized minimum absorption coefficient of the PA system to that of the DA system for different wavelengths and different laser powers in the case of unity system parameters $((\frac{\omega}{\omega_o})^{1.25}\omega_o^{1.75}\theta_{PA}l)$. The contour line represents the trajectory of unity ratio where for longer wavelengths and smaller powers, DAS is better. (b)-(c) NNEA of DAS of different detectors (solid curves) (detector diameter= 1 mm), PAS ($t_b = 10\ \mu m,$ cell diameter $= 5\ mm, f_o = 500\ Hz, \frac{\omega}{\omega_o} = 0.25$ (dash dot curves) where the path length = 1 m in figure (b) and the path length = 10 mm in figure (c).

.

1.4 FTIR spectroscopy

The FTIR spectrometers have a large spectral range which can simultaneously detect different gases. Good sensitivity can also be achieved using the FTIR but it is less than TDLS due to the use of a broadband light source instead of a laser. The Michelson interferometer is the main type used in FTIR spectroscopy. The output light from the interferometer is modulated in the form of an interferogram versus time due to the interferometer's mirror motion. This interferogram is mathematically an auto-correlation function and so its Fourier transform gives the spectrum of the input light. In the FTIR based DAS, a gas cell is placed between the light source and the interferometer. Thus, the spectrum measured by the spectrometer represents gas transmission, not the respective absorbance. The optical power is detected by an optical detector. In another configuration, the gas cell and interferometer positions can be swapped as shown in Figure 1-1(c). Replacing the gas cell and the optical detector with a PA cell and a cantilever leads to the FTIR based PAS as depicted in Figure 1-1(d). The output modulated light from the interferometer is coupled to the PA cell and the power corresponding to the absorption wavelengths are only absorbed by the gas. The absorbed light is further converted into an acoustic signal and detected by the microphone (cantilever). The acoustic signal is in the form of an interferogram (i.e., autocorrelation function) but its Fourier transform corresponds to the spectrum of absorbed power. Ideally, both systems should have the same absorption spectrum, either directly by the PAS or indirectly by the DAS. However, the detection method in the PAS depends on a heating mechanism and may cause broadening of the absorption peaks leading to spectra different from those measured with direct absorption spectroscopy using the FTIR spectrometer [134].

1.4.1 Direct absorption FTIR spectroscopy

The optical source used in the FTIR spectroscopy can be filament-based, a plasma source, a mode-locked laser[135], or a frequency-comb source. Usually, conventional filament sources are made from silicon carbide (SiC) (Globar source) or ceramic rod (Nernst source) for the MIR range, whereas tungsten lamps are used for wavelengths lower than 5.5 μm (tungsten-halogen has a spectrum limited to 2.6 μm). A plasma source can be used for wideband operation down to UV[136], [137] with a larger radiance (equivalent T_{src} =

9000K[136] or even more [138]) compared to filament-based sources at the expense of power consumption and source fluctuations. A frequency-comb source can be also used for wideband wavelength range measurements[139]. The gas cell can be a multi-pass cell such as a White cell[18] [37] or HWG [140]. An open-air configuration can be used instead of a gas cell for measuring gases over long distances (open-path FTIR). InGaAs detectors are often used when wavelengths are less than 2.5 μm, and InSb detectors have a maximum detectivity for wavelengths less than 5.5 μm and mercury cadmium telluride (MCT) detectors are used when the wavelength ranges from 7.7 μm to 14 μm[31], [70].

Theoretical detection limit

The power coupled into the detector is the summation of the contribution from a wide band of wavelengths. The average detector current is to some extent similar to Equation (1.7) and given by:

$$i = \int_{\lambda_{min}}^{\lambda_c} B_{src}(\lambda')\, \zeta\, TP_o\, \eta\, R_i(\lambda')\, d\lambda' + \int_0^{\lambda_c} B_{BG}(\lambda')\, TP_d R_i(\lambda') d\lambda', \qquad (1.28)$$

where the first term represents the output power from the interferometer followed by the gas cell, TP_o is the spectrometer output throughput in $Sr.m^2$ and TP_d is the detector throughput and is given by $\pi A_d \sin^2\theta_d$ (assuming Lambertian distribution of background emission), λ_{min} is the minimum operation wavelength of the interferometer (limited by the beam splitter material or the detector). The maximum limit of the integration in Equation (1.28) is λ_c, which is the peak sensitivity of the detector (cutoff wavelength in semiconductor detection), ζ represents the light transmission losses in the interferometer and B_{src} represents the spectral radiance of the black body source of temperature T_{src}.

The radiation pattern is assumed to be a Lambertian source (of constant radiance). The coupling reaches a maximum when TP_d equals to TP_o. In such a case, using Equation (1.1), (1.3) and Equation(1.28), the NEP is given by :

$$NEP = \frac{1}{R_i(\lambda)} \sqrt{2q\left(\int_{\lambda_{min}}^{\lambda_c} B_{src}(\lambda')\zeta\, TP_o\; R_i(\lambda')\, d\lambda' + \int_0^{\lambda_c} B_{BG}(\lambda') TP_o R_i(\lambda')\, d\lambda'\right)}. \qquad (1.29)$$

The second term under the square root can be neglected for the following conditions: small λ_{min}, compact spectrometer with low insertion losses (<10 dB) and $T_{src} > 500K$ (as the power $\propto T^4$ according to Stefan's law).

The linewidth of the gases is around a few GHz (tenths of cm^{-1} as mentioned before, while the reported resolution of FTIR in gas sensing ranges from a few tenths up to tens of cm^{-1} (see the next section). Thus, the spectrometer resolution affects the measured absorbance. From the definition of the SNR in Equation(1.5), one should take into account the spectrometer resolution as follows:

$$SNR(\lambda) = \frac{P_o(\lambda)\zeta l\, \alpha(\nu) * sinc(\nu\, \Delta\nu^{-1})\Delta\nu^{-1}}{NEP\sqrt{\Delta f}}, \tag{1.30}$$

where $\Delta\nu$ is the spectrometer resolution in wavenumber, $\nu = 1/\lambda$ and $*$ denotes convolution. The $sinc$ function represents the response function of the Fourier transform spectrometer (Fourier transform of a Boxcar function)[23]. The convolution term is written as a function of ν instead of λ^{-1}only as a simplification (convolution should be performed in the wavenumber domain). The mean output power P_o from the Michelson interferometer is expressed as the following ($\Delta\lambda = \lambda^2\Delta\nu$):

$$P_o(\lambda) = B_{src}(\lambda)\, \zeta\, TP_o\lambda^2\Delta\nu\,. \tag{1.31}$$

It is assumed that the source spectrum is slowly varying with respect to spectrometer resolution and gas absorption, thus it is excluded from convolution. Such an assumption is true since the light source has a wide spectral range (black body). The absorption coefficient $\alpha(\nu)$ is given by $\alpha(\nu) = \alpha_o f_g(\nu)$, where α_o is the absorption peak value and $f_g(\nu)$ is the gas line shape (normalized to one). The $f_g(\nu)$ has a Lorentzian profile ($\frac{\Delta\nu_g^2}{\Delta\nu_g^2+(\nu-\nu_o)^2}$) when the pressures are low as pressure broadening dominates. The $\Delta\nu_g$ represents the FWHM of the gas line shape and ν_o is its center. $f_g(\nu)$ has a Gaussian profile ($e^{-\frac{(\nu-\nu_o)^2 \ln 2}{\Delta\nu_g^2}}$) in case of high atmosphere (low pressure)[141]. Using the Fourier transform properties, the absorbance peak ($\nu = \nu_o$), for a Lorentzian gas profile, is given by:

$$A(\nu = \nu_o) = \alpha_o l\left(1 - e^{-\frac{\Delta\nu_g \pi}{\Delta\nu}}\right)\log_{10} e\,, \tag{1.32}$$

Whereas for a Gaussian gas profile, the absorbance is given by:

$$A(\nu = \nu_o) = \alpha_o l\, \mathrm{erf}\left(\frac{\pi\Delta\nu_g}{2\sqrt{\ln 2}\,\Delta\nu}\right)\log_{10} e\,, \tag{1.33}$$

where erf corresponds to the error function. It is obvious that when $\Delta\nu \to \infty$, the absorbance peak reaches the extreme value $\alpha_o l \log_{10} e$. The normalized absorbance is depicted in

Figure 1-7 (a). When $\Delta\nu \gg \Delta\nu_g$, the absorbance enhancement is linear with enhanced resolution ($\Delta\nu^{-1}\uparrow$) ($\sim\frac{\Delta\nu_g\pi}{\Delta\nu}$ in the case of Lorentzian and $\frac{\Delta\nu_g}{\Delta\nu}\sqrt{\frac{\pi}{\ln 2}}$). Saturation occurs for $\Delta\nu < \Delta\nu_g$.

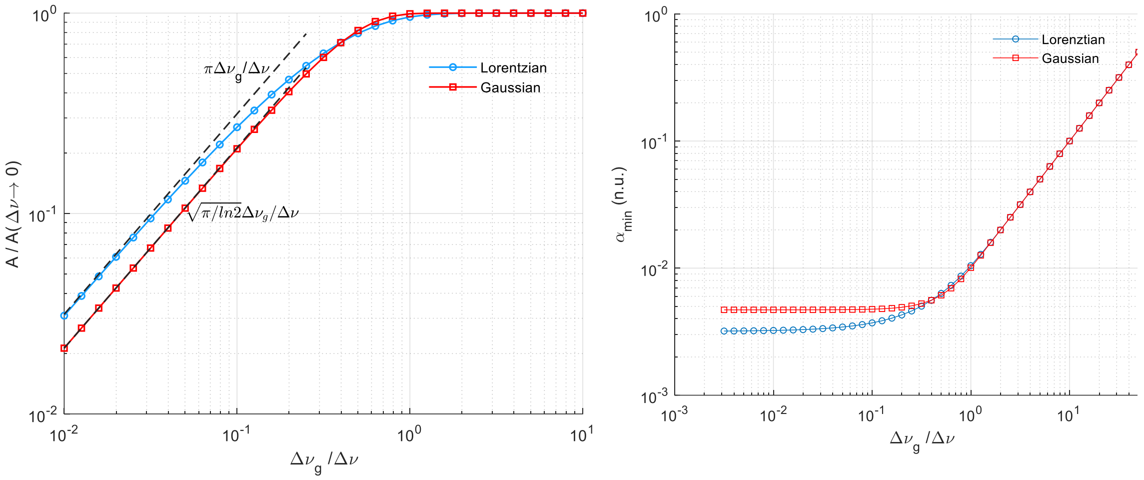

(a) (b)

Figure 1-7 (a) Normalized absorbance versus $\Delta\nu_g/\Delta\nu$ in the case of the Lorentzian and Gaussian profiles. Approximated linear lines for small $\Delta\nu_g/\Delta\nu$ are plotted in dashed black lines. (b) Normalized α_{min} versus $\Delta\nu_g/\Delta\nu$ in the case of the Lorentzian and Gaussian profile.

Thus, using Equations (1.6), (1.29) and (1.33) α_{min} at the absorbance peak is given by:

$$\alpha_{min}(\lambda)\sim\frac{\theta_{DAS}}{R_i(\lambda)B_{src}(\lambda)\,\lambda^2}\sqrt{2q\int_{\lambda_{min}}^{\lambda_c} B_{src}(\lambda')R_i(\lambda')\,d\lambda'}, \tag{1.34}$$

where θ_{DAS} is the only parameter which depends on the specifications of the different system components and is independent of the wavelength and it is given by $\left(\sqrt{\zeta\,TP_o}\,\Delta\nu l\left(1-e^{-\frac{\Delta\nu_g\pi}{\Delta\nu}}\right)\right)^{-1}$ or $\left(\sqrt{\zeta\,TP_o}\,\Delta\nu l\,\mathrm{erf}\left(\frac{\pi\Delta\nu_g}{2\sqrt{\ln 2}\Delta\nu}\right)\right)^{-1}$ $[cm.Sr^{-0.5}]$ The normalized α_{min} is plotted as a function of $\Delta\nu_g/\Delta\nu$ in Figure 1-7 (b). The α_{min} is saturated $\Delta\nu \gg \Delta\nu_g$ because within this region increasing the resolution increases both the absorbance and the noise collected, by the same factor. Further improving the resolution will not enhance the absorbance by the same factor and α_{min} degrades. Thus, the optimum point is to operate at low resolution. However, this is not practical as this means that the peaks of different gases will interfere and cannot be discriminated.

Increasing the interferometer throughput enhances α_{min}. Increasing the cell length also enhances the absorbance as long as no more losses are introduced, which can be further taken into consideration in ζ. The mirror velocity does not affect the normalized absorption coefficient.

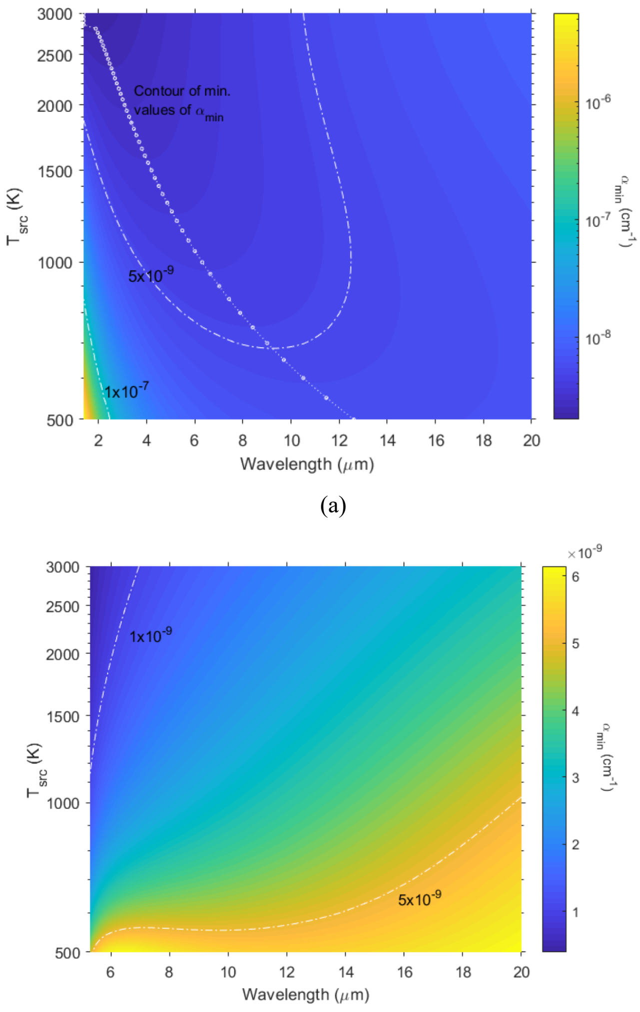

(a)

(b)

Figure 1-8 α_{min} versus wavelength and source temperature ($\theta_{sys} = 1$) in case of (a)$\lambda_{min} = 1\mu m$ (b) $\lambda_{min} = 5\mu m$ .Contour lines of different values of α_{min} are plotted. Also, contour of minimum value of α_{min} is plotted if found.

For a system having a minimum wavelength of detection, λ_{min} of $1\ \mu m$, one can plot color mapping of the α_{min} for different absorption wavelengths and different T_{src}, for a unity θ_{sys} (i.e. $\zeta = 1,\ TP = 0.01(cm)^2.Sr, \Delta\nu = 1cm^{-1}\ and\ l = 100\ mm$), as depicted in Figure 1-8 (a). The contour line of minimum value of α_{min} for each value of T_{src} is plotted (solid line with markers), showing that the corresponding absorption wavelength increases with decreasing source temperature. An example of using an optical source of T_{src} of 2000 K, the minimum absorption coefficient at the wavelength of 3 μm is $3 \times 10^{-9}\ cm^{-1}$, which corresponds to a detection limit of 0.1 *ppb* of methane (CH_4). For a system with a different θ_{sys}, one can directly multiply the plot by θ_{DAS}, where increasing θ_{DAS} means higher α_{min} (poorer detectivity).

Using a source of higher temperature enhances the detection limit only for short wavelengths (less than 8 μm for $\lambda_{min} = 1\ \mu m$) whereas this is not the case for longer wavelengths due to the increased shot noise (larger spectral power is absorbed). The situation is reversed in the case of increasing the minimum wavelength of detection (limiting the spectral range). That is why it is advised to use a filter to limit the spectral range of the spectrometer to only the spectral band of interest to decrease the shot noise.

1.4.2 Photoacoustic FTIR spectroscopy

In the FTIR based PAS, the spectrometer can be operated in one of two modes: rapid scanning or step scanning. The rapid mode is the conventional mode of operation, where the mirror of the Michelson interferometer is in continuous motion with a given velocity $\mathrm{v_M}$. Such motion leads to a wavelength-dependent modulation (sinusoidal amplitude modulation of each wavelength with a frequency related to its respective wavelength). The respective modulation frequency is given by $f = 2\mathrm{v_M}/\lambda$ [142], which is the same frequency as the PA signal. This leads to a high frequency of operation. In the case of step scanning, the mirror is moved in step scan motion, which requires an additional optical modulator after the interferometer to modulate the light for the PA cell. The next analysis will focus on the continuous scanning mode. Different optical sources are reported to be used in FTIR based PAS such as optical parametric oscillator OPO [28], supercontinuum source [143], and optical frequency comb [121]. Regarding the acoustic detector, it can be based on a microphone [144]–[146]or cantilever [147], [148].

Theoretical detection limit

As was seen in Figure 1-1 (d), and according to the prior analyses, having as small a PA cell area as possible is better given all the interferometer output power is coupled to the PA cell. Thus, the optimum cell area A_{cell} is given when the cell throughput $\pi A_{cell} \sin \theta_{cell}^2$ equals the interferometer throughput. Having a PA cell of a maximum acceptance angle ($\theta_{cell} = \pi/2$), the P_o is rewritten as:

$$P_o(\lambda) = B_{src}(\lambda)\zeta\pi A_{cell}\lambda^2\Delta\nu, \tag{1.35}$$

whereas Equation(1.6) will be as follows:

$$SNR = \frac{P_o C\, \alpha(\nu)*sinc(\nu\, \Delta\nu^{-1})\Delta\nu^{-1}}{\Delta x_n\sqrt{\Delta f}}. \tag{1.36}$$

Using Equation (1.24), (1.35) and (1.36), α_{min} for the Lorentzian peak is given by:

$$\alpha_{min} = \frac{4\omega}{(\kappa-1)\pi B_{src}(\lambda)\zeta\, \lambda^2\Delta\nu\left(1-e^{-\frac{\Delta\nu_g\pi}{\Delta\nu}}\right)}\sqrt{\frac{3K_B T_{BG}\,\pi\omega_o}{\lambda_n^2 t_b}\sqrt{\frac{3\rho_g\rho_b\omega\mu}{2E}}}. \tag{1.37}$$

The modulation frequency ω can be related to its respective wavelength λ (i.e. λ_o is the corresponding wavelength at the resonance frequency). The maximum frequency of operation $\omega_{max} = 0.25\omega_o$, for the operation out of the resonant mode of the cantilever. This means that the minimum wavelength of the operation of the interferometer can be related to λ_o by $\lambda_{min} = 4\lambda_o$. Then, α_{min} will be:

$$\alpha_{min} \sim 726\frac{\theta_{PA}}{B_{src}(\lambda)\ \lambda^{3.25}\,(\kappa-1)}\sqrt{\frac{K_B T_{BG}\sqrt{\rho_g\mu}}{\lambda_{min}}}, \tag{1.38}$$

where θ_{PA} is wavelength-independent and depends on the specifications of different components and is given by:

$$\theta_{PA} = \frac{1}{\zeta\,\Delta\nu\left(1-e^{-\frac{\Delta\nu_g\pi}{\Delta\nu}}\right)}\sqrt{\frac{\mathrm{v}_{\mathrm{M}}^{3.5}}{\lambda_n^2 t_b}\sqrt{\frac{\rho_b}{E}}}. \tag{1.39}$$

The α_{min} has the same dependence on the resolution as in the FTIR based DAS. It is important to note that the acoustical noise is assumed to be small with tight PA cell seals. To illustrate the dependence of the system on wavelength, the α_{min} is plotted for different source temperatures T_{src}, at unity θ_{PA} and $\lambda_{min} = 1\mu m$, in Figure 1-9. For a system with different θ_{PA}, one just multiplies the plot by $\theta_{sys_{PA}}$. From these curves, it is clear that for longer wavelengths, the detection limit is better. This is because the longer wavelengths correspond to lower frequencies of modulation (PA signal ∝ ω^{-1}, due to heat conduction response time). One can also observe the following: 1) increasing the resonance frequency (decreasing λ_{min} (down to UV)) degrades α_{min}.; 2) increasing source radiance (higher optical source temperature) and decreasing the background temperature enhances the detection limit; 3)the detection limit is enhanced linearly with the source brightness, which is an advantage compared to the DAS, and 4) the detection limit is directly proportional to $\mathrm{v}_{\mathrm{M}}^{1.75}$. Thus, the mirror velocity should be operated in step mode or with slow motion (less than 0.1 *m/s*) to avoid such notable degradation in the performance.

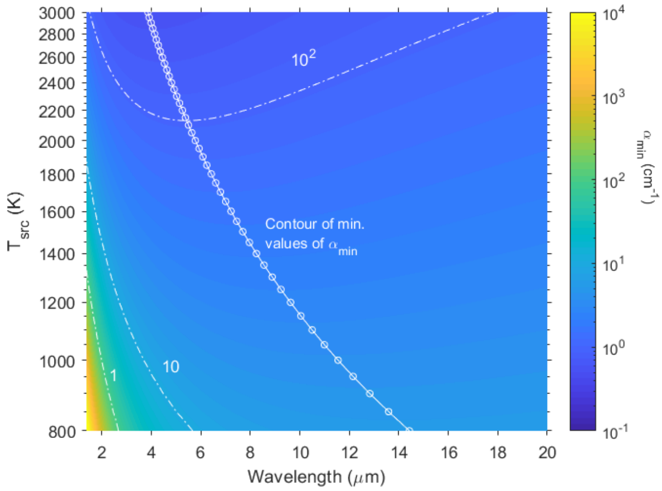

Figure 1-9 α_{min} of the FTIR based PAS as a function of wavelength and source temperature ($\theta_{sys_{PA}} = 1$).

1.4.3 Comparison between Acoustic and optical in Fourier transform spectroscopy

A comparison between the two systems based on FTIR spectroscopy, using (1.34)and (1.38), can be expressed by the ratio of the minimum absorption coefficient in the PAS system to that of the DAS. This is given by:

$$\gamma = \frac{\alpha_{min_{PA}}}{\alpha_{min_{DAS}}} = \Omega_g \frac{\theta_{PA}}{\theta_{DAS}} \frac{R_i(\lambda)}{\lambda^{1.25}\sqrt{\int_{\lambda_{min}}^{\lambda} B_{src}(\lambda\prime) R_i(\lambda\prime)\, d\lambda\prime}}, \tag{1.40}$$

where $\alpha_{min_{PA}}$ and $\alpha_{min_{DAS}}$ represent the normalized minimum absorption coefficient for the FTIR based PAS and the FTIR based DAS, respectively. The parameter Ω_g is given by:

$$\Omega_g = 513\sqrt{\frac{K_B T_{BG}\sqrt{\rho_g \mu}}{q\lambda_{min}(\kappa-1)^2}}. \tag{1.41}$$

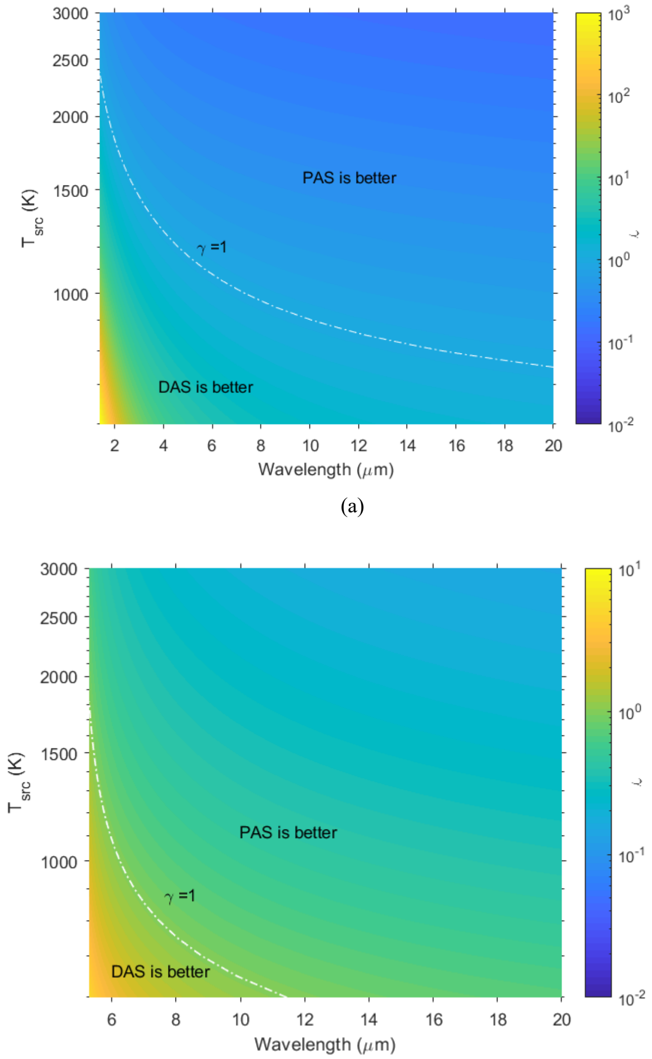

(a)

(b)

Figure 1-10 (a)-(b) Ratio of the absorption coefficient of the FTIR based PAS and FTIR based DAS as a function of wavelength for different light sources and unity ratio of $\frac{\theta_{PA}}{\theta_{DAS}} = 10^{-9}$ The contour line represents the trajectory of unity ratio where for longer wavelengths and higher source temperature, PAS is better: (a) $\lambda_{min} = 1\mu m$, (b) $\lambda_{min} = 5\mu m$.

From the above equation, the following conclusions can be drawn: 1) regarding the interferometer parameters, the ratio between the two systems is independent of the resolution as both have the same dependence on the resolution; 2) on the other hand, the smaller measurement time (i.e. higher mirror velocity $\mathrm{v_M}$), the better the DAS as compared to the PAS ($\theta_{PA} \propto \mathrm{v}_{\mathrm{M}}^{1.75}$). 3)The DAS is better for larger interferometer throughput (TP_o) given that the output light fills all the detectors (PA cell in PAS, the optical detector in DAS). This can be stated in another way; for the PAS having a smaller cell area is preferable (cell diameter is usually a few *mms* or even tenths of *mms*), thus there is no need for an interferometer with large throughput, whereas in the DAS based FTIR spectrometer, in the case of a shot-noise limited detector, having a larger throughput and detector area means more signal ($\theta_{DAS} \propto TP_o^{-0.5}$). 4) For the optical source, increasing its temperature enhances the performance of the photoacoustic based system compared to the optical one, due to the increased shot noise in the latter. This is clear in Figure 1-10 (a) – (b). In addition, this also applies to increase the wavelength for a given λ_{min} and for increasing λ_{min} (lower f_o), given that the seal effectively blocks acoustical noise. 5) Increasing the cell length, l, enhances the performance of the DAS over the PAS provided that the introduced losses, due to the mirrors, will not mask such enhancement. In general, the cell length and the mirror velocity are the dominating factors in specifying which is better.

1.5 Summary

A critical review has been conducted of gas sensing using direct absorption spectroscopy and photoacoustic spectroscopy. Each method was analyzed when using a tunable laser source or a Fourier transform spectrometer. In the case of PAS, the survey and the analysis were focused on the cantilever due to its high performance. The review includes analyses of the different cantilevers described in the literature that vary in size, material composition, and vibration detection methods. A theoretical analysis was conducted on these systems to find the extreme detection limits for each system. To compare the DAS and PAS, a figure of merit was used which was defined as the ratio between the normalized absorption coefficients (normalized with respect to measurement time) of each system. The normalized noise equivalent absorption coefficient (NNEA) was also used to compare the systems when using a tunable laser. The derived relations are a function of the specifications of the systems including their: source power, the wavelength of operation, system throughput, and detector parameters such as detector size, and cooling temperature. The relations allow the user to choose between the DAS and PAS given other system parameters. In the case of using a tunable laser, the direct absorption spectroscopy is better for lower laser powers and longer gas cells and the converse is also correct. For the FTIR-based systems, a direct absorption spectroscopy system is better than a PA-based system for lower source temperatures, higher spectrometer throughputs (bench-top spectrometer), faster mirror velocities, and longer gas cells. For a comparison between the capabilities of FTIR and TLS, one can check Table 1-1.

Since, the MEMS spectrometer is characterized by small throughput, fast mirror velocity and there is a need to have a long path lengths (to achieve low detection of limits), applying the photoacoustic spectroscopy with the MEMS spectrometer is not feasible.

Table 1-1 Performance comparison between FTIR and TLS

	Sensitivity (SNR)	Selectivity (resolution)	Detection range
TLS	High	High (down to 10^{-9} [149])	Narrow (i.e. 500 nm in the NIR or 1000 cm^{-1} [150])
FTIR	Relatively low	Relatively low (down to $10^{-3} cm^{-1}$ [151]) (down to $10^{-3} cm^{-1}$ [151])	Wide (up to 50,000 cm^{-1} [152])

CHAPTER 2: CONTRIBUTION TO MINIATURIZED SPECTROMETERS

2.1 Introduction to MEMS FTIR spectrometer

Micro-Electro-Mechanical System (MEMS) are miniaturized devices fabricated using micro-fabrication techniques. The size ranges from a few millimeters to a few micrometers [153][154]. The MEMS device could be static without any moving parts [155] or with multiple electro-mechanical moving parts actuated using electronic circuits either integrated into the same chip, such as accelerometers and pressure sensors, or outside such as spectrometers and RF MEMS[156]. Interestingly, MEMS have many applications which makes them impact our daily life. For example, in automotive, cars contain tens of sensors fabricated using MEMS technology[157]. Almost all smartphones contain typically 10 up to 20 MEMS sensors including mechanical gyroscopes and accelerometers. Video projectors contain the MEMS digital micromirror devices (DMD^{TM}) produced by Texas Instruments and is one of the most successful optical MEMS products. Now, MEMS spectrometers represent a new trend for miniaturizing optical spectrometers and convert them into portable devices. This trend leads to low-cost devices and brings the Lab. to the field thanks to the new on-site measurement capabilities offered by using such portable spectrometers. This trend is also compatible with the new era of internet of things (IoT), where MEMS are expected to play an important role due to its small size, cheap and its low cost due to its mass production. In this area, spectrometers have a great potential as multi-parameter chemical spectral sensor.

Using MEMS technology, the size and cost of spectrometers can be decreased while preserving relatively high performance. This extends the use of IR spectrometers in many applications and creates a new market for end-users. So, the market demand for portable IR spectrometers is increasing dramatically. According to reference [158], the annual growth rate of mini and micro spectrometers is at a rate of 11%. The market was worth $ 170M in 2016 and expected to reach $ 297 M in 2021. The main driver of this growth [158] is farmers’ application by bringing the handheld spectrometers to the farmers to easily test the crops quality, humidity of the soil, etc.. Other applications are controlling industrial process quality, bringing medical diagnosis capabilities to patients, to name a few.

The MEMS devices are fabricated using a variety of materials [159], but the most common are fabricated on silicon, due to the well-established microelectronic industry and CMOS process for integrated circuit (IC) fabrication. Silicon also has superior thermal and mechanical properties that can be summarized as follow [160][161]: 1) Doesn't suffer from hysteresis. 2) Large Young's modulus in the order of $2 \times 10^5 MPa$ as stiff as the steel while silicon is lighter and has smaller thermal expansion. 3) Large melting point temperature, which is about 1400 °C. 4) Its oxide (SiO_2) is stable. 5) Compatible with metals such as aluminum and gold that are commonly used in MEMS technology for pad metallization, electrical connectivity and mirror metallization. MEMS can be fabricated using either surface or bulk micromachining, where the etching is carried-out in deposited layers on the substrate (surface micromachining) or in the substrate itself (bulk micromachining), respectively [162].

Considering the miniaturization format, MEMS-based FTIR spectrometers using different architectures have already been implemented, such as the Michelson interferometer [25], lamellar grating [163], Mach-Zehnder interferometer [164], [165], moving wedge interferometer [166], low finesse Fabry-Pérot interferometer [167] and cascaded Fabry-Pérot interferometers [168]. However, all the reported solutions have a limited spectral resolution. On the one hand, the monolithic integration of all the components of the Michelson interferometer led to a resolution of approximately 33 cm^{-1} [25]. On the other hand, a better resolution could be achieved, but at the loss of the advantage of monolithic integration, leading to challenging alignment and high assembly costs; for instance, a resolution of approximately 25 cm^{-1} in the spectral range from 2 µm to 5 µm [169] has been obtained with a 3 mm-diameter MEMS mirror that requires further assembly with other discrete components to form the interferometer. A moving mirror with a relatively long physical travel range of approximately 600 µm was assembled perpendicular to the substrate with other Michelson components and led to a resolution of approximately 8 cm^{-1} [170]. In the case of the MEMS-lamellar grating spectrometer, a resolution of approximately 15 cm^{-1} within the mid-IR range has been achieved [163], and gas measurement has been demonstrated with a resolution of approximately 20 cm^{-1} [171]. In all FTIR spectrometers, the spectral resolution $\Delta\lambda$ is inversely proportional to the mirror travel range Δx, i.e., $\Delta\lambda \sim 1/\Delta x$, such that achieving fine spectral resolution requires a large travel range. Therefore, the limitation of the on-chip resolution arises from the restricted travel range of the micro-mirror, limited by the stability and reliability requirements of the MEMS actuators [172].

2.2 Concept of parallel spectrometer and its use for gas measurement.

Optical spectrometers enable contactless chemical analysis. However, decreasing both their size and cost appears as a requirement before their widespread deployment. Chip-scale implementation of the optical spectrometers still requires tackling two main challenges.

First, operation over a *broad spectral range extending to the infrared* is required to enable covering the molecular absorption spectrum of a broad variety of materials. This is addressed in our work with a MEMS-based Fourier transform infrared spectrometer with embedded movable micro-mirror on a silicon chip. Fourier transform infrared (FTIR) spectrometers appear as a promising option since its broad spectral range enables covering the absorption molecular spectrum of a broad variety of materials including gases, liquids and solids. In addition, high signal-to-noise ratio (SNR) can be achieved due to the detection of all wavelengths simultaneously with a single detector [9].

Second, *fine spectral resolution $\Delta\lambda$* is also required to facilitate screening over several chemicals. A fundamental limit states that $\Delta\lambda$ is inversely proportional to the mirror's motion range, which cannot exceed the chip size. To boost the spectral resolution beyond this limit, we propose the concept of parallel (or multi-core) FTIR, where multiple interferometers provide complementary optical paths using the same actuator and within the same chip.

The concept of parallel (or multi-core) spectrometer had been developed during my master thesis. The concept is summarized hereafter and then we demonstrate experimentally the advantage of its use in gas sensing.

2.2.1 Concept summary of the parallel spectrometer

Multiple interferometers are monolithically integrated into the same chip and sharing a single MEMS actuator. This new concept is intended to overcome the limitation in the spectral resolution, where the interferometers have complementary optical path differences (OPDs). The moving mirrors of the interferometers are mechanically coupled to the same actuator, while each of the N interferometers in the chip scans a different range of the OPD in the measured interferogram; thanks to the complementary shifts in the mirrors position implemented in the design. The interferogram of each interferometer is measured by a corresponding own detector, then signal processing is applied to produce an overall interferogram as concatenation of the different recorded interferograms. Therefore, one can increase the optical path difference by N times, and thus, enhance the wavelength resolution accordingly using the same MEMS actuator. The architecture consisting of 4 interferometers is depicted in Figure 2-1. Usually, broadband thermal light sources are larger than the input aperture of a single Micro-Optical Bench (MOP) interferometer. Therefore, splitting the source power over the 4 interferometers doesn't reduce the amount of light received by each of those interferometers. This interestingly means that the SNR per interferometer is not affected by the splitting of the light. Each interferometer has its own beam splitter, fixed mirror, moving mirror and detector. The 4 moving mirrors of the 4 interferometers are coupled to the same actuator, while the mirror positions are shifted with respect to each other by an increment Δ_M such that the resolution can be enhanced up to 4 times. For instance, if the actuator travel range is 200 µm and the increment Δ_M is 200 µm, a full OPD of approximately 1600 µm is obtained using the 4 interferometers. The first interferometer scans the OPD from -800 to -400 µm, the second one scans from -400 to 0 µm, the third one scans from 0 to +400 µm and the last one scans from +400 µm to +800 µm. The overall interferogram is the concatenation of the four complementary interferograms, and the corresponding spectral resolution is expected to be quadrupled compared to that of a single interferometer. Details on the concatenation algorithm can be found in our paper [173].

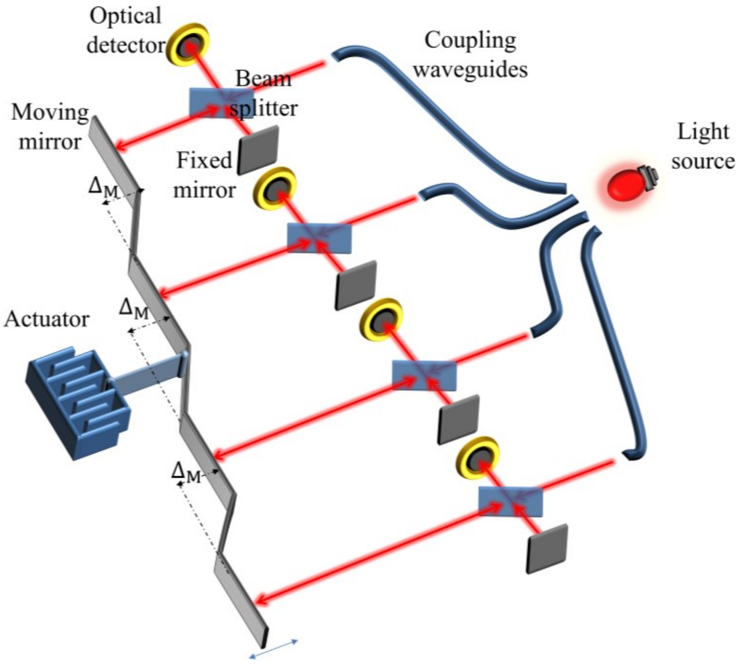

Figure 2-1 The parallel interferometers have a common actuator, where the moving mirrors are attached and spatially shifted to acquire the shifted interferograms. Each interferometer has its respective detector.

2.2.2. Experimental device.

The main target of the proposed design is to enhance the spectral resolution using four interferometers monolithically integrated on the same chip. This was obtained by replicating the core interferometer, previously reported in reference [25], design on-chip, but with shifts in the rest positions of the moving mirrors. A three-dimensional schematic of the chip with the four interferometers is depicted in Figure 2-2 (a). Since each of the four interferometer has a full travel range $2L$ of 360 μm, the total range is 1440 μm. Theoretically, this improves the resolution from 33 cm^{-1} to 8.3 cm^{-1}, according to the $FWHM$ criterion [13]. The interferogram of the first interferometer has OPD range from -860 μm to - 500 μm , the second has OPD range from -500 μm to - 140 μm, the third has OPD range from -140 μm to 220 μm and finally the fourth has OPD range from 220 μm to 580 μm. Thus, the centres of their OPD -corresponding to the rest position of the moving mirrors- are -680 μm, -320 μm, 40 μm and 400 μm, respectively. Additional overlap regions of range $2\Delta L$ equals to 40 μm was introduced for applying the concatenation algorithm described previously.

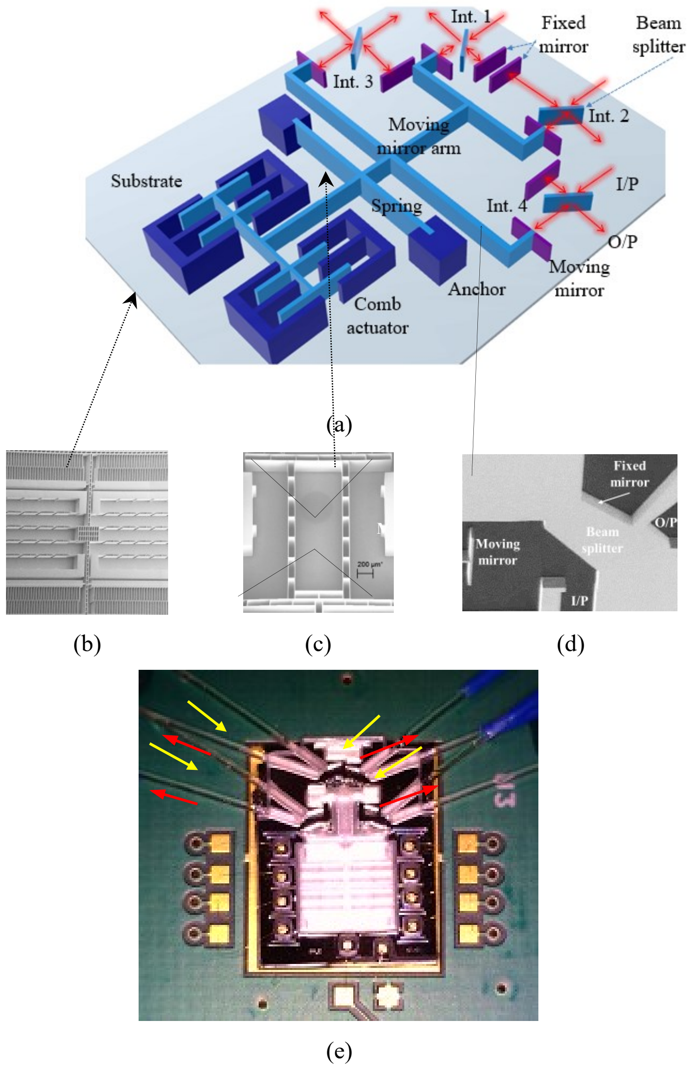

(a)

(b) (c) (d)

(e)

Figure 2-2(a) The chip-scale architecture of the MEMS spectrometer comprising four interferometers and a comb-drive actuator. The interferometers are denoted by *Int.* and numbered from 1 to 4. The moving mirrors of all interferometers are attached to the same moving arm. The light path is indicated by the red arrows. (b) An SEM image of the actuator. (c) An SEM image of the moving mirror arm. (d) An SEM image of an optical interferometer. (e) A camera photo for the corresponding fabricated die with the coupling fibers, where the yellow arrows represent the input directions of the light to the interferometers and the red arrows represent the output direction of the light.

Scanning electron microscope (SEM) images of the fabricated comb and mirrors arm are shown in Figure 2-2 (b) and (c), respectively. In Figure 2-2 (d), SEM image for the interferometer[174] is shown comprising the beam splitter, the fixed and the moving mirror. Such design is replicated for the parallel interferometers. Regarding the quality of surfaces, the RMS value of roughness is less than 20 nm using such technology[175] and the measured verticality of the surfaces is better than 0.05°. Mirrors reflectivity is more than 90%. A photo for the fabricated chip assembled on a PCB daughter board is shown in Figure 2-2 (e). The light from the optical source was coupled into the interferometers using a bundle of multimode fibers connected directly to the light source. From the other side, the optical fibers were cleaved and inserted into the MEMS chip in micromachined groves self-aligned with the interferometers. The MEMS actuator is operated at resonance using an actuation voltage of sinusoidal waveform. It has a maximum displacement of about 250 µm. The position of the MEMS actuator was determined by means of a capacitive sensing circuit. The relation between the mirror position and the capacitance was calibrated using a reference light at 1550 nm [176].

The output optical light from the interferometers are different, they can't be summed on the same detector and the output of each one should be coupled to its corresponding detector. Output electrical signal from corresponding detector is amplified by electronic amplifiers. These are followed by Analog-to-digital converter (ADC) to sample the analog signal and convert it to the digital domain where digital filtering is applied to obtain the corresponding interferogram. After time averaging of each of the four interferograms, the concatenation algorithm is applied, and the final spectrum is obtained. The scan time T_{scan} is about 1.5 ms while N_{scans} was 1000 scans or more.

2.2.3. White light characterization.

A white light source was measured by the four interferometers, where each one had its own interferogram versus the respective OPD. The overall interferogram after concatenation is shown in Figure 2-3 (a), where the interferogram comprises four parts of different colours corresponding to the 4 different interferograms. Applying Fourier transform on the concatenated interferograms, gives the corresponding spectrum of higher resolution, as depicted in Figure 2-3 (b). The intersection part of the interferograms of the interferometers 1 and 2 is shown in Figure 2-3 (c), the intersection part of the interferograms of the interferometers 2 and 3 is shown in Figure 2-3 (d) and the intersection part of the interferograms of the interferometers 3 and 4 is shown in Figure 2-3 (e). The intersection of the interferograms of the interferometers 2 and 3, and that of the interferometers 3 and 4 are smoother than that of the interferometers 1 and 2 because the signal power in these parts is higher and, thus, the noise effect in the transitions is smaller.

2.2.4 Characterization with narrow band filters.

To test the resolution enhancement achieved by the parallel interferometers, an optical filter with a FWHM of 2 nm cantered at 1.55 μm was placed after the white light lamp for obtaining a narrow band spectrum. Also, the same filter was measured using a benchtop spectrometer (Bruker Tensor II). The spectrum obtained from a single interferometer, which contains the main burst is shown in Figure 2-4 (a) (i) (depicted in blue bold line) and compared with a spectrum measured with the benchtop spectrometer for the same corresponding OPD range (depicted in red dash dot line). The spectrum of the concatenated interferograms of two consecutive interferometers, three consecutive interferometers and four consecutive interferometers are shown in Figure 2-4 (a) (i), (ii) and (iv), respectively. The figures show the gradual improvement of the resolution of the spectrum with increasing the number of the concatenated interferograms. The measured FWHM was improved from 8.4 nm to 2.7 nm (from 35cm^{-1} to 11 cm^{-1}).

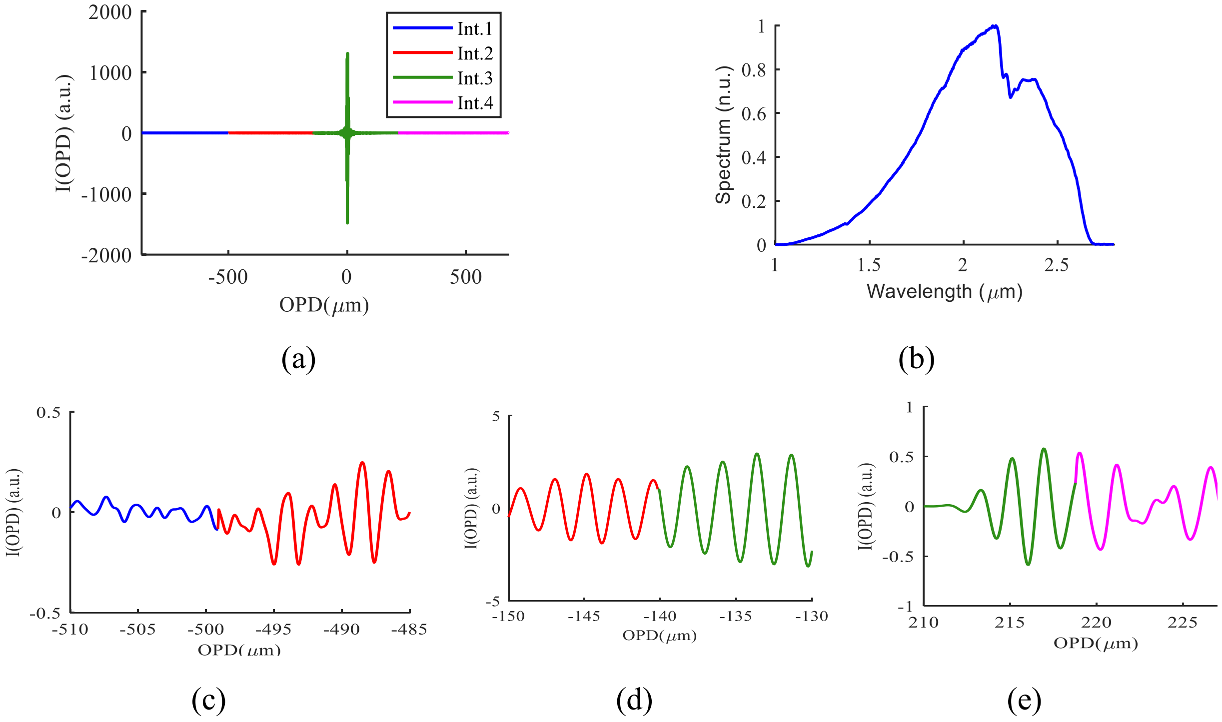

Figure 2-3 White light measurement using the parallel interferometers (a) The concatenated interferograms where the interferogram of each interferometer, nominated as Int., is drawn with different color (b) The corresponding spectrum of the concatenated interferograms. (c) Intersection part of the spectrum of Int.1 and Int.2. (d) Intersection part of the spectrum of Int.2 and Int.3. (e) Intersection part of the spectrum of Int.3 and Int.4.

Moreover, another filter centred at 2 μm with a FWHM of 1 nm, was also measured using the MEMS interferometers and the benchtop spectrometer. The obtained spectra are depicted in Figure 2-4 (b). The measured FWHM was 4.9 nm using the four interferometers. The corresponding value obtained using a single interferometer was 14.8 nm. At both wavelengths, the improvement in the resolution is about 3.1x, that is smaller than the ideal expected value of 4x. This is due to the self apodization of the interferogram that affects the achieved resolution [177].

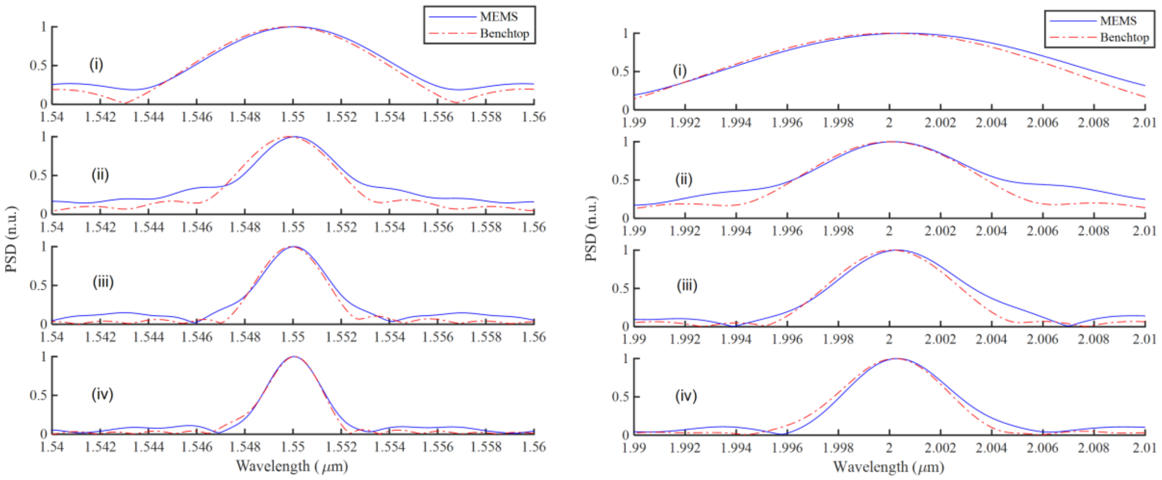

(a) (b)

Figure 2-4 Spectra of narrow band sources (white light followed by narrow band filters) measured by the parallel spectrometer design (blue bold) and by the benchtop spectrometer for the same corresponding OPD range (red dash dot). (i) spectrum of single interferometer, (ii), (iii) and (iv) spectrum of concatenated interferograms of two interferometers, three interferometers and four interferometers, respectively. (a) Spectra of the filter at 1.55 μm (b) Spectra of the filter at 2 μm.

2.2.5. Methane gas spectral analysis.

A gas measurement was conducted to show the ability of the parallel interferometers to discriminate between gas absorption bands. A gas cell that contains 10% methane CH_4 was inserted between the white light source and the spectrometer. Two back to back aspherical lenses are used to collimate the light from the light source and to focus the output light to the fiber of the MEMS spectrometer. The gas cell length is 10 cm. The content of the gas cell was analysed using the parallel interferometers and compared to a measurement using single interferometer. The obtained absorbance curves are shown in Figure 2-6. The absorption bands around 2.32 µm and 2.37 µm are discriminated (blue curve) compared to the spectrum measured by the single interferometer (red curve). The absorbance value was also enhanced dramatically, as shown by the wavelength range of 2.3-2.37 µm. For reference, the same gas cell was also measured using a benchtop spectrometer for two different resolutions, namely, 34 cm^{-1} and 8.5 cm^{-1}, and plotted in Figure 2-6. These resolutions are the theoretical resolutions of the single MEMS interferometer and the MEMS parallel interferometers. The comparison shows good agreement with the measurements of the MEMS spectrometer and proves the potential of using parallel spectrometer in environmental gas monitoring.

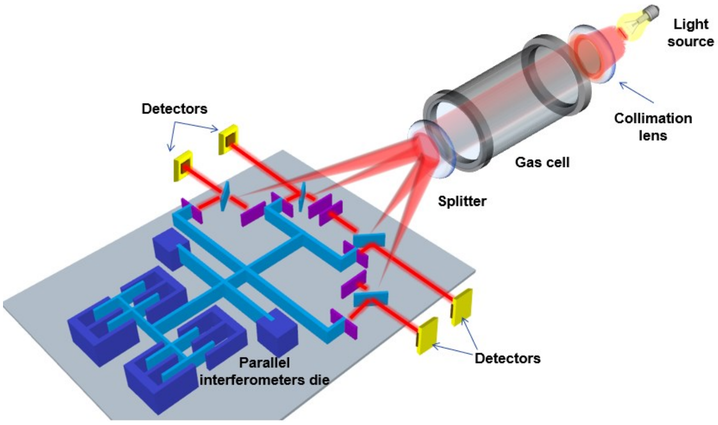

Figure 2-5 Measurement setup of Methane using the parallel spectrometers.

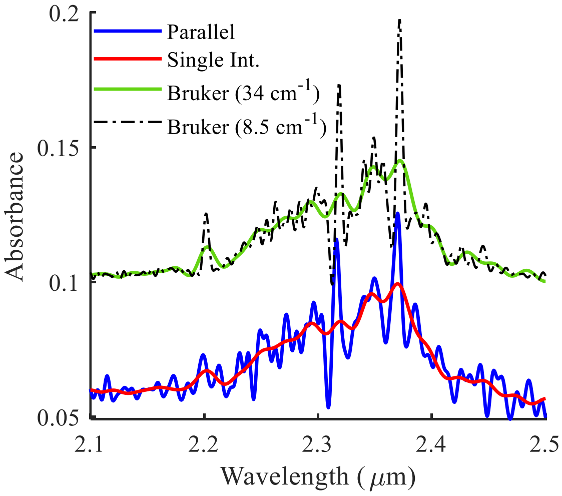

Figure 2-6 Measured absorbance curves of methane measured by the parallel interferometers (in blue) and the single interferometer (in red) and compared to the absorbance measured by the benchtop spectrometer for the two corresponding resolutions.

2.3 Differential Spectrometer based on Critical Angle Dispersion

Looking for further innovative concepts for simple and low-cost spectral sensing, we also explored the potential of dispersive spectrometers, which are another example of widely used spectrometers beside the FT spectrometer. A dispersive spectrometer can be based on a prism or a diffraction grating. In the case of the prism-based spectrometer, the collimated white light impinges a prism surface. It is refracted into different directions due to the wavelength dependence of material. Thus, different wavelength components are separated in different directions allowing one to couple each wavelength to its respective detector or by rotating the prism and coupling wavelengths one by one to a single detector. The prism can have different configurations such as Bunsen-Kirchhoff prism, Wadsworth prism mirror configuration, Pellin – Broca prism [178], compound prism [179] or others [180].

The spectrometer based on the diffraction grating comprises a grating of a periodic structure. The structure alters periodically the phase or the amplitude of the input light. Each wavelength of the modulated intensity/ phase is diffracted in a respective direction.

Using a moving detector, rotating grating, or multiple detectors one could measure the spectrum of input light. The diffraction grating could be a transmitting or reflecting grating. A combination of the prism and diffraction grating is also found [181], [182].
The prism is characterized by high transmission efficiency (only one order of refraction) compared to the diffraction grating. Regarding the resolution, the diffraction grating can achieve better resolution [183]. Prism-based spectrometer does not need a sorting filter to remove the overlap between the diffraction orders. Due to using off-axis parabolic mirrors, astigmatism aberration is encountered. This makes a limitation for the spatial and spectral resolution.

In this work, we present a novel spectrometer based on using a long dispersive stretched prism structure of beveled input and output interfaces. By sweeping the incidence angle and detecting the power at the other side using a single detector, one will have a wavelength integrated power. By differentiating such signal, the corresponding spectrum is retrieved. Thus, no exit slit is needed, and the spectral resolution will not be limited. The spatial resolution, for spectral imaging, will not also limited.

2.3.1 Concept

The spectrometer idea depends on injecting a collimated light inside a long stretched prism of dimensions much greater than the wavelength of operation. The structure could be made of any dispersive material such as silicon or glass. The stretched prism input and output interfaces are beveled with an angle α as depicted in Figure 2-7. The angle of incidence is θ_o . The angle of refraction at the input interface is θ_1 and θ_2 is the angle of incidence on the horizontal surface. Depending on the incidence angle, some wavelengths exit from the right side of the structure, and other wavelengths will completely radiate out laterally given a long stretched prism.

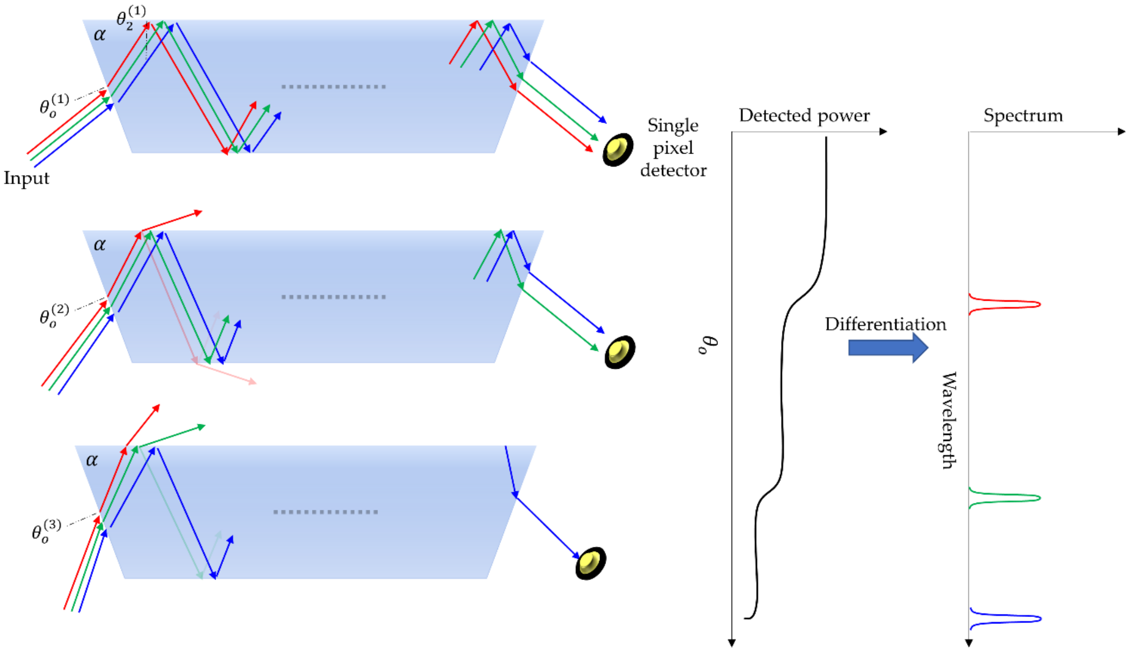

Figure 2-7 Ray tracing of light inside the stretched prism of the spectrometer. Stretched prism width is a. The light path (red rays) is drawn from the input to the output. The green dash line represents the refracted light which depends on the angle θ_2.

From the geometry, one can find that the relation between θ_2 and the incidence angle θ_o is given by the following:

$$\theta_2 = \alpha - \sin^{-1}(\frac{\sin\theta_o}{n(\lambda)}) \tag{2.1}$$

If $n(\lambda)\sin\theta_2 < 1$, corresponding to a certain range of wavelengths λ satisfying this condition, then the light will be totally reflected inside the structure until it exits from the other side. In the opposite case, corresponding to another range of wavelengths, a portion of the light will be refracted out of the structure, while the other complementary portion will be reflected inside the structure. Therefore, for a structure of relatively long length, no light of the corresponding λ will exit from the right side of the structure. There is a critical wavelength λ_c at the border between these two regimes, separating them into two spectral ranges. This critical wavelength λ_c is respective to a certain critical input angle θ_o according to Eq. (2.1), satisfies $n(\lambda_c)\sin\theta_2 = 1$.Thus, the output power is given by:

$$P(\theta_o) = \int_{\lambda_{min}}^{\lambda_c(\theta_o)} PSD(\lambda')d\lambda' \tag{2.2}$$

where λ_{min} corresponds to the minimum wavelength of operation depending on the stretched prism/ detector material and PSD is the input light power spectral density. Differentiating the above formula leads to the original spectrum as follow:

$$PSD(\lambda) = |\frac{dP}{d\theta_o}\frac{d\theta_o}{d\lambda}| \tag{2.3}$$

where $d\theta_o/d\lambda$ is obtained from Equation Eq. (2.1) and $n(\lambda)sin\theta_2 = 1$. In case of broadband light of black body radiation (source temperature $T_{src} = 3000\ K$) and a stretched prism made of ZnSe material and α =45, one could have the corresponding $P(\theta_o)$ of the white light source shown in Figure 2-8 (a) and the retrieved spectrum in Figure 2-8 (b). The term $d\theta_o/d\lambda$ can deduced either using the theoretical relation or by calibrating the spectrometer by a reference material or a light source of multiple emission lines such as Xenon or Krypton light sources.

Due to coupling all wavelengths to the same detector, two benefits are acquired; (1) there is no need for an exit slit, and (2) the resolution is not limited by the aberrations, such as spherical and astigmatism, as compared to the conventional dispersive spectrometers. Thus, better spatial and spectral resolution can be achieved.

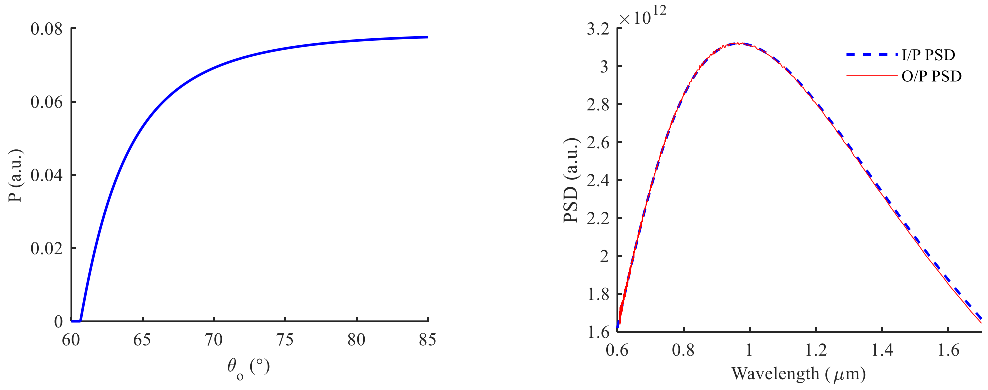

(a) (b)

Figure 2-8 (a) The output power versus input rotational angle. The input in this case is a broadband light source of a temperature of 3000 K. (b) Retrieved power spectral density PSD (after output differentiation). The curve is compared with the PSD of the input.

2.3.2 System specifications

Spectrometer resolution

Given the input collimated light has a divergence angle of $\pm\ \delta\theta_o$, the spectral resolution is governed by such value. In case of a laser and zero $\delta\theta_o$, the integrated power $P(\theta_o)$ versus θ_o has a step function (blue dash line), as depicted in Figure 2-9 (a). Differentiating such curve has an impulse shape at θ_c (blue solid curve). In case of limited divergence angle $\delta\theta_o$, $P(\theta_o)$ has a gradual decrease with θ_o (red dash curve) and the corresponding differentiated signal has a gaussian like shape with a full width at half-maximum of $2\delta\theta_o$(red solid curve). Multiplying the differentiated signal with $d\theta_o/d\lambda$ leads to a wavelength dependent resolution which depends on the material dispersion.

Regarding the length of the structure, it should be long enough to attenuate the power of the rejected wavelengths because once such wavelengths impinge on the horizontal surface, part of the power is transmitted, and the complementary part is reflected (residual power). The effect of an increasing number of reflections N_{ref} on the spectrum shape of the laser is shown in Figure 2-9 (b), where the limited number of reflections introduces a tail in the retrieved spectrum for incidence angle bigger than the critical angle which corresponds to wavelengths smaller than the laser wavelength.

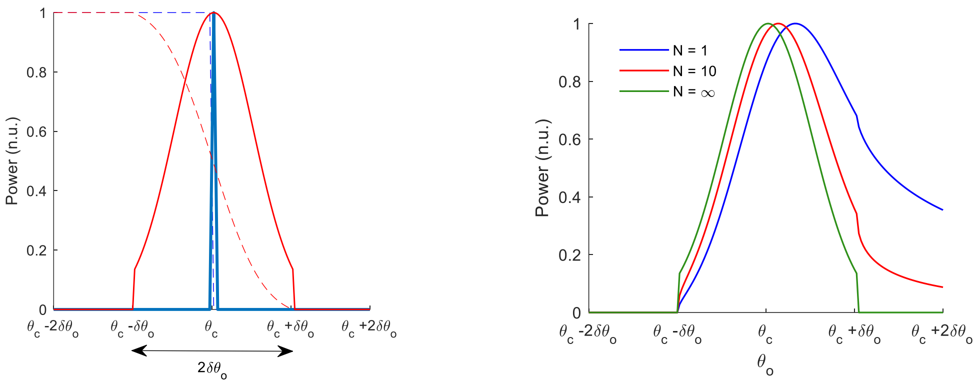

(a) (b)

Figure 2-9 (a)The integrated power P versus θ_o in case of laser (dash curves) in case of zero divergence angle (blue) and limited divergence angle (red). The corresponding $dP/d\theta_o$ are also drawn (solid curves). (b) The spectrum of a laser of limited divergence angle for a different number of reflections N. Increasing the number of reflections reduces the tail.

The relation between θ_o and the corresponding critical wavelength λ_c is shown in Figure *2-10* (a) for different values of α in the case of a stretched prism made of ZnSe. Differentiating such curves with respect to the critical wavelength $d\theta_o/d\lambda$ is the ratio between the angle of collimation and the achieved resolution. These curves are depicted in Figure *2-10* (b). Such curves relate to the degree of collimation with the required resolution. For example the value of $d\theta_o/d\lambda = 0.001\ (°/nm)$, means that the collimated light should have a divergence angle of about $0.001°$ to achieve a resolution of 1 nm. It is clear that the resolution worsens as the wavelength increases because the stretched prism's material is less dispersive for longer wavelengths. Also, it worsens for smaller values of α. However, using bigger values of α means bigger values of θ_o, as shown in Figure 2-10 (a), leads to lower irradiance (cosine law) in addition to limited spectral range as depicted in Figure *2-10* (b). The spectrometer resolving power can be deduced for such a spectrometer. Knowing that the resolving power R is given by [184]:

$$R = \frac{\lambda}{\Delta\lambda} = a\frac{d\theta_o}{d\lambda} \tag{2.4}$$

One can find $\frac{d\theta_o}{d\lambda}$ by differentiating the equation $1 = n\sin\theta_2$ with respect to λ in conjunction with the Eq. (2.1). After substituting in equation (2.4) the resolving power is given by:

$$R = a\frac{\sin\alpha}{\cos\theta_o\cos\theta_2}\frac{d\theta_o}{d\lambda} \tag{2.5}$$

The resolving power can be rewritten as follows:

$$R = \frac{d}{\sqrt{1-n^{-2}}}\frac{d\theta_o}{d\lambda} \tag{2.6}$$

Such resolving power represents the ultimate theoretical resolution which is limited by the Rayleigh diffraction limit of stretched prism aperture. In Figure *2-10* (c), such resolving power is compared with the prism resolving power equation ($R = a\frac{dn}{d\lambda}$, where the prism base is taken to be equal to stretched prism width a). It is clear that the resolving power of the new spectrometer is order of magnitudes bigger than the prism at the beginning of its spectral range and slightly better for longer wavelengths.

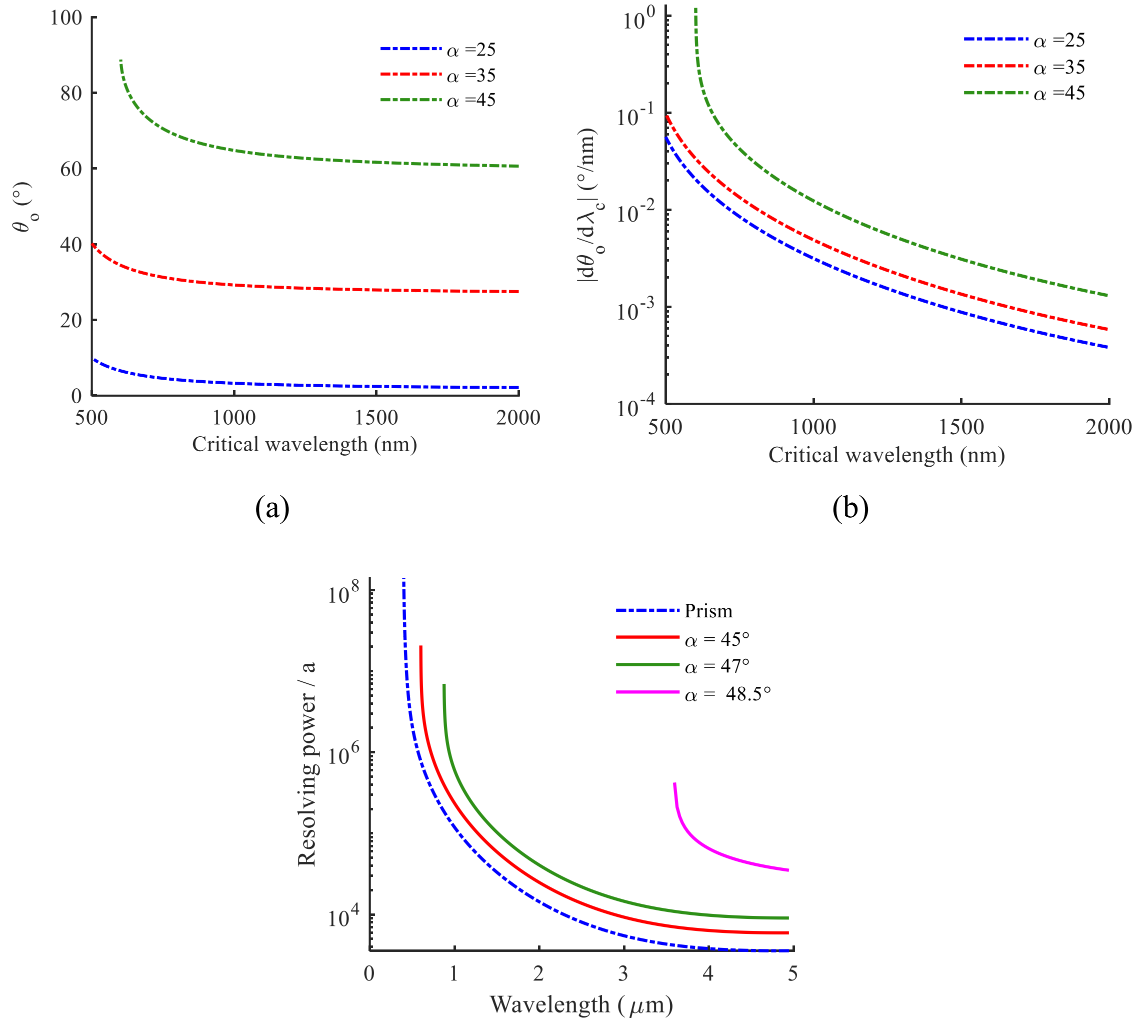

(a)

(b)

(c)

Figure 2-10 (a) Relation between the incident angle θ_o and the corresponding critical wavelength for different α. (b) Relation between $d\theta_o/d\lambda_c$ and the corresponding critical wavelength for different α. (c) Resolving power of prism based (dash) and differential spectrometer (solid) in case of different α.

Spectrometer SNR

In real-time measurement, the detected power will be sampled at different times (i.e. P(t)). The noisy detected power will be given by $P_n(t) = P(t) + n(t)$, where $n(t)$ is the noise. The noisy retrieved spectrum is given by:

$$PSD_n = |PSD + \frac{dn}{dt}\frac{dt}{d\theta_o}\frac{d\theta_o}{d\lambda}| \tag{2.7}$$

where $\frac{dt}{d\theta}$ is the inverse of an angular velocity of the input light. The first term represents the correct PSD and the second term represents a noise term. For a constant angular velocity, $\frac{dt}{d\theta} = \frac{T}{\Delta\theta_o}$, where the $\Delta\theta_o$ represents the range of θ_o scanned (which corresponds to the scanned spectral range) and T is the measurement time. The noise power spectral density of white is $N(f) = N_o\ (V^2.Hz^{-1})$, where f is the electrical frequency. The effect of differentiation leads to $N(f) = N_o(2\pi f)^2$. Thus, the root mean square of the noise n_{rms} (in the time domain) is the square root of the total integration of the noise power spectral density within the electrical bandwidth BW of interest. It is given by:

$$n_{rms} = \sqrt{\int_0^{BW} N(f)df} = 2\pi\sqrt{N_o BW^3/3} \tag{2.8}$$

The bandwidth of operation can be determined from the resolution. Since the divergence of collimation $\delta\theta_o$ determines the width of the spectrum as depicted in Figure 2-9, the corresponding electrical bandwidth is given by $BW = \frac{\Delta\theta_o}{T\, 2\delta\theta_o}$. After that, the signal to noise ratio SNR is given by:

$$SNR = \frac{PSD}{n_{rms}\frac{dt}{d\theta_o}\frac{d\theta_o}{d\lambda}} \tag{2.9}$$

Given the equations of BW and $\frac{dt}{d\theta_o}$, the SNR is given by:

$$SNR(\lambda) = \frac{\sqrt{6}}{\pi}\frac{PSD}{\sqrt{N_o/T}\,\sqrt{\Delta\theta_o/(\delta\theta_o)^3}\,\frac{d\theta_o}{d\lambda}} \tag{2.10}$$

which can be rewritten as follows:

$$SNR(\lambda) = \frac{\sqrt{6}}{\pi}\frac{PSD\ \delta\lambda(\lambda)}{\sqrt{N_o/T}\,\sqrt{M}} \tag{2.11}$$

where M is the number of wavelength points and $\delta\lambda(\lambda)$ is the spectrometer resolution which is wavelength dependent as mentioned before. Decreasing the number of spectral points M or increasing the measurement time T enhances the SNR. Also, SNR is better for higher wavelengths due to the limited resolution.

2.3.3 Results

Experimental setup

The spectrometer idea was applied using a ATR crystal (Length × width × depth = 60 mm × 3 mm × 20 mm, International crystal). A multimode fiber MMF (core/cladding = 50/ 125 μm, EuroMicron or core/cladding = 200/220 μm OZ Optics) was placed at the focal point of an off-axis parabolic mirror (focal length f = 25.4 mm) to collimate the light. The input light was bent by 90° using a 45° flat mirror, as depicted in Figure 2-11. The flat mirror was attached to an actuator (CD drive optical pickup unit). The actuator was excited using a sinusoidal voltage signal of a frequency of 50 Hz. To vary the incidence angle θ_o, the flat mirror was moved forward and backward which resembles a case that the MMF was placed at the focal point of a lens and moving in the lateral direction, which finally leads to varying θ_o.

At the output side of the crystal, the light was focused on a detector (InGaAs $\lambda_c = 1.7\mu m$) by the means of another off-axis parabolic mirror (f = 25.4 mm). Finally, the signal was detected using a high-speed oscilloscope. The other channel of the oscilloscope was connected to a voltage signal which actuated the actuator and configured as the trigger source. This was to synchronize each measurement at the same position of the flat mirror (corresponds to a given θ_o). The signals were filtered using a digital low pass filter to limit the noise without affecting the signal resolution.

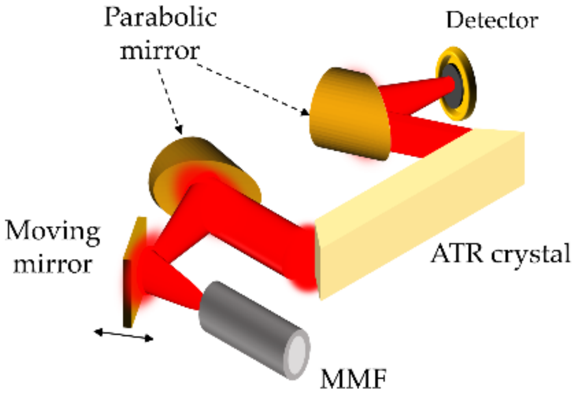

Figure 2-11 3D layout of the measurement setup.

Results

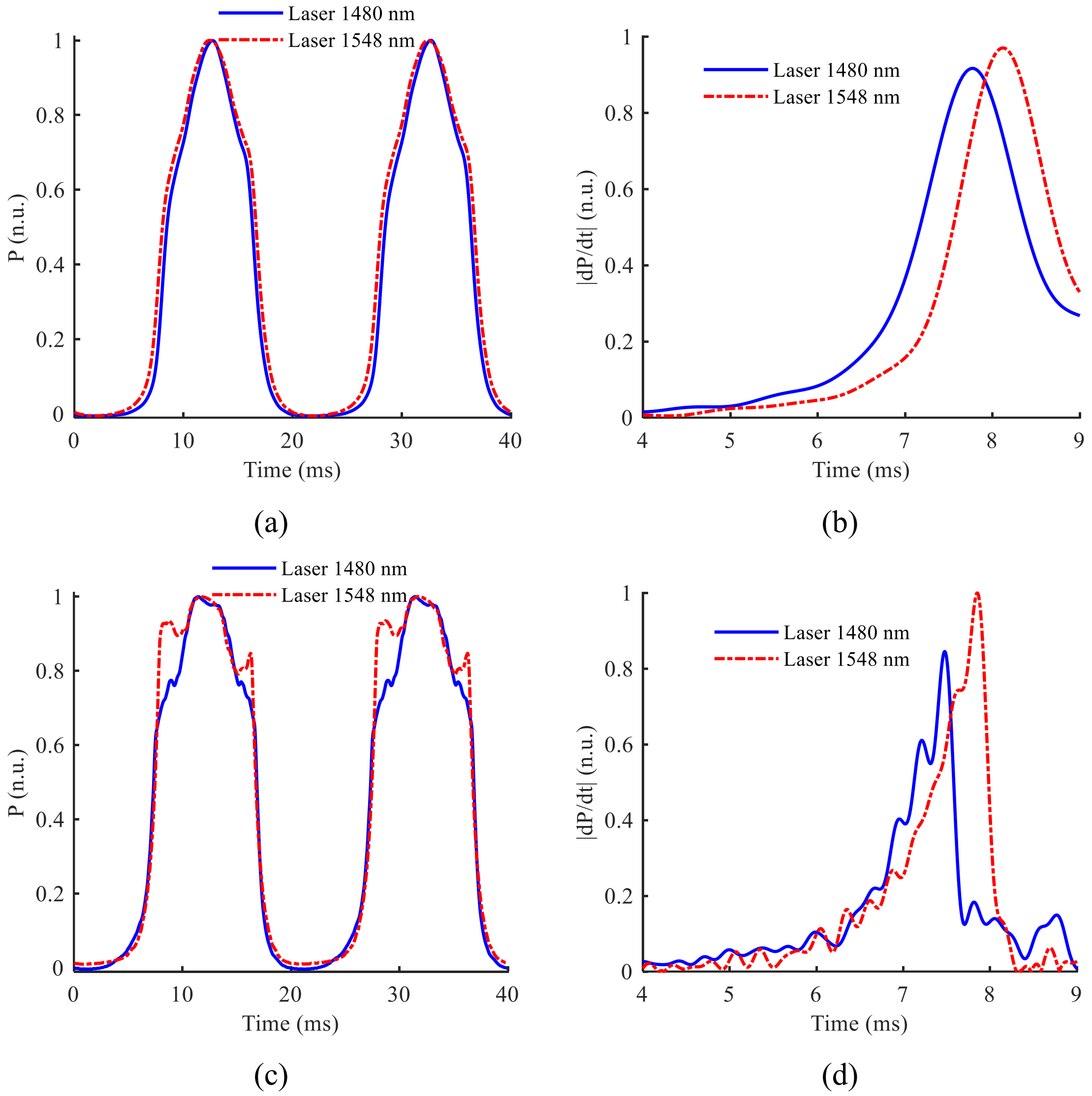

(a) (b)

(c) (d)

Figure 2-12 Laser measurements. (a) Laser power detected by the detector versus time using the MMF of core/cladding of 200/220 μm. (b) The corresponding differentiated signal versus time (corresponding to the spectrum). (c) Laser power detected by the detector versus time using the MMF of core/cladding of 50/125 μm, and the corresponding differentiated signals are plotted in (d).

Two different laser sources (1480 nm and 1548 nm) were measured. The experiment was performed using the MMF of core/cladding of 200/220 μm and repeated for the MMF of core/cladding 50/125 μm. Decreasing the source size using the same collimator leads to a smaller divergence of collimation, which leads to a better resolution. For the MMF of core/cladding of 200/220 μm, the measured signals versus time are plotted in Figure 2-12

(a) for the bigger MMF. After differentiation, the corresponding signals are plotted in Figure 2-12(b). The achieved FWHM resolution is around 230 nm. For the MMF of core/cladding 50/125 μm, the measured and the differentiated signals are plotted in Figure 2-12 (c) and (d), respectively. The achieved spectral resolution is around 120 nm.

After that, the outputs of two laser sources were combined using a coupler and coupled to the spectrometer. The differentiated signal is plotted in Figure 2-12 (a) for the bigger MMF and Figure 2-13 (b) in for the smaller one. Discrimination between the two lasers is only observed for the MMF of core/cladding 50/125 μm. This is expected for the bad resolution achieved using the bigger MMF.

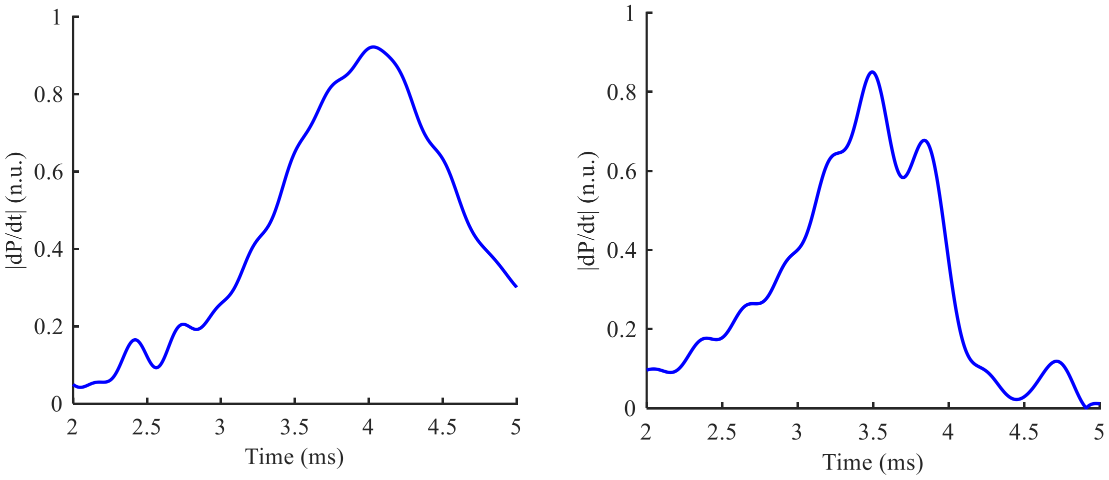

(a) (b)

Figure 2-13 Differentiated signal of two coupled lasers (1480 nm and 1548 nm) using (a) the MMF of core/cladding of 200/220 μm, (b) the MMF of core/cladding of 50/125 μm.

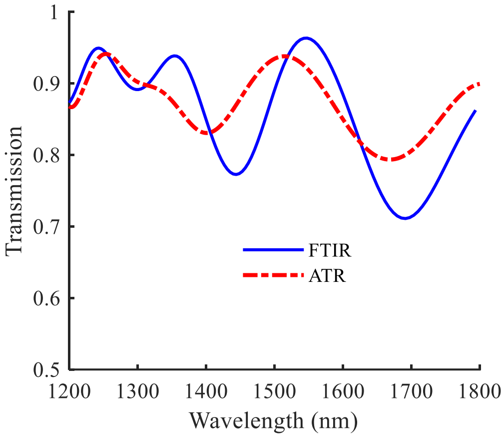

Figure 2-14 TS5 Transmission measured using the differential spectrometer and a reference FTIR spectrometer

To get spectrum versus wavelength, one has to perform wavelength calibration for the spectrometer (relate the actuator motion to the corresponding wavelength), Since, the relation between time and θ_o is sinusoidal relation (the applied voltage was sinusoidal), the coefficients of the relation can be solved using the data of the lasers measured in Figure 2-12 (there are laser peaks at a given time and each peak occurs at given critical angles, which are known from the theoretical curves in Figure 2-10 (a)). After that, the theoretical relation depicted in Figure 2-10 (a), is used to convert from θ_o to the corresponding wavelength.
White light from a halogen light source (AvaLight-HAL, Avanyes) followed by a reference material (TS5, Starna) was also measured. TS5 is an organic matrix which has many absorption lines in the near infrared. Thus, it is used in the wavelength calibration of spectrometers. The corresponding transmission is shown in Figure *2-14*, after performing time to wavelength conversion. The TS5 material was also measured using an FTIR spectrometer (Neospectra, Si-ware) for comparison.

2.3.4 Discussion

Using the parabolic mirror of a focal length of 25.4 mm, the collimated light from the MMF of core/cladding of 50/125 μm is 0.06°. Theoretically, this corresponds to a resolution of 20 nm according to Figure 2-10 (b). Such a resolution is expected to quadruple in the case of the MMF of core/cladding of 200/220 μm. By comparing with the measured spectra of lasers, one observes the following: 1) measured resolution was far from the theoretical resolution. b) Enhancement in the resolution in case of using the smaller fiber which enables one to discriminate the peaks of the two lasers as depicted in Figure 2-13 (b). 3) Ripples in the spectra are observed in the laser measurements of the smaller fiber.
A simulation model was built to understand such a degration in performance. The governing equation of model can be derived by modifying Equation (2.2) to take into account the stretched prism limited number of reflections in addition to an input light of a given divergence angle $\delta\theta_o$. The equation will be as follow:

$$P(\theta_o) = \int_{\lambda_{min}}^{\lambda_{max}} \int_{0}^{\pi/2} I(\theta - \theta_o)\ IL\,(\theta, \lambda)\ d\theta\, PSD(\lambda)\, d\lambda \qquad (2.12)$$

where $I(\theta - \theta_o)$ is the collimated light intensity distribution centered around an incident angle of θ_o. The width of such function corresponds to $\delta\theta_o$. The limits in the wavelength integration λ_{max} and λ_{min} are limited by the optical components. $IL\ (\theta,\lambda)$ is the stretched prism insertion loss as a function of the incidence angle and wavelength. For unpolarized light and neglecting the coupling between polarization, IL is given by:

$$IL\ (\theta,\lambda) = 0.5\left(\mathrm{T}_{\mathrm{in}_s} R_s^{N_{ref}} \mathrm{T}_{\mathrm{out}_s} + \mathrm{T}_{\mathrm{in}_p} R_p^{N_{ref}} \mathrm{T}_{\mathrm{out}_\mathrm{p}}\right) \zeta \cos\theta \tag{2.13}$$

where s and p subscript holds for s-polarization and p-polarization, respectively. R is the reflection coefficient upon stretched prism upper/lower surface. It is a function in θ_2 and λ. T_{in} is the input transmission and it is a function of θ and λ. T_{out} is the output transmission. Finally, $\cos\theta$ corresponds to the cosine law. Equation (2.12) can be rewritten in matrix form for faster calculations as follow:

$$\underline{\boldsymbol{P}} = \boldsymbol{\beta} * \underline{\boldsymbol{PSD}} \tag{2.14}$$

where $\boldsymbol{\beta} = \boldsymbol{I}\ * \boldsymbol{IL}$, a bar under the symbol represents a column vector, while symbols without bars are rectangular matrices. The two lasers used in the measurement were simulated with a divergence angle of 0.006°. The corresponding detected signals are depicted in Figure 2-15 (a) and the respective differentiated signals are depicted in Figure 2-15 (b). The simulation results don't show any degradation in resolution (power change from a high level to zero within 0.012°). It is to note that the gradual decrease of power just before the critical angle is attributed to the cosine law.

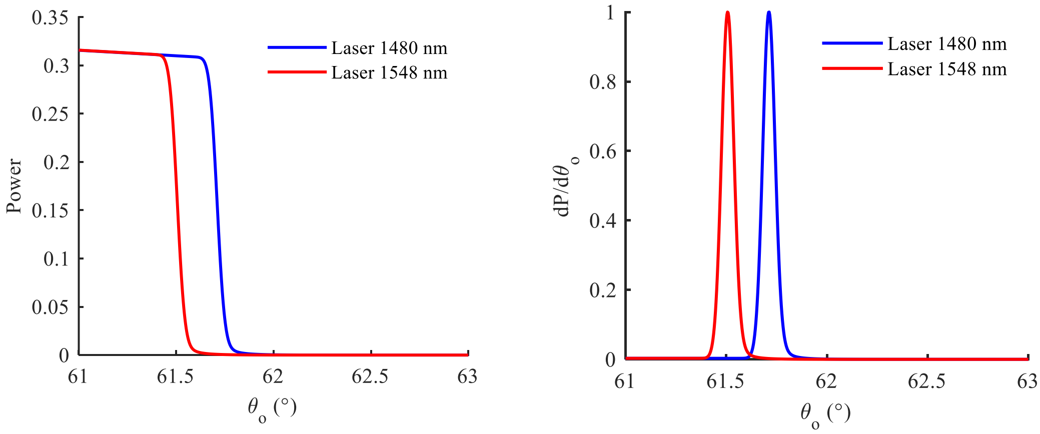

(a) (b)

Figure 2-15 Output simulations of the Differential spectrometer for two different lasers and a divergence angle of 0.006° (a) Power at the output versus the incidence angle. (b) Respective differentiated signal.

Ray tracing using commercial software (ZEMAX) was also performed to trace rays inside the stretched prism. This was to check if there are rays path which contributes to the output or an effect from the aberrations introduced by the optics. However, the detected signal at the output doesn't show any degradation in the resolution.

Diffraction due to the stretched prism limited width is also negligble as the width is about 4.2 mm. This corresponds to an intensity distribution in the far-field of a sinc distribution $sinc(\theta_{far}/\theta_{diffraction})$ where $\theta_{diffraction} = \frac{4.2mm}{\lambda}(\frac{180}{pi}) = 0.02°$ for a wavelength of $1.548\ \mu m$. Such an increase in divergence is smaller than the initial divergence of input light ($\delta\theta_o = 0.06°$).

One of the effects which may cause such a resolution degradation is the roughness on the stretched prism surface which scatter light to wider angles which can widen the divergence angle of the collimated beam due to multiple reflections inside the stretched prism. Thus, the roughness was measured and was taken into account in the modeling in the next part.

Surface roughness

In order to measure the roughness, surface profile $h(x, y)$ was measured for different positions of the ATR crystal. This was performed using a Digital Holographic Microscope (DHM). The DHM uses laser of a wavelength of 610 nm. Window size is 244 μm x 244 μm with a step size of 310 nm. A 2D plot of surface height is depicted in Figure 2-16.

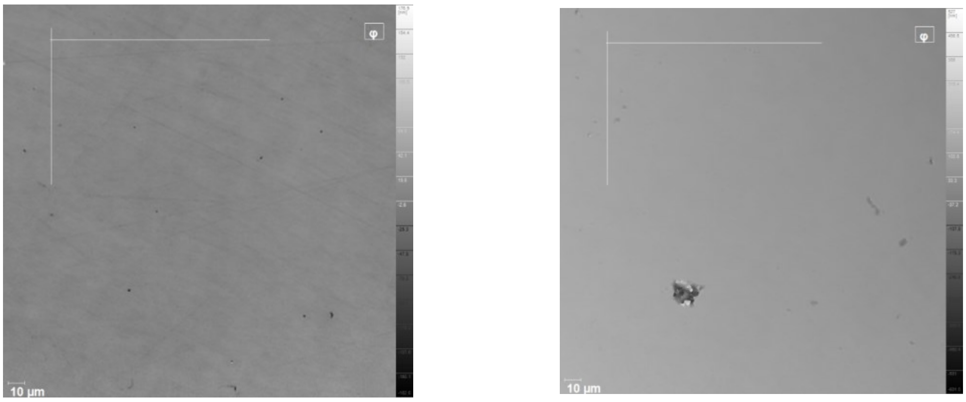

(a) (b)

Figure 2-16 Color plot of surface height at different positions on the stretched prism surface.

The surface power spectral density PSD of the roughness can be calculated by the square of Fourier transform of surface height. It is given as follows[185]:

$$PSD(f_x, f_y) = \lim_{L_x, L_y \to \infty,} \frac{1}{L_x L_y} \left[\int_0^{L_y} \int_0^{L_x} h(x, y) e^{-j2\pi(f_x x + f_y y)} dxdy \right]^2 \quad (2.15)$$

where f_x and f_y are the spatial frequencies of the surface roughness. The PSD was calculated for positions which are far away from each other. After that, the average was taken because the roughness in these positions are uncorrelated. The corresponding PSD is plotted in

Figure 2-17 (a). To quantify the surface roughness, the corresponding autocovariance function (ACF) is calculated by applying Fourier transform on the PSD. This is valid for a stationary roughness where roughness correlation function is independent of the absolute position. The calculated ACF can be found in

Figure 2-17 (b) and (c). From the ACF function, one can find the corresponding root mean square roughness $\sigma_{rms} = \sqrt{ACF(0,0)} = \sqrt{\int_{-\infty}^{\infty}\int_{-\infty}^{\infty} PSD(f_x, f_y) df_x df_y}$.

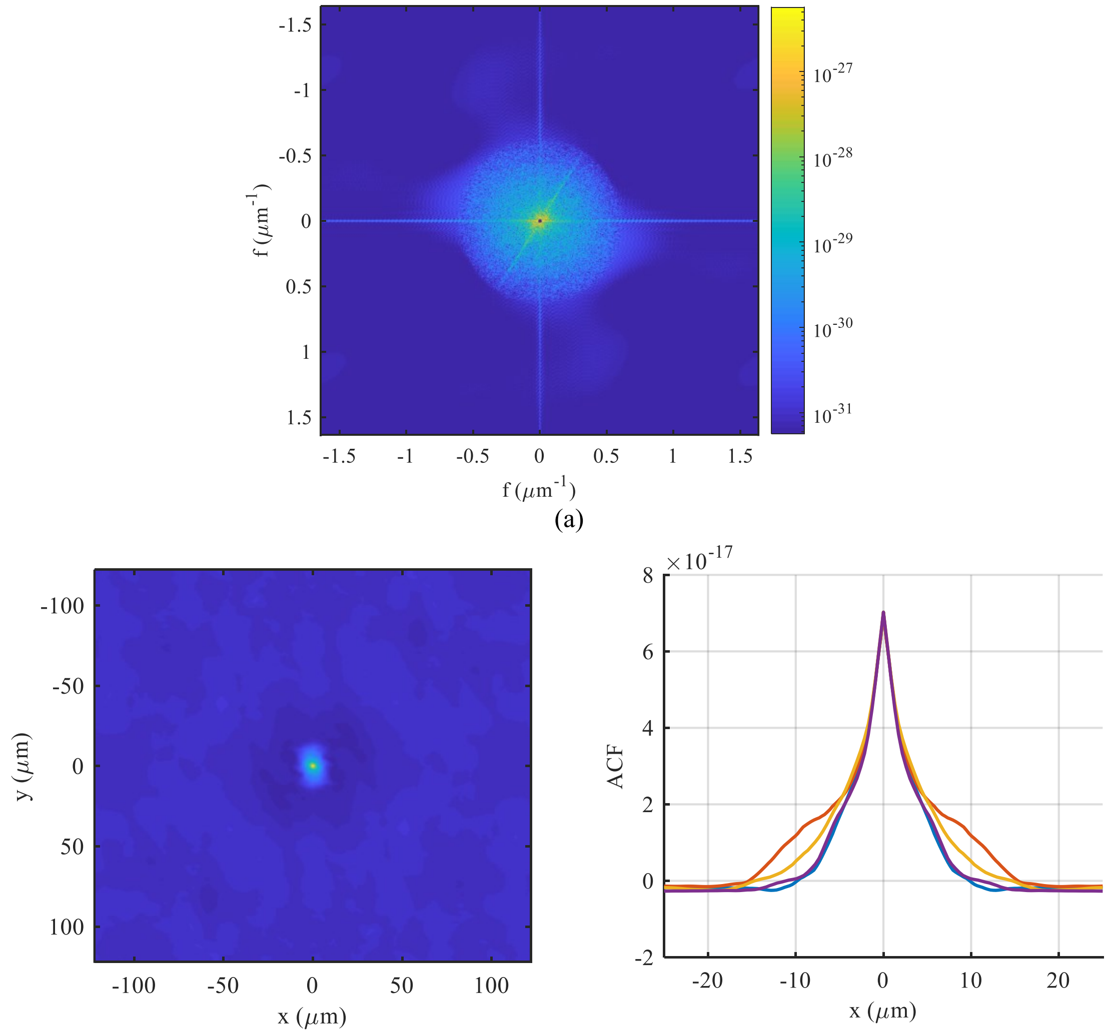

(a)

(b)

(c)

Figure 2-17 (a) Color plot of surface PSD versus the spatial frequencies. (b) Color plot of surface ACF. (c) Different slices of ACF.

Thus, surface roughness RMS is equal to 8.4 nm. The correlation length is defined as the length over which the ACF drops to 10% of its peak value[185]. It ranges from 7 to 12 μm (depending on the slice plane).

Effect of Roughness

Different scattering models are reported for modeling the effect of surface roughness on the reflected light such as [186], [187] : Beckmann-Kirchhoff theory, Rayleigh-Rice theory, and Harvey-Shack theory. Beckmann-Kirchhoff theory is scalar a model-based on Kirchhoff diffraction integral. It is valid for rough surfaces but contains a paraxial approximation limiting its application for wide-angle scattering. The Rayleigh-Rice theory is based on vector perturbation. It is valid for arbitrary incidence and scattering angles. but it is based on smooth surface criteria ($\frac{4\pi\sigma \cos\theta_i}{\lambda} \ll 1$, where θ_i is the incidence angle). The Harvey-Shack theory has different versions from the original one to the modified version, which has a limiting scattering angle approximation, to the generalized version, which can model wide-angle scattering from a rough surface beside the ability to model scattering upon transmission and reflection. Due to its wide validity, Harvey-Shack theory is used in modeling the effect of roughness on the spectrometer resolution

Harvey-Shack model is based on a scalar treatment using Fourier optics. It assumes also Gaussian distribution of roughness with arbitrary PSD. In the modified Harvey-Shack theory, a small scattering angle with respect to the specular reflection is assumed in calculating the phased difference between scattered rays as follows [161]:

$$\phi(\hat{x},\hat{y}) = \frac{2\pi}{\lambda} n(\cos\theta_i' + \cos\theta_o')h\,(x,y) \sim \frac{4\pi}{\lambda} n \cos\theta_i'\, h(x,y) \qquad (2.16)$$

where $\hat{x},\hat{y}$ are co-ordinates normalized to wavelength, θ_o' is the reflected scattered angle and n is the medium refractive index. These are depicted in Figure 2-18 (a). The corresponding surface transfer function is given by [161]:

$$H_s(\hat{x},\hat{y}\,) = e^{-\left(\frac{4\pi}{\lambda} \mathrm{n} \cos\theta_i' \sigma_r\right)^2 \left[1 - \frac{ACF(\hat{x},\hat{y})}{\sigma_s^2}\right]} \qquad (2.17)$$

where σ_s is the surface RMS roughness and σ_r is the band-limited RMS roughness (calculated from the PSD where roughness frequencies which generate evanescent scattered light are excluded). Applying the Fourier transform, one gets the corresponding angle spread function (ASF) which represents the scattering distribution. ASF was calculated for a laser of 1548 nm and an incidence angle of 24° on the glass-air interface This is the critical angle of total internal reflection angle on the stretched prism surface. The roughness parameters σ and ACF measured using the DHM were used. The respective ASF is plotted in Figure 2-18 (a). The percentage of the total power scattered is 2.3% of the input incident power while the specular reflection is still dominant. Light intensity (power per unit solid angle) is related to ASF as follow:

$$I(\theta_o, \theta_i) = ASF(\theta_o', \theta_i')R(\theta_i') \cos\theta_i' \qquad (2.1)$$

where $R(\theta_i)$ is the reflection coefficient of light of incidence angle of θ_i.

Applying these equations on the stretched prism structure is discussed as follows. As shown in Figure 2-18 (b), at every reflection of an incidence angle θ_{2_i}, the light is scattered into different directions with angles θ_{2_o}. Thus, the intensity after one reflection $I_{in}\left(\theta_{2_o}\right)$ is related to intensity before $I_{in}\left(\theta_{2_i}\right)$ as follow:

$$I_{in}\left(\theta_{2_o}\right) = \int_0^{\pi/2} I_{in}(\theta_{2_i}) ASF\left(\theta_{2_o}, \theta_{2_i}\right) R\left(\theta_{2_o}\right) \cos\theta_{2_o} \, d\theta_{2_i} \qquad (2.2)$$

The above equation should be applied for every reflection, till the light exits from the other side of the stretched prism. Monitoring the $P(\theta_2)$ after a different number of reflections help us to know what happens to the divergence of the beam inside the stretched prism. This is depicted in Figure 2-18 (d) after 10, 30, and 48 reflections. Increasing the number of reflections leads to 1) attenuation of the specular reflected where attenuated power difference is in the form of scattered power at both sides of specular reflected light. 2) Power of the scattered light in a given θ_2 direction also decreases as itself being scattered more. 3) Finally, for such roughness values, most of the power is contained in the specular reflected light and power of the scattering rays are still an order of magnitudes less than that of the specular reflected light. This is attributed to the small percentage of the scattered light (2.3%) which is spread along wide scattering angles (10 to 40°, as depicted in the ASF in Figure 2-18 (c)) compared to specular light at only one angle 24°.

By sweeping the input incidence angle θ_o, summing all the scattered and the specular rays, one could have the corresponding $P(\theta_o)$ depicted in Figure 2-18 (e). As seen, the output change is within the beam divergence showing that these roughness parameters does not affect the resolution.

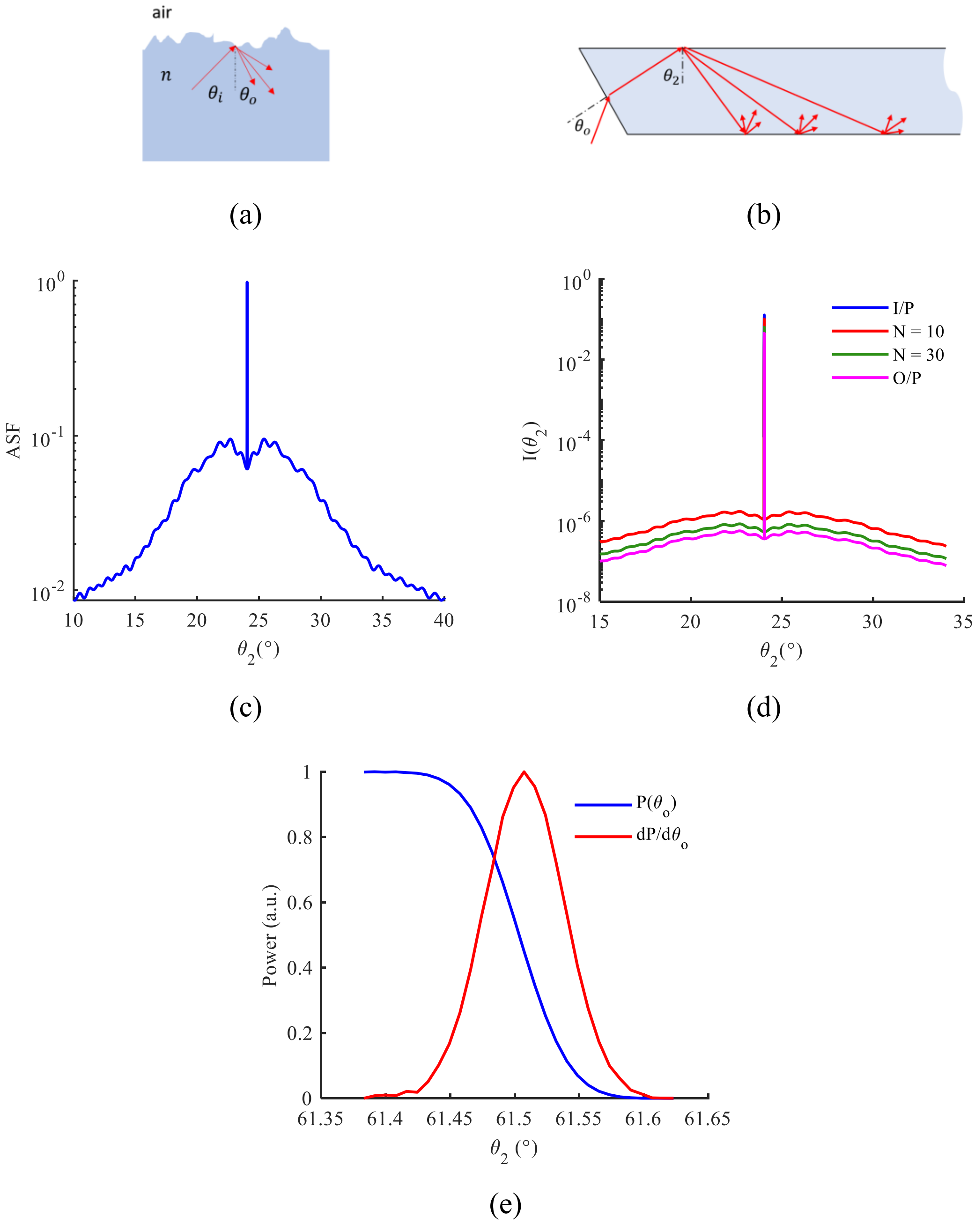

Figure 2-18 (a) Scattering upon reflection on a rough surface. (b) Scattering inside the stretched prism. (c) ASF function excluding the specular reflection. (d) Power distribution versus θ_2 after different number of reflections. (e) Integrated output power versus the incidence angle and the corresponding differentiated power.

Spectrometer non ideal effects

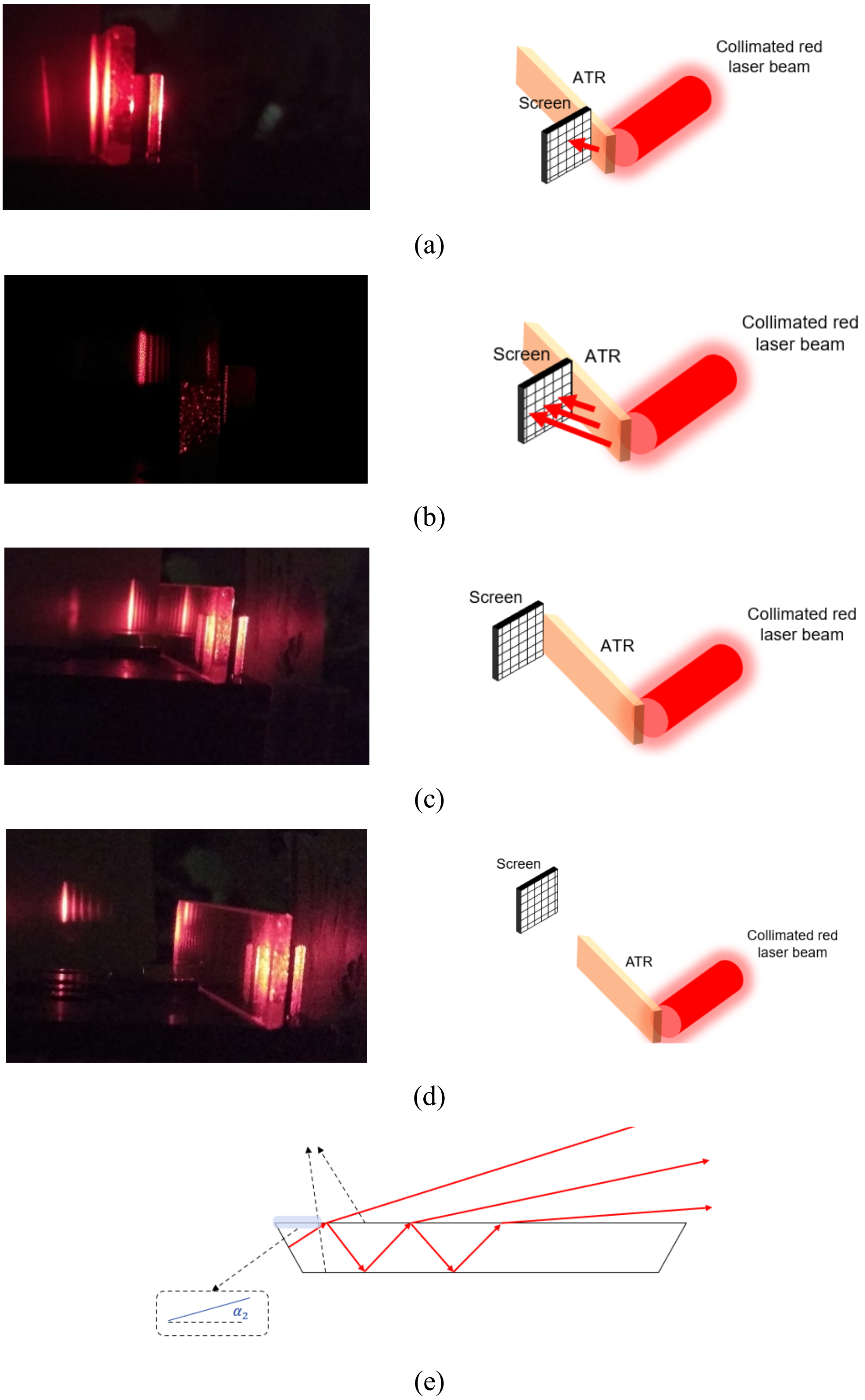

Figure 2-19 Investigation of the output spots of red laser which were emitted from the sides of the stretched prism. A screen was positioned at different positions on the stretched prism side in figures (a) to (d). Each

figure comprises at the left a camera photo for the measured laser spot and on the right the corresponding 3D layout of the experiment. (e) The figure shows that having unparalleled stretched prism surfaces leads to unparalleled emitted spots.

For a deeper measurement analysis, a visible laser (625 nm, FWHM = 1.3 nm) was injected to the stretched prism and the output spots from the stretched prism upper side are spotted as depicted in Figure *2-19*. The input light was injected to the stretched prism with an incidence angle greater than the critical angle ($\theta_o > 81°$). It is expected that the light in such case leaks successively after each reflection on the stretched prism. The screen was placed at the start of the ATR as depicted in Figure *2-19*(a). One rectangle spot was observed. Moving the screen away as seen in Figure *2-19*(b) to (d), the number of spots increased with lower intensity, as expected. However, one could observe that the spots become far away from each other as the screen moved away. This means they have different refraction angles which further means different incidence angles on the stretched prism surface. This happens only when the two sides of the ATR are not parallel. This is illustrated in Figure *2-19*(e).

ATR width at the two ends was measured using a digital microscope. The difference between widths ranges from 8 to 12 μm. Such variation arises from the microscope resolution. Thus, α_2, defined in Figure 2-19 (e), is in the vicinity of 0.01°. This value was taken an input to the model for investigating its effects. The laser has a wavelength of 625 nm, full width half maximum (FWHM) of 1.3 nm, and a divergence of collimation of 0.005°. The detected power versus the incidence angle of the input is depicted in Figure 2-20 (a) for positive and negative α. Such polarity will depend on the input side of injection (left or right one). One could observe different critical angles of θ_o depending on the polarity of α_2. This was observed experimentally where the critical angle of incidence was found to be 80.4° or 73° depending on the direction of excitation. Such a shift in the critical angle is expected and can be explained as follow 1) In the ideal stretched prism of parallel sides, once one injects the light at the critical angle, all reflections inside the stretched prism are at the corresponding critical angle of total internal reflection as the incident angle of light is the same everywhere. 2) For imperfect stretched prism, the incidence angle is different. Thus, the effective critical angle of incidence is the angle when the angle of incidence of light on the stretched prism surface is at the critical angle of total internal reflection at the

1st reflection or the last reflection depending on the polarity of α_2. The corresponding differentiated signals are depicted in Figure 2-20 (b), where a degradation in the resolution is observed (Light drops to zero in 1° instead of $2 \times 0.005°$). In Figure 2-20 (c), the differentiated signal of the output of spectrometer for different values of α_2 are depicted. Ripples in the spectra are observed, where the position of ripples depends on the value of α_2. The distance between two successive ripples is found to be $\alpha_2 \frac{\sqrt{n^2-(\sin\theta_o)^2}}{\cos\theta_o}$.

Concluding the above analysis, the unparallel surfaces of the stretched prism leads to 1) degradation in the resolution, 2) ripples in the spectrum, and 3) a shift in the critical angle depending on the excitation direction.

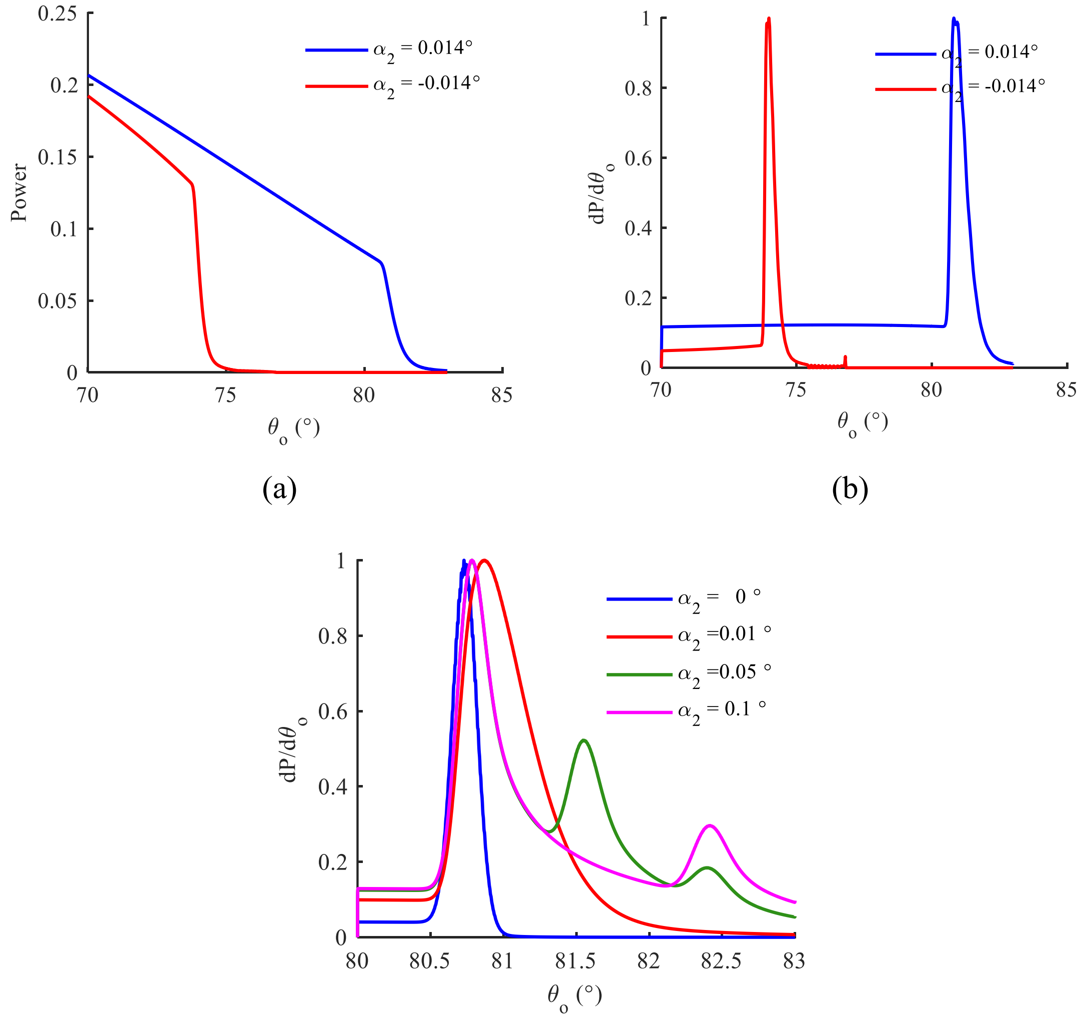

(a)

(b)

(c)

Figure 2-20 Simulation results taking into account the stretched prism unparallel surfaces ($|\alpha_2| = 0.014°$). (a) Output signal of laser 625 nm versus the angle of incidence. (b) Respective differentiated signals. (c) Differentiated signals for different values of α_2.

Signal correction

Mathematical correction could be performed to correct the resolution by removing the effect of unparallel surfaces of the stretched prism. The effect of unparallel surfaces appears in the matrix $\boldsymbol{\beta}$ in Equation (2.14). Replacing $\boldsymbol{\beta}$ with another corrected matrix $\boldsymbol{\beta_c}$ can solve this issue. First, one has to find $\boldsymbol{\beta}$ (whose row direction is a function in λ and the column direction is a function in θ_o). This is can be extracted from the laser measurements. The PSD of laser is expressed by $\delta(\lambda - \lambda_s)$(in vector form, it is $[0..010\ldots0]^T$). Thus, the measured $P_{Laser}(\theta_o)$ is given by:

$$\underline{\boldsymbol{P_{Laser}}} = \boldsymbol{\beta} * [\mathbf{0..010\ldots0}]^{\boldsymbol{T}} = \underline{\boldsymbol{\beta_{\lambda_s}}} \tag{2.18}$$

where $\underline{\boldsymbol{\beta_{\lambda_s}}}$ is the column vector in β which corresponds to λ_s (i.e. the signal in Figure 2-12 (c)). One can assume that the dependence of $\boldsymbol{\beta}$ on wavelength is just a shift in the position of the critical angle of incidence (see *Figure 2-9* (a) where the falling edge occurs at the critical angle. Thus, ideally $\underline{\boldsymbol{\beta_{\lambda_s}}}$ of different λ_s has the same shape but with shifting the position of falling edge or critical angle). Thus, the whole matrix can be estimated $\boldsymbol{\beta}$ using the laser measurement $\underline{\boldsymbol{\beta_{\lambda_s}}}$ with the help of Figure 2-10 (a). The estimated matrix is named $\boldsymbol{\beta_{est}}$. The corrected form of $\boldsymbol{\beta_c}$ can be generated from the Equation (2.13) and the input intensity distribution I, while the measured divergence angle of the light is 0.06° in case of the smaller fiber used. Finally, the corrected signal is given by the following:

$$\underline{\boldsymbol{P_c}} = \boldsymbol{\beta_c} * \boldsymbol{\beta_{est}^{-1}} * \underline{\boldsymbol{P}} \tag{2.19}$$

The corrected spectra of lasers measurements are shown in Figure 2-21 (a) after converting time to wavelength. Ripples has been removed and the resolution is enhanced from 120 nm to 50 nm at 1480 nm and 60 nm at 1548 nm. The corrected TS5 measurement is also depicted in Figure 2-21 (b).

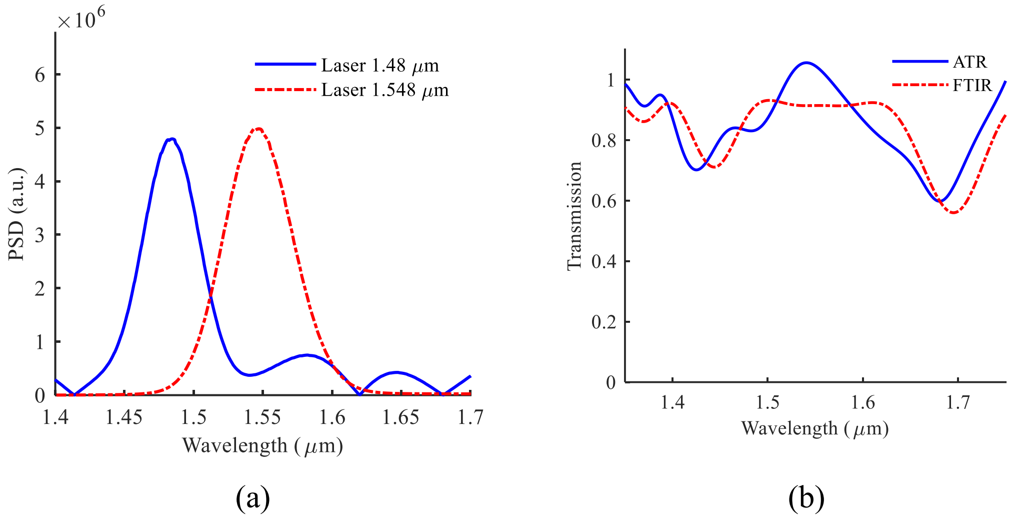

Figure 2-21 Corrected spectra of lasers measured by MMF of core/cladding of 50/125 μm. (b) Corrected TS5 spectrum.

2.4 Conclusion

Summarizing the results of the chapter; first, a MEMS chip which comprises a novel concept of parallel interferometers intended to provide better spectral resolution, was used to measure methane peaks with an enhanced spectral resolution enabling to discriminate peaks and identify methane. The parallel concept appears as a solution to the theoretically-limited resolution of MEMS FTIR spectrometers. Second, another novel concept of differential spectrometer based on a dispersive material was presented and studied in detail. Theoretical analysis, measurements and deep analysis were performed on the new structure. The concept was proved using a crystal. The achieved resolution was 60 nm around 1548 nm. A reference material was measured and compared with the measurements of FTIR spectrometer. Furthermore, the provided theoretical background provides a route for further improvements of the performance based on the proposed concept.

CHAPTER 3: MONITORING POLLUTION AND DE-POLLUTION OF AIR

3.1 Introduction

Air pollution is a critical problem that kills seven million people every year according to the world health organization [1]. Monitoring pollution and improving air quality is important for global health. Pollution can be also classified into indoor and outdoor pollution. Indoor pollution can arise from stoves, fireplaces, tobacco smoke, candles and incense, cleaning products and mosquito coils and even home furniture's and car's interior materials, whose surface can be the source of emission of harmful gases. The main source of outdoor pollution is human activities such as industries, factories, aircraft, automobiles, and power plants. Also, outdoor pollutants contribute to indoor pollution. Air pollutants are classified according to the state of matter to gaseous air pollutants and particulate air pollutants. Particulate airborne pollutants are in the form of suspended droplets or solid particles. They are out of the scope of this work/ Interested readers can check these references [188]–[190]. Examples for gaseous pollutants are Ozone (O_3), Sulphur dioxide (SO), carbon dioxide (CO), nitrogen dioxide (NO_2), nitrogen oxide (NO) and volatile Organic Compounds (VOCs). Examples for VOCs are toluene, benzene, acetone, aldehydes…. etc. Short term exposure limits (15 min.) are set to help prevent effects such as eye irritation, which can occur after a few minutes. An example of the limits of different gases can be found in Table 3-1 according to EH40/2005 Workspace exposure limits[16].

Table 3-1 Exposure limit for different gases

Chemical name	Short term exposure limit (ppm)	Long term exposure limit (ppm)
Acetaldehyde	50	20
Acetone	1500	500
Acrolein	0.05	0.02
Benzene	-	1
Carbon dioxide	15 000	5000
Ethylbenzene	125	100
Formaldehyde	2	2

Toluene	100	50
Xylene	100	50

Due to the harmfulness of pollutants, there is a need for a way to decrease the contaminants. This can be achieved by controlling pollution sources, increasing the air exchange rate, or by using air purifiers. Air purification methods either recover or destroy pollutants. Popular recovery techniques can be absorption, adsorption, or condensation while combustion and ionization are used for destroying pollutants. Another way is to eliminate such organic contaminants using photocatalytic oxidation whose final reaction products are safe and include carbon dioxide and water. For several decades, nanostructured metal oxide semiconductors such as zinc oxide ZnO, titanium dioxide TiO_2, iron (III) oxide Fe_2O_3, Cadmium sulfide CdS or Zinc sulfide have responded to the issue of destruction of VOCs [191]. Indeed, because of its wide bandgap (3.37 eV) and its great excitonic binding energy (60 meV), ZnO has very interesting properties. It can be used in several fields of applications such as energy harvesting [192], photovoltaics [193], photodetectors [194], gas sensing [195], and photo-catalysis [196]. ZnO-NWs can be easily obtained by hydrothermal synthesis, a simple and inexpensive method that can be implemented at low temperatures [197].

Real-time monitoring of pollutants in factories, stations, homes, and streets is important for the analysis of pollution sources and early alerting of exceeding the harmful limits. Thus, in this chapter, we are considering 3 activities:

1. Air pollution monitoring in a district scale: Onsite outdoor gas monitoring enables pollution mapping and control in cities and on the district scale. Having a low-cost and compact sensor that can monitor pollution over a long distance is needed. We are presenting an open-path Fourier transform infrared (FTIR) gas analyzer based on a mid-infrared (MIR) MEMS. The setup was deployed inside a huge climatic chamber (Sense-City, Paris, France) and a car was deployed inside the climatic chamber to create a pollution source. This is discussed in section 3.4.
2. Low concentration detection of VOCS in a localized gas cell: while the previous method allows retrieving average pollution levels over a wide space, there is also a strong need for the *localized* detection of these gases, in the part per billion ranges, for indoor air quality monitoring. We report the use of a MEMS FTIR spectrometer in the

mid-infrared for this purpose and Toluene, as an example, was measured using a multi-pass gas cell of 20 m long to achieve a lower limit of detection in the ppb range. This is discussed in section 3.4.

3. Air purification monitoring: We monitor a purification process of toluene and acetone using ZnO while applying the UV light for photo-oxidation. The monitoring was performed using the MEMS spectrometer and short gas cell (path length = 10 cm) to monitor and studythe decrease of pollutants with time and to assess the efficiency of the mentioned method. This is discussed in section 3.4.

3.2 Open-Path Air Pollution Monitoring

Sense city is a climate chamber that covers a surface area of 400 m^2 and a volume of 3200 m^3 along the following dimensions : 20 m x 20 m x 8 m. It is used to conduct experiments under controlled climatic conditions through the capability of tuning different atmospheric parameters such as temperature, humidity, sun, and rain. Sense-City is also equipped with different reference sensors. It was built with the aim to study different urban scenario dealing with the wider topic of Smart Cities. This include problems dealing with energy, environment including air, water and soil as well as the performance of urban and construction material. Camera photos for the Sens-City climatic chamber are shown in Figure 3-1.

Different high-performance analyzers are already existing in Sense city such as nitrogen oxide NOx analyzer, CO and CO_2 analyzer in addition to humidity and temperature sensors. The NOx analyzer (AC32M, ENVEA) is based on chemiluminescence where an oxidation of NOx with an internally generated ozone occurs. This reaction emits light which can be detected by a detector. The corresponding detection limit is 0.5 ppb. Regarding the CO analyzer (CO12e, ENVEA), it is based on a non-dispersive IR sensor (NDIR) in conjunction with a gas correlation filter to enhance the detectivity. The detection limit is 25 ppb. The analyzer is also equipped with a module for measuring CO_2.

Figure 3-1 Camera photos inside the Sense city climatic chamber.

The MEMS FTIR spectrometer (NeoSpectra MIR SWS6241, Si-Ware Systems) that we are considering to be used in our experiments for open-path measurements, is an extended wavelength prototype version of Neospectra SWS62221 NIR commercial products. This MIR prototype covers a spectral range from 1.5 to 4.9 μm. Such a range covers the absorption coefficient of CO, CO_2, and NOx. However, due to the limited throughput of the MEMS spectrometer, the respective detection limit may be greater than the typical values of gas concentrations inside the city. In section 3.2.1, such limits are discussed.

3.2.1 Optical coupling system design

In radiometry, the light power emitted from a circular source can be given by [198]:

$$P = \int_0^{\pi(0.5D)^2} \int_0^{2\pi} \int_0^{\theta_o} R_o\, cos\theta\ sin\theta d\theta\ d\phi dA = 0.25 R_o \pi^2 D^2 \sin^2\theta_o \qquad (3.1)$$

where θ_0 is the light divergence angle and R_o is the source radiance. Radiance is conservative in any optical system given negligible reflection losses or scattering which is our case, where very few optical components are used. In the case of Lambertian source, the radiance is independent of viewing angle or the position on the source. In the case of a small divergence angle, $\sin\theta_o \sim \theta_o$. The product of the area and the divergence angle is the called the throughput, noted TP, which is varaible among the system depending on the spot diameter D and θ_o. For simple writing, the constants are omitted and $TP = D^2\theta_o^2$.

To avoid chromatic aberrations (mainly due to material's dispersive refraction), off-axis parabolic mirrors are used instead of lenses (Figure 3-2). The off-axis parabolic mirrors will be used to collimate light at the source side and refocus light at the spectrometer side. The off-axis parabolic mirrors have an acceptance angle < 0.5 rad. (focal length ≥ half the diameter).

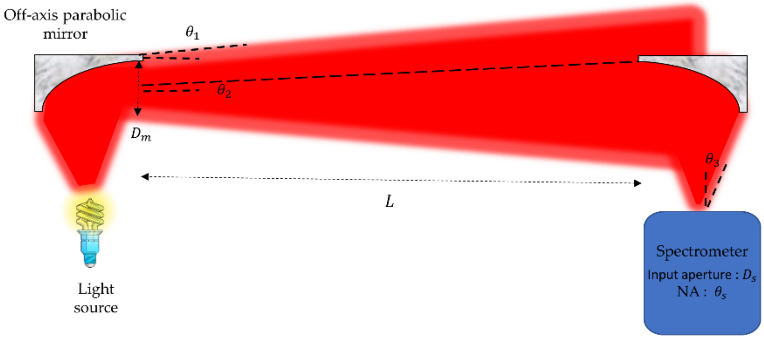

Figure 3-2 Layout of open-path setup using off-axis parabolic mirrors to transfer light from light source to the spectrometer.

Filament sources have a big throughput compared to that of the input of the MEMS spectrometer. The divergence angle is big (in other words it is $> 0.5\ rad$). This means that all the area of the mirror (diameter of the mirror is D_m) will be illuminated. Thus, light throughput from the collimating mirror is $TP_1 = D_m^2\theta_1^2$, where θ_1 is the divergence angle of the collimated light, as depicted in Figure 3-2.

Light received by the other mirror is given by $D_m\theta_2$, where θ_2 is the divergence angle of the light received by the mirror and it is equal to $\frac{0.5D_m}{L}$, where L is the path length. Thus, the light throughput received by the 2nd mirror is given by $TP_2 = 0.25D^4/L^2$. It is obvious that increasing the path length L, the transmission, that is given by TP_2/TP_1, will degrade. On the other side, the spectrometer has a numerical aperture θ_s and the diameter of the input fiber D_s. Such throughput is much smaller than the source throughput or even TP_1. There is a range of path lengths from 0 to L_{max} where the power received by the spectrometer is constant. L_{max} holds when the light throughput TP_2 the second mirror is equal to that of the spectrometer. Thus, L_{max} is given by:

$$L_{max} = \frac{0.5D^2}{\theta_s D_s} \tag{3.2}$$

In order to fit the received power within the acceptance of the spectrometer, the optimum focal length of the mirror should satisfy $\theta_s = 0.5D_m/f_{opt}$ or $f_{opt} = \frac{0.5D_m}{\theta_s}$. In the case of the MEMS spectrometer, this value is much larger than the mirror diameter (θ_s is in the vicinity of 0.05 rad,). However, one is restricted with the available off-the-shelf components, which is comparable to the mirror diameter (i.e. $2D$, $3D$). Using the off-the-shelf mirrors of a focal length f_m shorter than the f_{opt} means that the divergence of the light received by the spectrometer $\theta_3 > \theta_s$ which directly means that the imaged spot at the spectrometer input will be of a diameter $D_3 < D_m$ (because at L_{max}, $D_m\theta_2 = D_s\theta_s = D_3\theta_3$ and $D_3 = \frac{f_m}{f_{opt}} D_s$). Thus, in such case, the maximum path length should be decreased by a factor $\frac{f_m}{f_{opt}}$ to increase the percentage of received power by $\left(\frac{f_m}{f_{opt}}\right)^2$ increasing D_3 back to D_s. Thus, the maximum path length of a given mirror of diameter D_m and a focal length f_m should be modified to be

$$L_{max} = \frac{f_m D_m}{D_s} \tag{3.3}$$

Thus, the maximum path length is increased by the product of both focal length and diameter of parabolic mirror.

If one is going to increase the path length > L_{max} using the same mirror, losses will be introduced and the absorption path length indeed will be increased. However, the percentage of power decrease is proportional to $\left(\frac{L_{max}}{L}\right)^2$ while the enhancement in the absorption path length is only proportional to L. Thus, decreasing the path length greater than L_{max} decreases the absorbed power by the gas (This is $P_r - P_r e^{-\alpha L}$ according to Beer's Lambert law where P_r is the received power in the absence of gas) and the optimum path length is still L_{max} . Using a parabolic mirror of a focal length of 152.4 mm and a diameter of 50.8 mm, the corresponding optimum length is $L_{opt} = 26$ m.

The insertion loss (IL) of the coupling system (2 parabolic mirrors of a diameter 50.8 mm and a focal length of 152.4 mm) versus distance was simulated using a ray-tracing software (ZEMAX software). The result is shown in Figure *3-3*. The IL around 26 m is -3.7 dB which is attributed to optics aberrations which degrade the IL. For a distance of 38 m, the corresponding losses are -7dB.

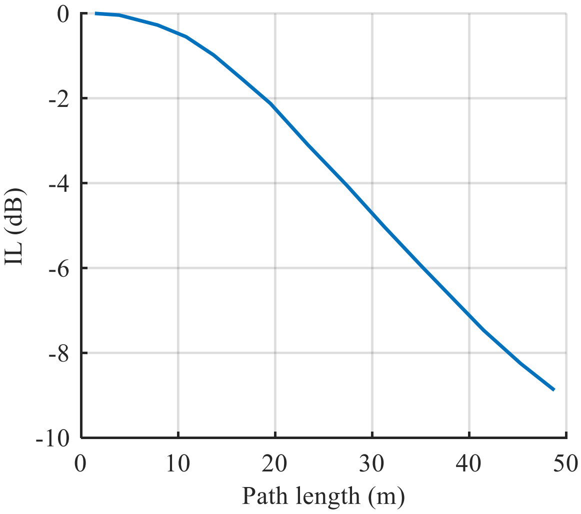

Figure 3-3 Insertion loss (IL) of the coupling system for the open-path FTIR.

3.2.2 Optical setup in Sense city

The optical system used in the open-path FTIR measurements comprised a bulb (Temperature = 2796 K, SLS252, Thorlabs) placed at the focal point of the off-axis parabolic mirror (Diameter = 50.8 mm, effective focal length = 152.4 mm, MPD269-G01, Thorlabs) as shown in Figure 3-4. The collimated light from the source was refocused at the detector side using another off-axis parabolic mirror. The light is focused into the input of the MIR spectrometer. The mechanical part holding different optical parts is designed by a CAD tool and made of plastic using 3D-printing.

Figure 3-4 Camera photo of an optical system used in the open-path FTIR.

Figure 3-5 Top schematic view of Sense city for air pollution monitoring using open-path FTIR in addition to camera photos in different positions inside the city.

As shown in Figure 3-5 (a), the source side held on a stand and positioned at one corner of the Sense city while the detector is placed at the opposite corner. The collimated light from the source side travels along the road to the bottom left corner of Sense city and bent by 90° using a flat mirror to the top left corner while passing near to the car. The spectrometer is positioned at the top left corner. The reference gas analyzers (AC32M and CO12E) were placed inside a housing beside the car. The analyzer measures concentration by sucking local air. Other sensors were used to monitor temperature and humidity. The total distance between the source and detector is about L= 38.1 m. The FTIR measures the *average* gas concentration along the path of length L while the reference analyzer measures the *local* gas concentration besides the car.

3.2.3 Results and discussion

The spectrum measured by the FTIR is plotted in Figure 3-6(a). It is compared to the spectrum measured at 0 m. The spectrum's shape is the same except for the water absorption around the wavelength of 1.87 μm and 2.7 μm and carbon dioxide absorption around 4.25 μm. The SNR was measured at a distance 38 m using a spectral resolution of 80 cm^{-1} and average measurement time of 1 minute. The SNR was calculated using a 100%-line method. The method is based on acquiring many successive measurements and 100%-lines are calculated by dividing each two succeeded measurements. Calculating the average across these lines, the SNR can be obtained [13]. Using the SNR curve, the detection limits of different gases can be calculated. Noise standard deviation in absorbance can be calculated from the SNR by the following equation:

$$\sigma_A(\lambda) = \frac{\log_{10} e}{SNR(\lambda)\sqrt{2}} \tag{3.4}$$

where λ is the wavelength. Optimum wavelength λ_{opt} of detecting a gas is the wavelength which has a maximum ratio between absorbance value and the noise. Once finding this value, the minimum concentration is the concentration when the absorbance $A(\lambda) = \sigma_A(\lambda_{opt})$. The detection limit of different gases was calculated, and the results are mentioned in

Table 3-2. These are compared to that of the reference analyzers. In table 2, the detection limits of CO, NO and NO_2 using the FTIR appear as being far from the typical measured values inside the room as will be shown later. It is worth reminding that in this experiment, Neospectra is giving an average value of the gas concentration over the whole path length of 38.1 m, while the gas analyzer is taking local measurements at the close vicinity of the gas pollutant source, where the concentration is expected to be much higher.

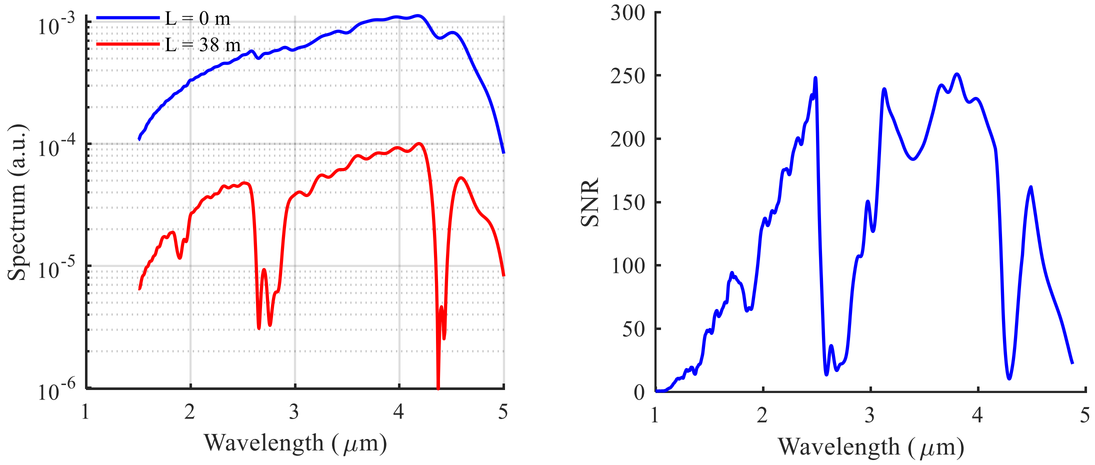

(a) (b)

Figure 3-6 (a) Measured spectrum at a distance of 0 m and 38 m. (b) The measured SNR at a distance of L= 38 m and a resolution of 80 cm^{-1}. The average measurement time is 1 minute.

Table 3-2 Detection limit of different gases in case of the open-path FTIR and the reference analyzers in Sense city.

Gas	Open-path FTIR		Analyzer
	Wavelength (nm)	Detection limit (1σ) (ppb)	Detection limit (1σ) (ppb)
CO	4595.8	800	25
CO_2	4255.6	40	NA
NO	2677.1	50,000	0.2
NO_2	3445.6	1000	0.2

Methodology for Background removal

The background effect on the raw measured spectrum is due to the non-idealities in the optical source spectrum, collimation optics, and spectrometer line shape function. All these effects deform the spectral response and should be removed. Conventionally this is carried out by measuring a first spectrum in the absence of the sample under test. This is not accessible in our case since we are measuring in the open air. This difficulty can be removed using baseline correction methods such as Polynomial fit [199], adaptive iteratively weighted penalized least squares [200], wavelet transform [201]….etc. Polynomial fitting is considered as a popular and fast method. The procedure is explained as follow:

1. A polynomial fit of a low order is applied to the measured absorbance A_0 as depicted in Figure 3-7(a). This absorbance is a typical measurement captured in Sense city. Such fit represents the initially estimated baseline.
2. New absorbance A_1 is calculated according to $A_1 = \min([A_0\,,\,Poly.\ fit])$. This tends to remove the absorption peaks as depicted in Figure 3-7 (b).
3. A new fit is applied to A_1 as depicted in Figure 3-7 (b).
4. Step 2 and 3 are repeated until the baseline curve (fitting curve) does not change within a certain threshold as depicted in Figure 3-7 (c).
5. The baseline-corrected spectrum is given by subtracting the final baseline from A_0. This final absorption spectrum is shown in Figure 3-7 (d).

This method was repeated for all the measured spectra, also to overcome the source stability with time which leads to a wavelength-dependent shift in the baseline as time evolves.

At the start of the measurement, it is expected that the concentration of gases is almost the same (steady-state) in the whole room since there is no local pollution perturbation that happened for a long time (chamber is sealed from the outer environment and the chamber was closed for more than 12 hours). Thus, the absorbance value measured by the MEMS FTIR at the absorption wavelength of each gas corresponds to the concentration measured by the reference analyzer, also meaning that calibration of the MEMS FTIR can be done at this stage by comparison with the data given by the reference analyzer. Since the absorbance is directly proportional to the gas concentration (absorbance = constant x concentration) according to Beer Lambert's law. Therefore, the proportional constant can be retrieved from the concentration measured by the analyzer at time 0 and the absorbance value measured by the FTIR. Measurement recordings started at time 0. After 6 hours and 10 minutes, the car, whose position depicted in Figure 3-5, was turned on and was turned off at 6 hours and 30 minutes. After 10 minutes, the car was turned on again for only 5 minutes.

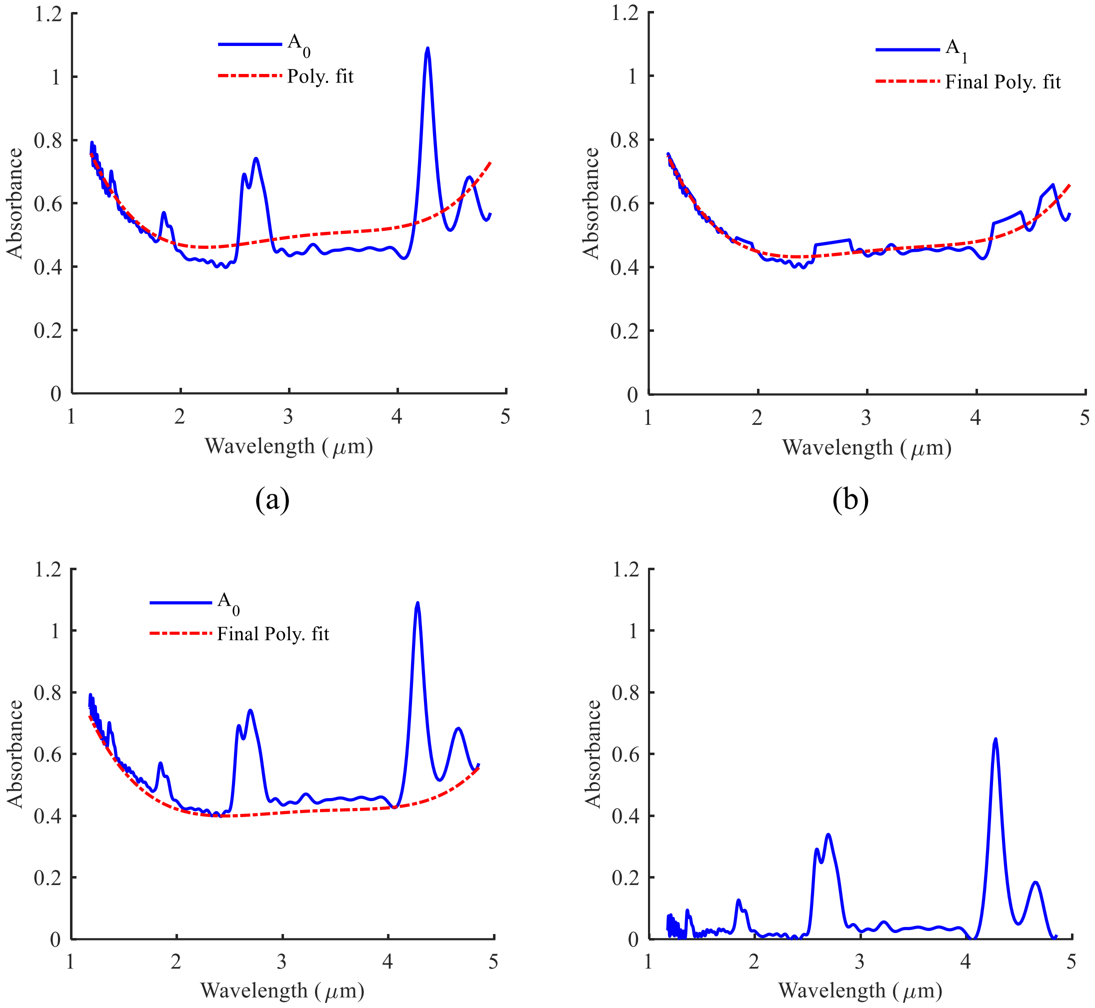

(a) (b)

(c) (d)

Figure 3-7 Procedure of baseline correction of the measured spectrum using the polynomial fit method.

The concentration of the carbon dioxide measured versus time is depicted in Figure 3-8(a). The analyzer measurement is also plotted in the same figure for comparison. The transparent red part represents the duration when the car was running (pollution was introduced). A spike in CO_2 concentration was observed in the measurement of the analyzer as the analyzer was placed in close proximity to the car. After the car was turned off, CO_2 concentration started to decrease due to diffusion inside the room. On the other side, the open-path FTIR measured a fast increase of the CO_2, once the car was turned on, but no faster than that of the analyzer and also didn't reach the same peak. This is because the FTIR averaged the concentration over a long distance. After, a while it measured a gradual increase in carbon dioxide with a slower rate due to the continuous diffusion of carbon dioxide inside the room.

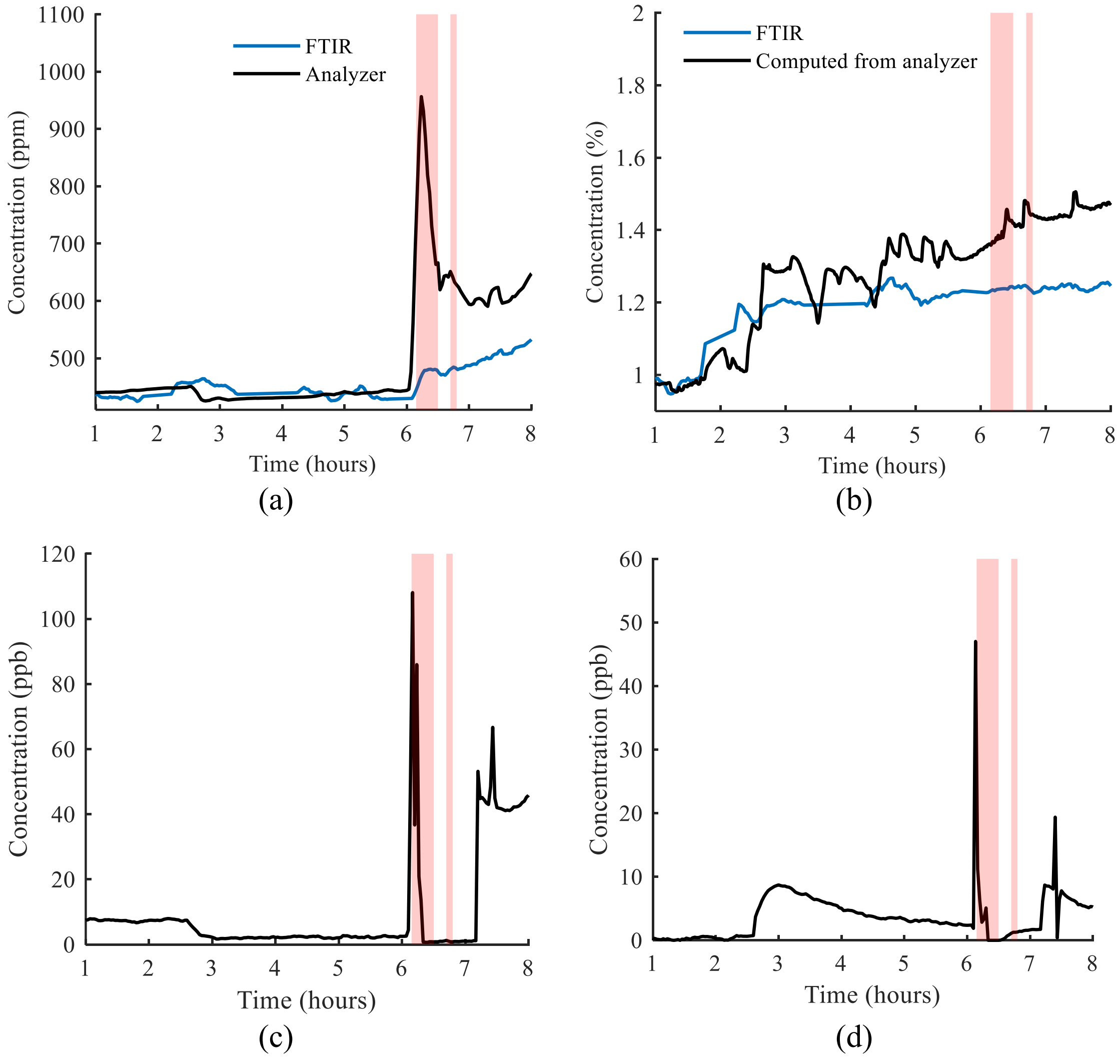

Figure 3-8 (a) Carbon dioxide concentration versus time (b) Water concentration versus time. The red region represents the interval of introducing pollution using car acceleration. (c) NO concentration measured by the analyzer. d) NO_2 concentration measured by the analyzer.

The concentration of water was monitored for a peak at 1.848 μm in the FTIR measurement. This was compared using the water concentration calculated from the humidity sensor and temperature sensor, as depicted in Figure 3-8 (b). Saturated water vapor pressure (Pascal) is calculated using the Magnus formula as follow [202]:

$$P_{H_2O_{sat.}} = exp\left(\frac{17.62T}{243.12 + T}\right) \tag{3.5}$$

where T is the temperature in (C°) and the corresponding water concentration is given by:

$$C_{H_2O}(\%) = RH(\%) * \frac{P_{H_2O_{sat.}}}{P} \tag{3.6}$$

where P is the air total pressure. The concentration of NO and NO_2 measured by the analyzer are plotted in Figure 3-8(c) and Figure 3-8(d), respectively. There was a failure in the analyzer from 6:10 to 7:10 causing a drop in the signal during this period. However, a spike in both gases is observed once the pollution is started.

Finally, the presented setup present a promising solution of open path measurements surpassing conventional open-path FTIR sensors which suffers from high cost, bulky and heavy[33], [203], [204].

3.3 VOCs analysis using MEMS spectrometer and multi-pass gas cell

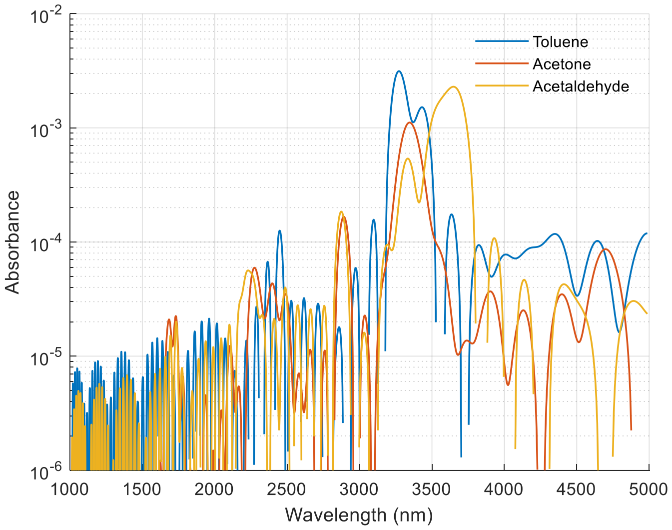

Figure 3-9 The absorbance of 1 ppm of different VOCs calculated for FTIR spectrometer of a resolution of 80 cm^{-1}.

The experiments presented in this section were conducted in laboratory. Since the spectrometer is operated in the wavelength range of 1.6 µm - 4.9 µm, the absorption spectrum of water vapor, BTEX and Aldehydes are detected around 2.65 µm, 3.27 µm, and 3.6 µm, respectively. The absorbance spectrums of the different VOCs are plotted in Figure 3-9. The simulation was conducted using the PNNL database. The simulation configuration was an ideal FTIR with resolution 80 cm^{-1} and a boxcar apodization.

The corresponding detection limit of these gases can be calculated using the same method specified in section 3.2.2. The detection limit was detected for toluene, acetone, and acetaldehyde for different SNR and path lengths. The detection limit is inversely proportional to the path length and the SNR. For a detection limit (1 σ) less than 100 ppb, SNR greater than 2000:1 and a path length of 20 m are required.

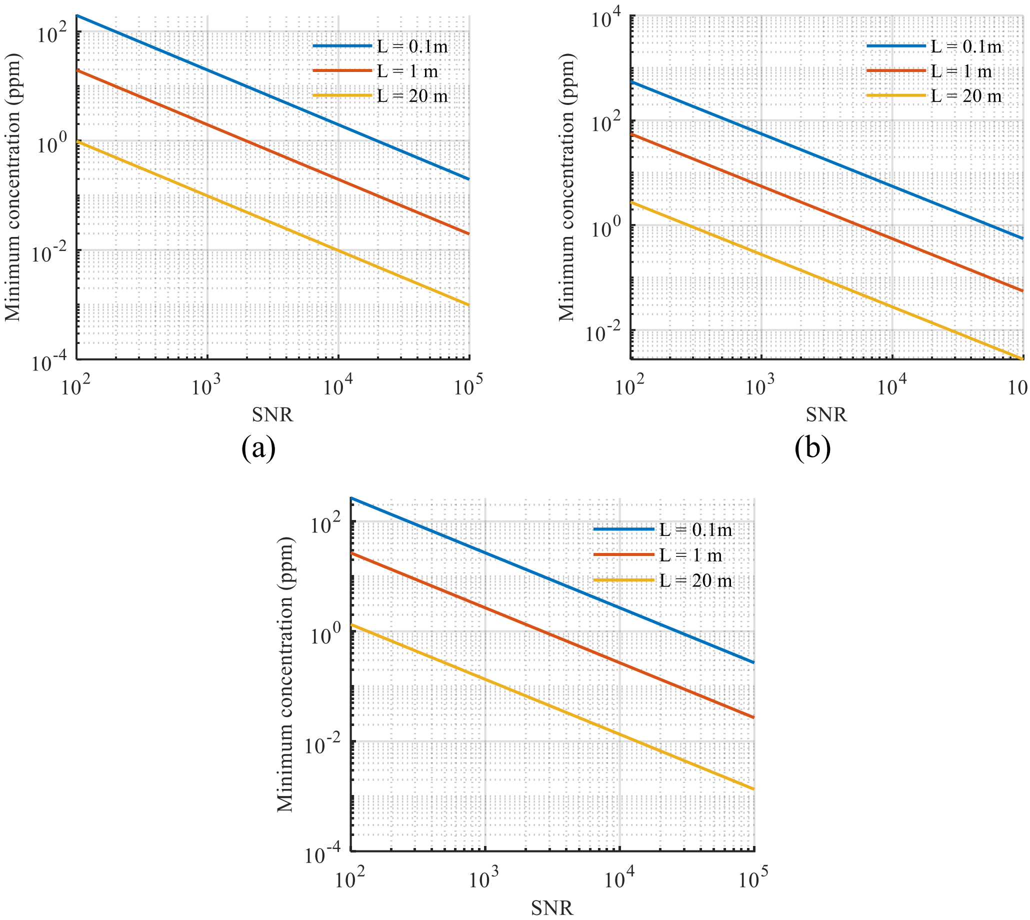

(a) (b)

(c)

Figure 3-10 Detection limit of (a) toluene (b) acetone and (c) acetaldehyde using FTIR of a resolution of 80 cm^{-1}.

3.3.1 Experimental setup

The Toluene has a strong absorption at 3.27 μm. For the preparation of Toluene gas inside a Tedlar bag with a given concentration, the corresponding volume of Toluene liquid can be calculated from the gas law. Thus, the volume of liquid analyte required is given by [11] :

$$V_{anal} = \frac{C\,PM_W V_{bag}}{10^6(T + 273.15)\,\rho\,R} \tag{3.7}$$

where C is the required gas concentration in ppm, P is the gas pressure, V_{bag} is the Tedlar bag volume, M_w is gas molecular weight and ρ is the gas-liquid density (for toluene $\rho = 967Kg/m^3$ [12]). The volume of the analyte can be obtained using a liquid syringe. In this experiment, 100 µL and 0.5 µL syringes were used.

Regarding the steps for preparing different concentrations of toluene gas, a Tedlar bag was first filled with nitrogen with a volume equals to the gas cell V_{cell}. Using the syringe, a controlled volume amount of toluene in liquid phase was added to the Tedlar bag. After that, the bag was shaken to vaporize the volatile liquid so as it is diluted in the gas phase. To get a more diluted concentration (ppb concentrations), a syringe (manual syringe 5190-0464/ 5190-1509, Agilent), specific for gases, can be used to take a gas sample of volume V_{gas} from the bag to a new bag filled with the nitrogen of volume V'_{bag}. The new concentration is related to the concentration in the old bag by:

$$C_2 = C_1 \frac{V_{gas}}{V'_{bag}} \tag{3.8}$$

The experimental setup for measuring gas concentration is depicted in Figure 3-11 (a). A multi-pass gas cell (Tornado T20, Specac) of a base length of 0.5 m long, 40 reflections, and a total effective length of 20 m was used. A detailed discussion about the multi-pass cells can be found in chapter 4. The light from the source was injected into the gas cell using a collimation lens. After 40 multiple passes in the gas cell, the light at the output of the cell was coupled into the input of the MEMS spectrometer using another lens. The spectrum was retrieved from a computer connected to the spectrometer. The multi-pass gas cell was evacuated using an air pump. A background spectrum was measured using the spectrometer. This is shown in Figure 3-11 (b). After that, the Tedlar bag which contained the Toluene with a given controlled concentration is connected to the gas cell to allow air to flow into the gas cell. After filling the cell, the inlet valve was closed. The spectrum of gas was then obtained. Thus, the transmission curve of Toluene could be obtained, and the corresponding absorbance curve. Concentrations of Toluene in ppm range and ppb range were measured using the former steps.

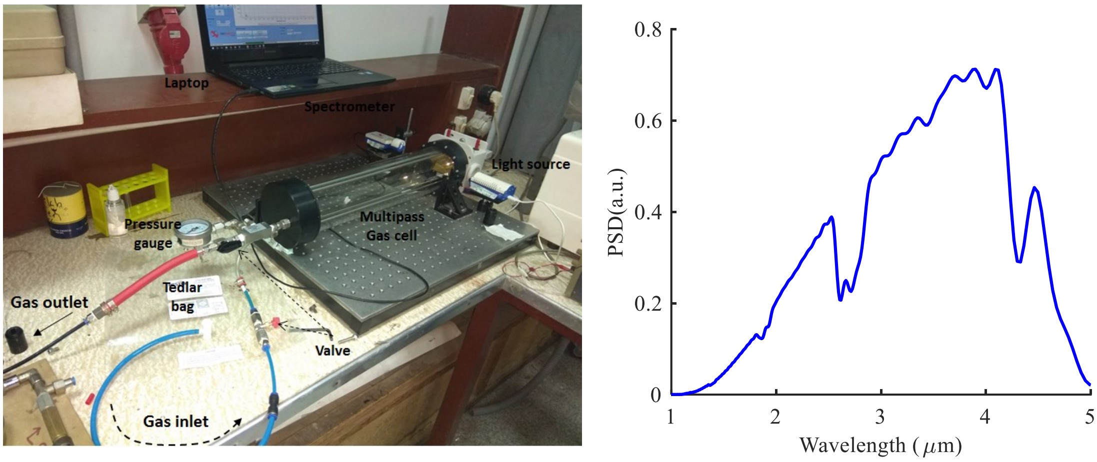

(a) (b)

Figure 3-11. (a) Experimental setup for measuring Toluene. The Toluene with a given concentration is transferred from the Tedlar gas to the multi-pass gas cell. A light source is used to inject light into the cell and finally detected by the spectrometer. (b) Background spectrum.

3.3.2 Results and discussion

The measured transmission spectrum through 8 *ppm* of Toluene was measured with a resolution of 80 cm^{-1}. The measured transmission curve is plotted together with the simulated curves in Figure 3-12. The measurement shows a good agreement with the simulation. The discrimination in the curve after 3400 *nm* is attributed to the self apodization of the MEMS spectrometer which is different from the ideal case.

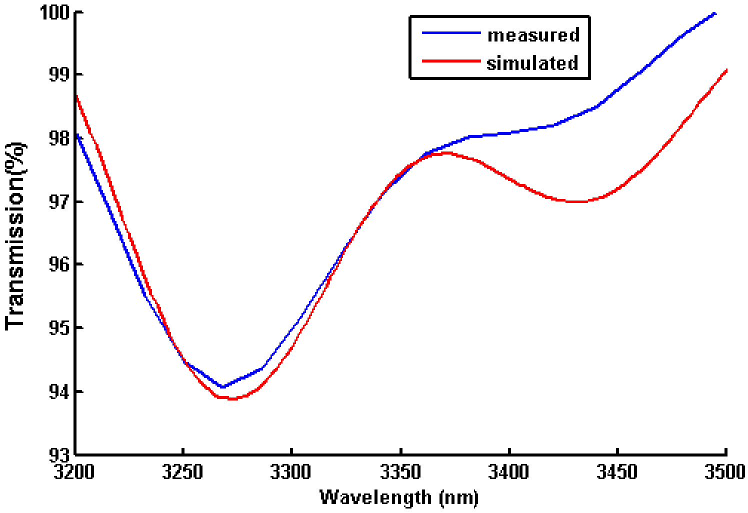

Figure 3-12 Simulated and measured spectrum of Toluene at concentration 8 ppm

The measured transmission curves of 3, 8, 28, and 55 ppm are depicted in Figure 3-13. The curves show a gradual decrease in the transmission curve with decreasing concentration. In Figure 3-14, the transmission curves of 700 and 2000 *ppb* are depicted. For smaller concentrations, the spectrum is affected by the side lobes of the residual water in the gas cell. These lobes mask the absorbance of the Toluene around 3.27 µm.

To study the linearity of the system, the absorbance of Toluene is plotted versus the corresponding concentration C. The curve is fitted to a straight line as shown in Figure 3-15. The slope of the line is $m = 0.003\, ppm^{-1}$ and the offset is 0.0036. The figure shows a good linearity (coefficient of determination $R^2 = 0.9992$) with a quite large dynamic range.

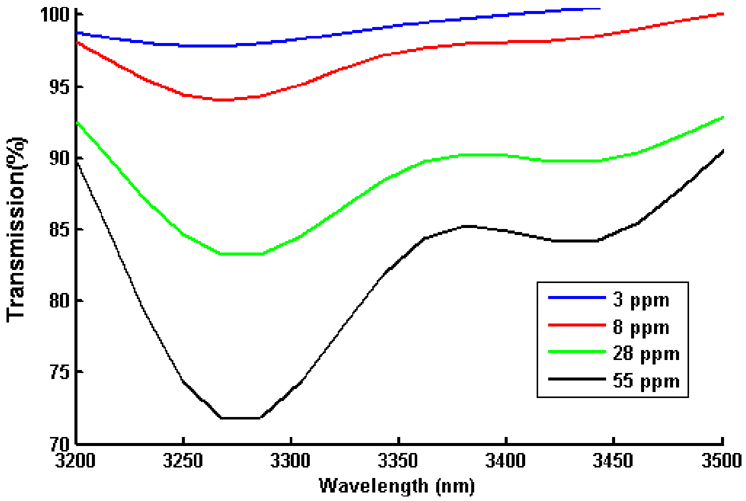

Figure 3-13 Spectra of measured Toluene at different concentrations in the ppm range.

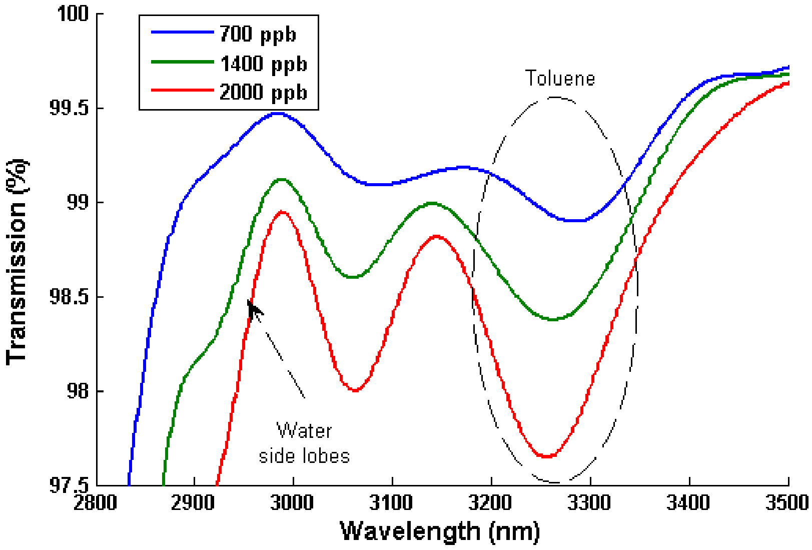

Figure 3-14. Spectra of measured Toluene at different concentrations in the ppb range. The spectrum is affected by the side lobes of water absorption, whose effect is apparent especially at low concentrations of Toluene.

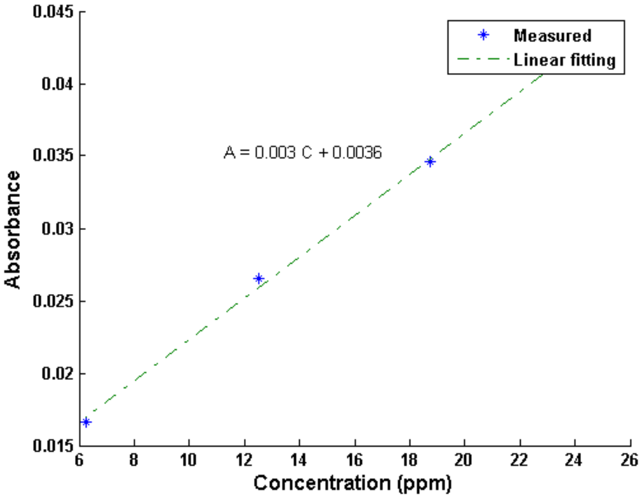

Figure 3-15 Linearity of measured absorbance versus the corresponding concentrations. The measured points are fitted to a straight line showing good linearity. The coefficient of determination $R^2 = 0.9992$.

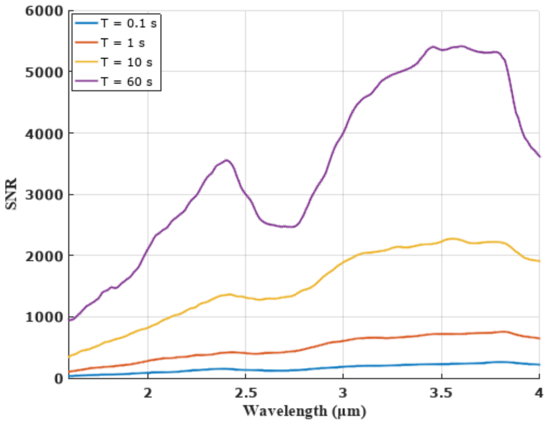

Figure 3-16 Measured SNR for a different average time.

The SNR of the system was measured by filling the gas cell with Nitrogen and calculated using the 100%-line method. The SNR was measured for a different average time as depicted in Figure 3-16. The measured SNR at $\lambda = 3.27\mu m$ was found to be 5000:1. This value correspondence to a standard deviation σ in the absorbance around 10^{-4}. From the fitted equation in Figure 3-15, the corresponding minimum detectable concentration is calculated by:

$$C_{min} = \frac{\sigma}{m} \tag{3.9}$$

where m is the slope of the fitted line. Based on this, the minimum detectable concentration was found to be 30 *ppb*.

3.4 Monitoring of air purification using ZnO NWs chip

Here, we focused our study on the demonstration of the photocatalytic effect of ZnO-NWs on degradation reactions of the polluting gases contained in tobacco smoke, to evaluate its efficiency in the purification of indoor air. For the study of simple gases contained in tobacco smoke, acetone and toluene are chosen as models. We aim to study the efficiency of ZnO-NWs of these pollutants, by distinguishing the contributions of the two main mechanisms involved, that is, adsorption and photocatalysis. Therefore, both capturing by adsorption and photocatalysis reactions were continuously tracked by using the MEMS spectrometer. The setup for continuous monitoring of the depollution process is depicted in Figure 3-17.

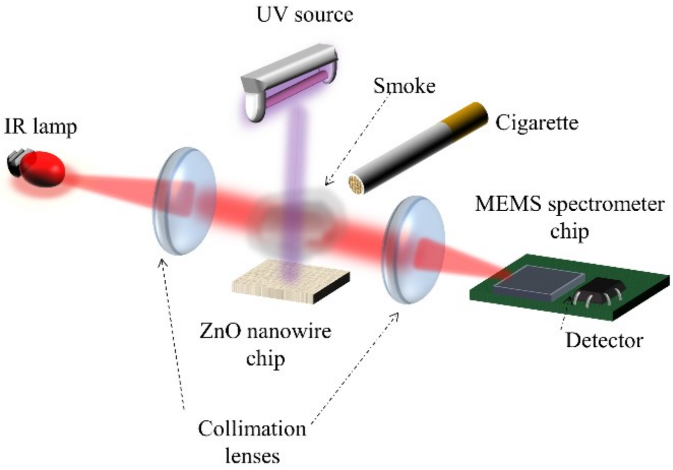

Figure 3-17 Photocatalysis setup with timely monitoring of air purification.

3.4.1 Experimental setup using MEMS-based FTIR spectrometer

The used ZnO nanowire arrays had been synthesized as described in reference [205]. The average length of nanowires is 1.8 ± 0.1 µm with an average diameter of 51 ± 5 nm. The whole experimental setup that we developed for our analysis is presented in Figure 3-18. Photocatalysis is implemented as a remediation solution to reduce different gas pollutants, such as acetone and Toluene. It was conducted inside a direct path gas cell (cell volume is Vcell =132 mL and path length is 10 cm). The wall of the gas cell was made of Pyrex while 2 Potassium Bromide (KBr) windows were used for coupling the IR light in and out. First, background measurement was taken with a gas cell containing pure air. After that, the ZnO-

NWs sample is deployed inside the cell. Pollutants were also added inside the cell. By adding a controlled volume of pollutants in the liquid state, its volatility leads to a well-controlled concentration in the gas state after complete evaporation. After that, the pollutants are introduced inside the cell by heating the whole cell. For acetone, $V_{liquid} = 20\ \mu L$ are used and this corresponds to concentration around 5% calculated from the following equation:

$$C\ (ppm) = \frac{P_{gas}}{P_{Total}} = \frac{R\ (T + 273.15)\ \rho V_{liquid}}{P_{Total} V_{cell} M_W} \tag{3.10}$$

where P_{gas} corresponds to the partial pressure of pollutant, P_{Total} is the total pressure inside the gas cell which is equal to 1 atm., R is Boltzmann constant, ρ is the pollutant density in liquid state and M_w is the molecular weight of pollutant. The cell was sealed and irradiated with a UV lamp (Hamamatsu LC8, 4500 mW/cm², $\lambda = 365$ nm) localized above the cell with a distance of 10 cm between the lamp and ZnO-NWs sample. After starting the UV illumination, gas pollutant concentration was monitored every 20 minutes during 3h, by Neospectra (Si-Ware MEMS FTIR, resolution 80 cm^{-1}) and confirmed by FTIR (Perkin Elmer, Spectrum Two, resolution 4 cm^{-1}). Also, the same experiment was repeated using 10 µL of toluene corresponding to a gas concentration of 1.7%.

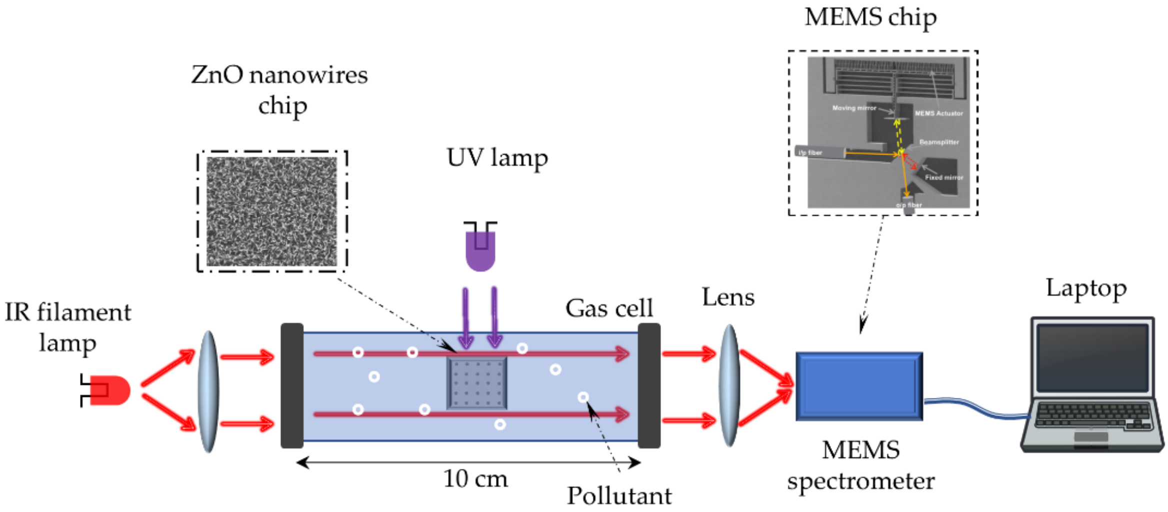

Figure 3-18 Experimental setups of pollutant purification within the gas cell by photocatalysis on the ZnO-NWs chip. The de-pollution process is continuously monitored using the MEMS spectrometer coupled to the gas cell.

3.4.2 Results and discussion

Monitoring purification of air polluted with Acetone

The transmission of acetone was measured using the MEMS spectrometer every 20 minutes. The transmission spectra during the purification process of acetone using ZnO is shown in at different acquisition times. The elimination is also calculated for the four different cases: without/with ZnO chip in the absence/presence of UV light. The elimination ratio at an observation time t is calculated as follows:

$$E(t) = 100 \times \frac{A(t_0) - A(t)}{A(t_0)} \tag{3.11}$$

where $A(t_0)$ and $A(t)$ represents the absorbance at a given wavelength at an initial time t_0 and observation time t, respectively. The absorbance value at 2970 cm^{-1}, which corresponds to the C-H bond, was used to monitor the degradation of acetone with time. The transmission of acetone was recorded every 20 min for 3 hours. In the absence of UV, the recorded transmission curves at different sampling times are shown in Figure 3-19 (a).

Figure 3-19 (c) shows the degradation of the acetone with time when one looks at the decrease of absorbance around 2970 cm^{-1}. The elimination ratio versus time was calculated in the presence of ZnO and compared to the case of absence of ZnO as depicted in Figure 3-19 (c). Using ZnO enhances the elimination ratio during all the observation time. The elimination ratio after 3 hours is around 14% in the case of ZnO compared to only 3 % in case of without ZnO, as shown in Figure 3-19 (c). This shows an enhancement of the elimination ratio by 4.6 times. Also, returning to Figure 3-19 (b), one observes that the CO_2 absorption line at 2350 cm^{-1} increases with time proving the increase in CO_2 concentration as a by-product of the photo-oxidation process. This is aligned with the theoretical expectations described in Fig

The experiments are then repeated using UV light. This leads to the photo-oxidation process in the absence of ZnO chip and photo-catalysis in the presence of the ZnO chip. The transmission of acetone at different time are depicted in Figure 3-19 (c) showing the degradation versus time. The elimination ratio is also plotted in Figure 3-19 (d). The enhancement can be seen clearly when using ZnO. For example, after three hours the elimination ratio in the case of ZnO was 11% while removing the ZnO chip leads to nearly 0%. Elimination ratio fluctuates around zero in case of absence of ZnO for measurement time less than two hours, as shown in Figure 3-19 (d), because the decrease in the concentration of acetone is within the spectrometer noise/ systematic variation. It is worth mentioning that the use of UV light leads to a faster elimination (time constant of nearly 30 minutes) at the early stage as shown in Figure 3-19 (d), while the elimination ratio is slower without UV light as shown in Figure 3-19 (c), even though the final states reach the same order of magnitude of about 10% after 3 hours.

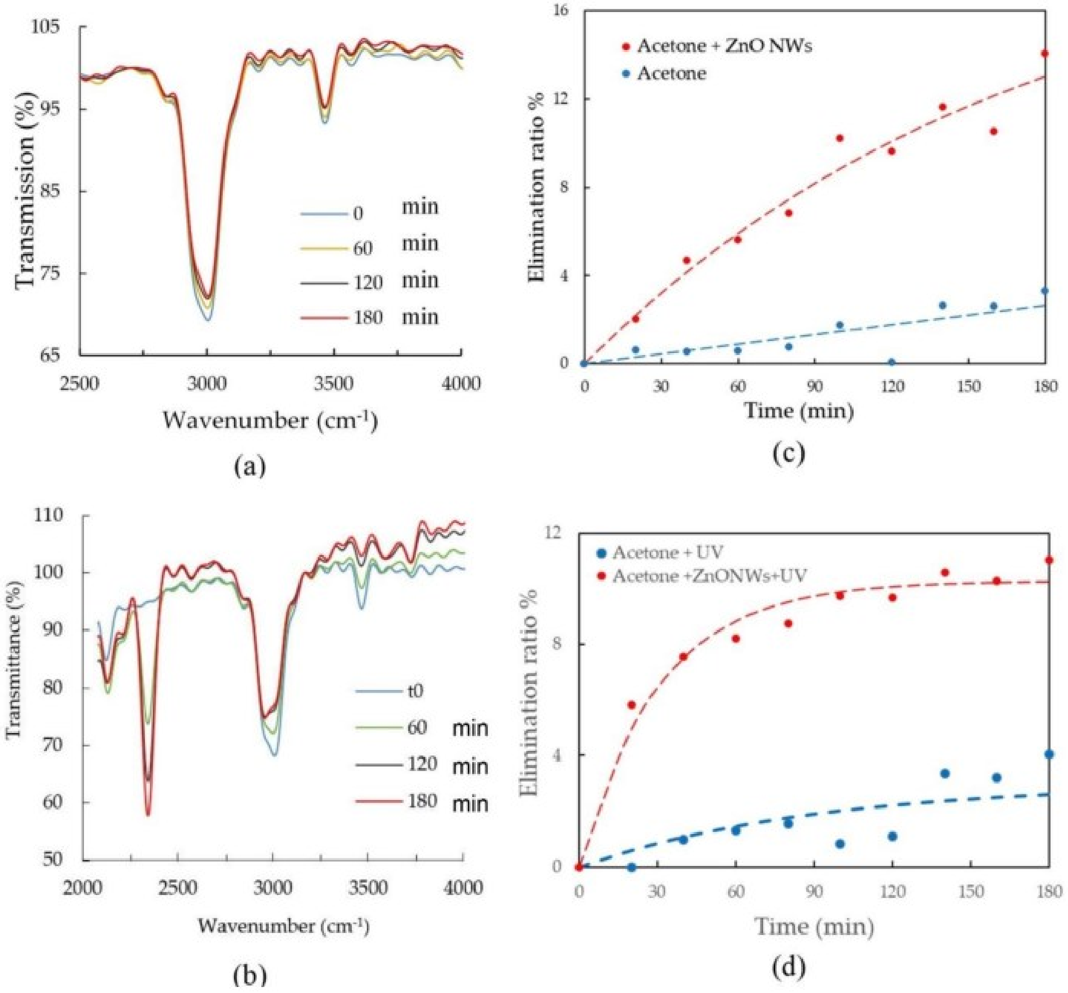

Figure 3-19 (a) & (b) Transmission of acetone measured using MEMS spectrometer at different measurement time (in min.) (a) without and (b) with the presence of UV. (c) & (d) The elimination ratio of acetone versus time in case of absence and presence of ZnO (c) without and (d) with the presence of UV. Dash lines represent exponential fit $(1 - e^{-t/\tau})$ for the measured points, where τ is a time constant.

Monitoring purification of air polluted with Toluene

To extend the study to different VOCs, a similar experiment has been carried out for toluene degradation. First, the toluene concentration variation was monitored using the MEMS spectrometer without applying the UV light. The transmission spectra measured at different acquisition times are shown in Figure 3-20 (a). The elimination ratio is calculated using the absorbance value at 3042 cm^{-1} and shown in Figure 3-20 (c). After three hours of adsorption, the elimination ratio reaches around 63% in the case of ZnO while it reaches 35% in the absence of ZnO. The elimination ratio is enhanced over all the observation time. In Figure 3-20 (b), the transmission curves of toluene in case of applying UV are shown. The elimination ratio of the respective process is also plotted in Figure 3-20 (d). The figure shows an elimination ratio of around 55% in the case of using the ZnO with the UV light compared to 38% without using ZnO with UV.

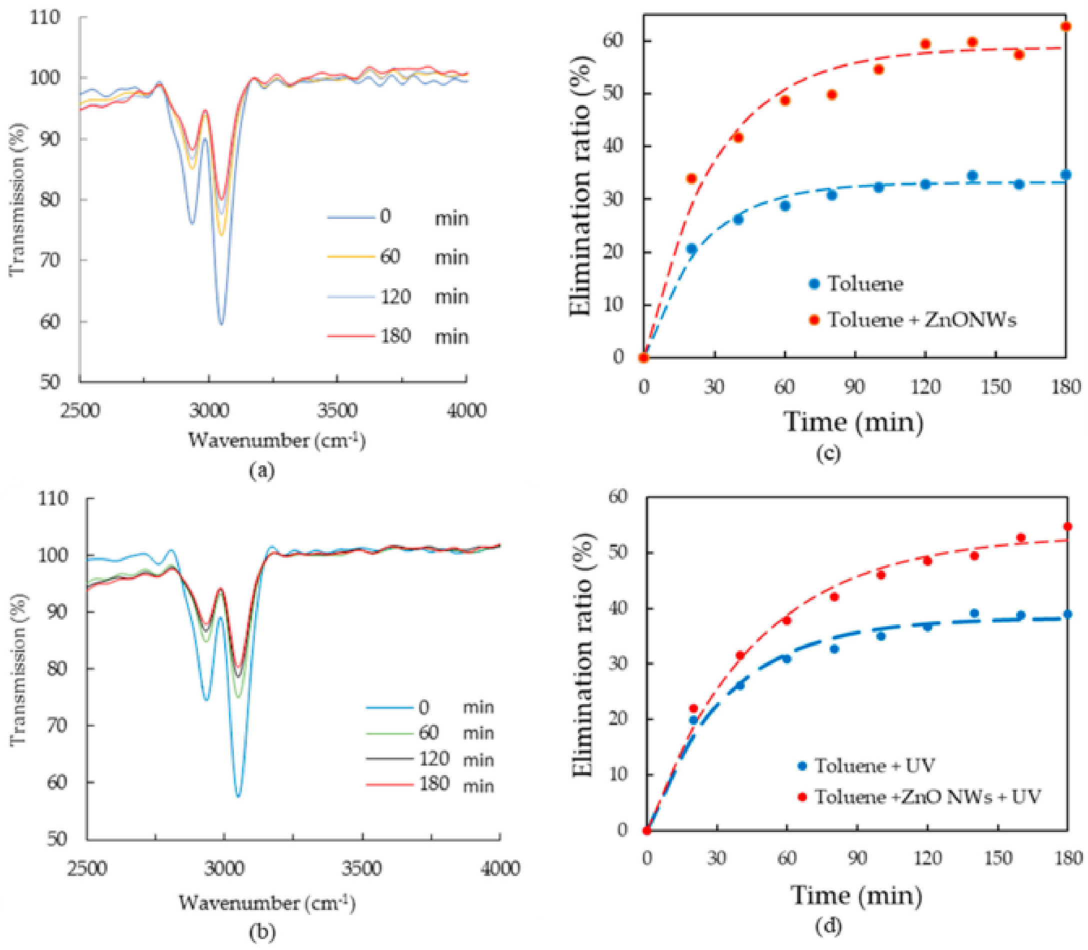

Figure 3-20 (a) & (b) Transmission of toluene measured using the MEMS spectrometer at different measurement time (a) without and (b) with the presence of UV. (c) & (d) The elimination ratio of toluene versus time in case of absence and presence of ZnO (c) without and (d) with the presence of UV. The elimination ratio is calculated using the gas absorbance at 3042 cm^{-1}. Dash lines represent an exponential fit for the measured points.

When comparing the experimental results obtained with the two VOCs considered in this work, namely acetone and toluene, it appears that much higher elimination ratios are attained with Toluene (up to 63%) compared to Acetone (14%) after 3 hours. However, one can also note that ZnO improves the purification up to 1.4 times for toluene. It appears that ZnO plays a crucial role in the efficiency of the acetone removal since almost no elimination (nearly 3%) is observed in the absence of ZnO (Figure 3-19). On the contrary, when considering the removal of toluene (Figure 3-20), the presence of ZnO is not as crucial as for acetone since a significant elimination of toluene (35% up to 38 %) is obtained even without ZnO. However, the presence of ZnO for the removal of the toluene leads to further enhancement of elimination (55% to 63%), in both cases of with and without using UV light. These results suggest that both adsorption and photocatalysis play a role in the degradation of toluene. It is also worth mentioning that elimination of the acetone is also obtained in both cases of using UV light or not, reaching quite similar levels (11% up to 14%), suggesting that in this case, ZnO NWs enhances adsorption only, with almost no effect on photocatalysis. Furthermore, we can clearly see from both Figure 3-20 (c), (d) that saturation occurs at levels much below 100%. This saturation occurs after nearly 90 minutes, corresponding to the diffusion time τ at this scale of the gas cell. This can be ascribed to a saturation of physisorption, which is related to the limited specific surface area and hence to the limited sites for physisorption to occur.

3.5 Conclusion

Three studies were introduced in this chapter. The studies covered pollution and depollution monitoring over different scales. First, an open-path FTIR sensor based on a MEMS-based MIR spectrometer was proposed. The setup was placed inside a climate room. Pollution was introduced inside the room using a car. Onsite measurement of carbon dioxide and water was performed using the MEMS spectrometer which measured the pollution along 38 m inside the chamber. The experiment shows the opportunity of using the MEMS-based spectrometer for long path onsite measurements. The setup surpassed conventional open-path FTIR sensors by its low cost and compactness.

The second study was about measuring one of the most harmful VOCs, which is the toluene, using a 20 m multi-pass cell. This is for localized measurement with a low ppb-detection limit. Toluene was measured at different concentrations. The achieved detection limit was 30 ppb.

The last study was about localized monitoring of VOCs depollution in the presence of ZnO-NWs array(NWA). The amount of pollutant gases was continuously monitored using the MEMS-FTIR spectrometer. Elimination ratio of 63% in 3 hours was achieved for toluene, while it was only 14% for acetone. The presence of ZnO-NWs appeared as crucial in the case of acetone removal since almost no elimination (nearly 3%) was obtained in the absence of ZnO-NWs. On the contrary, ZnO-NWs are not as crucial for the elimination of toluene; however, it significantly enhances the removal ratio. Finally, it also appeared that in both cases of using UV light or not, ZnO NWs produces an enhancement suggesting that both adsorption and photocatalysis are enhanced by ZnO-NWs.

The three studies that were conducted show the applicability of using the MEMS spectrometer in different applications of pollution and depollution monitoring. In the next chapter, we are presenting a mm scale gas cell for a very localized lab measurement. This was achieved using a silicon integrated silicon gas cells instead of using bulky gas cells or open-path measurement as considered in this chapter. This is expected to open even wider perspectives of using the MEMS spectrometer as a multi-parameter spectral gas sensor.

CHAPTER 4: INTREGRATED GAS CELLS

4.1 Introduction

According to Beer-Lambert Law: the absorbance is given by $\mathrm{A} = \log_{10} \mathrm{e}^{-\alpha(\nu)\mathrm{L}}$, where α is the wavelength-dependent absorption coefficient and L is the interaction path length of light within the gas. Thus, increasing L enhances the signal and hence it improves the detection limit. The path length between the source and the spectrometer can be elongated while maintaining good light coupling using large optics like in open FTIR measurements. This is for open air gas sensing over a big area. To perform localized measurements while taking advantage of a long interaction length, there are three main technologies which can be used: (i) cavity enhancement, (ii) multi-pass cell or (iii) hollow waveguide (HWG).

In case of the cavity, the gas is placed between two highly reflective mirrors forming a resonant Fabry Pérot cavity. Upon coupling light to the cavity, light propagates back and forth multiple times according to multiple reflections in the same gas volume before getting transmitted and coupled to the spectrometer. This leads to high interaction path length within a small gas volume, whose effective length is proportional to the finesse of the cavity[206]. Multi-pass cells are well-known in gas sensing for increasing the sensitivity by bouncing light in a long path within a gas volume using high reflectivity mirrors without any optical resonance in this case. The larger path length to cell volume ratio means a smaller gas cell which leads to a compact gas sensor. The more interaction with the light without introducing losses, the better the sensitivity of the gas sensor.

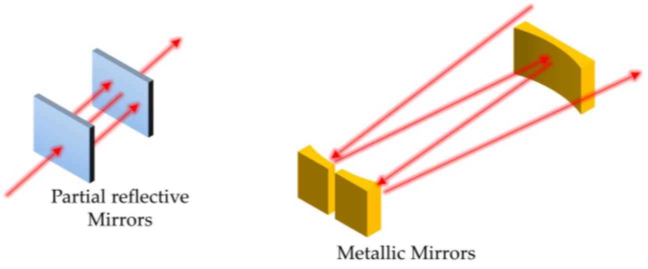

Figure 4-1 3D layouts showing the difference between the cavity for sensing enhancement(on the left) and multi-pass gas cell (on the right).

The main differences between the cavity cell and the multi-pass cell, which are depicted in Figure 4-1, can be summarized as following:

In the case of the cavity gas cell

1) light goes back and forward following the same path many times and hits the same position on the mirrors.
2) Number of round trips is mainly dependent on the reflectivity of the mirrors. The more its reflectivity the more round-trips (the higher the cavity finesse). Note that this enhancement occurs only at the resonant wavelength of the cavity. Instead of metallic mirrors, Bragg mirrors with special coating are usually used to achieve high reflectivity while limiting the spectral range.
3) Mirrors are partially transmitting.

On the other hand, the multi-pass cell is characterized by the following:

1) Light goes back and forward following the different shifted paths and may or not hit the same position on the mirrors.
2) Number of paths is governed by the optical design of mirrors and its orientation. High quality finished metallic mirrors are used. Also, a single layer of special coating can be applied to protect the mirrors and enhance reflectivity. It is characterized by wide spectral range.
3) Finally, mirrors are not transmitting any power.

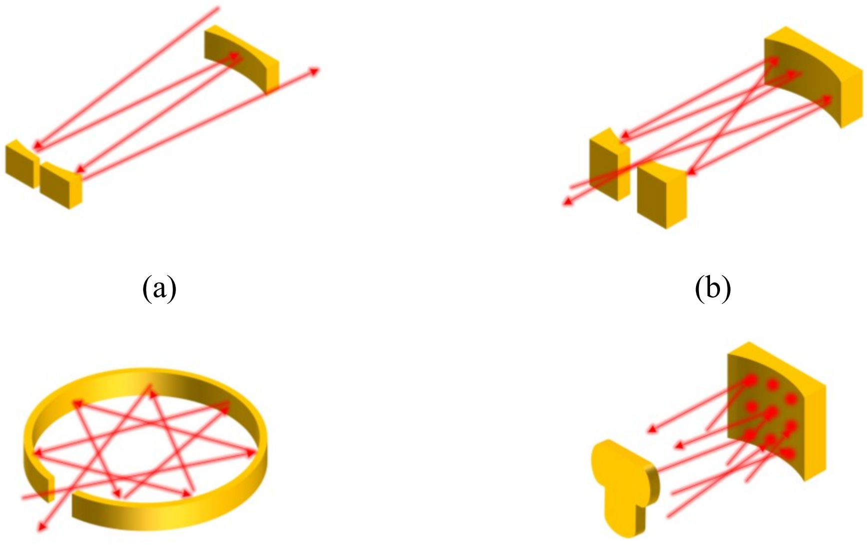

(a) (b)

(c) (d)

Figure 4-2 Multi-pass cell different types (a) White cell, (b) Herriott, (c) Circular, (d) Matrix-based cell.

Multi-pass cells have also different applications [207] such as optical delay line, a non-linear tool for a spectral broadening of laser pulses[208], [209], and are used in magnetometers[210]. In fact, the design of gas cells benefits from rich research background. Gas cells classification include White[211], Herriott [207], astigmatic Herriott [212], multi-pass matrix system [213], circular gas cells [214] and integrating sphere [215]. The different multi-pass cells are depicted in Figure 4-2. Circular multi-pass cells can be implemented using flat concentric mirrors (mirror for each reflection) [216], spherical concentric mirrors (light hits each mirror more than once) [217], a single toroidal mirror (different radius of curvature in sagittal and tangential plane to correct astigmatism aberration) [218], or circular cell of multiple rows in the vertical direction [219].

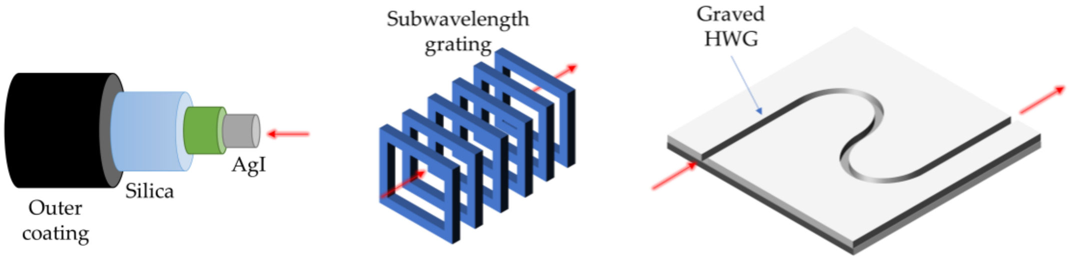

(a) (b) (c)

Figure 4-3 Different types of reported HWGs. (a) Metallic waveguide internally coated with AgI. (b) HWG made of subwavelength grating. (c) HWG graved in the aluminum substrate.

Macro HWG can be a simple hollow metallic guide or metallic waveguide internally coated with dielectric material such as AgI [220]or ZnS [221] for enhanced reflection. This is depicted in Figure 4-3(a). Ppb detection limit of CO_2 was achieved using metallic HWG in conjunction with a benchtop FTIR spectrometer [140]. Ppb range of BTX (Benzene, Toluene, Xylene) and N_2O was also achieved using the HWG in conjunction with a pre-concentrator and the FTIR [222], [223]. Poly HWG using 3D printing was presented in reference [224]. Multi dielectric layer coating on the metal was theoretically studied in reference [225]. Another HWG which is formed from a multilayer of dielectric instead metallic walls are discussed in references [226], [227]. Finally, idea of having HWG made of subwavelength grating is discussed in reference [228] as shown schematically in Figure 4-3(b). A detailed review on HWGs can be found in reference [229].

Regarding the integration on a substrate, metallized V-grooved is proposed in reference [230] . A gold coated HWG on aluminum substrate, like the one shown in Figure 4-3(c), was already measured with a benchtop FTIR spectrometer [231] or with a micro-spectrometer [232].

In our work, a first study was conducted to check in general the feasibility of using the cavity with the MEMS spectrometer. This is different from the case of multi-pass cells where a previous work was already reported on using macro cell to enhance the detection limit down to ppb in conjunction with the MEMS spectrometer, as discussed in chapter 3. Returning to the MEMS technology which represents a promising trend for implementing low cost spectrometer, building the gas cell with the same technology enables whole integration of the whole spectral gas sensor. This leads to a compact gas cells with low volume of gas to be probed. In this chapter, we are introducing a silicon integrated gas cell such as HWG then in the format of a multi-pass cell. They are characterized with the MEMS FTIR spectrometer and then using gas to demonstrate and study gas sensing measurements. Design methodology and models are derived leading to guidelines and important considerations. The chapter is organized as following: feasibility of using the cavity with MEMS spectrometer is discussed in section two. Section three discusses the fabrication process used. In section four and five the fabricated HWG and multi-pass cell are discussed, respectively. Finally, results are summarized in section six.

4.2 Cavity Enhancement Absorption Spectroscopy

Cavity Enhancement Absorption Spectroscopy CEAS technique is based on using a resonant Fabry Perot cavity as a gas cell where light interacts multiple time with a gas placed between the two mirrors of the cavity. Thus, the effective absorption length can be increased dramatically within the same gas volume depending on the cavity finesse. The cavity is characterized by 1) its base path length L, 2) a free spectral range in the wavenumber domain FSR_ν and it is given by $c/(2L)$, 3) The ratio between the FSR_ν and FWHM_ν which is the Finesse F and it is given by $\pi R/(1-R)$, where R is the mirror power reflectivity. In laser spectroscopy, laser source of small linewidth and cavity resonance are tuned at the desired absorption line of gas. The effective path length is $2F/\pi$.

Regarding the FT spectroscopy, wideband source is used in conjunction with the spectrometer with a limited spectral resolution which can be comparable to/ bigger than the cavity FSR. Within the cavity FSR, there is a maximum transmission at resonance and the transmitted power falls drastically out of resonance. Thus, the measured light intensity is attenuated which means lower power signal compared to noise. Thus, the enhancement in the path length may be faded away by the signal attenuation. Thus, there is a need to find the dependence of sensitivity on different system parameters. According to the former discussion, the system has four effecting parameters: the spectrometer resolution $\Delta\nu_s$, gas absorption linewidth $\Delta\nu_g$, the cavity FSR and the cavity FWHM. Depending on the relation between these parameters, one can conclude the expected enhancement in sensitivity.

The foregoing analysis assumes the following: 1) losses in the cavity due to diffraction or mirror absorbance are neglected, 2) negligible wavelength dependence of light source intensity (constant source spectrum $B(\nu) = B_o$), 3) cavity resonance is already aligned at the gas absorbance peak, 4) High Finesse cavity $F = \frac{\pi\sqrt{R}}{1-R} \sim \frac{\pi}{1-R}$ (error$\leq$10% for reflectivity R $\geq$80%) and 5) weak absorption or in other words $\alpha L \ll (1-R)$ and $e^{-\alpha L} \sim 1-\alpha(\nu)L$, where $\alpha(\nu)$ is the gas absorption coefficient and ν is the wavenumber.

The enhancement in the detection limit increases with the transmitted power and percentage of absorbed power $(1-T)$, and noise decreasing. Thus, the enhancement factor E will be defined as the ratio between the products of these parameters in case of using a cavity with the product of the parameters in case of using a direct gas cell with the same base length of the cavity. This is defined as below:

$$E = \frac{\left[\frac{(1-T(\nu))S_B(\nu)}{\sigma}\right]_{CEAS}}{\left[\frac{(1-T(\nu))S_B(\nu)}{\sigma}\right]_{DT}} \tag{4.1}$$

where subscript DT referes to direct transmission, S is the measured spectrum by the spectrometer and σ is the noise standard deviation.

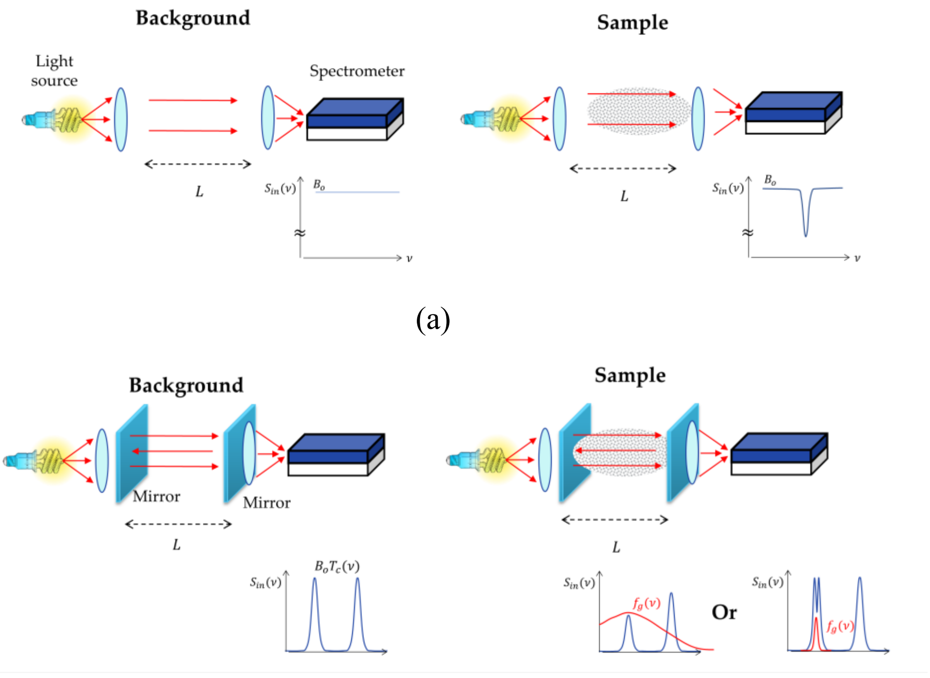

(a)

(b)

Figure 4-4 (a) Direct Transmission (DT) configuration where left is the background measurement and the right is the sample measurement. (b) CEAS configuration. S_{in} is the spectrum of light just before the spectrometer.

In case of direct transmission shown in Figure 4-4(a), the background spectrum measured by the spectrometer S_B is given by:

$$S_B(\nu) = B_o * 2\Delta\nu_s^{-1}\mathrm{sinc}(2\nu\Delta\nu_s^{-1}) = B_o \tag{4.2}$$

where sinc is the spectrometer response function and * holds for convolution. The spectrometer resolution $\Delta\nu_s$ equals to the inverse of half of full travel range of spectrometer. Once placing the gas sample, the corresponding spectrum S_G is given by

$$S_G(\nu) = B_o e^{-\alpha(\nu)L} * 2\Delta\nu_s^{-1}\mathrm{sinc}(2\nu\Delta\nu_s^{-1}) \tag{4.3}$$

where $\alpha(\nu)$ is the gas absorption coefficient, it is equal to $\alpha_o f_G(\nu)$ and $f_G(\nu)$ is normalized to 1. Using $\alpha L \ll 1$, the corresponding transmission is given by

$$T = \frac{S_G(\nu)}{S_B(\nu)} = 1 - \alpha_o L\left[f_g(\nu) * 2\Delta\nu_s^{-1}\mathrm{sinc}(2\nu\Delta\nu_s^{-1})\right] \tag{4.4}$$

The second term represents the percentage of the absorbed power. In CEAS the configuration, as depicted in Figure 4-4(b), the corresponding background spectrum is given by

$$\mathrm{S_B}(\nu) = \mathrm{B_o}\ \mathrm{T_c}(\nu) * 2\Delta\nu_s^{-1}\mathrm{sinc}(2\nu\Delta\nu_s^{-1}) \qquad (4.5)$$

where $\mathrm{T_c}(\nu)$ is the cavity transfer function without the gas. The spectrum of the sample is given by:

$$\mathrm{S_G}(\nu) \sim \mathrm{B_o}[\ \mathrm{T_c}(\nu) - \alpha_o \mathrm{L}\frac{2\mathrm{F}}{\pi}\mathrm{f_g}(\nu)\mathrm{T_c^2}(\nu)] * 2\Delta\nu_s^{-1}\mathrm{sinc}(2\nu\Delta\nu_s^{-1}) \qquad (4.6)$$

One can return to appendix A.1 for further details. Thus, the corresponding transmission is given by:

$$\mathrm{T_G} \sim 1 - \frac{\alpha_o \mathrm{L}\frac{2\mathrm{F}}{\pi}\left[(\ \mathrm{f_g}(\nu)\mathrm{T_c^2}(\nu)\ ) * 2\Delta\nu_s^{-1}\mathrm{sinc}(2\nu\Delta\nu_s^{-1})\right]}{[\mathrm{T_c}(\nu) * 2\Delta\nu_s^{-1}\mathrm{sinc}(2\nu\Delta\nu_s^{-1})]} \qquad (4.7)$$

Substituting equations (4.2), (4.4), (4.5), (4.7) in equation (4.1), one get the following equation:

$$\mathrm{E} = \frac{\frac{2\mathrm{F}}{\pi}\left[(\ \mathrm{f_g}(\nu)\mathrm{T_c^2}(\nu)\ ) * \mathrm{sinc}(2\Delta\nu_s^{-1}\nu)\right]\sigma_{\mathrm{DT}}}{\left[\mathrm{f_g}(\nu) * \mathrm{sinc}(2\Delta\nu_s^{-1}\nu)\right]\sigma_{\mathrm{CEAS}}} \qquad (4.8)$$

Such Enhancement will be solved at $\nu = \nu_o$ which is the wavenumber corresponding to maximum absorption and it is also integer multiple of the FSR. In such case E will be given by:

$$\mathrm{E}(\nu_o) = \frac{\frac{2\mathrm{F}}{\pi}\int_{-\infty}^{\infty}\mathrm{f_g}(\nu)\mathrm{T_c^2}(\nu)\,\mathrm{sinc}(2\Delta\nu_s^{-1}(\nu-\nu_o))d\nu\ \sigma_{\mathrm{DT}}}{\int_{-\infty}^{\infty}\mathrm{f_g}(\nu)\mathrm{T_c^2}(\nu)\,\mathrm{sinc}(2\Delta\nu_s^{-1}(\nu-\nu_o))d\nu\ \ \sigma_{\mathrm{CEAS}}} \qquad (4.9)$$

In the extreme relation between several parameters, one can find the corresponding enhancement factors in Table 4-1 while clarifying plots of the different regions of operation, in the same order, are shown in Figure 4-5. If the system is thermal noise limited which is case of low power detected by the spectrometer detector $\sigma_{\mathrm{DT}} = \sigma_{\mathrm{CEAS}}$. If the system is dominated by shot noise (cooled detectors), the noise standard deviation is directly proportional to the square root of power. The ratio is given by:

$$\frac{\sigma_{\mathrm{DT}}}{\sigma_{\mathrm{CEAS}}} = \sqrt{\frac{\int_{-\infty}^{\infty}\mathrm{S_B}(\nu)d\nu\,|_{\mathrm{DT}}}{\int_{-\infty}^{\infty}\mathrm{S_B}(\nu)d\nu\,|_{\mathrm{CEAS}}}} = \sqrt{\frac{2\mathrm{F}}{\pi}} \qquad (4.10)$$

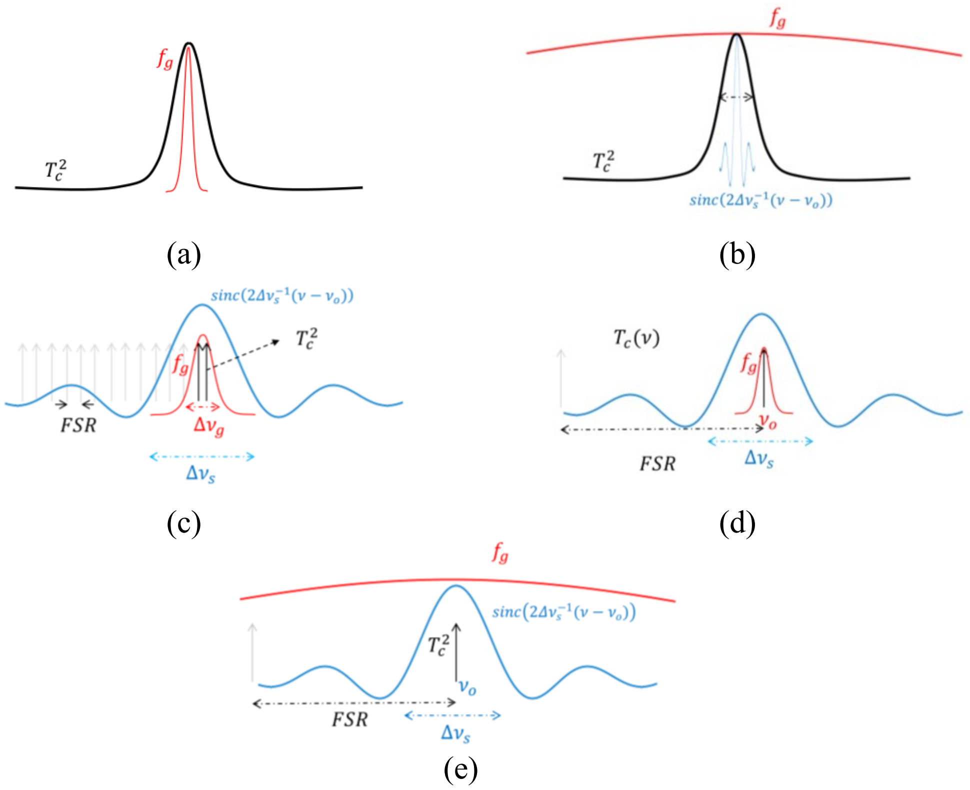

Figure 4-5 Different region of operation of cavity enhancement technique. Faded cavity modes are faded because they are nearly zero due to multiplication by other functions.

The MIR MEMS spectrometer which we are using is limited by the thermal noise. Thus, we are concentrating on this mode. To have a real sense, a simulation was conducted to calculate the enhancement using the following parameters $\Delta\nu_g = 10\ \text{cm}^{-1}$, $\text{FSR}_\nu = 1000\ \text{cm}^{-1}$ in addition to changing the FWHM_ν from $100\ \text{cm}^{-1}$ to $0.01\ \text{cm}^{-1}$ ($R = 0.7$ to 0.99995). The result is depicted in Figure 4-6. The Enhancement increases according to $2F/\pi$ till it saturates at $\frac{\text{FSR}_\nu}{\Delta\nu_s}$ for $\Delta\nu_s = 0.1\ \text{cm}^{-1}$ and saturates to $\frac{\text{FSR}_\nu}{\pi\Delta\nu_g}$ on degrading the resolution to $\Delta\nu_s = 100\ \text{cm}^{-1}$.

Thus, one can conclude the following in case of thermal noise limited system that (1) continue increasing of reflectivity (Finesse) saturate the enhancement to $\frac{\text{FSR}_\nu}{\pi\Delta\nu_g}$, or $\frac{\text{FSR}_\nu}{\Delta\nu_s}$ depending on if $\Delta\nu_g$ is smaller than $\Delta\nu_s$, or $\Delta\nu_s$ is smaller than $\Delta\nu_g$, respectively. (2) Having FSR less than both $\Delta\nu_g$ and $\Delta\nu_s$, no enhancement is achieved with respect to a direct gas cell of the same base length. In case of the system limited by the shot noise, the enhancement continues theoretically to increase with the reflectivity. In reality, the introduced cavity losses will limit the enhancement and one will have an optimum reflectivity for a given loss per round trip where after that the enhancement continue to degrade [233].

Table 4-1 Summarizing the enhancement in detection limits of cavity enhancement techniques

Region No.	Condition	Enhancement	
		Thermal limited	Shot limited
1	$\Delta\nu_g \ll \mathrm{FWHM}_\nu$	$\frac{2F}{\pi}$	$\left(\frac{2F}{\pi}\right)^{1.5}$
2	$\Delta\nu_s \ll \mathrm{FWHM}_\nu \ll \Delta\nu_g$	$\frac{2F}{\pi}$	$\left(\frac{2F}{\pi}\right)^{1.5}$
3	$\mathrm{FSR}_\nu \ll \Delta\nu_g$ & $\Delta\nu_s$	0.5	$\sqrt{\frac{F}{2\pi}}$
4	$\mathrm{FWHM}_\nu \ll \Delta\nu_g \ll \mathrm{FSR}_\nu$ $\Delta\nu_g \ll \Delta\nu_s$	$\frac{\mathrm{FSR}_\nu}{\pi\Delta\nu_g}$	$\frac{\mathrm{FSR}_\nu}{\Delta\nu_g}\sqrt{\frac{2F}{\pi^3}}$
5	$\mathrm{FWHM}_\nu \ll \Delta\nu_s \ll \mathrm{FSR}_\nu$ $\Delta\nu_s \ll \Delta\nu_g$	$\frac{\mathrm{FSR}_\nu}{\Delta\nu_s}$	$\frac{\mathrm{FSR}_\nu}{\Delta\nu_s}\sqrt{\frac{2F}{\pi}}$

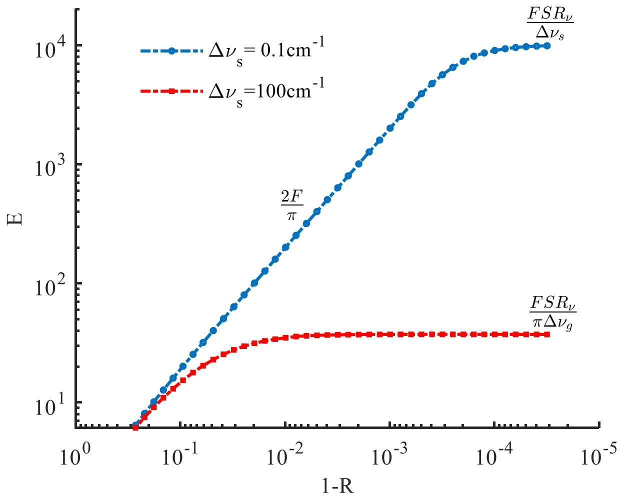

Figure 4-6 Enhancement *E* versus (1-R) in case of thermal noise limited CEAS.

The effective path length L_{eff} which can be gained using CEAS will be the product of base path length L and the enhancement E. In other words, any losses in the CEAS is taken into account in the effective path length.

For the 1st region, where $\Delta\nu_g \ll \mathrm{FWHM}_\nu$, and $\Delta\nu_g$ has a typical value in the vicinity of 0.01 cm^{-1} at atmospheric pressure, FWHM_ν>0.1 cm^{-1}. The effective path length is $\mathrm{L}_{\mathrm{eff}} = \frac{1}{\pi \mathrm{FWHM}_\nu}$ which comply $\mathrm{L}_{\mathrm{eff}} < 3.2$ cm. Such a constraint makes such a region of operation is not important for gas sensing where long path lengths are required to achieve small detection limits as discussed in Chapter 3.

For the 2nd region $\Delta\nu_s \ll \mathrm{FWHM}_\nu \ll \Delta\nu_g$, $\Delta\nu_s$ has to be smaller than 0.001 cm^{-1} which is something unachievable nowadays with the MEMS spectrometer.

For the 4th region, constant $\mathrm{L}_{\mathrm{eff}} = \frac{1}{2\pi\Delta\nu_g}$ ~16 cm which is still not a big path length if one is going to use macro mirrors in conjunction with the MEMS spectrometer. Also, such analysis assumes only one absorption line while in reality gases have many absorption lines which are nearer to each other and are seen by the MEMS spectrometer as a big absorbance band of a FWHM of few cm^{-1}. This predicts that the maximum achievable path length will be smaller than 16 cm.

Finally, in the 5th region, $\mathrm{L}_{\mathrm{eff}} = \frac{1}{2\pi\Delta\nu_s}$ which is equal to (for the MEMS spectrometer of maximum resolution of 30 cm^{-1}) $\mathrm{L}_{\mathrm{eff}} = 53$ µm. Thus, in conclusion using the CEAS with the MIR MEMS spectrometer will not lead to a considerable enhancement in the detection limit.

4.3 Silicon integrated HWGs

4.3.1 Design considerations

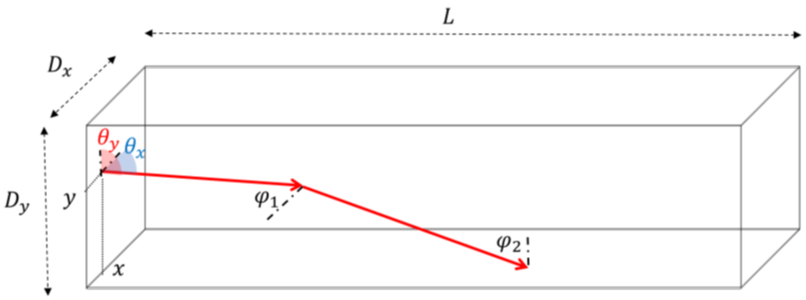

Figure 4-7 3D sketch of the hollow waveguide.

Considering the HWG structure of rectangular cross-section as depicted in Figure 4-7, the power detected from the output of the HWG can be given as following:

$$\mathrm{P_{out}} = \iint \iint I_s\left(x, y, \theta_x, \theta_y\right) \sum_i R(\varphi_i)\, d\theta_x d\theta_y\, dxdy \tag{4.11}$$

where θ_x (resp. θ_x) is the angles between the ray and x- coordinate (resp. θ_y) as depicted in Figure 4-7. I_s is the input/source power distribution, φ_i is the angle of incidence of the i^{th} reflection on the HWG walls and it is a function of the excitation position of the ray (x, y) and the direction cosines of the initial ray (θ_x, θ_y). The number of reflections is dependent on the previous parameters and HWG dimensions shown in Figure 4-7. The longer HWG, the increased number of reflections. HWG of a bigger lateral cross-section area means a decreased number of reflections, also meaning decreased insertion loss. This motivates us to use the deep reactive ion etching DRIE to achieve bigger depths for the HWG. The output power can be calculated easily by tracing the rays inside the structure of HWG using ray tracing software.

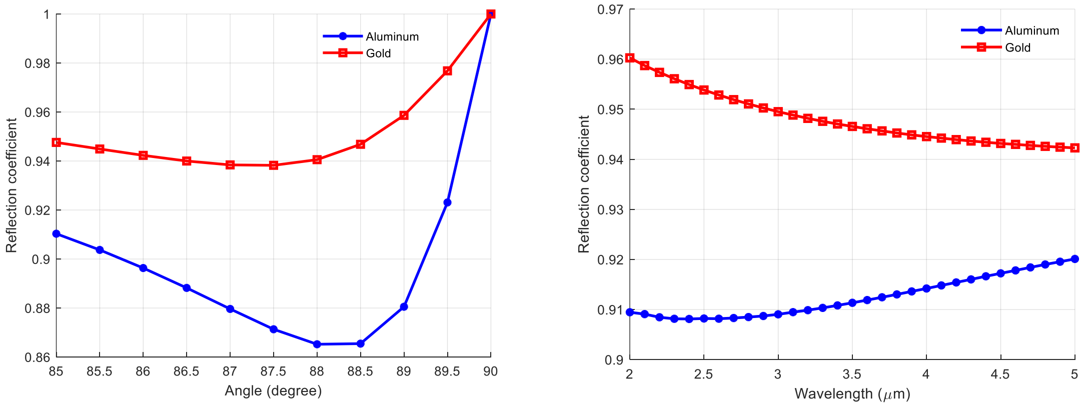

(a) (b)

Figure 4-8 (a) Reflection coefficient versus angle of incidence for a metallized wall considering two different materials. (b) Reflection coefficient versus wavelength of operation for a metallized wall considering two different materials at incidence angle of 85 ̊.

Implementing HWG on a silicon chip is based on etching the HWG in the device layer of the SOI wafer. The HWG will be covered from the top by another wafer. Both wafers are totally covered by metal before being bonded to each other. The choice of the metallization material is dependent on the higher reflection coefficient within the incidence angle of light. Since light is along the optical axis of HWG, light impinges the walls with an incidence angle greater than 85° which corresponds to the maximum acceptance angle of the used MIR spectrometer (which is limited to 5°). Using Fresnel equations, reflection coefficient versus the incidence angle, for gold compared to aluminum, are depicted in Figure 4-8 (a). Reflection coefficient versus wavelength of operation is depicted in Figure 4-8 (b). Since gold has a higher reflectivity, it was chosen for the metallization.

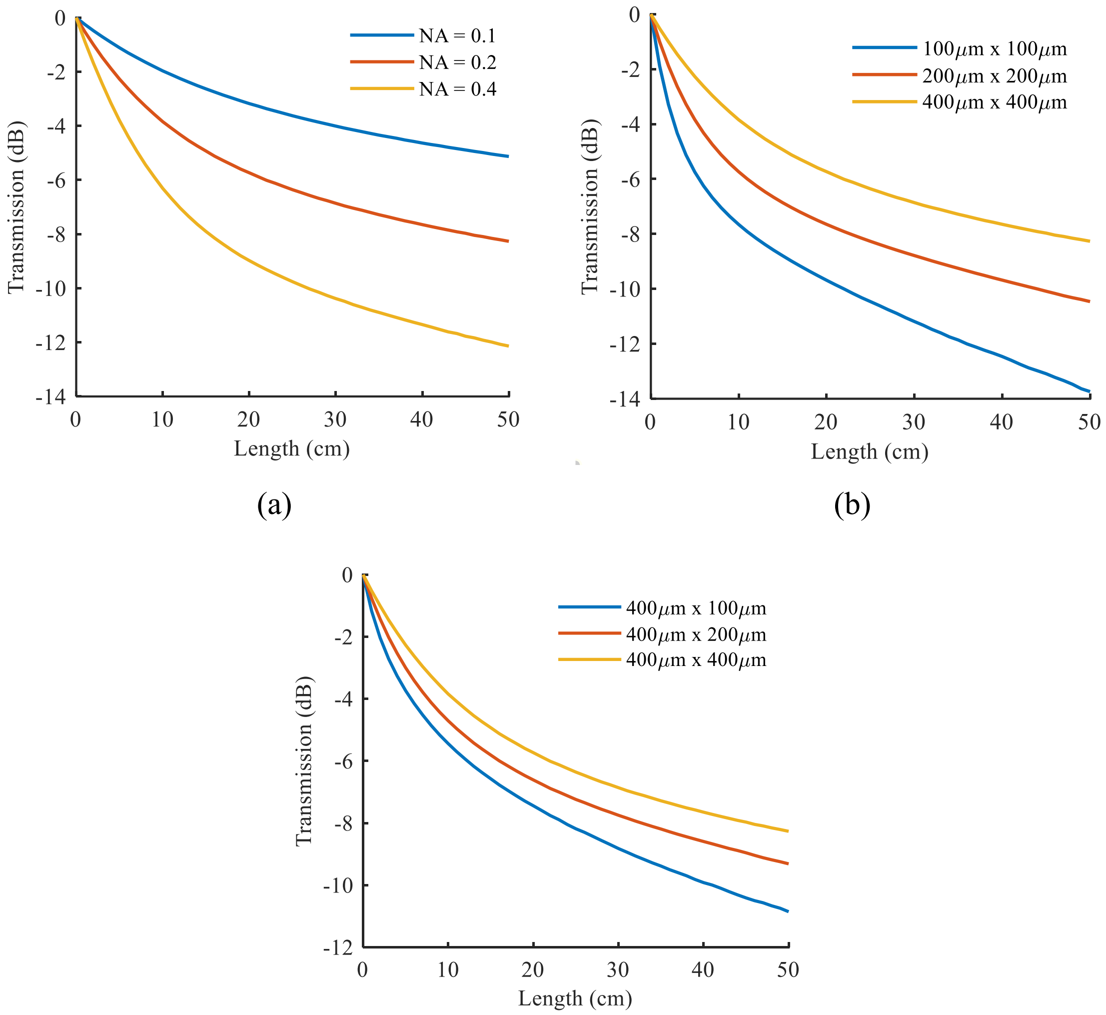

(a)

(b)

(c)

Figure 4-9 HWG insertion loss (a) for a source of different angle of divergence, (b) for different square cross section. (c) for different depths (rectangular cross section).

HWG of different lengths was simulated using the ray tracing software (ZEMAX). Transmission of the HWG versus HWG length L is shown in Figure 4-9 (a) in case of different numerical apertures NA of the source. Increasing the NA of the input increases the losses. Such losses increase with increasing the HWG length (i.e. on increasing the NA from 0.1 to 0.4 radian, losses increase by 4 dB at 10 cm and by 7 dB at 50 cm).

Given the HWG cross section is square, increasing the side length also enhances transmission due to the decreased number of reflections. This is depicted in Figure 4-9 (b) for a source of an NA = 0.2. In case of a rectangular cross section (i.e. HWG depth is different from its width), increasing the depth enhances the insertion loss. The enhancement is not big as the previous case because the number of reflections is only decreased in the vertical direction. Simulation was also conducted for different depths 100, 200 and 400 μm using a source of an NA of 0.2 radian. The results are depicted in Figure 4-9 (c). The insertion loss in these different cases can be modelled with a rational function $\frac{1}{1+ L/a}$, where increasing a leads to slower increase in the losses with increasing the HWG length. The coefficient a is bigger for smaller angle of divergence, bigger cross-section. It is more sensitive to the source divergence compared to other parameters, while increasing the depth has the lowest effect on increasing the losses.

To be able to build the HWG with a long path inside a silicon chip, multiple HWG segments can be used. However, they should be distributed and joined in a manner that fulfill the following: 1) efficient usage of the chip area HWGs to increase the path length and 2) input and output ports of HWG should be at the chip sides. The S-shape pattern of HWG inside the chip can fulfill such conditions. This is depicted in Figure 4-10 (a) showing 3 HWGs of different lengths. The HWG segments are joint together using corner cube mirrors. Three HWGs of different path lengths are integrated on the same chip. The chip size is 2 cm x 2 cm. The base length of the HWG segment is about 1.95 cm. The designs HWG1, HWG2 and HWG3 have a total path length of 9.75 cm, 21.45 cm and 33.15 cm, respectively. The width of the HWG is 400 µm and the depth is 200 µm. Gas through holes for injecting the gas inside the HWG, implemented on the upper wafer, are distributed as shown in Figure 4-10 (b) (white holes). 3D layout of HWG 1 with ray tracing is depicted in Figure 4-10 (c).

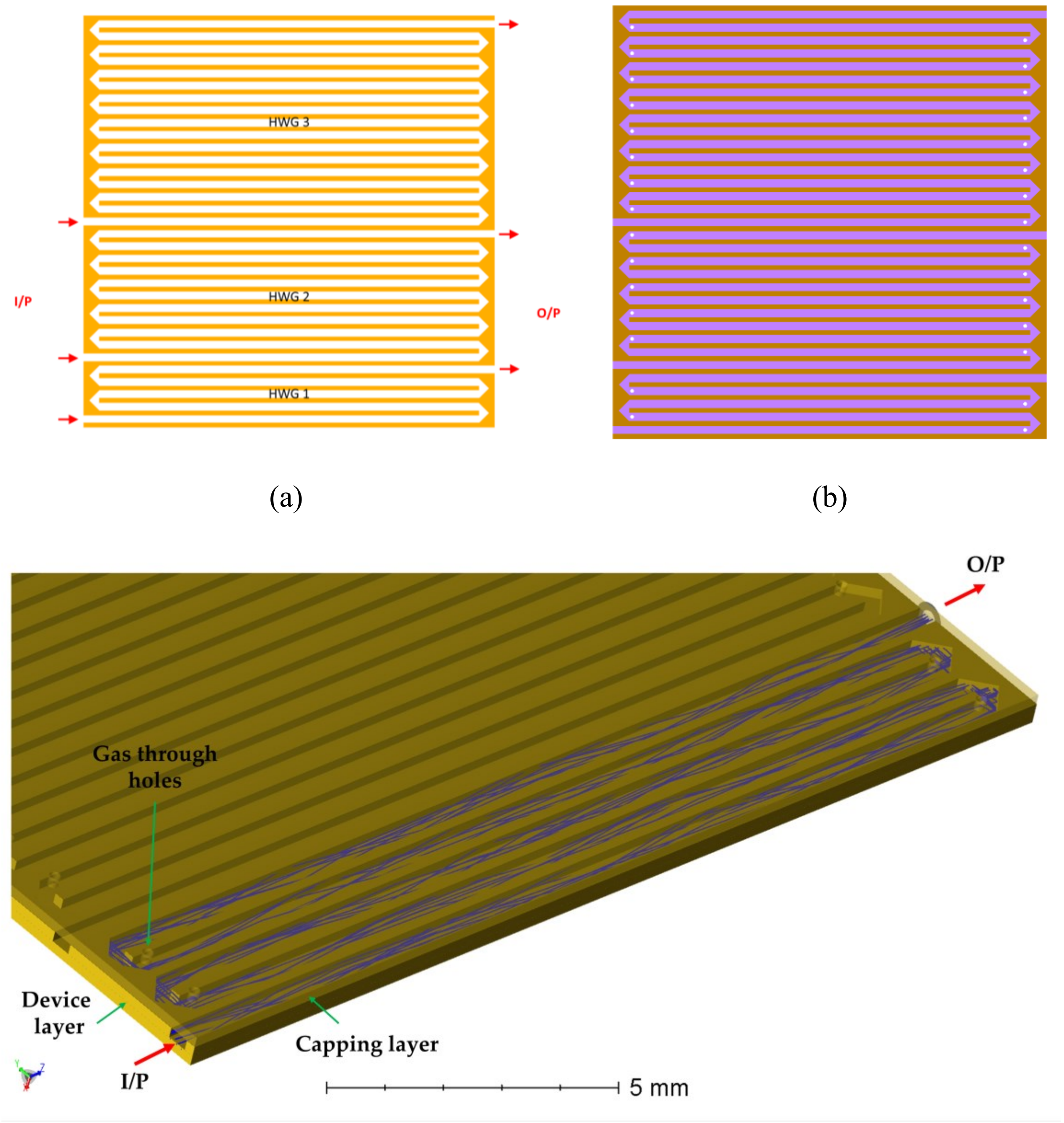

(a) (b)

(c)

Figure 4-10 Layout of the HWG design (a) Device layer. (b) Device layer in light color + capping layer in dark color. (c) 3D layout of HWG1 where the blue lines represent the ray paths from the input to the output.

4.3.2 Fabrication process

The silicon wafer is first thermally oxidized to form a thick SiO2 layer which serves as a hard mask for the deep reactive-ion etching (DRIE) process, as depicted in Figure 4-11(a). The whole-cell design was then transferred to the oxide layer by using a photolithography process followed by a plasma etching of the hard mask, as depicted in Figure 4-11(b-c).

The next step consists of a deep silicon etching using the Bosch process in an etch tool (Alcatel, Annecy, France A601E). The etching process used a time-multiplexed plasma etch including an etch step with SF6 gas s and a passivation step with C4F8 gas. The etching process was carried-out to achieve an etch depth of 200 µm hence shaping the gas cell profile. A smoothing process was then used to reduce the surface roughness of the walls and mirrors that are originated from the DRIE process and, thus, to reduce the reflection losses. This smoothing process was carried out by oxidizing the wafer. A 2 µm-thick oxide was thermally grown and then removed with wet etching in hydrofluoric acid (HF). Another silicon wafer was used as the capping for the structure. A final sputtering step was used to metalize the cap wafer, as well as the whole gas cells' wafer, with a 30 nm-thick TiW layer covered by a 500 nm-thick gold layer. This is shown in as depicted in Figure 4-11(e).

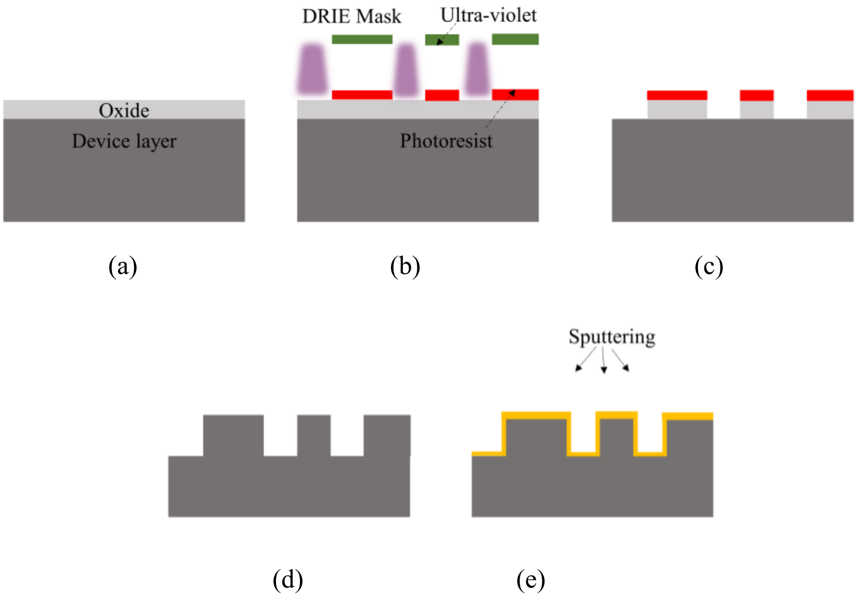

Figure 4-11 Fabrication process of the integrated gas cells

4.3.3 Experimental Results and discussion

For characterizing the HWG and to measure gases, the MEMS based MIR FTIR was used. Zirconium fluoride multimode fiber (Le verre fluoré, ZFG MM, length: 0.5 m, core/cladding: 400/450 µm, NA = 0.2 rad.) was used to couple the output light from a filament based light source (Thorlabs, SLS252) to one side of the HWG. The output light from the other side of the HWG was coupled to the input of a MEMS spectrometer, as depicted in Figure 4-12. The resolution of the spectrometer was adjusted to 80 cm^{-1}.

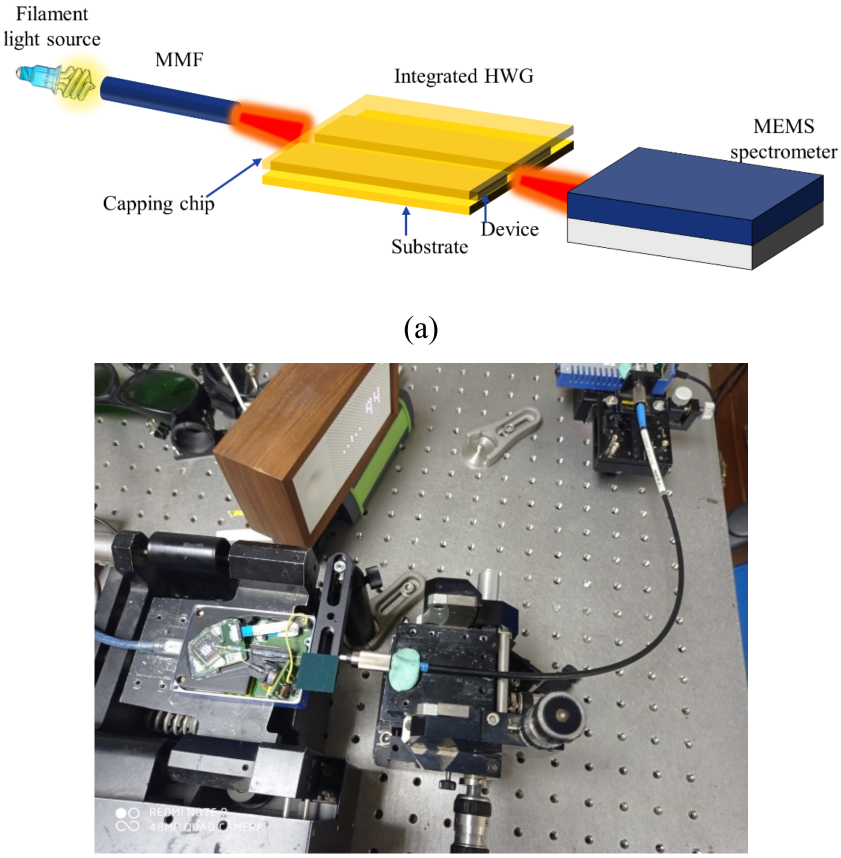

(b)

Figure 4-12 (a) 3D view of the experimental setup used to measure the integrated HWG. (b) Camera photo of the setup.

The measured insertion losses of the waveguides are plotted in Figure 4-13 (a) These are shown in bold lines. These are compared with expected losses from simulations. The background was direct transmission between the input fiber and the MEMS spectrometer. The decrease in the transmission versus wavelength is attributed to the reflection coefficient of the gold which decreases with the wavelength as shown in Figure 4-8 (b). The insertion losses of the shorter hollow waveguide (HWG1) ranges from 10 to 13 dB across the range from 1500 nm to 4500 nm. Such losses increase dramatically to 30 dB for the longest waveguide HWG3. For HWG3, the losses increase for shorter wavelengths which is attributed to the roughness (roughness losses increase with decreasing wavelength of operation). There is a discrepancy of 4 dB between the measurements and the simulations in case of the HWG1 and HWG2, while the difference increases to 15 dB in case of the HWG3.

From the insertion losses measurements, one could extract information about the CO_2 concentration. This peak is around 4.25 µm. First, the wavelength dependence losses of the HWG in the transmission measurement was removed using the baseline correction method (polynomial of 4th order), which was explained in chapter 3. The peaks of the CO_2 measured by the three HWGs are plotted in Figure 4-13 (c). The CO_2 concentration was also directly measured using a chemical-based sensor (Awair). The average concentration was around 700 ppm in the air. Using such a concentration value, the absorption coefficient of CO_2 from HITRAN database, FT spectrometer system model and HWGs path length, the corresponding absorbance of Carbon dioxide of the three HWGs are also plotted in Figure 4-13 (c). The measurements show a good agreement with the chemical-based sensor measurements within a variation which can be attributed to the variation of CO_2 inside the laboratory. The deformation of the signal measured by the HWG3 is attributed to the noisy signal acquired due to the high losses (30 dB). Water absorbance was also monitored and depicted in Figure 4-13 (d) showing the increase of absorbance with increasing the path length. Signal to noise ratio was measured for HWG1. The average time was 1 second. The result is depicted in Figure 4-13 (e). From the measured SNR, we can conclude that the lower limit of detection (1σ) of CO_2 is 130 ppm for an average time of 1 second.

Despite the big losses inside the HWG, it is still compact gas cell which can be integrated easily with the MEMS spectrometer. This is besides of its low sampling volume which makes it fast compared to chemical sensors [232]. This was apparently observed on measuring the carbon dioxide from man-exhaling and butane gas emitted from a lighter.
The butane emitted from a lighter was measured using HWG1. The corresponding absorbance is apparent around 3.4 µm as seen in Figure 4-14 (a). Different measurements were sampled at different time each 3s once a small volume of butane was burst out of the lighter. The measurement was repeated for CO_2 emitted from a man-exhaling who stands near to the chip. The measurements show the gradual increase of CO_2 upon exhaling and the gradual decrease due to diffusion. Such compact sensor opens different daily applications in people life related to comfort and safety indoor.

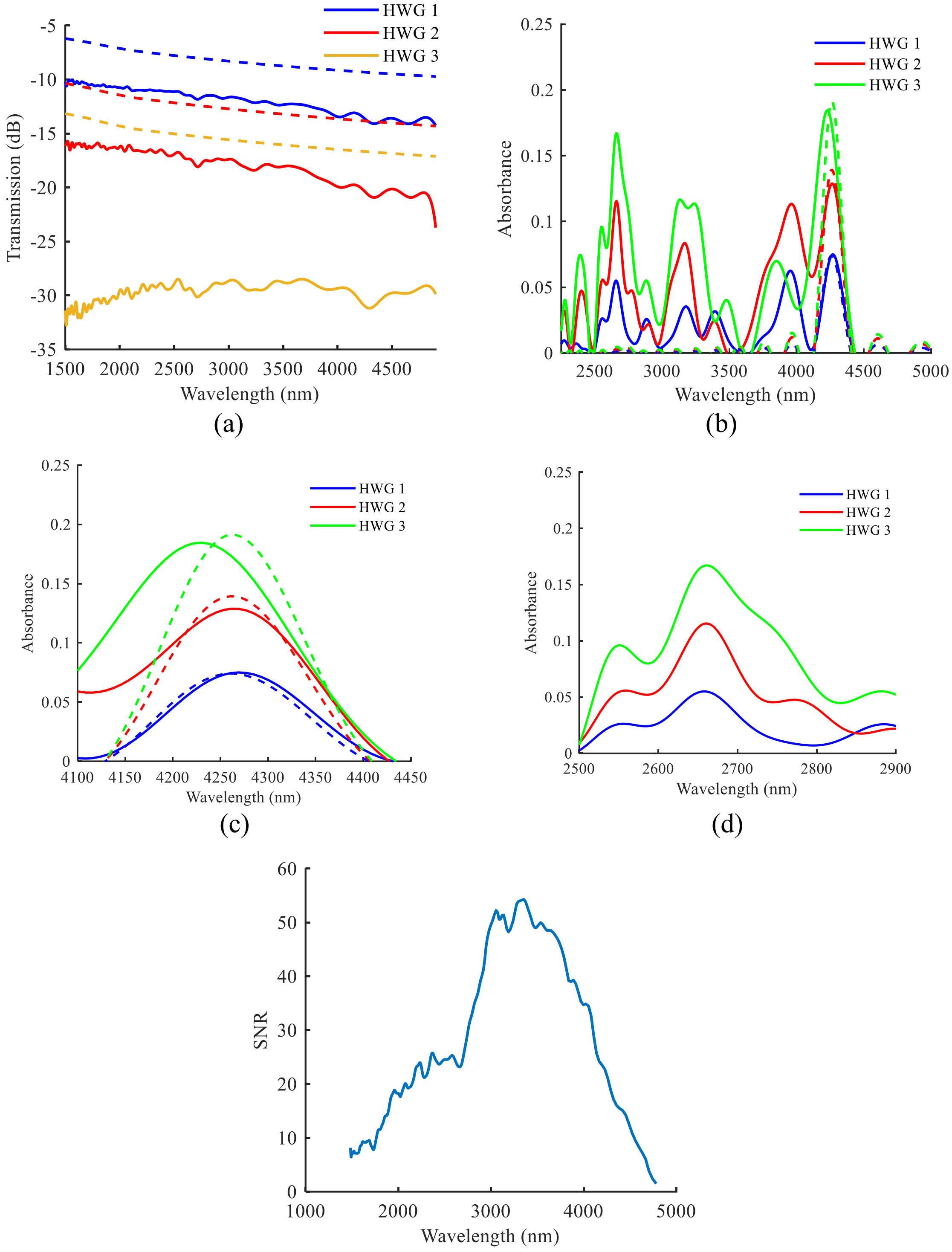

(a) (b) (c) (d) (e)

Figure 4-13 (a) HWG insertion losses. Bold lines are the measured and dash lines are the simulated insertion losses. (b) Measured absorbance of the different HWGs. (c) Measured (zoomed version of (b)) and the corresponding simulated carbon dioxide of the different HWGs. (d) Measured water absorbance (zoomed version of (b)). (e) Measured SNR of HWG1. Average time is 1 s.

Despite the big losses inside the HWG, it is still compact gas cell which can be integrated easily with the MEMS spectrometer. This is besides of its low sampling volume which makes it fast compared to chemical sensors [232]. This was apparently observed on measuring the carbon dioxide from man-exhaling and butane gas emitted from a lighter.

The butane emitted from a lighter was measured using HWG1. The corresponding absorbance is apparent around 3.4 µm as seen in Figure 4-14 (a). Different measurements were sampled at different time each 3s once a small volume of butane was burst out of the lighter. The measurement was repeated for CO_2 emitted from a man-exhaling who stands near to the chip. The measurements show the gradual increase of CO_2 upon exhaling and the gradual decrease due to diffusion. Such compact sensor opens different daily applications in people life related to comfort and safety indoor.

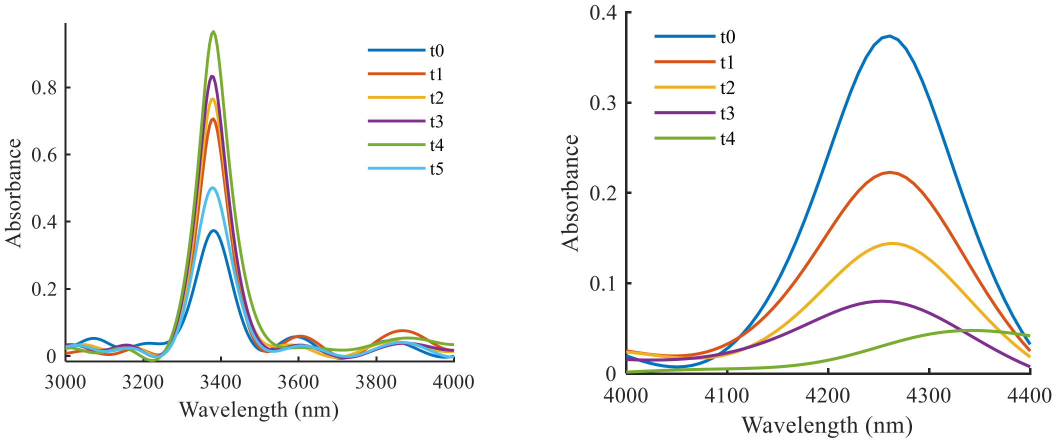

(a) (b)

Figure 4-14 (a) Butane measurement at different time when small volume of butane was burst outside the lighter (b) Exhaling measurement at different time when someone exhales.

4.4 Silicon integrated multi-pass gas cell

When dealing with a gas cell at the chip scale, as considered in our work, we are facing two major difficulties related to miniaturization. First, the lateral dimensions of a chip are limited to a few millimeters, which is a severe limitation to the optical path L, hence reducing the light–gas interaction. One can deal with this first limitation by adopting the concept of multi-pass gas cells. Second, one also has to accommodate other optical considerations related to the miniaturization of the gas cells. For instance, we need to make sure that optical loss is mainly governed by gas absorption, hence the need for careful optical design to minimize the insertion loss. The loss can be significantly affected by the small thickness of silicon wafers, which is limited to no more than a few hundred micrometers. Such small thickness hinders the optical throughput of the cell operating with free-space propagating light as it makes it difficult to collimate an incident light of small spot-size with large throughput into the silicon chip. On the other side, the use of the lithographic process offers the great advantage of high-quality self-alignment of the micro-fabricated optical parts according to a given computer-aided design (CAD) mask design. This can lead to high mechanical stability as well since all components are micromachined in the same substrate. This allows implementing sophisticated designs without the need for post-fabrication alignment.

4.4.1 Design considerations

An example of the conventional circular multi-pass cell is shown in Figure 1a. The light path (red rays) forms a star polygon [23]. The star polygon is characterized by a radius r , the number of vertices p lying on the circle circumstance and density of the star q . Each segment is connected from a vertex to another one spaced q positions. The input tilt angle is given by $\theta = \frac{\pi}{2}\left(1 - \frac{2q}{p}\right)$. In our work, cylindrical mirrors can be placed at the positions of the vertices as shown in Figure 1b. These mirrors can improve cell insertion loss and coupling efficiency by tuning its radius of curvature and even by using an acylindrical profile. This can be also used to reduce the aberrations due to multiple reflections inside the cell. In both designs, the circular multi-pass cell suffers from complexity in light coupling because the input and output are on the same side with an angle of 2θ. To mitigate such a limitation, the last mirror impinged by rays in Figure 4-15 (b) can be omitted, as shown in Figure 4-15 (c). This will reduce the total path length by ratio of $p/(p-1)$, which can be neglected for large values of p. Light-guiding/focusing in the plane parallel to the substrate is achieved using cylindrical mirrors (inside the cell), as depicted in Figure 4-15 (d). In the proposed configuration and the plane perpendicular to the substrate, light is guided using the metalized substrate and a metalized capping wafer, as depicted in Figure 4-15 (e).

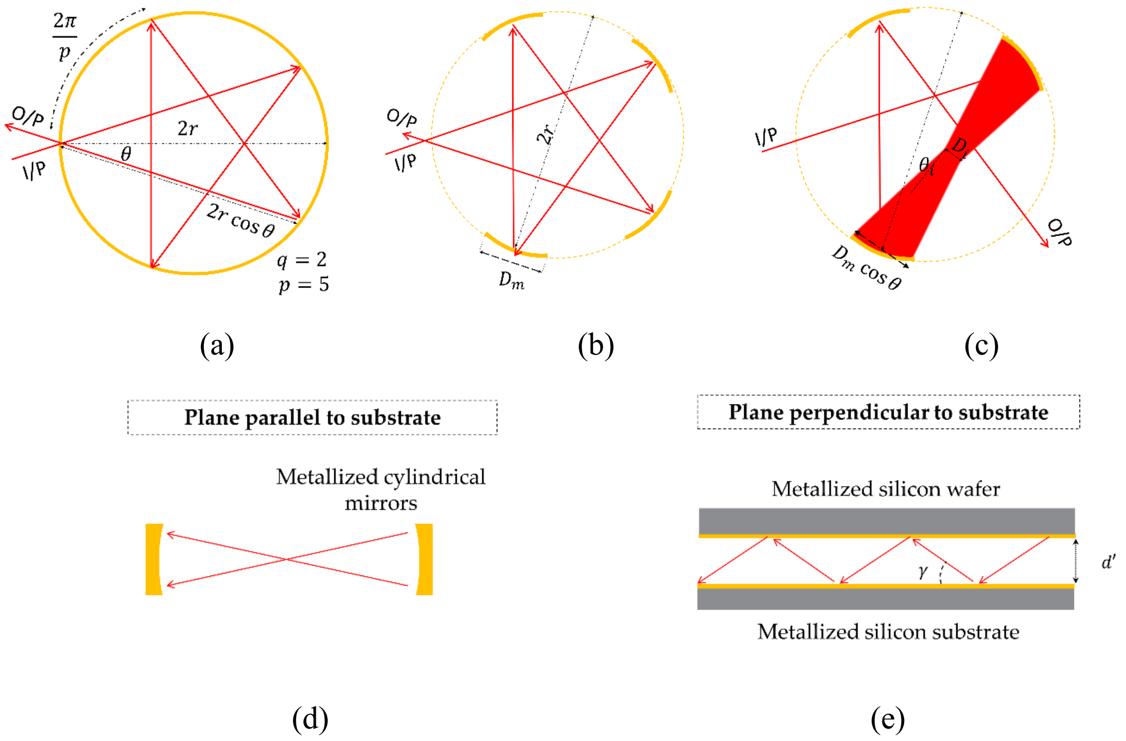

(a) (b) (c)

(d) (e)

Figure 4-15. Schematic top views of circular multi-pass gas cells of radius R . (a) Conventional. (b) Using cylindrical mirrors instead of a one-piece circular mirror. (c) Modified with cylindrical mirrors, where the last mirror of the light path is omitted. Red rays represent the central light path. The extended beam is only drawn here to avoid figure complexity. (d) Configurations for light guiding in integrated gas cells. The drawing illustrates guiding light in the plane parallel to the substrate where cylindrical mirrors are used. (e) The drawing shows a side view illustrating an alternative method for guiding light in the plane perpendicular to the substrate using the horizontal metalized silicon substrate and the metalized capping (silicon wafer). d denotes the cell height and γ is the angle between the ray and the substrate.

In the next part, we are going to evaluate the cell throughput leading us to deduce the absorbed power by the gas as a function of cell parameters. Such equation will be optimized to find the optimum cell parameters given technology constraints. From optical point-of-view, the system throughput is limited by the input/output aperture size and numerical aperture NA. Thus, to avoid additional losses inside the gas cell, the latter should be designed to maintain the throughput without truncation. First, we take into effect the losses in the in-plane where the throughput in such plane is defined as:

$$\mathrm{TP} = \mathrm{d}\,\gamma_{\mathrm{d}} = \mathrm{D_i}\theta_{\mathrm{i}} \tag{4.12}$$

where d is the width of the optical aperture, D_i is the image width, γ_d is the device numerical aperture and θ_i is the image divergence angle. The design idea depends on using a cylindrical mirror, which performs 1:1 imaging as depicted in Figure 4-15 (c). The source image is halfway between the two opposite mirrors. Thus, cylindrical mirrors focal length f_m is one quarter the length between two successive mirrors, which is equal to $2r \cos\theta$. As depicted in Figure 4-15 (c), the divergence angle of the image is given by:

$$\theta_i = \frac{D_m \cos\theta - D_i}{2r\cos\theta} \tag{4.13}$$

where $D_i < D_m$. In view of Equation (4.12) and (4.13), one can find $D_i = 0.5(D_m \cos\theta - \sqrt{(D_m \cos\theta)^2 - 8\, d\gamma_d\, r\cos\theta}\,)$. This implies that the sum of the terms under the square root to be positive. Knowing that $D_m = \frac{2\pi r}{p}$, then one could get the following condition:

$$p^{-2} \sin\pi\frac{q}{p} \geq \frac{2}{\pi^2}\frac{d}{r}\gamma_d \tag{4.14}$$

The absorbed power by the gas is given by $A_P = P_{out}(1 - e^{-\alpha L_T})$, where P_{out} is the output power from the cell, α is the gas absorption coefficient, and L_T is the total cell path length and it is equal to $(p-1)2r\cos\theta$. For a cell with invariant throughput, $P_{out} = R^p P_{in}$ where R is the mirror reflectivity (p-2) mirrors inside the cell and 2 mirrors for input and output coupling). It can be shown that it is a function of the star polygon parameters p and q. For small gas concentrations ($\alpha L_T \ll 1$), the absorbed power is given by:

$$A_P(p, q) \propto (p-1)\sin\frac{\pi q}{p} R^p \tag{4.15}$$

Best performance is achieved when A_P is maximum. However, one should take into consideration the following characteristics of the star polygon:

- q and p are integers.
- q/p is relatively prime (co-prime).
- $q < 0.5p$
- $q > 1$

Thus, maximizing Equation (4.15) given the above conditions in addition to Equation (4.14), one could find the optimum values of p and q that specify the corresponding L_T and θ. It is also apparent that these values are dependent on the ratio between $TP = d\,\gamma_d$ and r. The optimum values of q and p and the corresponding L_T/r is given in Table 4-2 for different reflectivity R and $\gamma_d\, d/r$. The longer path length can be achieved for the highest reflectivity and the smaller source throughput to the cell radius. Thus, given a detection system of throughput TP, cell volume (consequently radius *r*) and technological mirror reflectivity, one can use the table to find the parameters of the optimum design.

Table 4-2. Optimum values of $(q\ ,p\ ,L_T/R)$ for different mirror reflectivity and TP/R.

$\gamma_d \frac{d}{r}$ (rad.) R	0.01	0.03	0.05	0.07	0.09
0.91	(5, 11, 19.8)	(5, 11, 19.8)	(4, 9, 15.8)	(3, 7, 11.7)	(3, 7, 11.7)
0.93	(6, 13, 23.8)	(5, 11, 19.8)	(4, 9, 15.8)	(3, 8, 12.9)	(3, 7, 11.7)
0.95	(9, 19, 35.9)	(5, 12, 21.3)	(4, 9, 15.8)	(3, 8, 12.9)	(3, 7, 11.7)
0.97	(10, 21, 39.9)	(5, 12, 21.3)	(4, 9, 15.8)	(3, 8, 12.9)	(3, 7, 11.7)
0.99	(10, 21, 39.9)	(5, 12, 21.3)	(4, 9, 15.8)	(3, 8, 12.9)	(3, 7, 11.7)

The analysis assumes that the reflection losses due to the substrate and capping are negligible. This is the case when the gas cell has a large height, where the light can be easily collimated in the out-of-plane direction or the case of the light with small divergence angle. In the case of the MEMS chip, the height is limited to hundreds of µm and the light divergence angle is not negligible. In such a case, one should take into account the reflectivity losses in the out-of-plane. For simplicity, one can assume that the two directions are independent. The number of reflections in the out-of-plane (the structure acts as a parallel plate multimode waveguide in such a plane) is dependent on the ray angle. It is given by $\mathrm{L_T}/(\mathrm{d}'/\tan\gamma)$, γ is the ray angle with respect to longitudinal direction and $(\mathrm{d}'/\tan\gamma)$ is the longitudinal distance between two successive reflections, as defined in Figure 4-15(e). Thus, the output power should be modified to be:

$$\mathrm{P_{out}} \propto \mathrm{R}(\theta)^{\mathrm{p}} \int_0^{\frac{\pi}{2}} \mathrm{I}(\gamma)\ \mathrm{R}(90-\gamma)^{\frac{\mathrm{L_T}\tan\gamma}{\mathrm{d}'}} \mathrm{d}\gamma \tag{4.16}$$

where $\mathrm{I}(\gamma)$ is the radiation intensity of the input light, $\mathrm{R}(90-\gamma)$ represents the reflection coefficient in out-of-plane with an incidence angle of $(90-\gamma)$ and $\mathrm{R}(\theta)$ represents the reflection coefficient on the cylindrical mirrors with an incidence angle of θ. Then, the percentage of the absorbed power is given by:

$$A_P(p,q) \propto (p-1)\sin\frac{\pi q}{p} R(\theta)^p \int_0^{\frac{\pi}{2}} I(\gamma)\ R(90 - \gamma)^{2(p-1)\sin\frac{\pi q}{p}\tan\gamma\left(\frac{d'}{r}\right)^{-1}} d\gamma \tag{4.17}$$

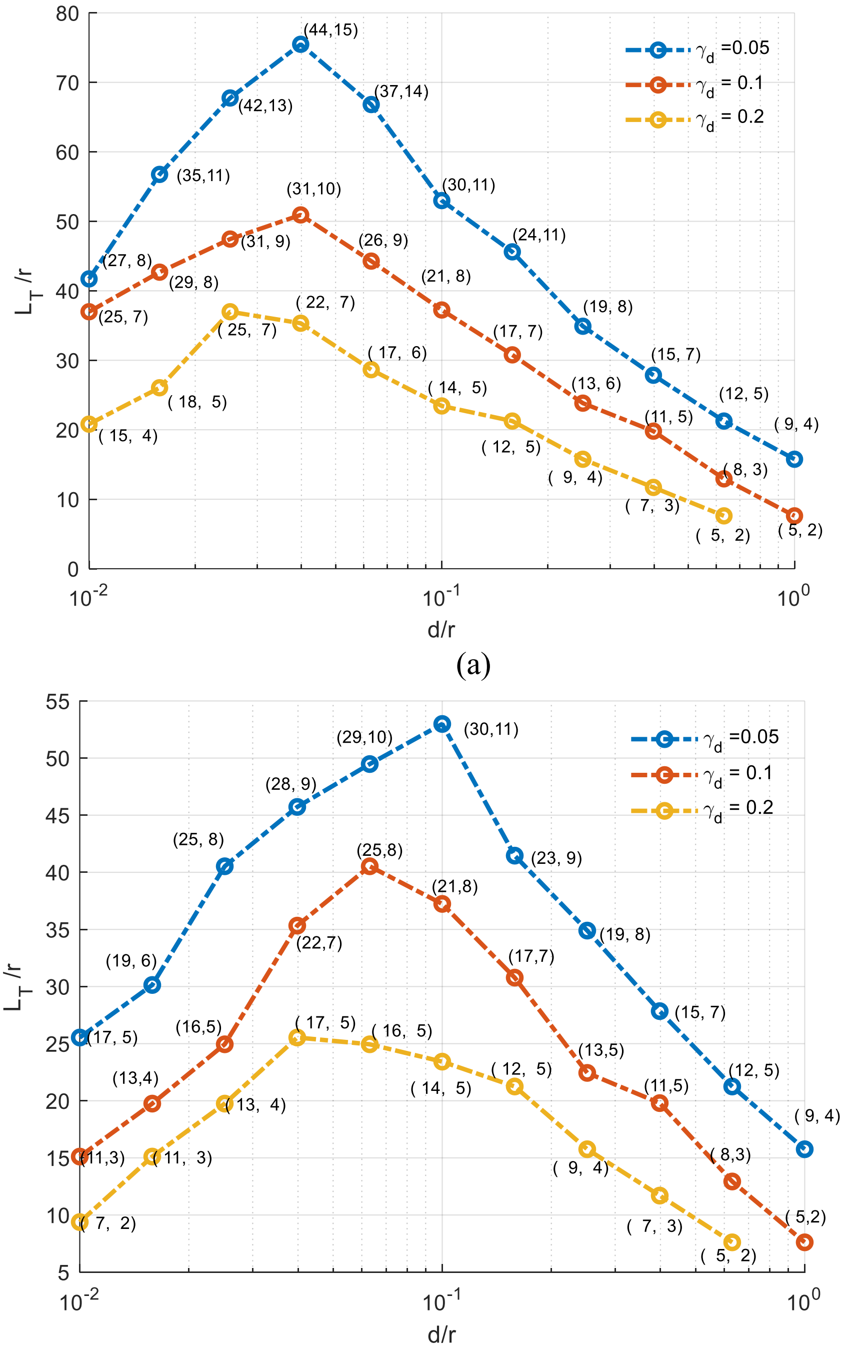

(a)

(b)

Figure 4-16 Total path length with respect to cell radius L_T/r versus cell height/depth with respect to cell radius d/r for different divergence angle γ_d in case of (a) gold metallization. (b) aluminum metallization. Text at every point represents (p, q).

On maximizing the above equation, it is found that the optimum p and q are dependent on the ratio $\mathrm{d'/r}$, out-of-plane divergence angle γ_d and metallization reflectivity R. For gold metallization and a square input aperture ($\mathrm{d = d'}$), $\mathrm{L_T/r}$ is plotted versus $\mathrm{d/r}$ in Figure 4-16 (a) for different divergence angle at a wavelength of operation of 2 µm. Another set of design curves are plotted for aluminum metallization in Figure 4-16 (b). The intensity distribution is assumed Gaussian distribution of FWHM of γ_d. There is an optimum cell height (or depth) with respect to its radius, which corresponds to a maximum total path length with respect to the cell radius. Such a length is longer for a smaller divergence angle. Using gold metallization, longer path length can be achieved by about 30 % over what can be achieved using the aluminum metallization at a wavelength of 2 µm. Knowing the cell sizes (d and r) and metallization material, the corresponding $\mathrm{p, q, \theta}$ and total path length $\mathrm{L_T}$ can be deduced for a given design.

4.4.2 Fabricated gas cell

A 3D layout of the proposed gas cell is depicted in Figure 4-17 (a). The input and output light directions are perpendicular to each other for easy light coupling. A cylindrical input mirror is used to couple light from the source to the cell. The mirror images the light from a width of d to a width D_i. The opposite is carried-out in the output by another cylindrical mirror. The cell itself comprises cylindrical mirrors which are concentric. The mirrors are self-aligned, where they are micromachined in the same silicon block which is attached to a substrate. The substrate contains the gas through holes as well as optical the input/output. The capping is metalized with another silicon wafer. Gas through holes in the substrate for gas injection into the cell.

Optimized gas cell with gold metallization was targeted for fabrication and further characterization. The corresponding target depth d is around 190 µm, while the cell radius r is in the vicinity of 3 mm. The corresponding $\mathrm{d/r}$ ratio is around 0.06, close to maximum sensitivity according to the optimal ratio for $\mathrm{L_T/r}$ as shown in Figure 4-16(a). According to the above-mentioned analysis, the specifications of the fabricated cell are calculated and can be found in Table *4-3*. The radius of curvature of mirrors was optimized using ray tracing simulator ZEMAX. The ray tracing for the cell is shown in Figure 4-17 (b)

Table 4-3. Simulated dimensions of the cell. All dimensions are in mm. r is the mirror radius of curvature, and D is the mirror diameter.

Parameter	Value
Metallization material	gold
Cell radius	3
Cell (p, q)	22, 9
Depth	0.19
Input mirror (r_{in} , D_{in},)	8.8, 1.2
Output mirror (r_{out}, D_{out},)	6.7, 1.4
Cell mirrors (r_m,D_m]	5.3, 0.9
Cell area	7 x 8

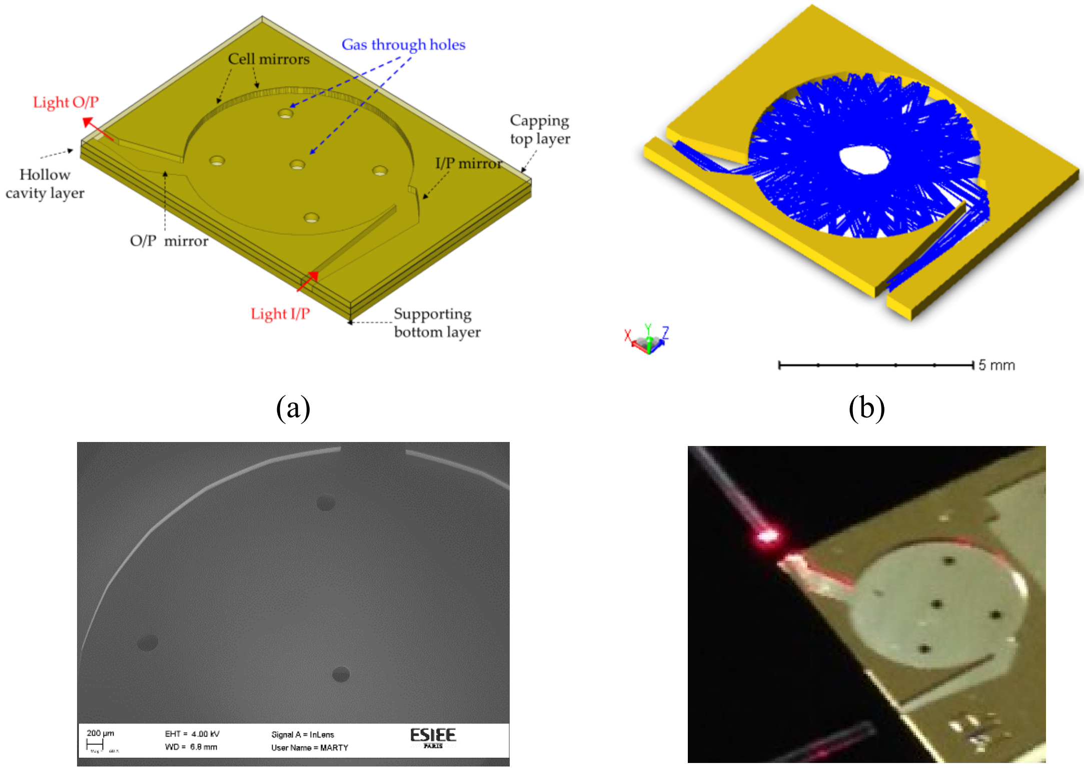

(a) (b)

(c) (d)

Figure 4-17 (a) 3D layout of silicon integrated gas cell. The device layer contains the gas cell. The substrate contains the gas through holes. Capping layer for covering the cell. (b) Ray tracing for the integrated multi-pass using ZEMAX. (c) close view Scanning Electron Microscope image, (d) photo of the fabricated device with optical fiber light coupling in and out.

A SEM image of the gas cell can be found in Figure 4-17 (c). The cell was illuminated with a red laser from a fiber as depicted in Figure 4-17 (d). Shiny spots at some mirrors are observed. These are the mirrors that are expected to be hit by a laser once entering the gas cell while the other mirrors are not shiny due to light diffraction from the upper side due to the absence of the capping.

4.4.3 Experimental measurements and discussion

To perform gas sensing measurements, an optical setup was used, as depicted in Figure 4-18 . The gas cell was placed inside a macro gas chamber (Specac, Orpington, England Storm 10). The macro gas cell was used to control gas pressure and concentration. Light from a filament-based light source was coupled to the cell input using a lens. The output from the cell is coupled using another lens to a multimode fiber MMF (Thorlabs, New Jersey, USA core/cladding $400/440\ \mu\text{m}, \text{NA} = 0.39$) . The MMF was connected to the optical MEMS spectrometer (Si-ware, Cairo, Egypt Neospectra). The resolution of the spectrometer was down to 33 cm^{-1} and its wavelength range extended from 1.2 μm to 2.5 μm.

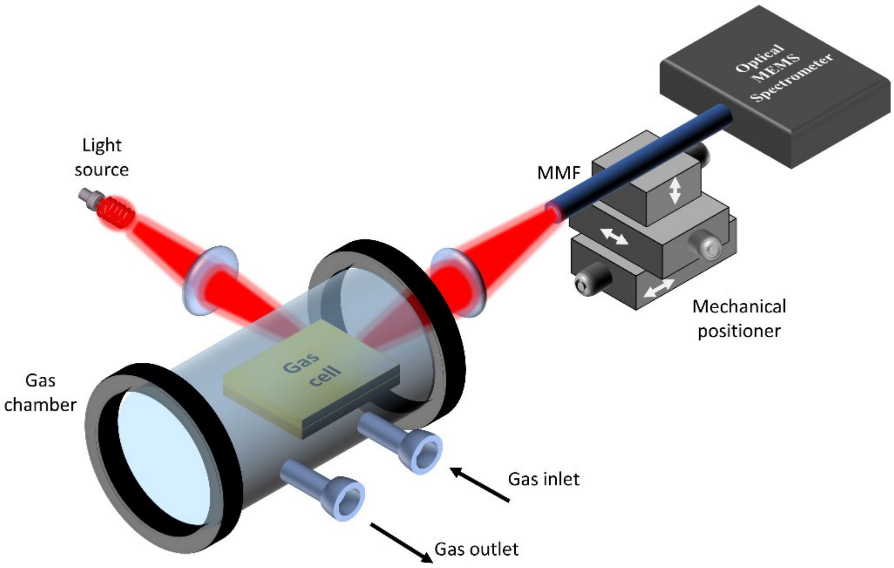

Figure 4-18 Schematic 3D view of the optical setup used for conducting gas sensing measurements using the silicon integrated multi-pass cell. SEM and camera photo insets of the multi-pass cell without the capping are shown.

Carbon dioxide CO_2 gas is injected into the chamber inlet from a gas cylinder. The pressure was adjusted using a pressure valve and monitored using an analog pressure gauge. Different pressures were measured which corresponds to different absorbance values (0.9 bar to 1.6 bar). The corresponding absorbance curves are plotted in Figure 4-19 (a). The absorbance values at 2.01 μm versus the pressure applied are scattered in Figure 4-19 (b) in addition to a linear fit with a root mean square error of 10^{-3}. An effective path length was found to be 9 cm compared to the theoretical path length of 12 cm. The corresponding lower limit of detection is 30 mbar. The cell volume is too small. It is about 6 μL. This means a small sampling volume of gases. The path length to the volume ratio PVR is an important Merit factor for the gas cells [234], the more this value the more compact cell will be. The corresponding PVR is about 17,000 m/L. Such value is two orders of magnitudes bigger than that of the conventional gas cells (macro gas cells have PVR values ranging from tens to hundreds, according to the survey conducted in the reference [48], [234]). A comparison with other reported circular gas cells (reviewed in the reference [48]) can be found in Table *4-4*. However, this is at the expense of the sensitivity where the benchtop gas cells have larger throughput and lower losses (a smaller number of reflections).

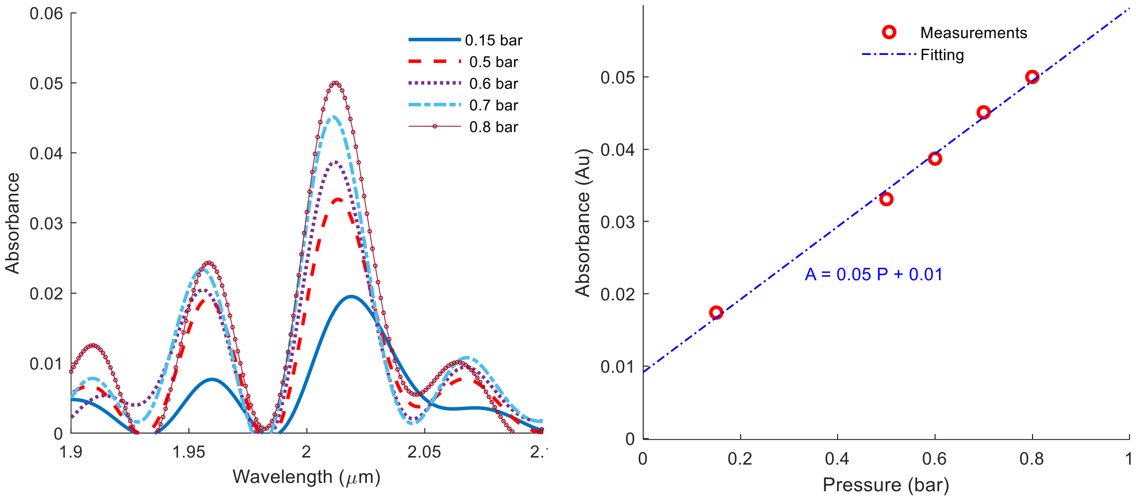

(a) (b)

Figure 4-19 Carbon dioxide measurements (a)Carbon dioxide (CO2) absorbance at different pressure measured using the integrated multi-pass cell. (b) The corresponding absorbance at 2.01 μm versus different pressures. A linear fitting is also plotted.

Table 4-4 Comparison between reported circular multi-pass cells. Last three rows are related to the HWGs

Number of mirrors	L (m)	Volume (L)	PVR (m/L)	References
1	1.05	0.078	13.5	[235]
6	3.1	0.024	129.2	[217]
1	2.16	0.04	54	[218]
1	4.08	0.04	102	[236]
6	0.69	0.013	53.1	[237]
1	12.24	n.a.	n.a.	[238]
1	9.9	0.05	198	[239]
65	10	0.14	71.4	[240]
22	0.09	6×10^{-6}	17 000	Our work
-	0.098	7.8×10^{-6}	12 453	Our work (HWG1)
-	0.215	17.1×10^{-6}	12 453	Our work (HWG2)
-	0.332	26.5×10^{-6}	12 453	Our work (HWG3)

4.5 Conclusion

In a first part of this chapter, theoretical feasibility study was conducted on using cavity enhancement technique with the MEMS spectrometer. It was performed for different operation regimes. The conclusion of this study shows that there is either no enhancement or a small expected enhancement, depending on system parameter values. This means that cavity enhancement has very limited potential for miniaturized spectral gas sensors.

Second, Hollow Waveguides were studied for their potential of sensitivity enhancement of ultra-compact gas cells. After a promising theoretical study, three integrated HWGs were fabricated on a silicon chip using MEMS technology. Three HWGs of lengths range from 10 to 33 cm are implemented within a 2 cm x 2 cm chip. The insertion loss of the cell was ranges from 10 to 30 dB. The HWG was successfully used to measure carbon dioxide from exhaling, with a lower limit of detection of 130 ppm. The HWG was also successfully used to detect butane gas.

Finally, a multi-pass gas cell was implemented on-chip using MEMS technologies. Design methodology and guidelines for optimal design are derived and presented. These results show the optimum dimensions of the gas cell (optimum sensitivity) given technology parameters such as reflectivity and the depth to be achieved besides the spectrometer throughput. The cell in conjunction with a MEMS-based spectrometer was successfully used to measure carbon dioxide under different pressures. Implementing the gas cell on silicon enabled sophisticated designs with no need for further optical alignment, thanks to the lithography-defined geometric features allowing self-alignment capabilities. One can further implement a design incorporating a large number of mirrors of different radii of curvature and acylindrical profiles. In addition to that, the mechanical stability is high as all components are monolithically integrated on the same substrate. However, MEMS technology doesn’t provide a straightforward solution for the out-of-plane focusing [241]. This problem was solved by guiding light using the metalized capping and the metalized substrate acting as a multimode parallel plate waveguide.

The overall conclusion is that both HWG and Multi-pass gas cells appear as promising options towards full integration of ultra-compact gas sensors. While the effective path lengths were limited to nearly 30 cm, for a compromise between insertion loss and gas absorption, the resulting lower limit of detection, although limited at the ppm range today, could be improved in a near future. To this end, either higher quality coatings will enable reducing the insertion loss, at least the part which is due to multiple reflections. Another promising option would come from using light sources of higher power.

Chapter 5: Conclusion and Future Work

5.1 Conclusions

The goal of the thesis was to explore the potential of optical MEMS spectrometers for gas sensing applications, with the ultimate objective of producing a *micro-spectral gas sensor*, that is an ultra-compact device that is capable of sensing multiple gas, based on optical spectroscopy. Different aspects related to this subject were investigated from theoretical and experimental point-of-view, along a proposed methodology, which takes into account the latest technological advances with the best of their advantages and their practical constraints and physical limitations.

First, a critical review has been conducted on gas sensing using direct absorption spectroscopy (DAS) and photoacoustic spectroscopy (PA). Each method was analyzed when using either a tunable laser source or a Fourier transform spectrometer. A theoretical analysis was conducted on these systems to find the ultimate detection limits for each case. To compare the DAS and PAS, a figure of merit was used which was defined as the ratio between the normalized absorption coefficients (normalized with respect to measurement time) of each system. The normalized noise equivalent absorption coefficient (NNEA) was also used to compare the systems when using a tunable laser. In the case of using a tunable laser, the direct absorption spectroscopy was found to be better for lower laser powers and longer gas cells and the converse is also correct. For the FTIR-based systems, a direct absorption spectroscopy system was found to be better than a PA-based system for lower temperatures of the optical source, higher spectrometer throughputs (bench-top spectrometer), faster mirror velocities, and longer gas cells.
Using the cavity enhancement technique implemented with the MEMS spectrometer was proven not to have a considerable enhancement in the gas detection limits.

Then, a new concept of parallel spectrometer was introduced as a candidate for enhancing the gas selectivity of the original MEMS-FTIR spectrometer. Four co-integrated interferometers can enhance the spectral resolution by 4 times, hence contributing to improve gas selectivity. Methane was identified and measured with the parallel spectrometer and compared to the spectral response measured with a single spectrometer. The measurement shows a better resolving of the methane absorption bands.

Looking for a simpler architecture than FTIR, another new concept, the differential spectrometer, was proposed. It is based on critical angle dispersion was presented. Theoretical analysis of the spectrometer was performed in the sense of the principle of operation, spectrometer resolution, and signal to noise ratio. The spectral responses of lasers and reference materials were measured using a prototype of this differential spectrometer as a proof of concept. Unparalleled sides of the waveguide introduce degradation in the resolution that was understood from further analysis supported by detailed theoretical investigations. Signal processing was presented to reduce such effects. A resolution of 50 nm around 1548 nm was achieved after the correction. The structure was shown to have a better resolution than the prism-based spectrometer as wavelength decreases.

We then conducted a series of studies to investigate more in detail the application of MEMS-FTIR for gas sensing and analysis.

We started tackling air pollution sensing using an open-path Fourier transforms spectroscopy in Sense city (huge climate chamber) with large available length for light-gas interaction, up to 38 meters, leading to measurement of the *spatial average pollution*. This was performed using the mid-infrared (MIR) MEMS spectrometer. Pollution stimulated by a car was monitored and compared to the measurements of localized reference analyzers.

Then, *localized* sensing of toluene, chosen as an example for the most common VOCs, was conducted using a benchtop multi-pass cell gas cell of 20 m length coupled to the MIR MEMS-FTIR spectrometer. 30 ppb of Toluene as a lower limit of detection was achieved.

Then, using a setup of direct gas cell of path length of 10 cm, we conducted monitoring of air de-pollution, which was also an opportunity to conduct an investigation on the mechanisms of air purification by photocatalysis. An air purification device based on ZnO nanowires was monitored using the MEMS spectrometer. Elimination ratio of 63% in 3 hours was achieved for toluene, while it was only 14% for acetone. The presence of ZnO-NWs appeared as crucial in the case of acetone removal since almost no elimination (nearly 3%) was obtained in the absence of ZnO-NWs. On the contrary, ZnO-NWs are not as crucial for the elimination of toluene; however, it enhances significantly the removal ratio. Finally, it also appeared that in both cases of using UV light or not, ZnO NWs produces an enhancement suggesting that both adsorption and photocatalysis are enhanced by ZnO-NWs.

Finally, we moved one step forward towards a full miniaturization of spectral gas sensors. Contrary to the above experiments, where gas cells were macroscopic, the technological breakthrough that we aimed tackling was to integrate the gas cell into a silicon chip. We designed and fabricated silicon-based mm-scale gas cells and silicon-based hollow waveguides, whose footprint did not exceed 2 cm x 2 cm, but enabling effective path lengths ranging from 10 to 33 cm. The insertion loss ranges from 10 to 30 dB depending on the length of the HWG. Characterization and gas sensing measurements of HWGs were performed using the MEMS spectrometer. A circular multi-pass cell fabricated on a silicon chip was also presented. It has an effective path length of 9 cm. Design considerations and characterization using the MEMS spectrometer were performed and serves as a tool for further optimization. Different gases were measured such as acetylene, butane, carbon dioxide, and water vapor. The path length to volume ratio is about 17,000 m/L, an unpreceded value among all gas cells reported to date. Such value is indeed two orders of magnitudes bigger than that of the conventional gas cells, although this is at the expense of sensitivity, at least with today’s technological constraints.

5.2 Future Work

Regarding the open-path FTIR applications, longer path length can be achieved for averaging pollution for longer distances, which will enable reaching sub-ppb concentrations, either for indoor or outdoor smart sensing at district scale. This can be achieved using bigger parabolic mirrors so as to minimize insertion loss.

On the contrary, localized measurements will require ultra-compact spectral gas sensors, whose low cost will enable large-scale deployment along an IoT network, where each spectral sensor will be within a node of a dense network. Attaining this ultimate goal necessitates further efforts in integration.

Integration of compact gas cells with the MEMS spectrometer

The gas cell can be further integrated with the MEMS spectrometer on the same chip. These can be also integrated with a light source like a black silicon source, leading to a monolithic micro-spectral gas sensor. Such a source is compatible with the MEMS fabrication process.

Such integration is clarified in Figure 5-1. The black silicon source is placed at the light input port of the gas cell. After light interaction with the gas inside the cell, the output light is coupled to the interferometer. Inside the interferometer, light is modulated using the actuator to get an interferogram versus time at the output. This output signal is coupled directly to the detector.

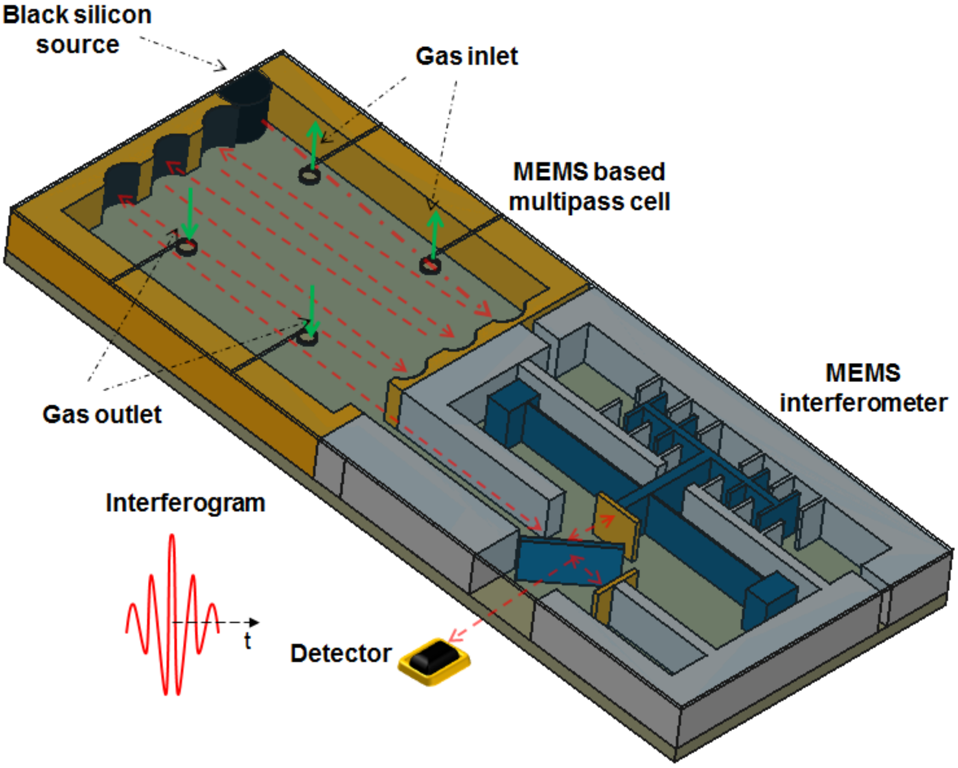

Figure 5-1 Integration of gas cell with the MEMS spectrometer on the same die or obtained by coupling two separate dies.

The integrated gas cells can be also used to monitor the air purification using the ZnO nanowires where the gas cell can be placed beside the chip of the ZnO nanowires. This allows the precise study of reactions/purification process just over the ZnO nanowire due to the localized measurement.

Integration with other sensors

The gas cell in conjunction with the spectrometer can be co-integrated with other sensors such as pressure sensor, air flow sensor, humidity sensor, temperature sensor, …. The sensors can be either made based on implementing electrical transduction or optical transduction of those physical parameters.

The pressure sensor can be made of a vertical membrane. One of the sides of the membrane faces the gas cell and the other side faces the ambient. Thus, any pressure difference leads to membrane deflection. Such deflection can be detected either optically or by measuring the capacitance. In the case of optical detection, a fiber is inserted to one side of the membrane as depicted in the top view in Figure 5-2 (a). Fiber tip with the metalized membrane forms a Fabry Pérot, whose length is dependent on the membrane deflection. Thus, by measuring the Fabry Pérot FSR, one can deduce the pressure inside the gas cell. Another way is to measure the capacitance between two electrodes where one of the electrodes is the membrane itself and the over electrode is a fixed structure as shown in Figure 5-2 (b).

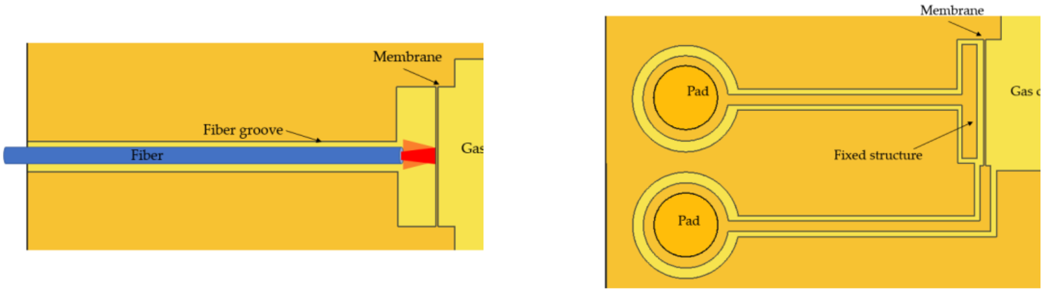

(a) (b)

Figure 5-2 Pressure sensors monolithic integrated on silicon (top view). The pressure sensor is based on measuring the deflection of the membrane. The detection is performed (a) optically using a fiber where fiber tip with the membrane constitute a Fabry Pérot. (b) or electrically by measuring the variation in the capacitance.

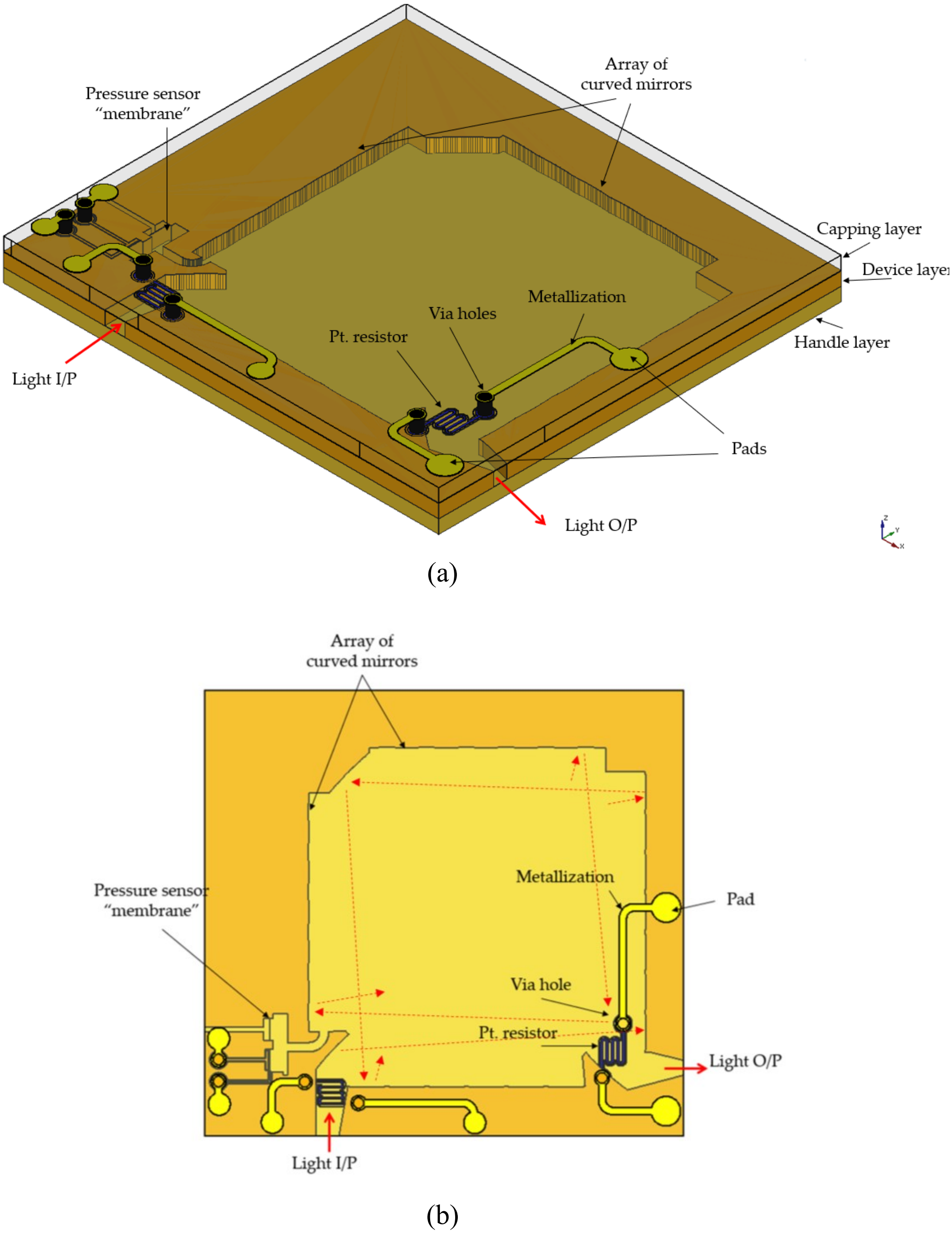

Figure 5-3 (a) 3D view for the integration of the multi-pass cell, pressure sensor, temperature sensor, and flow meter on the same chip. The capping layer is shown transparent only for illustration. (b) Top view of the integrated components.

For measuring the temperature, a resistor made of platinum deposited on the capping layer from the bottom can be used for this purpose. The resistance of the platinum increases with temperature linearly according to the relation $R(T) = R_o (1 + \alpha (T-To))$, where R_o is the resistance at temperature To and α is the temperature coefficient.

By using two resistors one at the inlet and other at the outlet, one can measure the temperature gradient across the gas cell. From such a gradient, one can conclude the airflow. Such sensors can be integrated with the multi-pass cell on the same chip as depicted in Figure 5-3.

Three layers are drawn; handle, device, and capping layer. The capping layer is drawn as transparent to show the structures beneath. The handle and the device layer are all coated with the gold (different colors only for illustration). Resistors, made of platinum for measuring airflow and air temperature, are patterned on the bottom of the capping layer. The remaining part of the capping layer is all coated with the gold for light guiding where there is an unmetallized region between the platinum and the gold to prevent electric short. The resistors' ends are connected using a via to the top layer of the capping layer. Such vias can be also hollow to act also as air inlet/outlet Then, the metalized tracks are used to connect between electric vias and pads as shown in Figure 5-3(b). In the depicted configuration, two temperature sensors are drawn to measure the temperature gradient to measure the airflow.

Pressure sensors are placed at the side of the multi-pass cell. The two configurations of the pressure sensors, previously mentioned, are drawn. The pressure sensor measures the pressure inside a small chamber which is directly connected to the multi-pass cell through a curved waveguide. In the case of the pressure sensor based on capacitance sensing, the electrodes are connected to the top of the capping layer using vias which are further connected to their corresponding pads.

AUTHOR'S PUBLICATIONS

Journal Publications:

1- A. Fathy, Y. M. Sabry, S. Nazeer, T. Bourouina, and D. A. Khalil, "On-chip parallel Fourier transform spectrometer for broadband selective infrared spectral sensing," *Microsystems Nanoeng.*, vol. 6, no. 1, pp. 1–9, 2020.(https://www.nature.com/articles/s41378-019-0111-0).

2- A. Fathy *et al.*, "Continuous Monitoring of Air Purification: A Study on Volatile Organic Compounds in a Gas Cell," *Sensors*, vol. 20, no. 3, p. 934, 2020. (https://www.mdpi.com/1424-8220/20/3/934).

3- A. Fathy, Y. M. Sabry, M. Gnambodoe-Capochichi, F. Marty, D. Khalil, and T. Bourouina, "Silicon Multi-Pass Gas Cell for Chip-Scale Gas Analysis by Absorption Spectroscopy," *Micromachines*, vol. 11, no. 5, p. 463, 2020. (https://www.mdpi.com/2072-666X/11/5/463).

4- A. Fathy, Y. M. Sabry, D. A. Khalil, and T. Bourouina, "Differential Spectrometer based on Critical Angle Dispersion".

5- A. Fathy, Y. M. Sabry, Ian W. Hunter, and T. Bourouina, "Direct absorption and photoacoustic spectroscopy for gas sensing and analysis: A critical review"

International Conference Publications:

1- A. Fathy, Y. M. Sabry, T. Bourouina, and D. Khalil, "On-Chip Parallel Architecture Mems FTIR Spectrometers Enabling High Spectral Resolution for Environmental Gas Analysis," in *2019 20th International Conference on Solid-State Sensors, Actuators and Microsystems & Eurosensors XXXIII (TRANSDUCERS & EUROSENSORS XXXIII)*, 2019, pp. 1515–1517.(https://ieeexplore.ieee.org/abstract/document/8808185/).

2- A. Fathy *et al.*, "MEMS FTIR optical spectrometer enables detection of volatile organic compounds (VOCs) in part-per-billion (ppb) range for air quality monitoring," in *MOEMS and Miniaturized Systems XVIII*, 2019, vol. 10931, p. 1093109. (https://www.spiedigitallibrary.org/conference-proceedings-of-spie/10931/1093109/MEMS-FTIR-optical-spectrometer-enables-detection-of-volatile-organic-compounds/10.1117/12.2508239.full?webSyncID=8531ab0d-3a6b-

03c9-7c00-9b6bcd746b80&sessionGUID=d8e8abee-aed6-ae05-c117-aac5a9199362).

3- A. Fathy *et al.*, "Mems Meets Zinc-Oxide Nanowires for Real-Time Monitoring of Air Purification: Case of Tobacco Smoke," in *2019 20th International Conference on Solid-State Sensors, Actuators and Microsystems & Eurosensors XXXIII (TRANSDUCERS & EUROSENSORS XXXIII)*, 2019, pp. 1385–1388.(https://ieeexplore.ieee.org/abstract/document/8808242/).

4- Gnambodoe-Capo-Chichi, Martine, et al. "Monitoring the purification of tobacco smoke in air assisted by ZnO nanowires and using MEMS-FTIR spectrometer for online continuous analysis of volatile organic compounds (VOCs)." *Optical Components and Materials XVI*. Vol. 10914. International Society for Optics and Photonics, 2019. (https://www.spiedigitallibrary.org/conference-proceedings-of-spie/10914/109141N/Monitoring-the-purification-of-tobacco-smoke-in-air-assisted-by/10.1117/12.2507983.full?webSyncID=d49a2853-1ab0-d3a6-b03c-97c009b6bcd7&sessionGUID=46b80d8e-8abe-eaed-6ae0-5c117aac5a91).

5- A. Fathy, Y. M. Sabry, F. Marty, D. Khalil, and T. Bourouina, "Silicon based integrated hollow waveguide for gas sensing applications," in Micro-Structured and Specialty Optical Fibres VI, 2020, vol. 11355, p. 113550T.(https://www.spiedigitallibrary.org/conference-proceedings-of-spie/11355/113550T/Silicon-based-integrated-hollow-waveguide-for-gas-sensing-applications/10.1117/12.2554947.full?webSyncID=46e9e6ec-7a49-dab6-a0cb-ad059329ad88&sessionGUID=3c9d902b-c999-3ced-268b-ead49a28531a).

APPENDIX

A.1 Transfer function of a gas filled cavity

For a cavity of length L filled with a gas of absorption coefficient $\alpha(\nu)$, the lossless cavity has a transmission as following:

$$\mathrm{T}_c'(\nu) = \frac{(1-\mathrm{R})^2 e^{-\alpha(\nu)\mathrm{L}}}{(1-\mathrm{R}e^{-\alpha(\nu)\mathrm{L}})^2 + 4\mathrm{R}e^{-\alpha(\nu)\mathrm{L}} \sin^2 \mathrm{kL}} \tag{A.1}$$

where $\mathrm{k} = 2\pi\nu$. For $\alpha\mathrm{L} \ll 1$, the equation is rewritten as following

$$\mathrm{T}_c'(\nu) \sim \frac{(1-\mathrm{R})^2}{1+\alpha(\nu)\mathrm{L} - 2\mathrm{R} + \mathrm{R}^2(1-\alpha\,(\nu)\mathrm{L}) + 4\mathrm{R}\sin^2 \mathrm{kL}} \tag{A.2}$$

which can be rewritten as follow:

$$\mathrm{T}_c'(\nu) = \frac{1}{1+\alpha(\nu)\mathrm{L}\frac{(1+\mathrm{R})}{1-\mathrm{R}} + \frac{4\mathrm{R}}{(1-\mathrm{R})^2}\sin^2 \mathrm{kL}} \tag{A.3}$$

For high Finesse cavity, $\mathrm{R}+1 \rightarrow 2$ and $\mathrm{F} \sim \frac{\pi}{1-\mathrm{R}}$. Thus, the transmission can be given by:

$$\mathrm{T}_c'(\nu) \sim \frac{1}{1+\left(\frac{2\mathrm{F}}{\pi}\right)^2 \sin^2 \mathrm{kL} \ + \alpha(\nu)\mathrm{L}\frac{2\mathrm{F}}{\pi}} \tag{A.4}$$

It can be proven easily that around the resonance for high Finesse cavity and too low absorption that the last term in the denominator is too small with respect to other terms, Thus, using Taylor one can simplify the following:

$$\mathrm{T}_c'(\nu) \sim \frac{1}{1+\left(\frac{2\mathrm{F}}{\pi}\right)^2 \sin^2 \mathrm{kL}} (1 - \frac{\alpha(\nu)\mathrm{L}\frac{2\mathrm{F}}{\pi}}{1+\left(\frac{2\mathrm{F}}{\pi}\right)^2 \sin^2 \mathrm{kL}}) \tag{A.4}$$

Thus, the cavity filled with gas has a transmission compared to that of unfilled cavity T_c by the following relation

$$\mathrm{T}_c'(\nu) \sim \mathrm{T}_c(\nu) - \frac{2\mathrm{F}}{\pi}\mathrm{L}\mathrm{T}_c^2(\nu) \tag{A.4}$$

In case of $\Delta\nu_g \ll \mathrm{FWHM}_\nu$ (FWHM_ν is FWHM in wavenumber domain),

$\mathrm{f}_g(\nu)\mathrm{T}_c^2(\nu) \sim \mathrm{f}_g(\nu)$ and $\mathrm{E}(\nu_o) = \frac{2\mathrm{F}}{\pi}\frac{\sigma_{\mathrm{DT}}}{\sigma_{\mathrm{CEAS}}}$.

A.2 ENHANCEMENT IN CAVITY ENHANCEMENT TECHNIQUE

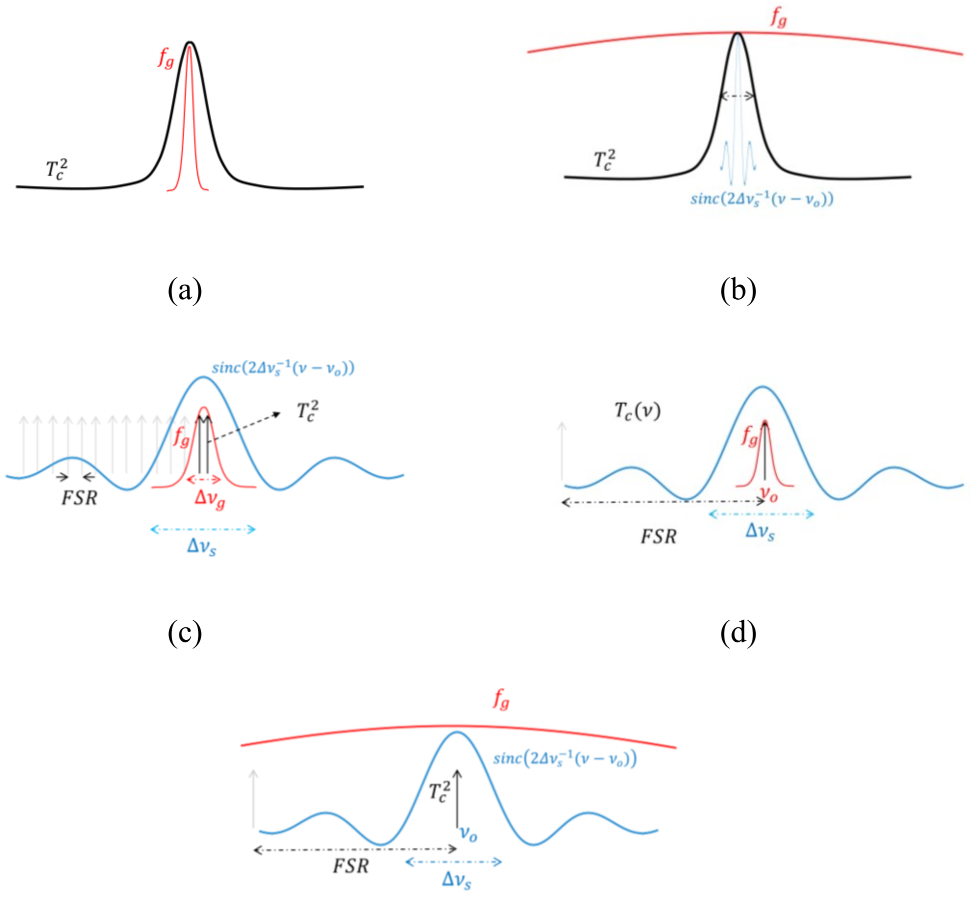

(a) (b) (c) (d) (e)

Figure A2.1 Different regions of operation of cavity enhancement technique. Faded cavity modes are faded because they are nearly zero due to multiplication by other functions.

Let the Equation (4.9)and (4.8) be rewritten as following

$$E(\nu_o) = \frac{2F}{\pi}\frac{A}{B}\frac{\sigma_{DT}}{\sigma_{CEAS}}$$

where $A = \int_{-\infty}^{\infty} f_g(\nu)T_c^2(\nu)\,\mathrm{sinc}(2\Delta\nu_s^{-1}(\nu-\nu_o))d\nu$ and $B = \int_{-\infty}^{\infty} f_g(\nu)\,\mathrm{sinc}(2\Delta\nu_s^{-1}(\nu-\nu_o))d\nu$.

For the 1st region in Table 4-1, where $\Delta\nu_g \ll FWHM_\nu$ (see Figure A2.1 (a)), $f_g(\nu)T_c^2(\nu) \sim f_g(\nu)$ and $E \sim \frac{2F}{\pi}\frac{\sigma_{DT}}{\sigma_{CEAS}}$.

For the 2nd region where $\Delta\nu_s \ll FWHM_\nu \ll \Delta\nu_g$ (see Figure A2.1 (b)), the integration of A is dominated by the function $T_c^2(\nu)$ which is much wider than the resolution. Thus,

$A \sim 0.5\Delta\nu_s$ (the integration of $\int_{-\infty}^{\infty} \mathrm{sinc}\, ax\, dx = 1/a$). A similar reason holds for B which is equal to $0.5\Delta\nu_s$ and the enhancement is given by $\frac{2F}{\pi}\frac{\sigma_{DT}}{\sigma_{CEAS}}$.

the absorption line is nearly constant as seen by the resolution. Therefore, $B \sim 0.5\Delta\nu_s$. The same holds for A, where the dominating function $T_c^2(\nu)$ is much wider than the resolution. Thus, $A \sim 0.5\Delta\nu_s$ and the enhancement will be $E \sim \frac{2F}{\pi}\frac{\sigma_{DT}}{\sigma_{CEAS}}$.

For the 3rd region where $FSR_\nu \ll \Delta\nu_g$ & $\Delta\nu_s$ (see Figure A2.1 (c)), $FWHM_\nu$ is intuitively $\ll \Delta\nu_s$. Regarding the integration of A is the integration of periodic function $T_c^2(\nu)$ multiplied by $f_g(\nu)$ (sinc is much wider $FWHM_\nu \gg \Delta\nu_g$). The integration results will be equal to the product of fill factor of one period of $T_c^2(\nu)$ ($\frac{0.25\pi FWHM_\nu}{FSR_\nu}$) and the area of f_g. Thus, $A \sim \frac{\Delta\nu_g}{8}\frac{\pi^2}{F}$. The gas profile $f_g(\nu)$ is seen as an impulse of a given area inside the integration of B. The integration will be equals to area of the $f_g(\nu)$ (For Lorentzian, area is $\pi\nu_g/2$) and $B \sim \pi\nu_g/2$. Finally, $E \sim 0.5\frac{\sigma_{DT}}{\sigma_{CEAS}}$.

For the 4th region where $FWHM_\nu \ll \Delta\nu_g \ll FSR_\nu$ and $\Delta\nu_g \ll \Delta\nu_s$ (see Figure A2.1 (d)), there is only one resonance peak of $T_c^2(\nu)$ in the integration A as $FSR \gg \Delta\nu_g$. Thus, the integration of A is just the area of this resonance peak and $A = 0.25\pi FWHM_\nu$. For B, $B \sim 0.5\pi\nu_g$ as the 3rd region and the enhancement $E \sim \frac{FSR}{\pi\Delta\nu_g}$.

Finally for the 5th region, where $FWHM_\nu \ll \Delta\nu_s \ll FSR_\nu$ and $\Delta\nu_s \ll \Delta\nu_g$, one can check Figure A2.1 (e). Regarding A, it is an integration of one resonance peak of $T_c^2(\nu)$ which is equal to $0.25\pi FWHM_\nu$. The integration of B is equal to $0.5\Delta\nu_s$ as in the 2nd region. The respective enhancement is given by $\frac{FSR}{\Delta\nu_s}$.

Long Résume de la Thèse

L'objectif de cette thèse est d'explorer le potentiel des spectromètres MEMS optiques pour les applications de détection de gaz, avec l'objectif ultime de produire un capteur de gaz micro-spectral, c'est-à-dire un dispositif ultra-compact capable de détecter plusieurs gaz simultanément, basé sur la spectroscopie optique. Différents aspects liés à ce sujet ont été étudiés d'un point de vue théorique et expérimental, selon une méthodologie proposée, qui prend en compte les dernières avancées technologiques avec le meilleur de leurs avantages ainsi que les limites physiques et les contraintes technologiques.

Premièrement, une revue critique a été menée sur la détection de gaz en utilisant la spectroscopie d'absorption directe (DAS) et la spectroscopie photoacoustique (PAS). Chaque méthode a été analysée lors de l'utilisation d'une source laser accordable ou d'un spectromètre à transformée de Fourier. Une analyse théorique a été menée sur ces systèmes pour trouver les limites de détection ultimes pour chaque cas. Afin de comparer le DAS et le PAS, une figure de mérite a été proposée, définie comme le rapport entre les coefficients d'absorption normalisés (normalisés par rapport au temps de mesure) de chaque système. Une fois la figure de mérite définie, nous avons pu comparer le PAS et le DAS en termes de paramètres affectant les limites basses de détection.

Dans le cas de la spectroscopie laser, les conclusions suivantes peuvent être tirées:

1) Le DAS surpasse le PAS en cas de puissance laser basse et de longueur de trajet optique longue.

2) Le système PAS peut être préféré lorsque la taille est une limitation et qu'il existe un besoin d'une cellule à gaz compacte.

3) Avec des lasers d'une puissance de quelques mWs, le DAS avec des trajets optiques supérieurs à quelques dizaines de mms devraient offrir une meilleure sensibilité.

4) L'augmentation de la puissance du laser à des centaines de mW ou plus résulte en un PAS ayant une meilleure sensibilité par rapport au DAS avec une longueur de trajet inférieure à des centaines de mm.

Dans le cas de la spectroscopie FTIR, les conclusions suivantes peuvent être tirées:

1) En ce qui concerne les paramètres de l'interféromètre, la différence entre les deux systèmes est indépendante de la résolution car les deux ont la même dépendance vis-à-vis de celle-ci.

2) Plus le temps de mesure par balayage est petit (c'est-à-dire une vitesse de miroir v_M élevée), meilleur est le DAS par rapport au PAS.

3) Le DAS est meilleur pour un flux d'interféromètre plus important.

4) Pour la source optique, l'augmentation de sa température rend le système PAS plus intéressant par rapport au système DAS, du fait de l'augmentation du bruit de grenaille dans ce dernier.

5) L'augmentation de la longueur du trajet optique dans la cellule améliore les performances du DAS par rapport à celle du PAS, à condition que les pertes d'insertion, introduites, principalement du fait des miroirs, ne masquent pas une telle amélioration.

Étant donné que le spectromètre MEMS est caractérisé par un faible flux optique, une vitesse de miroir rapide et un fort besoin de longues distances du trajet optique (pour atteindre une faible limite de détection), l'application de la spectroscopie photoacoustique avec le spectromètre MEMS n'est pas intéressante.

Architecture parallèle de spectromètre MEMS

Les spectromètres MEMS sont caractérisés par une faible résolution limitée par la plage de déplacement de l'actionneur. Il a été prouvé que le nouveau concept de spectromètre parallèle améliore la résolution spectrale du spectromètre. A cet effet, plusieurs interféromètres sont intégrés de manière monolithique dans la même puce et partagent un seul et même actionneur MEMS. Les interféromètres ont des différences de chemin optique (OPD) complémentaires. Les miroirs mobiles des interféromètres sont couplés mécaniquement au même actionneur, tandis que chaque interféromètre de la puce balaye une plage différente de l'OPD dans l'interférogramme mesuré; grâce aux décalages complémentaires de la position des miroirs, implémentés dans la conception du dispositif. L'interférogramme produit par chaque interféromètre est mesuré par son détecteur correspondant, puis un traitement de signal est appliqué pour produire un interférogramme global, sous forme de concaténation des différents interférogrammes enregistrés. Par conséquent, on peut augmenter artificiellement la différence de chemin optique, d'un facteur égal au nombre d'interféromètres parallèles, et ainsi, améliorer la résolution de longueur d'onde dans les mêmes proportions, en utilisant le même actionneur MEMS.

Une architecture composée de 4 interféromètres est représentée sur la figure 1 (a) ; elle a été ensuite fabriquée sous forme d'une puce MEMS. Habituellement, les sources optiques thermiques radiatives à large spectre sont plus grandes que l'ouverture d'entrée d'un seul interféromètre MEMS. Par conséquent, diviser la puissance de la source sur les 4 interféromètres ne réduit pas la quantité de lumière reçue par chacun de ces interféromètres pris individuellement. Cela signifie que, de manière intéressante, le rapport signal-sur-bruit (SNR) par interféromètre n'est pas affecté par la division de la lumière. Chaque interféromètre a son propre séparateur de faisceau, miroir fixe, miroir mobile et détecteur. Après concaténation des quatre interférogrammes complémentaires, la résolution spectrale correspondante est quadruplée par rapport à celle d'un seul interféromètre.

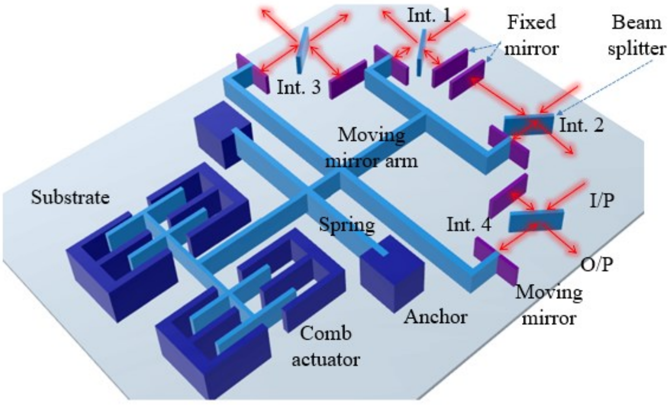

(a)

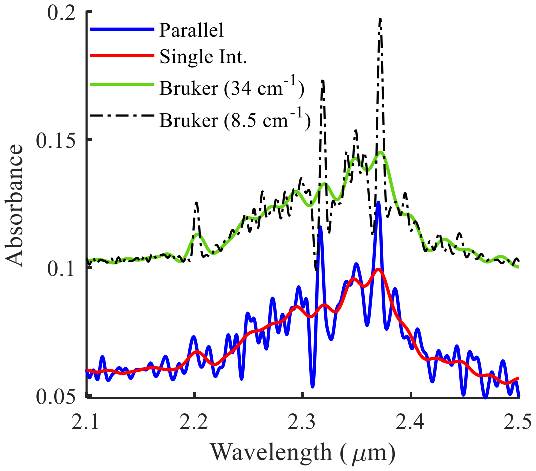

(b)

Figure 4 (a) L'architecture à l'échelle de la puce du spectromètre MEMS comprenant quatre interféromètres et un actionneur électrostatique à peignes. Les interféromètres sont désignés par *Int.* et numérotés de 1 à 4. Les miroirs mobiles de tous les interféromètres sont fixés au même bras mobile. Le trajet lumineux est indiqué par les flèches rouges. (b) Courbes d'absorbance du méthane mesurées par les interféromètres parallèles (en bleu) et l'interféromètre unique (en rouge) et comparées à l'absorbance mesurée par le spectromètre macroscopique de référence pour les deux résolutions correspondantes.

Une mesure de gaz a été réalisée pour montrer la capacité des interféromètres parallèles à faire la distinction entre les bandes d'absorption de gaz. Une cellule à gaz d'une longueur de 10 cm, contenant 10% de méthane $\mathrm{CH_4}$, a été insérée entre une source de lumière blanche et le spectromètre parallèle. Le contenu de la cellule à gaz a été analysé à l'aide des interféromètres parallèles et comparé à une mesure utilisant un interféromètre unique. Les courbes d'absorbance obtenues sont représentées sur la figure 1 (b). Les bandes d'absorption autour de 2,32 µm et 2,37 µm sont bien discriminées (courbe bleue) en comparaison au spectre mesuré par l'interféromètre unique (courbe rouge). La valeur d'absorbance a également été considérablement améliorée, comme le montre la gamme de longueurs d'onde de 2,3-2,37 µm. Pour référence, la même cellule à gaz a également été mesurée à l'aide d'un spectromètre de paillasse pour les deux résolutions correspondant à l’expérience, à savoir, 34 cm^{-1} et 8,5 cm^{-1}, et tracée sur la figure 1 (b). La comparaison montre un bon accord avec les mesures du spectromètre MEMS et prouve le potentiel de l'utilisation d'un spectromètre parallèle dans la surveillance des gaz environnementaux.

Spectromètre différentiel

En visant une architecture encore plus simple que le FTIR, un nouveau concept est proposé, celui du spectromètre différentiel. Il est basé sur l'utilisation de la longue structure d’un guide d'ondes dispersif dont les interfaces d'entrée et de sortie sont biseautées. En balayant l'angle d'incidence et en détectant la puissance à l'autre extrémité du guide, à l'aide d'un seul détecteur, on mesure une puissance intégrée en longueur d'onde. En différenciant un tel signal, le spectre correspondant de la lumière incidente est récupéré. Le degré de collimation est le paramètre clé qui contrôle la résolution spectrale. Le choix de l'angle de biseau

α affecte également la résolution spectrale et la bande passante. Le pouvoir de résolution du spectromètre différentiel a été comparé à l'équation de puissance de résolution du prisme. La comparaison est représentée sur la figure 2. Il est clair que le pouvoir de résolution du nouveau spectromètre est d'un ordre de grandeur plus grand que le prisme au début de sa gamme spectrale et légèrement meilleur pour les longueurs d'onde plus grandes. Un cristal ATR a été utilisé pour prouver le concept du spectromètre différentiel. Deux sources laser différentes (1480 nm et 1548 nm) ont été mesurées. L'expérience a été réalisée en utilisant une fibre multi-mode (MMF) dont le diamètre de cœur / gaine cœur / gaine 50/125 µm. Les signaux mesurés en fonction du temps sont représentés sur la figure 3 (a). Après différenciation, les signaux correspondants sont représentés sur la figure 3 (b). La résolution spectrale obtenue est d'environ 120 nm.

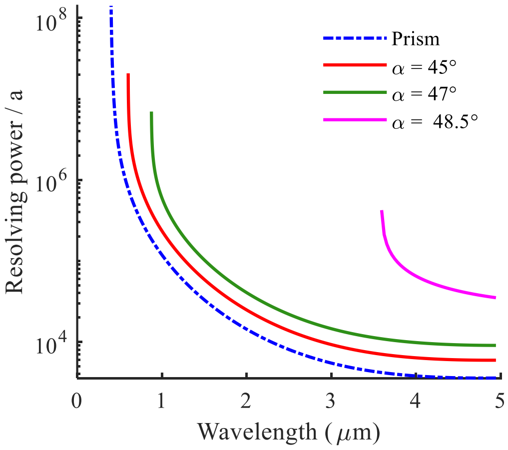

Figure 5 Pouvoir de résolution du spectromètre à base de prisme (tiret) et à base d'ATR (traits pleins) pour différentes valeurs de α.

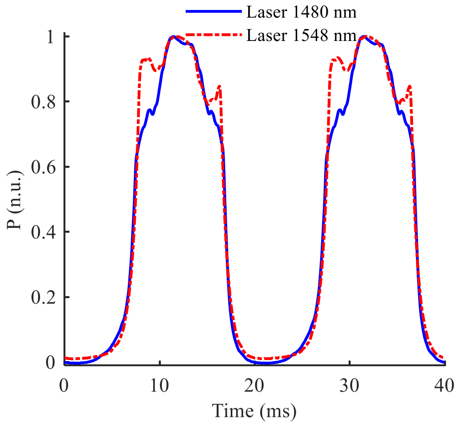

(a)

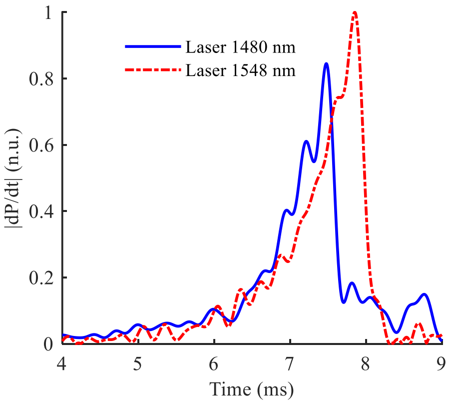

(b)

Figure 6 (a) Puissance laser mesurée par le détecteur en fonction du temps en utilisant une fibre multimode (MMF) de diamètre cœur/gaine de 50/125 µm. (b) Les signaux différenciés correspondants.

Cependant, la résolution mesurée était loin de la résolution théorique et on observe des ondulations dans les spectres mesurés de la source laser. Un modèle de simulation a été construit pour comprendre une telle dégradation des performances. Comme la rugosité diffuse la lumière vers des angles plus larges, son effet sur la résolution a été étudié. L'ATR a été caractérisé, et la rugosité de surface mesurée RMS est égale à 8,4 nm et la longueur de corrélation varie de 7 à 12 µm. L'effet de rugosité a été modélisé à l'aide du modèle Harvey-Shack. Le modèle de rugosité est intégré dans le modèle du spectromètre différentiel. Au final, le modèle ne révèle toujours pas de dégradation de la résolution en utilisant ces valeurs mesurées.

La caractérisation a été répétée à l'aide d'un laser rouge. A partir des taches observées, nous avons conclu que les surfaces latérales de l’ATR ne sont pas parfaitement parallèles, ce qui a été vérifié plus tard en mesurant l'angle entre les surfaces latérales à l'aide d'un microscope. Une telle imperfection de l'ATR a donc été intégrée dans le modèle du spectromètre et les résultats du modèle étaient au final cohérents avec les mesures en termes d'apparition d'ondulations et de dégradation de la résolution.

Une correction mathématique a été appliquée pour corriger la résolution en supprimant l'effet des surfaces non parallèles de l'ATR. L'effet des surfaces non parallèles peut être réduit en: 1) estimant son effet sur différentes longueurs d'onde grâce à la mesure de son effet sur une seule mesure de longueur d'onde. 2) Après cette estimation, on peut remplacer un tel effet par la réponse idéale par multiplication matricielle. Une telle correction a été appliquée sur les mesures. Les spectres corrigés des mesures de sources lasers sont représentés sur la figure 4 (a) après conversion du temps en longueur d'onde. Les résultats montrent que les ondulations ont été supprimées et que la résolution est améliorée, portée de 120 nm à 50 nm à une longueur d’onde de 1480 nm et à 60 nm à 1548 nm. Une telle amélioration est claire une fois comparée avec les résultats présentés sur la figure 3 (a). Un matériau de référence (TS5) a également été mesuré à l'aide du spectromètre différentiel. La mesure corrigée de ce matériau est également représentée sur la figure 4 (b). La mesure a été comparée au spectromètre FTIR pris comme référence.

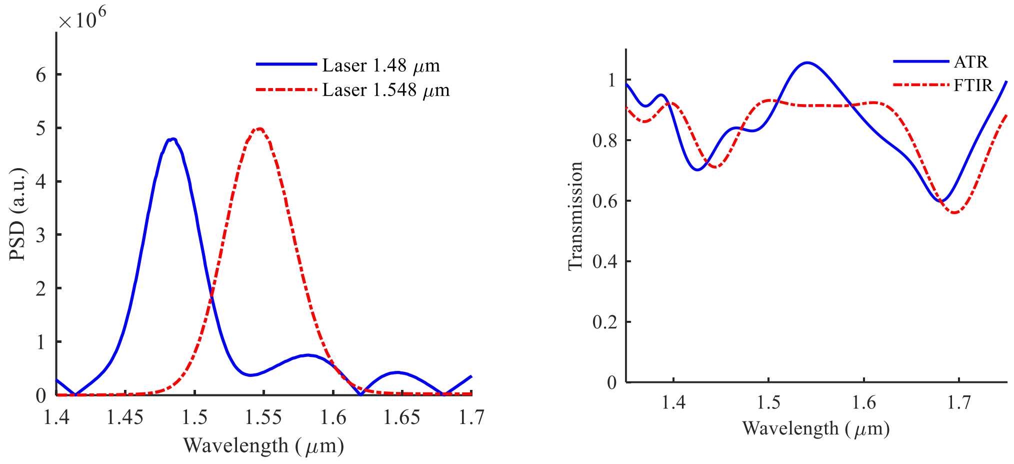

(a) (b)

Figure 7 Spectres corrigés des lasers mesurés par MMF de diamètres de coeur/gaine de 50/125 µm. (b) Spectre corrigé du matériau de reference TS5.

Applications de détection de gaz utilisant le spectromètre MEMS

Nous avons ensuite mené une série d'études pour étudier plus en détail l'application du spectromètre MEMS-FTIR pour la détection et l'analyse de gaz. Nous avons commencé à nous atteler au problème de la détection de la pollution de l'air sur un grand espace, à l'aide d'un microspectromètre FTIR. A cet effet, et afin de profiter du grand espace disponible et de la possibilité d'interaction de la lumière avec le gaz sur de longs chemins optiques, nous avons mis en œuvre le spectromètre en mode chemin optique ouvert dans la chambre climatique de l'EquipEx Sense-City située dans notre campus de Marne-la-Vallée. Avec la grande longueur disponible pour l'interaction lumière-gaz, jusqu'à 38 mètres, nous avons pu mesurer la pollution moyennée spatialement. Ceci a été réalisé en utilisant un prototype de spectromètre MEMS fonctionnant dans infrarouge moyen (MIR) jusqu'à 4,8 µm. La pollution provoquée par une voiture a été surveillée et comparée aux mesures des analyseurs de référence localisés disposés dans Sense-City. Une vue schématique de la chambre montrant les positions de la voiture, de l'analyseur de référence, de la source lumineuse et du spectromètre MEMS est représentée sur la figure 5.

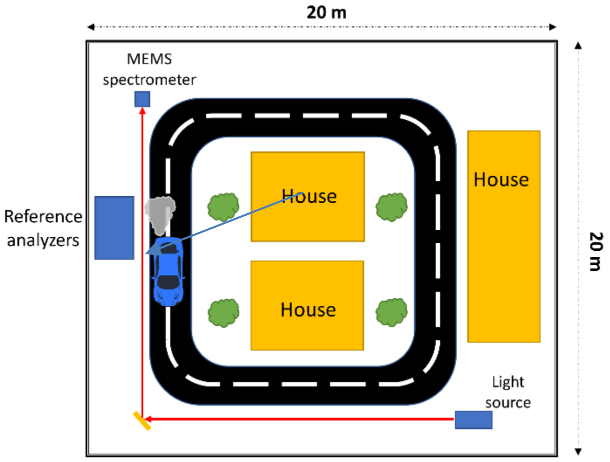

Figure 8 Vue schématique de dessus de Sense City, espace utilisé pour la mise en œuvre de la surveillance de la pollution de l'air à l'aide du FTIR en mode de trajet ouvert.

Le bruit de fond a été supprimé à l'aide de la méthode de correction de la ligne de base polynomiale. Les enregistrements de mesure ont commencé au temps 0. Après 6 heures, le moteur de la voiture a été démarré pendant deux périodes. La concentration du dioxyde de carbone mesurée en fonction du temps est représentée sur la figure 6 (a). La mesure de l'analyseur est également représentée sur la même figure à des fins de comparaison. La partie rouge transparente représente la durée pendant laquelle la voiture avait son moteur allumé (la pollution a été introduite). Un pic de concentration de CO_2 a été observé dans la mesure de l'analyseur alors que l'analyseur était placé à proximité immédiate de la voiture. Après l'arrêt de la voiture, la concentration de CO_2 a commencé à diminuer en raison de la diffusion à l'intérieur de la pièce. En parallèle, le FTIR a mesuré une augmentation rapide du CO_2, une fois la voiture allumée, mais pas aussi vite que celle de l'analyseur et n'a pas non plus atteint le même pic. En effet, le FTIR a fait la moyenne de la concentration sur l’ensemble de la chambre. Après, un certain temps, il a mesuré une augmentation progressive du dioxyde de carbone avec une croissance plus lente en raison du temps nécessaire à la diffusion continue de dioxyde de carbone à l'intérieur de la pièce.

La concentration de vapeur d'eau a été surveillée en suivant un pic à 1,848 µm également accessible dans le spectre mesuré par le FTIR. Ceci a été comparé en utilisant la concentration en eau calculée à partir du capteur d'humidité et du capteur de température en utilisant la formule Magnus, comme illustré sur la figure 6 (b).

Au final, la configuration présentée d'un capteur spectral de gaz à base de FTIR-MEMS présente une solution prometteuse de mesures de chemin ouvert surpassant les systèmes FTIR à chemin ouvert conventionnels qui souffrent d'un coût élevé, encombrant et lourd.

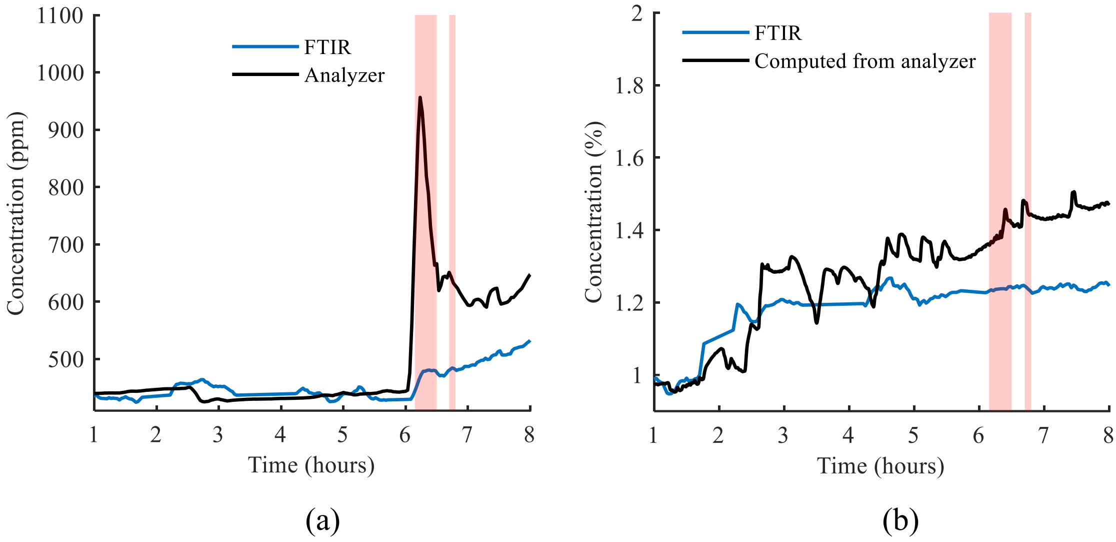

Figure 9 (a) Concentration de dioxyde de carbone en fonction du temps (b) Concentration d'eau en fonction du temps. La région rouge représente l'intervalle d'introduction de la pollution en utilisant l'accélération de la voiture.

La détection localisée du toluène, choisie comme exemple des COV les plus courants de la famille des BTEX, a été réalisée en utilisant une cellule de gaz à passages multiples de 10 cm de longueur couplée au spectromètre MIR MEMS-FTIR. 30 ppb de toluène comme limite inférieure de détection ont été atteints. Pour arriver à ce résultat, différentes concentrations de toluène gazeux ont été préparées en diluant des volumes contrôlés de toluène à l'état liquide dans un sac Tedlar rempli d'azote. Le gaz est ensuite transféré vers la cellule de gaz à passages multiples d'une longueur totale effective de 20 m. La lumière de la source a été injectée dans la cellule à gaz à l'aide d'une lentille de collimation. La lumière à la sortie de la cellule a été couplée à l'entrée du spectromètre MEMS à l'aide d'une seconde lentille. Les concentrations de toluène dans la gamme du ppm ont été mesurées en utilisant les étapes précédentes. L'absorbance mesurée à la longueur d'onde de 3,27 μm pour chacune des concentrations préparées est représentée sur la figure 7. La courbe est ajustée sur une ligne droite comme indiqué sur la figure. La pente de la droite est $m = 0.003\ ppm^{-1}$

et le biais est de 0,0036. La figure montre une bonne linéarité (coefficient de détermination $R^2 = 0.9992$) avec une plage dynamique assez large.

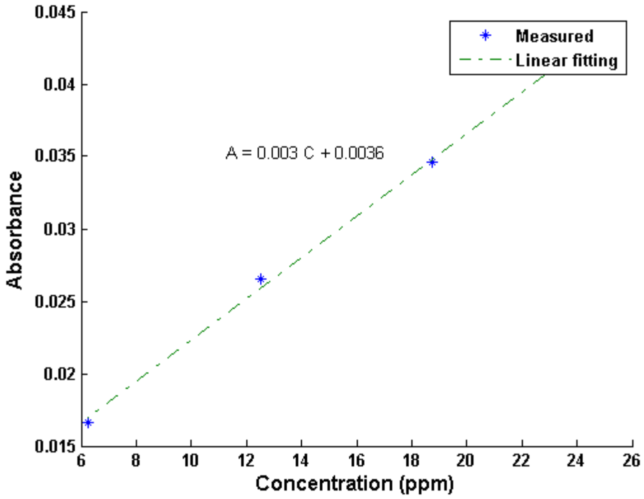

Figure 10 Linéarité de l'absorbance mesurée en fonction de la concentration. Les points mesurés sont ajustés par une ligne droite présentant une excellente linéarité. Le coefficient de regression linéaire est $R^2 = 0.9992$.

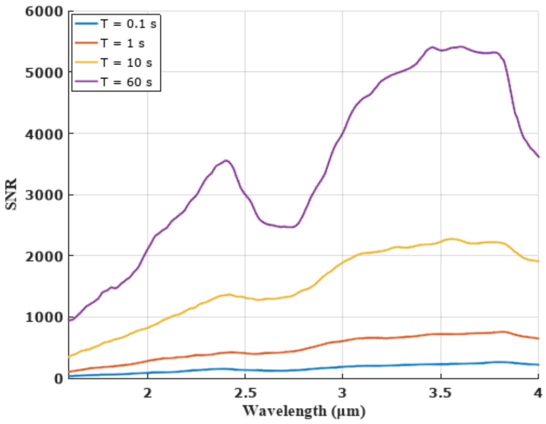

Figure 11 Rapport signal-sur-bruit (SNR) mesuré pour différentes durées de moyennage

Le rapport signal-sur-bruit (SNR) a été mesuré pendant un temps moyen différent comme illustré sur la figure 8. Le SNR mesuré à λ = 3,27 µm s'est avéré être de 5000: 1 pendant une durée moyenne de 60 s. Cette valeur correspond à un écart type σ de l'absorbance autour de 10^{-4}. Sur cette base, la concentration minimale détectable s'est avérée être de 30 *ppb*.

En utilisant une cellule à gaz directe d'une longueur de 10 cm (au lieu de la cellule de gaz à passages multiples), nous avons réalisé un suivi de la dépollution de l'air, ce qui a également été l'occasion de mener une étude sur les mécanismes de purification de l'air par photocatalyse. A cet effet un échantillon de silicium recouvert de nanofils de ZnO, connu pour ses propriétés photocatalytiques, est déployé à l'intérieur de la cellule. Une concentration contrôlée de polluants a également été ajoutée à l'intérieur de la cellule. La concentration en acétone était de 5% tandis que la concertation du toluène était de 1,7%. Le taux d'élimination, défini comme le pourcentage de la diminution de l'absorbance, est calculé pour quatre cas différents : sans / avec puce de nanofils de ZnO et en l'absence / présence de lumière UV. Le rapport d'élimination en fonction du temps a été calculé en présence de ZnO et comparé au cas d'absence de ZnO. Le rapport d'élimination est calculé en utilisant la valeur d'absorbance à 2970 cm^{-1} et illustré sur la figure 9 (a). L'utilisation de ZnO améliore le taux d'élimination pendant tout le temps d'observation. Le taux d'élimination après 3 heures est d'environ 14% dans le cas du ZnO contre seulement 3% sans ZnO avec une augmentation du taux d'élimination de 4,6 fois. Les expériences sont ensuite répétées en utilisant de la lumière UV. Ceci conduit au processus de photo-oxydation en l'absence de puce ZnO et de photo-catalyse en présence de la puce ZnO. Le rapport d'élimination correspondant est représenté sur la figure 9 (b). L'amélioration est clairement visible lors de l'utilisation de ZnO. Par exemple, après trois heures, le taux d'élimination dans le cas du ZnO était de 11% tandis que l'absence de la puce ZnO conduit à une élimination négligeable. Il est à noter que l'utilisation de la lumière UV conduit à une élimination plus rapide (constante de temps de près de 30 minutes) au stade précoce, tandis que le taux d'élimination est plus lent sans lumière UV même si les états finaux atteignent le même ordre de magnitude d'environ 10% après 3 heures.

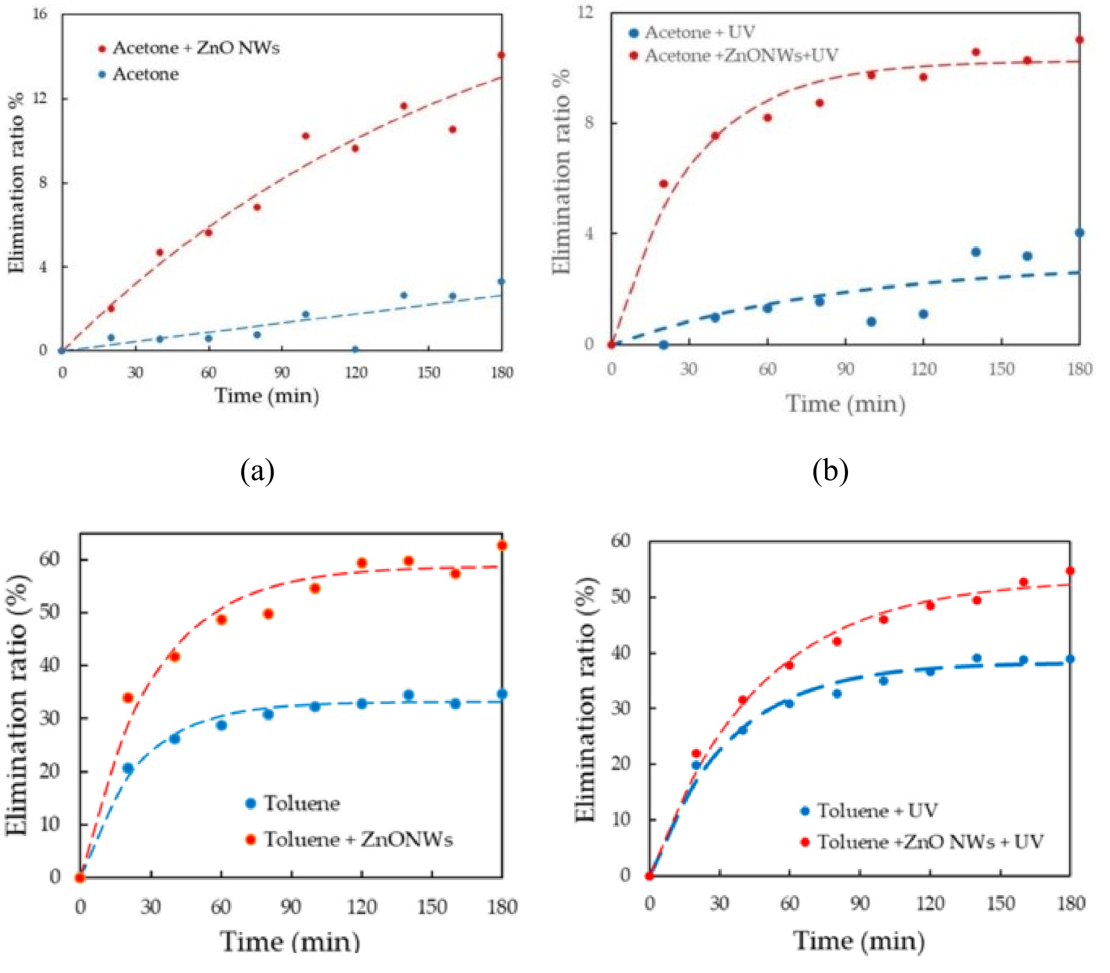

(a) (b)

(c) (d)

Figure 12 (a) & (b) Le rapport d'élimination de l'acétone en fonction du temps en cas d'absence et de présence de ZnO (a) sans et (b) avec présence d'UV. Les lignes pointillées représentent l'ajustement exponentiel $(1 - e^{-t/\tau})$ pour les points mesurés, où τ est une constante de temps. (c) et (d) Le rapport d'élimination du toluène en fonction du temps en cas d'absence et de présence de ZnO (c) sans et (d) avec présence d'UV. Le rapport d'élimination est calculé en utilisant l'absorbance du gaz à 3042 cm^{-1}. Les lignes pointillées représentent un ajustement exponentiel des points mesurés.

Pour étendre l'étude à différents COV, une expérience similaire a été menée pour la dégradation du toluène. Tout d'abord, la variation de concentration de toluène a été surveillée en utilisant le spectromètre MEMS sans appliquer la lumière UV. Le rapport d'élimination est calculé en utilisant la valeur d'absorbance à 3042 cm^{-1} et illustré sur la figure 9 (c). Après trois heures d'adsorption, le taux d'élimination atteint environ 63% dans le cas du ZnO alors qu'il atteint 35% en l'absence de ZnO. Sur la figure 9 (d), le ratio d'élimination du toluène en cas d'application d'UV est présenté. La figure montre un taux d'élimination d'environ 55% dans le cas de l'utilisation du ZnO avec la lumière UV par rapport à 38% sans l'utilisation du ZnO avec les UV.

En comparant les résultats expérimentaux obtenus avec les deux COV considérés dans ce travail, à savoir l'acétone et le toluène, un taux d'élimination de 63% en 3 heures a été atteint pour le toluène, alors qu'il n'était que de 14% pour l'acétone. La présence de ZnO est apparue comme cruciale dans le cas de l'élimination de l'acétone puisque quasiment aucune élimination (presque 3%) n'a été obtenue en l'absence de ZnO. Au contraire, les nanofils de ZnO ne sont pas aussi cruciaux pour l'élimination du toluène ; cependant, ils améliorent considérablement le rapport d'élimination. Enfin, il est également apparu que dans les deux cas d'utilisation de la lumière UV ou non, le ZnO produit une amélioration suggérant que l'adsorption et la photocatalyse sont améliorées par les nanofils de ZnO.

Guides d'ondes creux intégrés

Enfin, nous avons fait un pas en avant vers une miniaturisation complète des capteurs de gaz spectraux. Contrairement aux expériences ci-dessus, où les cellules à gaz étaient macroscopiques, la percée technologique que nous visons est d'intégrer la cellule à gaz dans une puce de silicium. Nous avons conçu et fabriqué de telles cellules à gaz à l'échelle mm à base de silicium ainsi que des guides d'ondes creux (HWG) à base de silicium, dont l'empreinte ne dépasse pas 2 cm x 2 cm, mais permettant toutefois des longueurs de trajets optiques efficaces allant de 10 à 33 cm.

Pour pouvoir construire le HWG avec un long chemin optique à l'intérieur d'une puce de silicium, plusieurs segments HWG peuvent être utilisés. Les segments HWG sont assemblés à l'aide de miroirs réflecteurs cubiques. Trois HWG de différentes longueurs de chemin optique ont été intégrés sur la même puce. La longueur de base du segment HWG est d'environ 1,95 cm. Les modèles HWG1, HWG2 et HWG3 ont une longueur totale du trajet optique de 9,75 cm, 21,45 cm et 33,15 cm, respectivement. La largeur du HWG est de 400 µm et la profondeur de 200 µm. Les trous traversants de gaz pour injecter le gaz à l'intérieur du HWG, mis en œuvre sur la tranche supérieure, sont répartis comme le montre la figure 10 (b) (trous blancs). La disposition 3D du HWG 1 avec traçage de rayons est représentée sur la figure 10 (c).

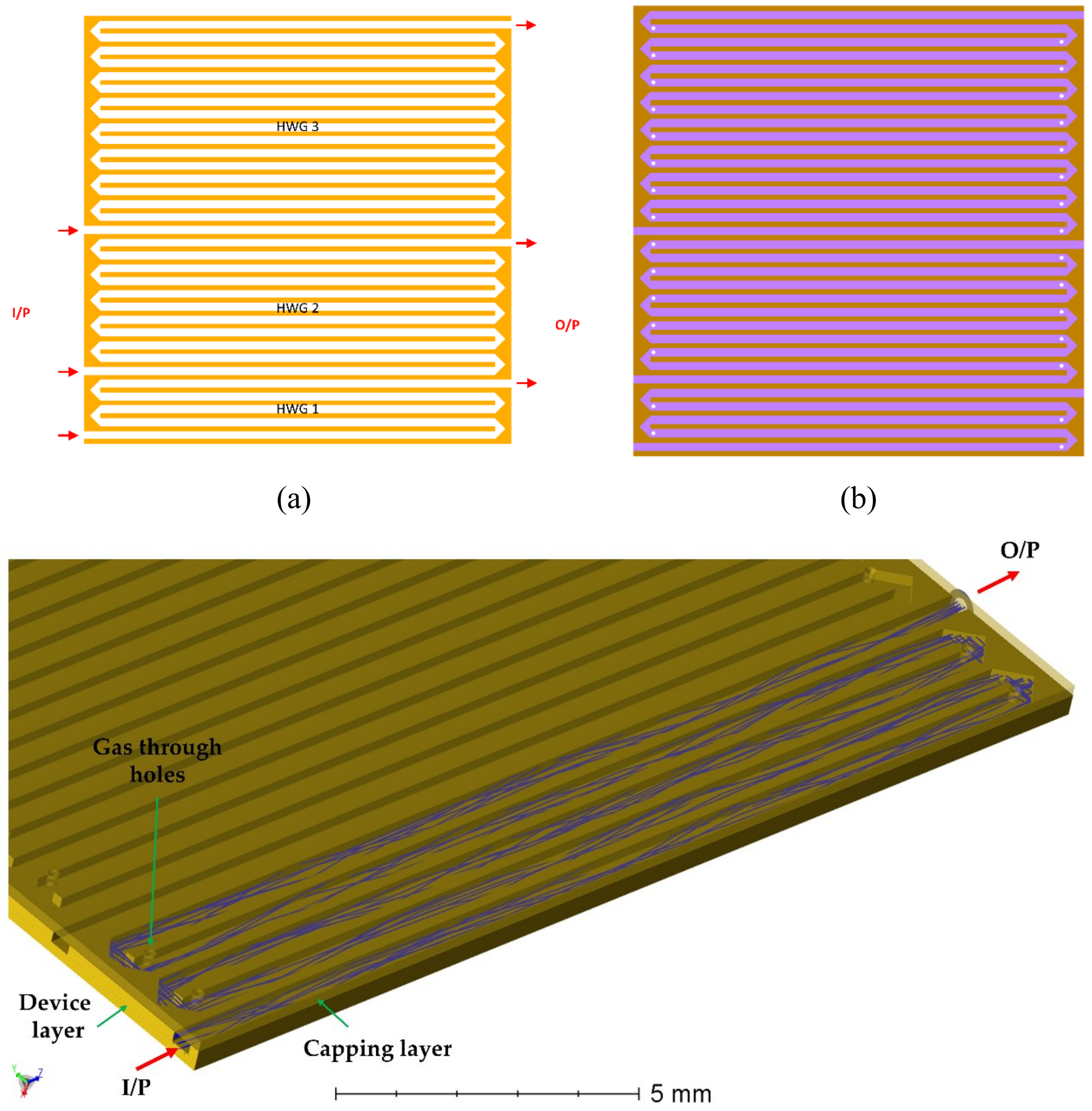

(a) (b)

(c)

Figure 13 Schéma de conception du guide d’ondes creux (HWG) (a) Couche utile du dispositif. (b) Couche utile en couleur claire et couche du capot en couleur sombre. (c) Schéma 3D du HWG1 où les lignes bleues représentent les trajets des rayons de l'entrée à la sortie.

For characterizing the HWG and to measure gases, the MEMS based MIR FTIR was used. The measured insertion losses of the waveguides are plotted in Figure 14 (a) These are shown in bold lines. These are compared with expected losses from simulations. The insertion losses of the shorter hollow waveguide (HWG1) ranges from 10 to 13 dB across the range from 1500 nm to 4500 nm. Such losses increase dramatically to 30 dB for the longest waveguide HWG3. For the HWG3, the losses increase for shorter wavelengths which is attributed to the roughness (roughness losses increase with decreasing wavelength of operation). There is a discrepancy of 4 dB between the measurements and the simulations in case of the HWG1 and HWG2, while the difference increases to 15 dB in case of the HWG3.

From the insertion losses measurements, one could extract information about the $\mathrm{CO_2}$ concentration. This peak is around 4.25 µm. First, the wavelength dependence losses of the HWG in the transmission measurement was removed using the baseline correction method. The peaks of the $\mathrm{CO_2}$ measured by the three HWGs are plotted in Figure 14 (b). The $\mathrm{CO_2}$ concentration was also directly measured using a chemical-based sensor. The average concentration was around 700 ppm in the air. Using such a concentration value, the absorption coefficient of $\mathrm{CO_2}$ from HITRAN database, FT spectrometer system model and HWGs path length, the corresponding absorbance of Carbon dioxide of the three HWGs are also plotted in in Figure 14 (b). The measurements show a good agreement with the chemical-based sensor measurements within a variation which can be attributed to the variation of $\mathrm{CO_2}$ inside the laboratory. The deformation of the signal measured by the HWG3 is attributed to the noisy signal acquired due to the high losses (30 dB). Water absorbance was also monitored and depicted in Figure 14 (c) showing the increase of absorbance with increasing the path length. Signal to noise ratio was measured for the HWG1. The average time was 1 second. The result is depicted in Figure 14 (d). From the measured SNR, we can conclude that the lower detection limit (1σ) of CO_2 is 130 ppm for an average time of 1 second.

Pour caractériser le HWG et mesurer les gaz, le spectromètre FTIR-MEMS opérant dans la gamme MIR a été utilisé. Les pertes d'insertion mesurées des guides d'ondes sont représentées sur la figure 11 (a). Elles sont indiquées en traits gras. Celles-ci sont comparées aux pertes attendues des simulations. Les pertes d'insertion du guide d'ondes creux le plus court (HWG1) vont de 10 à 13 dB sur la plage de 1500 nm à 4500 nm. Ces pertes augmentent considérablement jusqu'à 30 dB pour le guide d'ondes le plus long HWG3. Pour le HWG3, les pertes augmentent pour les longueurs d'onde plus courtes, ce qui est attribué à la rugosité (les pertes dues à la rugosité augmentent avec la diminution de la longueur d'onde de fonctionnement). Il y a un écart de 4 dB entre les mesures et les simulations dans le cas du HWG1 et du HWG2, tandis que la différence augmente à 15 dB dans le cas du HWG3.

À partir des mesures des pertes d'insertion, on pourrait extraire des informations sur la concentration de CO_2. Le pic caractéristique correspondant est à environ 4,25 µm. Premièrement, la dépendance vis-à-vis de la longueur d'onde des pertes du HWG, dans la mesure de la transmission ont été supprimées en utilisant la méthode de correction de la ligne de base évoquée plus haut. Les pics du CO_2 mesurés par les trois HWG sont représentés sur la figure 11 (b). La concentration de CO_2 a également été mesurée directement à l'aide d'un capteur chimique. La concentration moyenne était d'environ 700 ppm dans l'air. En utilisant une telle valeur de concentration, le coefficient d'absorption de CO_2 de la base de données HITRAN, le modèle du système de spectromètre FT et la longueur du trajet des HWG, l'absorbance correspondante du dioxyde de carbone des trois HWG sont également représentés sur la figure 11 (b). Les mesures montrent un bon accord avec les mesures obtenues directement au moyen de capteurs chimiques, dans une variation qui peut être attribuée à la variation de la teneur en CO_2 à l'intérieur du laboratoire. La déformation du signal mesuré par le HWG3 est attribuée au signal bruyant acquis en raison des pertes élevées (30 dB). L'absorbance de l'eau a également été surveillée et représentée sur la figure 11 (c) montrant l'augmentation de l'absorbance avec l'augmentation de la longueur du trajet. Le rapport signal sur bruit (SNR) a été mesuré pour le HWG1. Le temps moyen était de 1 seconde. Le résultat est illustré sur la figure 11 (d). À partir du SNR mesuré, nous pouvons conclure que la limite de détection inférieure (1σ) de CO_2 est de 130 ppm pour un temps moyen de 1 seconde.

Malgré les pertes optiques importantes à l'intérieur du HWG, il s'agit toujours d'une cellule à gaz compacte qui peut être intégrée facilement avec le spectromètre MEMS. C'est d'ailleurs son faible volume d'échantillonnage qui la rend plus rapide que capteurs chimiques. Cela a également été observé lors de la mesure du dioxyde de carbone provenant de l'expiration humaine et du gaz butane émis par un briquet.

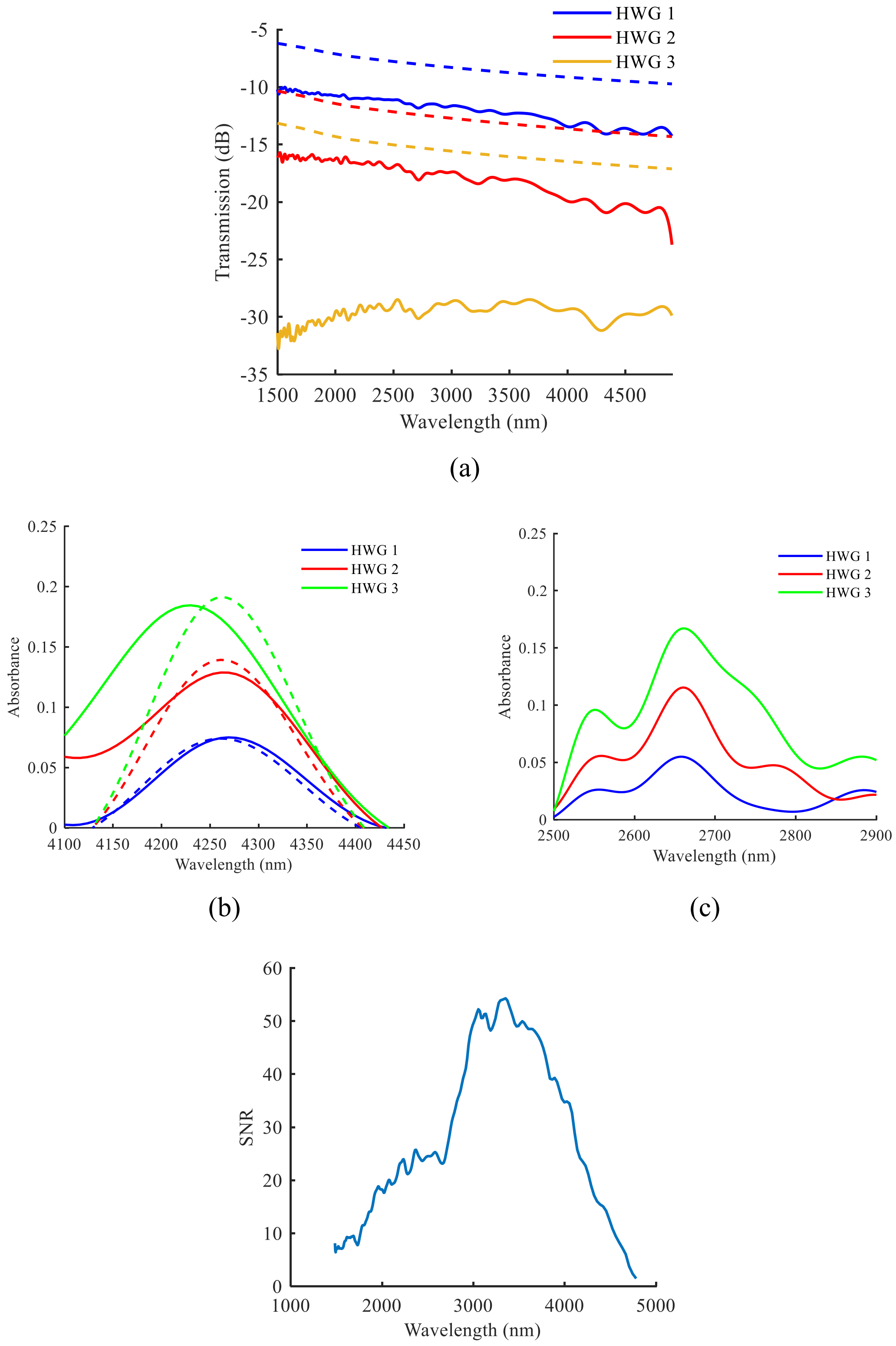

(a)

(b)

(c)

(d)

Figure 14 (a) Pertes d'insertion du guide d'ondes creux (HWG). Les lignes en gras sont les valeurs mesurées et les lignes en pointillés les pertes d'insertion simulées. (c) Dioxyde de carbone mesuré et simulé pour les différents HWG. (d) Absorbance mesurée de vapeur d'eau. (e) Rapport signal-sur-bruit (SNR) mesuré au moyen du HWG1. Le temps moyen est de 1 s.

Cellule de gaz intégrée à passages multiples

Lorsqu'il s'agit d'une cellule à gaz à l'échelle de la puce, comme envisagé dans nos travaux, nous sommes confrontés à deux difficultés majeures liées à la miniaturisation. Premièrement, les dimensions latérales d'une puce sont limitées à quelques millimètres, ce qui constitue une limitation sévère pour le chemin optique L, réduisant ainsi l'interaction lumière-gaz. On peut faire face à cette première limitation en adoptant le concept de cellule de gaz à passages multiples. Deuxièmement, il faut également tenir compte d'autres considérations optiques liées à la miniaturisation des cellules à gaz. Par exemple, nous devons nous assurer que la perte optique est principalement régie par l'absorption de gaz, d'où la nécessité d'une conception optique soignée pour minimiser les pertes d'insertion. La perte peut être significativement affectée par la faible épaisseur des plaquettes de silicium, qui est limitée à quelques centaines de micromètres au maximum. Une telle faible épaisseur gêne le flux optique de la cellule fonctionnant avec une lumière se propageant en espace libre car elle rend difficile la collimation d'une lumière incidente de petite taille de faisceau avec un grand flux dans la puce de silicium. D'un autre côté, l'utilisation du procédé lithographique offre le grand avantage d'un auto-alignement de haute qualité des pièces optiques microfabriquées selon une conception de masque assistée par ordinateur (CAO). Cela peut également conduire à une stabilité mécanique élevée puisque tous les composants ont été micro-usinés dans le même substrat. Cela permet de mettre en œuvre des conceptions sophistiquées sans avoir besoin d'un alignement post-fabrication.

Une représentation 3D de la cellule à gaz proposée est représentée sur la figure 12 (a). Les directions de la lumière d'entrée et de sortie sont perpendiculaires l'une à l'autre pour faciliter le couplage de la lumière. Un miroir d'entrée cylindrique est utilisé pour coupler la lumière de la source à la cellule. Le contraire est réalisé en sortie par un autre miroir cylindrique. La cellule elle-même comprend des miroirs cylindriques concentriques. Les miroirs sont auto-alignés, du fait qu'ils ont été micro-usinés dans le même bloc de silicium qui est fixé à un substrat. Le substrat contient le gaz traversant les trous ainsi que l'entrée / sortie optique. La couverture est métallisée et consiste en une autre tranche de silicium. Dans le plan perpendiculaire au substrat, le guidage de la lumière se fait à l'aide du substrat métallisé et de la plaquette de couverture métallisée. Le guidage / focalisation de la lumière dans le plan parallèle au substrat est réalisé à l'aide de miroirs cylindriques. L'injection du gaz dans la cellule se fait à travers des trous dans le substrat. Une cellule à gaz optimisée avec métallisation en or a été ciblée pour la fabrication et une caractérisation plus poussée. La profondeur cible correspondante d est de l'ordre de 190 µm, tandis que le rayon de cellule r est voisin de 3 mm.

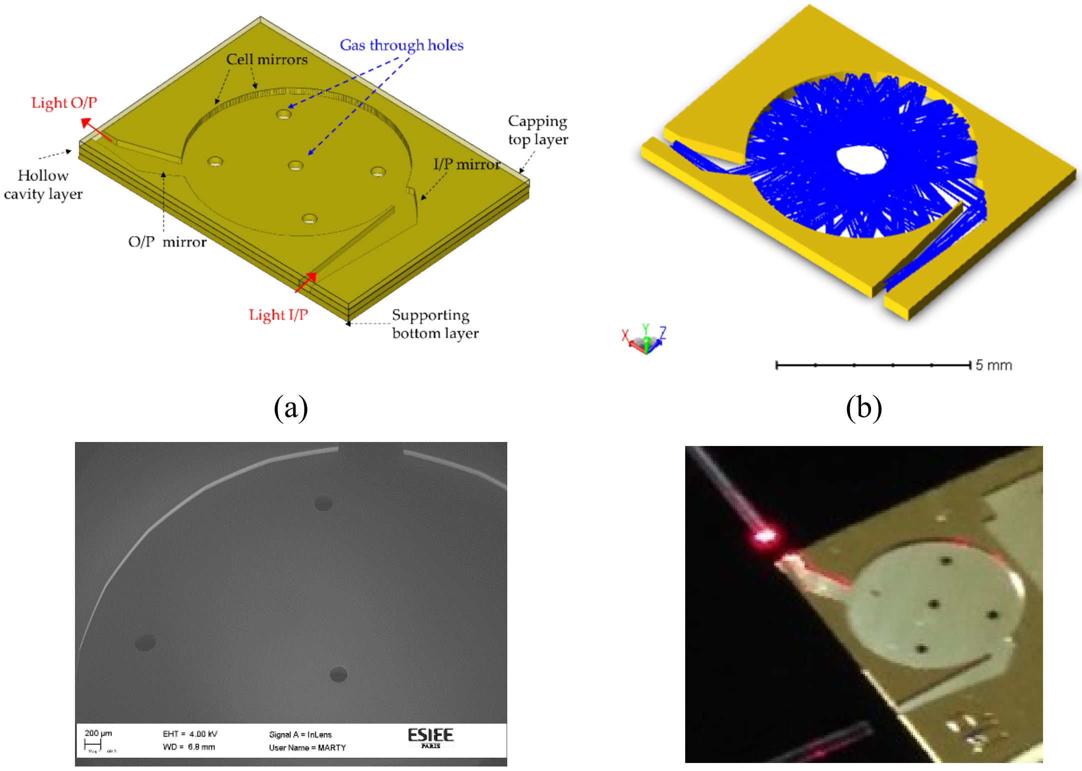

(a) (b)

(c) (d)

Figure 15 (a) Schéma 3D de la cellule de gaz intégrée au silicium. La couche utile du dispositif contient la cellule à gaz. Le substrat contient des trous traversant pour l'accès du gaz. La couche-capot sert à recouvrir la cellule. (b) Tracé de rayons au moyen du logiciel ZEMAX pour la cellule de gaz intégrée à passages multiples. (c) vue rapprochée obtenue au microscope électronique à balayage, (d) photo du dispositif fabriqué avec couplage de lumière par fibre optique en entrée et en sortie de la cellule.

Une image de la cellule à gaz obtenue au microscope électronique à balayage est présentée sur la figure 12 (c). La cellule a été éclairée avec un laser rouge à partir d'une fibre comme illustré sur la photographie présentée en figure 12 (d). Des taches brillantes sur certains miroirs sont observées. Ce sont les miroirs qui devraient être atteints par un laser une fois dans la cellule à gaz, tandis que les autres miroirs ne sont pas brillants en raison de la diffraction de la lumière du côté supérieur en raison de l'absence de la couverture.

Carbon dioxide CO_2 gas is injected into a chamber from a gas cylinder. The chamber comprises the integrated multi-pass cell. Different pressures were measured which corresponds to different absorbance values (0.9 bar to 1.6 bar). The corresponding absorbance curves are plotted in Figure 16 (a). The absorbance values at 2.01 µm versus the pressure applied are scattered in Figure 16 (b) in addition to a linear fit with a root mean square error of 10^{-3}. An effective path length was found to be 9 cm compared to the theoretical path length of 12 cm. The corresponding lower detection of limit is 30 mbar. The cell volume is too small. It is about 6 µL. This means a small sampling volume of gases. The path length to the volume ratio PVR is an important Merit factor for the gas cells, the more this value the more compact cell will be. The corresponding PVR is about 17,000 m/L. Such value is two orders of magnitudes bigger than that of the conventional gas cells (macro gas cells have PVR values ranging from tens to hundreds, according to the survey conducted in the reference). However, this is at the expense of the sensitivity where the benchtop gas cells have larger throughput and lower losses (a smaller number of reflections).

Le gaz carbonique CO_2 est injecté dans une chambre à partir d'une bouteille de gaz. La chambre comprend la cellule de gaz intégrée à passages multiples. Différentes pressions ont été mesurées ce qui correspond à différentes valeurs d'absorbance (0,9 bar à 1,6 bar). Les courbes d'absorbance correspondantes sont tracées sur la figure 13 (a). Les valeurs d'absorbance à 2,01 µm en fonction de la pression appliquée sont présentées sur la figure 13 (b) en plus d'un ajustement linéaire avec une erreur quadratique moyenne de 10^{-3}. Une longueur de chemin optique efficace s'est avérée être de 9 cm par rapport à la longueur de chemin théorique de 12 cm. La limite de détection inférieure correspondante est de 30 mbar. Le volume de la cellule est trop petit, environ 6 µL. Cela signifie un petit volume d'échantillonnage de gaz. La longueur du trajet au rapport volumique PVR est un facteur de mérite important pour les cellules à gaz, plus cette valeur est élevée, plus la cellule sera compacte. Le PVR correspondant est d'environ 17 000 m/L. Cette valeur est de deux ordres de grandeur plus grande que celle des cellules à gaz conventionnelles (les macro-cellules à gaz ont des valeurs PVR allant de quelques dizaines à quelques centaines, selon la comparaison avec l’état de l’art). Cependant, cela se fait au détriment de la sensibilité où les cellules à gaz de paillasse bénéficient d’un flux optique plus important et des pertes plus faibles (un plus petit nombre de réflexions).

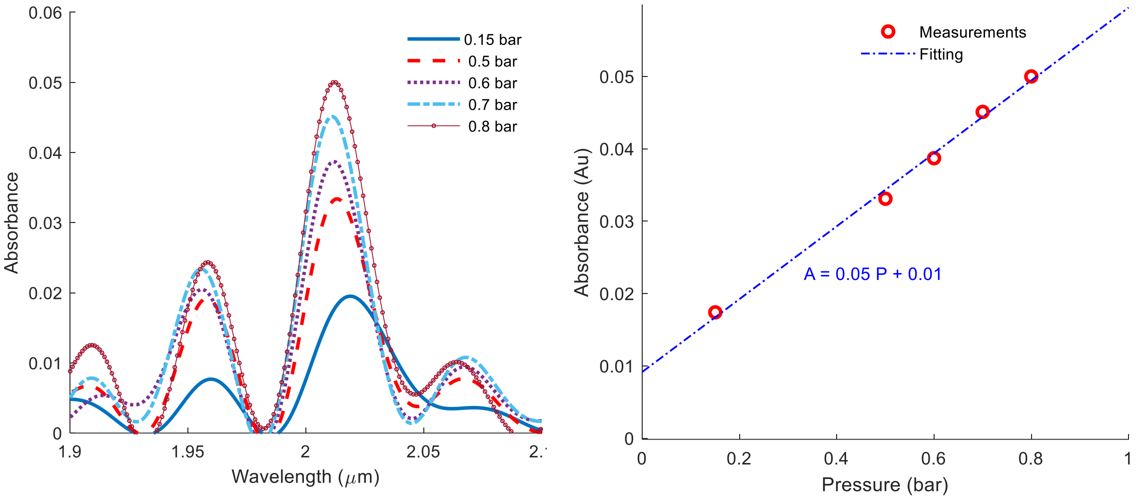

(a) (b)

Figure 16 Mesures du dioxyde de carbone (a) Absorbance du dioxyde de carbone (CO2) à différentes pressions, mesurée à l'aide de la cellule de gaz intégrée à passages multiples. (b) L'absorbance correspondante à 2,01 µm en fonction de la pression. Un ajustement linéaire est également tracé.

BIBLIOGRAPHY

[1] "Air pollution." [Online]. Available: https://www.who.int/health-topics/air-pollution#tab=tab_1. [Accessed: 16-Aug-2020].

[2] G. F. Fine, L. M. Cavanagh, A. Afonja, and R. Binions, "Metal oxide semi-conductor gas sensors in environmental monitoring," *sensors*, vol. 10, no. 6, pp. 5469–5502, 2010.

[3] X. Liu, S. Cheng, H. Liu, S. Hu, D. Zhang, and H. Ning, "A survey on gas sensing technology," *Sensors*, vol. 12, no. 7, pp. 9635–9665, 2012.

[4] A. Dey, "Semiconductor metal oxide gas sensors: A review," *Mater. Sci. Eng. B*, vol. 229, pp. 206–217, 2018.

[5] S. Feng *et al.*, "Review on smart gas sensing technology," *Sensors*, vol. 19, no. 17, p. 3760, 2019.

[6] T. Han, A. Nag, S. C. Mukhopadhyay, and Y. Xu, "Carbon nanotubes and its gas-sensing applications: A review," *Sensors Actuators A Phys.*, vol. 291, pp. 107–143, 2019.

[7] J. Hodgkinson and R. P. Tatam, "Optical gas sensing: a review," *Meas. Sci. Technol.*, vol. 24, no. 1, p. 12004, 2012.

[8] S. Zhang, W. Bin, X. Zheng, H. San, and W. Hofmann, "A Compact MEMS-Based Infrared Spectrometer for Multi-Gases Measurement," in *2019 IEEE 32nd International Conference on Micro Electro Mechanical Systems (MEMS)*, 2019, pp. 926–929.

[9] N. P. Ayerden and R. F. Wolffenbuttel, "The miniaturization of an optical absorption spectrometer for smart sensing of natural gas," *IEEE Trans. Ind. Electron.*, vol. 64, no. 12, pp. 9666–9674, 2017.

[10] M. Meinig *et al.*, "Tunable Fabry-Pérot interferometer with subwavelength grating reflectors for MWIR microspectrometers," in *Advanced Fabrication Technologies for Micro/Nano Optics and Photonics IX*, 2016, vol. 9759, p. 97590W.

[11] T. Scharf, D. Briand, S. Bühler, O. Manzardo, H. P. Herzig, and N. F. de Rooij, "Miniaturized Fourier transform spectrometer for gas detection in the MIR region," *Sensors Actuators B Chem.*, vol. 147, no. 1, pp. 116–121, 2010.

[12] T. Tanahashi, M. Toda, H. Miyashita, and T. Ono, "Miniature Fourier transform infrared spectrometer for middle infrared wavelength range," in *2013 Transducers & Eurosensors XXVII: The 17th International Conference on Solid-State Sensors, Actuators and Microsystems (TRANSDUCERS & EUROSENSORS XXVII)*, 2013, pp. 2509–2512.

[13] A. A. Elsayed, M. Sakr, M. Erfan, Y. M. Sabry, and D. Khalil, "On the environmental gas sensing using MEMS FTIR spectrometer in the near-infrared region," in *2016 33rd National Radio Science Conference (NRSC)*, 2016, pp. 348–355.

[14] J. Chai *et al.*, "Review of MEMS Based Fourier Transform Spectrometers," *Micromachines*, vol. 11, no. 2, p. 214, 2020.

[15] Y. M. Sabry, D. Khalil, and T. Bourouina, "Monolithic silicon-micromachined free-space optical interferometers onchip," *Laser and Photonics Reviews*. 2015.

[16] H. S. E. EH40 and others, "Workplace exposure limits," *London Heal. Saf. Exec.*, 2011.

[17] L. Shao, P. R. Griffiths, and A. B. Leytem, "Advances in data processing for open-path fourier transform infrared spectrometry of greenhouse gases," *Anal. Chem.*, vol. 82, no. 19, pp. 8027–8033, 2010.

[18] D. W. T. Griffith, N. M. Deutscher, C. G. R. Caldow, G. Kettlewell, M. Riggenbach, and S. Hammer, "A Fourier transform infrared trace gas and isotope analyser for atmospheric applications," *Atmos. Meas. Tech. Discuss*, vol. 5, no. 10, pp. 3717–3769, 2012.

[19] J. B. McManus, J. H. Shorter, D. D. Nelson, M. S. Zahniser, D. E. Glenn, and R. M. McGovern, "Pulsed quantum cascade laser instrument with compact design for rapid, high sensitivity measurements of trace gases in air," *Appl. Phys. B*, vol. 92, no. 3, p. 387, 2008.

[20] E. C. Richard *et al.*, “A fast-response near-infrared tunable diode laser absorption spectrometer for in situ measurements of CH 4 in the upper troposphere and lower stratosphere,” *Appl. Phys. B*, vol. 75, no. 2–3, pp. 183–194, 2002.

[21] W. Chen *et al.*, “Photonic sensing of environmental gaseous nitrous acid (HONO): opportunities and challenges,” *Wonder Nanotechnol. Quantum Optoelectron. Devices Appl. M. Razeghi. L. Esaki, K. von Klitzing, Eds., SPIE Press. Bellingham, WA*, pp. 693–737, 2013.

[22] T. A. Aarhaug, A. Ferber, H. Gaertner, S. Kolås, S. O. Ryman, and P. Geiser, “Validation of Online Monitoring of PFC by QCL with FTIR Spectroscopy,” in *Light Metals 2018*, 2018, pp. 1487–1493.

[23] P. R. Griffiths and J. A. De Haseth, *Fourier transform infrared spectrometry*, vol. 171. John Wiley & Sons, 2007.

[24] P. L. Hanst, A. S. Lefohn, and B. W. Gay Jr, “Detection of atmospheric pollutants at parts-per-billion levels by infrared spectroscopy,” *Appl. Spectrosc.*, vol. 27, no. 3, pp. 188–198, 1973.

[25] M. Erfan, Y. M. Sabry, M. Sakr, B. Mortada, M. Medhat, and D. Khalil, “On-Chip Micro-Electro-Mechanical System Fourier Transform Infrared (MEMS FT-IR) Spectrometer-Based Gas Sensing,” *Appl. Spectrosc.*, 2016.

[26] N. A. Saliba, H. Yang, and B. J. Finlayson-Pitts, “Reaction of gaseous nitric oxide with nitric acid on silica surfaces in the presence of water at room temperature,” *J. Phys. Chem. A*, vol. 105, no. 45, pp. 10339–10346, 2001.

[27] F. A. F. Winiberg *et al.*, “Direct measurements of OH and other product yields from the\hack{\break} HO$_{2}$\,$+$\,CH$_{3}$C(O)O$_{2}$ reaction,” *Atmos. Chem. Phys.*, vol. 16, no. 6, pp. 4023–4042, 2016.

[28] B. T. Thompson and B. Mizaikoff, “Real-time fourier transform-infrared analysis of carbon monoxide and nitric oxide in sidestream cigarette smoke,” *Appl. Spectrosc.*, vol. 60, no. 3, pp. 272–278, 2006.

[29] J. Heland and K. Schäfer, “Determination of major combustion products in aircraft

exhausts by FTIR emission spectroscopy," *Atmos. Environ.*, vol. 32, no. 18, pp. 3067–3072, 1998.

[30] M. Adachi, Y. Yamagishi, K. Inoue, and K. Ishida, "Automotive emission analyses using FTIR spectrophotometer," 1992.

[31] D. W. T. Griffith, "FT-IR measurements of atmospheric trace gases and their fluxes," *Handb. Vib. Spectrosc.*, 2006.

[32] F. M. Kelliher, A. R. Reisinger, R. J. Martin, M. J. Harvey, S. J. Price, and R. R. Sherlock, "Measuring nitrous oxide emission rate from grazed pasture using Fourier-transform infrared spectroscopy in the nocturnal boundary layer," *Agric. For. Meteorol.*, vol. 111, no. 1, pp. 29–38, 2002.

[33] J. W. Childers *et al.*, "Multi-pollutant concentration measurements around a concentrated swine production facility using open-path FTIR spectrometry," *Atmos. Environ.*, vol. 35, no. 11, pp. 1923–1936, 2001.

[34] M. Grutter, E. Flores, R. Basaldud, and L. G. Ruiz-Suárez, "Open-path FTIR spectroscopic studies of the trace gases over Mexico City," *Atmos. Ocean. Opt. C/C Opt. Atmos. I OKEANA*, vol. 16, no. 3, pp. 232–236, 2003.

[35] L. A. Todd, M. Ramanathan, K. Mottus, R. Katz, A. Dodson, and G. Mihlan, "Measuring chemical emissions using open-path Fourier transform infrared (OP-FTIR) spectroscopy and computer-assisted tomography," *Atmos. Environ.*, vol. 35, no. 11, pp. 1937–1947, 2001.

[36] C. Oppenheimer, P. Francis, M. Burton, A. J. H. Maciejewski, and L. Boardman, "Remote measurement of volcanic gases by Fourier transform infrared spectroscopy," *Appl. Phys. B*, vol. 67, no. 4, pp. 505–515, Oct. 1998.

[37] R. J. Yokelson, I. T. Bertschi, T. J. Christian, P. V Hobbs, D. E. Ward, and W. M. Hao, "Trace gas measurements in nascent, aged, and cloud-processed smoke from African savanna fires by airborne Fourier transform infrared spectroscopy (AFTIR)," *J. Geophys. Res. Atmos.*, vol. 108, no. D13, 2003.

[38] A. Miklós, P. Hess, and Z. Bozóki, "Application of acoustic resonators in

photoacoustic trace gas analysis and metrology," *Rev. Sci. Instrum.*, vol. 72, no. 4, pp. 1937–1955, 2001.

[39] A. Miklós, S.-C. Pei, and A. H. Kung, "Multipass acoustically open photoacoustic detector for trace gas measurements," *Appl. Opt.*, vol. 45, no. 11, pp. 2529–2534, 2006.

[40] A. Keller *et al.*, "Open photoacoustic sensor as smoke detector," *Sensors Actuators B Chem.*, vol. 104, no. 1, pp. 1–7, 2005.

[41] J. Wojtas *et al.*, "Cavity-enhanced absorption spectroscopy and photoacoustic spectroscopy for human breath analysis," *Int. J. Thermophys.*, vol. 35, no. 12, pp. 2215–2225, 2014.

[42] J. Huber, C. Weber, A. Eberhardt, and J. Wöllenstein, "Photoacoustic CO2-sensor for automotive applications," *Procedia Eng.*, vol. 168, pp. 3–6, 2016.

[43] J. Karhu *et al.*, "Broadband photoacoustic spectroscopy of CH 4 14 with a high-power mid-infrared optical frequency comb," *Opt. Lett.*, vol. 44, no. 5, pp. 1142–1145, 2019.

[44] J. Zhou, G. Meng, Y. Zheng, Y. Peng, and J. Zou, "Advanced Photoacoustic Spectrometer for Air Monitoring in Manned Spacecraft," 2015.

[45] F. J. M. Harren, J. Mandon, and S. M. Cristescu, "Photoacoustic spectroscopy in trace gas monitoring," *Encycl. Anal. Chem. Appl. Theory Instrum.*, 2006.

[46] C. ZHANG and F. WANG, "Application of Photo-Acoustic Spectroscopy Technology to Dissolved Gas Analysis in Oil of Oil-Immersed Power Transformer [J]," *High Volt. Eng.*, vol. 2, 2005.

[47] T. Tomberg, M. Vainio, T. Hieta, and L. Halonen, "Sub-parts-per-trillion level sensitivity in trace gas detection by cantilever-enhanced photo-acoustic spectroscopy," *Sci. Rep.*, vol. 8, no. 1, p. 1848, 2018.

[48] Z. Du, S. Zhang, J. Li, N. Gao, and K. Tong, "Mid-Infrared Tunable Laser-Based Broadband Fingerprint Absorption Spectroscopy for Trace Gas Sensing: A Review," *Appl. Sci.*, vol. 9, no. 2, p. 338, 2019.

[49] M. A. Bolshov, Y. A. Kuritsyn, and Y. V Romanovskii, “Tunable diode laser spectroscopy as a technique for combustion diagnostics,” *Spectrochim. Acta Part B At. Spectrosc.*, vol. 106, pp. 45–66, 2015.

[50] Y. Yao, A. J. Hoffman, and C. F. Gmachl, “Mid-infrared quantum cascade lasers,” *Nat. Photonics*, vol. 6, no. 7, p. 432, 2012.

[51] F. K. Tittel, R. Lewicki, R. Lascola, and S. McWhorter, “Emerging infrared laser absorption spectroscopic techniques for gas analysis,” *Trace Anal. Spec. Electron. gases. Hoboken Wiley*, pp. 71–110, 2013.

[52] K. E. Whittaker, “Development and application of spectroscopic techniques in the mid-infrared,” Oxford University, UK, 2014.

[53] M. W. Raynor, K. A. Bertness, K. C. Cossel, F. Adler, and J. Ye, “Trace water vapor analysis in specialty gases: sensor and spectroscopic approaches,” *Trace Anal. Spec. Electron. Gases, WM Geiger MW Raynor, Eds*, pp. 195–249, 2013.

[54] S. Bergin, “Pathlength calibration of integrating sphere based gas cells,” 2016.

[55] J. Hodgkinson, D. Masiyano, and R. P. Tatam, “Gas cells for tunable diode laser absorption spectroscopy employing optical diffusers. Part 1: single and dual pass cells,” *Appl. Phys. B*, vol. 100, no. 2, pp. 291–302, 2010.

[56] S. Schilt, F. K. Tittel, and K. P. Petrov, “Diode laser spectroscopic monitoring of trace gases,” *Encycl. Anal. Chem. Appl. Theory Instrum.*, 2006.

[57] M. Pushkarsky, M. Weida, T. Day, D. ARNONE, R. PRITCHETT, and D. CAFFEY, “Performance characteristics of a compact widely tunable external cavity quantum cascade laser,” *Rev. Laser Eng.*, vol. 36, no. 2, pp. 80–83, 2008.

[58] A. Rogalski, *Infrared detectors*. CRC press, 2010.

[59] A. Rogalski, M. Kopytko, and P. Martyniuk, “Infrared Detector Characterization,” in *Antimonide-based Infrared Detectors: A New Perspective*, SPIE.

[60] A. R. Kost, “Materials for mid-infrared semiconductor lasers,” *MRS Online Proc. Libr. Arch.*, vol. 484, 1997.

[61] A. Bauer *et al.*, “Mid-infrared semiconductor heterostructure lasers for gas sensing applications,” *Semicond. Sci. Technol.*, vol. 26, no. 1, p. 14032, 2010.

[62] J. Hecht, “The laser guidebook,” 1986.

[63] M. Tacke, “Lead--salt lasers,” *Philos. Trans. R. Soc. London. Ser. A Math. Phys. Eng. Sci.*, vol. 359, no. 1780, pp. 547–566, 2001.

[64] J. Faist, F. Capasso, D. L. Sivco, C. Sirtori, A. L. Hutchinson, and A. Y. Cho, “Quantum cascade laser,” *Science (80-.).*, vol. 264, no. 5158, pp. 553–556, 1994.

[65] N. Bandyopadhyay, M. Chen, S. Sengupta, S. Slivken, and M. Razeghi, “Ultra-broadband quantum cascade laser, tunable over 760 cm- 1, with balanced gain,” *Opt. Express*, vol. 23, no. 16, pp. 21159–21164, 2015.

[66] I. Vurgaftman *et al.*, “Interband cascade lasers,” *J. Phys. D. Appl. Phys.*, vol. 48, no. 12, p. 123001, 2015.

[67] W. Nakwaski, S. Grzempa, M. Dems, and T. Czyszanowski, “New structure of semiconductor lasers: quantum-cascade vertical-cavity surface-emitting laser (QC VCSEL),” in *Laser Technology 2018: Progress and Applications of Lasers*, 2018, vol. 10974, p. 109740A.

[68] W. W. Bewley *et al.*, “Room-temperature mid-infrared interband cascade vertical-cavity surface-emitting lasers,” *Appl. Phys. Lett.*, vol. 109, no. 15, p. 151108, 2016.

[69] A. Rogalski, “Infrared detectors: status and trends,” *Prog. quantum Electron.*, vol. 27, no. 2–3, pp. 59–210, 2003.

[70] H. Photonics, “Characteristics and use of infrared detectors,” *Small*, vol. 43, 2004.

[71] A. Rogalski, “History of infrared detectors,” *Opto-Electronics Rev.*, vol. 20, no. 3, pp. 279–308, 2012.

[72] “Vigo Website,” 2020. .

[73] “Hamamatsu website,” 2020. .

[74] C. Dyroff, *Tunable Diode Laser Absorption Spectroscopy for Trace Gas*

Measurements with High Sensitivity and Low Drift. Univ.-Verlag, 2009.

[75] R. Yang, X. Dong, Y. Bi, and T. Lv, “A method of reducing background fluctuation in tunable diode laser absorption spectroscopy,” *Opt. Commun.*, vol. 410, pp. 782–786, 2018.

[76] C. Li *et al.*, “High-speed multi-pass tunable diode laser absorption spectrometer based on frequency-modulation spectroscopy,” *Opt. Express*, vol. 26, no. 22, pp. 29330–29339, 2018.

[77] J. M. Nicely, T. F. Hanisco, and H. Riris, “Applicability of neural networks to etalon fringe filtering in laser spectrometers,” *J. Quant. Spectrosc. Radiat. Transf.*, vol. 211, pp. 115–122, 2018.

[78] C.-T. Zheng *et al.*, “Performance improvement of a near-infrared CH4 detection device using wavelet-denoising-assisted wavelength modulation technique,” *Sensors Actuators B Chem.*, vol. 190, pp. 249–258, 2014.

[79] A. Klein, O. Witzel, and V. Ebert, “Rapid, time-division multiplexed, direct absorption-and wavelength modulation-spectroscopy,” *Sensors*, vol. 14, no. 11, pp. 21497–21513, 2014.

[80] X. Chao, J. B. Jeffries, and R. K. Hanson, “Wavelength-modulation-spectroscopy for real-time, in situ NO detection in combustion gases with a 5.2 $µ$m quantum-cascade laser,” *Appl. Phys. B*, vol. 106, no. 4, pp. 987–997, 2012.

[81] M. Niu, Q. Liu, K. Liu, Y. Yuan, and X. Gao, “Temperature-dependent photoacoustic spectroscopy with a T shaped photoacoustic cell at low temperature,” *Opt. Commun.*, vol. 287, pp. 180–186, 2013.

[82] M. Vainio and L. Halonen, “Mid-infrared optical parametric oscillators and frequency combs for molecular spectroscopy,” *Phys. Chem. Chem. Phys.*, vol. 18, no. 6, pp. 4266–4294, 2016.

[83] J. Kauppinen, K. Wilcken, I. Kauppinen, and V. Koskinen, “High sensitivity in gas analysis with photoacoustic detection,” *Microchem. J.*, vol. 76, no. 1–2, pp. 151–159, 2004.

[84] T. Kuusela and J. Kauppinen, “Photoacoustic gas analysis using interferometric cantilever microphone,” *Appl. Spectrosc. Rev.*, vol. 42, no. 5, pp. 443–474, 2007.

[85] E. W. Slocum, “Tables of thermal properties of gases. Joseph Hilsenralh, CW Beckett, WS Benedict, Lilla Fano, HJ Hoge, JF Masi, RL Nuttoll, YS Touloukian, and HW Woolley. National Bureau of Standards Circular 564. Government Printing Ofice, Washington 25, DC (1955). 408,” *AIChE J.*, vol. 2, no. 4, pp. 11D--11D, 1956.

[86] D. P. E. Smith, “Limits of force microscopy,” *Rev. Sci. Instrum.*, vol. 66, no. 5, pp. 3191–3195, 1995.

[87] F. R. Blom, S. Bouwstra, M. Elwenspoek, and J. H. J. Fluitman, “Dependence of the quality factor of micromachined silicon beam resonators on pressure and geometry,” *J. Vac. Sci. Technol. B Microelectron. Nanom. Struct. Process. Meas. Phenom.*, vol. 10, no. 1, pp. 19–26, 1992.

[88] D. R. Lide, *CRC handbook of chemistry and physics: a ready-reference book of chemical and physical data*. CRC press, 1995.

[89] K. Chen *et al.*, “Research on fiber-optic cantilever-enhanced photoacoustic spectroscopy for trace gas detection,” in *2017 International Conference on Optical Instruments and Technology: Optoelectronic Measurement Technology and Systems*, 2018, vol. 10621, p. 1062108.

[90] K. Chen, B. Zhang, S. Liu, and Q. Yu, “Parts-per-billion-level detection of hydrogen sulfide based on near-infrared all-optical photoacoustic spectroscopy,” *Sensors Actuators B Chem.*, vol. 283, pp. 1–5, 2019.

[91] W. Wei, Y. Zhu, C. Lin, L. Tian, Z. Xu, and J. Nong, “All-optical cantilever-enhanced photoacoustic spectroscopy in the open environment,” *Int. J. Thermophys.*, vol. 36, no. 5–6, pp. 1116–1122, 2015.

[92] J. Suchánek *et al.*, “First application of multilayer graphene cantilever for laser photoacoustic detection,” *Measurement*, vol. 101, pp. 9–14, 2017.

[93] P. G. Westergaard and M. Lassen, “All-optical detection of acoustic pressure waves

with applications in photoacoustic spectroscopy," *Appl. Opt.*, vol. 55, no. 29, pp. 8266–8270, 2016.

[94] T. Kuusela, J. Peura, B. A. Matveev, M. A. Remennyy, and others, "Photoacoustic gas detection using a cantilever microphone and III--V mid-IR LEDs," *Vib. Spectrosc.*, vol. 51, no. 2, pp. 289–293, 2009.

[95] R. Coutu, I. Medvedev, and D. Petkie, "Improved Sensitivity MEMS Cantilever Sensor for Terahertz Photoacoustic Spectroscopy," *Sensors*, vol. 16, no. 2, p. 251, 2016.

[96] N. E. Glauvitz, R. A. Coutu, I. R. Medvedev, and D. T. Petkie, "Terahertz photoacoustic spectroscopy using an MEMS cantilever sensor," *J. Microelectromechanical Syst.*, vol. 24, no. 1, pp. 216–223, 2015.

[97] N. Ledermann, P. Muralt, J. Baborowski, M. Forster, and J.-P. Pellaux, "Piezoelectric Pb (Zrx, Ti1- x) O3 thin film cantilever and bridge acoustic sensors for miniaturized photoacoustic gas detectors," *J. Micromechanics Microengineering*, vol. 14, no. 12, p. 1650, 2004.

[98] J. Fonsen, V. Koskinen, K. Roth, and J. Kauppinen, "Dual cantilever enhanced photoacoustic detector with pulsed broadband IR-source," *Vib. Spectrosc.*, vol. 50, no. 2, pp. 214–217, 2009.

[99] S. Zhou, M. Slaman, and D. Iannuzzi, "Demonstration of a highly sensitive photoacoustic spectrometer based on a miniaturized all-optical detecting sensor," *Opt. Express*, vol. 25, no. 15, pp. 17541–17548, 2017.

[100] J. Saarela, J. Toivonen, A. Manninen, T. Sorvajärvi, and R. Hernberg, "Wavelength modulation waveforms in laser photoacoustic spectroscopy," *Appl. Opt.*, vol. 48, no. 4, pp. 743–747, 2009.

[101] K. Chen, Z. Yu, Z. Gong, and Q. Yu, "Lock-in white-light-interferometry-based all-optical photoacoustic spectrometer," *Opt. Lett.*, vol. 43, no. 20, pp. 5038–5041, 2018.

[102] T. Laurila, H. Cattaneo, T. Pöyhönen, V. Koskinen, J. Kauppinen, and R. Hernberg,

"Cantilever-based photoacoustic detection of carbon dioxide using a fiber-amplified diode laser," *Appl. Phys. B*, vol. 83, no. 2, p. 285, 2006.

[103] B. D. Adamson, J. E. Sader, and E. J. Bieske, "Photoacoustic detection of gases using microcantilevers," *J. Appl. Phys.*, vol. 106, no. 11, p. 114510, 2009.

[104] E. D. McNaghten, K. A. Grant, A. M. Parkes, and P. A. Martin, "Simultaneous detection of trace gases using multiplexed tunable diode lasers and a photoacoustic cell containing a cantilever microphone," *Appl. Phys. B*, vol. 107, no. 3, pp. 861–871, 2012.

[105] A. Szabó, A. Mohacsi, G. Gulyas, Z. Bozoki, and G. Szabo, "In situ and wide range quantification of hydrogen sulfide in industrial gases by means of photoacoustic spectroscopy," *Meas. Sci. Technol.*, vol. 24, no. 6, p. 65501, 2013.

[106] E. L. Holthoff, D. A. Heaps, and P. M. Pellegrino, "Development of a MEMS-scale photoacoustic chemical sensor using a quantum cascade laser," *IEEE Sens. J.*, vol. 10, no. 3, pp. 572–577, 2010.

[107] A. A. Kosterev, Y. A. Bakhirkin, R. F. Curl, and F. K. Tittel, "Quartz-enhanced photoacoustic spectroscopy," *Opt. Lett.*, vol. 27, no. 21, pp. 1902–1904, 2002.

[108] Q. Wang, J. Wang, L. Li, and Q. Yu, "An all-optical photoacoustic spectrometer for trace gas detection," *Sensors Actuators B Chem.*, vol. 153, no. 1, pp. 214–218, 2011.

[109] Y. Cao, W. Jin, H. L. Ho, and J. Ma, "Miniature fiber-tip photoacoustic spectrometer for trace gas detection," *Opt. Lett.*, vol. 38, no. 4, pp. 434–436, 2013.

[110] A. Kachanov, S. Koulikov, and F. K. Tittel, "Cavity-enhanced optical feedback-assisted photo-acoustic spectroscopy with a 10.4 $μ$m external cavity quantum cascade laser," *Appl. Phys. B*, vol. 110, no. 1, pp. 47–56, 2013.

[111] R. E. Lindley, A. M. Parkes, K. A. Keen, E. D. McNaghten, and A. J. Orr-Ewing, "A sensitivity comparison of three photoacoustic cells containing a single microphone, a differential dual microphone or a cantilever pressure sensor," *Appl. Phys. B*, vol. 86, no. 4, pp. 707–713, 2007.

[112] K. Wilcken and J. Kauppinen, "Optimization of a microphone for photoacoustic

spectroscopy," *Appl. Spectrosc.*, vol. 57, no. 9, pp. 1087–1092, 2003.

[113] C. B. Hirschmann, J. Lehtinen, J. Uotila, S. Ojala, and R. L. Keiski, "Sub-ppb detection of formaldehyde with cantilever enhanced photoacoustic spectroscopy using quantum cascade laser source," *Appl. Phys. B*, vol. 111, no. 4, pp. 603–610, 2013.

[114] V. Zeninari, B. Parvitte, D. Courtois, V. A. Kapitanov, and Y. N. Ponomarev, "Methane detection on the sub-ppm level with a near-infrared diode laser photoacoustic sensor," *Infrared Phys. Technol.*, vol. 44, no. 4, pp. 253–261, 2003.

[115] V. Spagnolo *et al.*, "THz Quartz-enhanced photoacoustic sensor for H 2 S trace gas detection," *Opt. Express*, vol. 23, no. 6, pp. 7574–7582, 2015.

[116] P. Patimisco *et al.*, "High finesse optical cavity coupled with a quartz-enhanced photoacoustic spectroscopic sensor," *Analyst*, vol. 140, no. 3, pp. 736–743, 2015.

[117] Y. HE, Y. MA, Y. A. O. TONG, X. I. N. YU, and F. K. TITTEL, "Ultra-high sensitive light-induced thermoelastic spectroscopy sensor with a high Q-factor quartz tuning fork and a multipass cell."

[118] A. A. Kosterev, P. R. Buerki, L. Dong, M. Reed, T. Day, and F. K. Tittel, "QEPAS detector for rapid spectral measurements," *Appl. Phys. B*, vol. 100, no. 1, pp. 173–180, 2010.

[119] V. Spagnolo, P. Patimisco, S. Borri, G. Scamarcio, B. E. Bernacki, and J. Kriesel, "Mid-infrared fiber-coupled QCL-QEPAS sensor," *Appl. Phys. B*, vol. 112, no. 1, pp. 25–33, 2013.

[120] A. Sampaolo *et al.*, "Improved tuning fork for terahertz quartz-enhanced photoacoustic spectroscopy," *Sensors*, vol. 16, no. 4, p. 439, 2016.

[121] I. Sadiek, T. Mikkonen, M. Vainio, J. Toivonen, and A. Foltynowicz, "Optical frequency comb photoacoustic spectroscopy," *Phys. Chem. Chem. Phys.*, vol. 20, no. 44, pp. 27849–27855, 2018.

[122] V. Spagnolo, P. Patimisco, A. Sampaolo, M. Giglio, and F. K. Tittel, "Recent advances in quartz enhanced photoacoustic sensing," in *Optics and Photonics for*

Energy and the Environment, 2017, pp. ETh1A--6.

[123] J. Rakovsk\\`y and O. Votava, “A simple photoacoustic detector for highly corrosive gases,” *Rev. Sci. Instrum.*, vol. 88, no. 1, p. 13103, 2017.

[124] K. Chen *et al.*, “Fiber-optic Fabry-Perot interferometer based high sensitive cantilever microphone,” *Sensors Actuators A Phys.*, vol. 279, pp. 107–112, 2018.

[125] K. Liu, Y. Cao, G. Wang, W. Zhang, W. Chen, and X. Gao, “A novel photoacoustic spectroscopy gas sensor using a low cost polyvinylidene fluoride film,” *Sensors Actuators B Chem.*, vol. 277, pp. 571–575, 2018.

[126] N. E. Glauvitz, R. A. Coutu, M. Kistler, I. R. Medvedev, and D. T. Petkie, “MEMS cantilever sensor for photoacoustic detection of terahertz radiation,” in *MEMS and Nanotechnology, Volume 5*, Springer, 2014, pp. 73–79.

[127] S. Zhou and D. Iannuzzi, “A fiber-tip photoacoustic sensor for in situ trace gas detection,” *Rev. Sci. Instrum.*, vol. 90, no. 2, p. 23102, 2019.

[128] J. Uotila, V. Koskinen, and J. Kauppinen, “Selective differential photoacoustic method for trace gas analysis,” *Vib. Spectrosc.*, vol. 38, no. 1–2, pp. 3–9, 2005.

[129] I. Kauppinen, “Optical audio microphone arrangement including a Michelson type interferometer for providing a phase difference between different parts of light beams.” Google Patents, 2009.

[130] Z. Yu and A. Wang, “Fast white light interferometry demodulation algorithm for low-finesse Fabry--Pérot sensors,” *IEEE Photonics Technol. Lett.*, vol. 27, no. 8, pp. 817–820, 2015.

[131] G. Gruca, K. Heeck, J. Rector, and D. Iannuzzi, “Demonstration of a miniature all-optical photoacoustic spectrometer based on ferrule-top technology,” *Opt. Lett.*, vol. 38, no. 10, pp. 1672–1674, 2013.

[132] Y. Cao, W. Jin, H. L. Ho, L. Qi, and Y. H. Yang, “Acetylene detection based on diode laser QEPAS: combined wavelength and residual amplitude modulation,” *Appl. Phys. B*, vol. 109, no. 2, pp. 359–366, 2012.

[133] J. Peltola, T. Hieta, and M. Vainio, “Parts-per-trillion-level detection of nitrogen dioxide by cantilever-enhanced photo-acoustic spectroscopy,” *Opt. Lett.*, vol. 40, no. 13, pp. 2933–2936, 2015.

[134] S. Campbell, “Development of idealized practices for photoacoustic spectroscopy,” Memorial University of Newfoundland, 2017.

[135] A. M. Othman, H. E. Kotb, Y. M. Sabry, and D. Khalil, “EXPRESS: Micro--Electro--Mechanical Fourier Transform Infrared (MEMS FT-IR) Spectrometer Under Modulated--Pulsed Light Source Excitation,” *Appl. Spectrosc.*, p. 0003702819886091, 2019.

[136] D. J. Lahneman, T. J. Huffman, P. Xu, S. L. Wang, T. Grogan, and M. M. Qazilbash, “Broadband near-field infrared spectroscopy with a high temperature plasma light source,” *Opt. Express*, vol. 25, no. 17, pp. 20421–20430, 2017.

[137] D. K. Smith, “Laser-driven light source.” Google Patents, 2008.

[138] H. Zhu and P. Blackborow, “LDLS sheds light on analytical-sciences applications,” *Laser Focus World*, vol. 47, no. 12, pp. 53–60, 2011.

[139] A. Khodabakhsh *et al.*, “Fourier transform and Vernier spectroscopy using an optical frequency comb at 3--5.4 $μ$m,” *Opt. Lett.*, vol. 41, no. 11, pp. 2541–2544, 2016.

[140] S.-S. Kim, N. Menegazzo, C. Young, J. Chan, C. Carter, and B. Mizaikoff, “Mid-infrared trace gas analysis with single-pass Fourier transform infrared hollow waveguide gas sensors,” *Appl. Spectrosc.*, vol. 63, no. 3, pp. 331–337, 2009.

[141] “HITRAN on the Web.” [Online]. Available: http://hitran.iao.ru/. [Accessed: 04-Mar-2020].

[142] T. Hasegawa, *Quantitative Infrared Spectroscopy for Understanding of a Condensed Matter*. Springer, 2017.

[143] T. Mikkonen, C. Amiot, A. Aalto, K. Patokoski, G. Genty, and J. Toivonen, “Broadband cantilever-enhanced photoacoustic spectroscopy in the mid-IR using a supercontinuum,” *Opt. Lett.*, vol. 43, no. 20, pp. 5094–5097, 2018.

[144] D. P. Baldwin, R. W. Jones, and J. F. McClelland, "Exploration of FTIR-based PAS for on-site analysis of volatile contaminants in air," in *Photoacoustic and Photothermal Phenomena III*, Springer, 1992, pp. 3–5.

[145] G. Busse and B. Bullemer, "Use of the opto-acoustic effect for rapid scan Fourier spectroscopy," *Infrared Phys.*, vol. 18, no. 5–6, pp. 631–634, 1978.

[146] R. S. Wright, G. B. Howe, and R. K. M. Jayanty, "Evaluation of a portable Fourier transform infrared gas analyzer for measurements of air toxics in pollution prevention research," *J. Air Waste Manage. Assoc.*, vol. 48, no. 11, pp. 1077–1084, 1998.

[147] J. Uotila and J. Kauppinen, "Fourier transform infrared measurement of solid-, liquid-, and gas-phase samples with a single photoacoustic cell," *Appl. Spectrosc.*, vol. 62, no. 6, pp. 655–660, 2008.

[148] C. B. Hirschmann, J. Uotila, S. Ojala, J. Tenhunen, and R. L. Keiski, "Fourier transform infrared photoacoustic multicomponent gas spectroscopy with optical cantilever detection," *Appl. Spectrosc.*, vol. 64, no. 3, pp. 293–297, 2010.

[149] Y. Fan *et al.*, "Hybrid integrated InP-Si 3 N 4 diode laser with a 40-Hz intrinsic linewidth," *Opt. Express*, vol. 28, no. 15, pp. 21713–21728, 2020.

[150] I. Moskalev *et al.*, "140 W Cr: ZnSe laser system," *Opt. Express*, vol. 24, no. 18, pp. 21090–21104, 2016.

[151] S. Albert *et al.*, "Global analysis of the high resolution infrared spectrum of methane 12CH4 in the region from 0 to 4800 cm- 1," *Chem. Phys.*, vol. 356, no. 1–3, pp. 131–146, 2009.

[152] "Vertex-Bruker." [Online]. Available: https://www.bruker.com/products/infrared-near-infrared-and-raman-spectroscopy/ft-ir-research-spectrometers/vertex-series.html.

[153] W. O. Soboyejo and T. S. Srivatsan, *Advanced structural materials: properties, design optimization, and applications*. CRC press, 2006.

[154] M. Gad-el-Hak, *The MEMS handbook*. CRC press, 2001.

[155] B. Mi, D. A. Smith, H. Kahn, F. L. Merat, A. H. Heuer, and S. M. Phillips, “Static and electrically actuated shaped MEMS mirrors,” *J. microelectromechanical Syst.*, vol. 14, no. 1, pp. 29–36, 2005.

[156] A. C. Fischer *et al.*, “Integrating mems and ics,” *Microsystems Nanoeng.*, vol. 1, no. 1, pp. 1–16, 2015.

[157] B. P. Gogoi and D. Mladenovic, “Integration technology for MEMS automotive sensors,” in *IEEE 2002 28th Annual Conference of the Industrial Electronics Society. IECON 02*, 2002, vol. 4, pp. 2712–2717.

[158] C. Bouyé and B. d’Humières, “Miniature and micro spectrometers market: who is going to catch the value?,” in *Photonic Instrumentation Engineering IV*, 2017, vol. 10110, p. 101101P.

[159] Z. Zhou, Z. Wang, and L. Lin, *Microsystems and nanotechnology*. Springer, 2012.

[160] A. R. Jha, *MEMS and nanotechnology-based sensors and devices for communications, medical and aerospace applications*. CRC Press, 2008.

[161] T.-R. Hsu, *MEMS and microsystems: design, manufacture, and nanoscale engineering*. John Wiley & Sons, 2008.

[162] V. Kaajakari, “Practical MEMS: Analysis and design of microsystems, MEMS sensors, electronics, actuators, rf mems, optical mems, and microfluidic systems,” *Small Gear Publ.*, 2009.

[163] N. P. Ayerden *et al.*, “High-speed broadband FTIR system using MEMS,” *Appl. Opt.*, vol. 53, no. 31, pp. 7267–7272, 2014.

[164] M. C. M. M. Souza, A. Grieco, N. C. Frateschi, and Y. Fainman, “Fourier transform spectrometer on silicon with thermo-optic non-linearity and dispersion correction,” *Nat. Commun.*, 2018.

[165] H. Omran, M. Medhat, B. Mortada, B. Saadany, and D. Khalil, “Fully integrated Mach-Zhender MEMS interferometer with two complementary outputs,” *IEEE J. Quantum Electron.*, vol. 48, no. 2, pp. 244–251, 2012.

[166] T. A. Al-Saeed and D. A. Khalil, “Spot size effects in miniaturized moving-optical-wedge interferometer,” *Appl. Opt.*, vol. 50, no. 17, pp. 2671–2678, 2011.

[167] T. A. Al-Saeed and D. A. Khalil, “Fourier transform spectrometer based on Fabry--Perot interferometer,” *Appl. Opt.*, vol. 55, no. 20, pp. 5322–5331, 2016.

[168] Y. M. Eltagoury, Y. M. Sabry, and D. A. Khalil, “Novel Fourier transform infrared spectrometer architecture based on cascaded Fabry-Perot interferometers,” in *MOEMS and Miniaturized Systems XV*, 2016, vol. 9760, p. 97600L.

[169] T. Sandner, A. Kenda, C. Drabe, H. Schenk, and W. Scherf, “Miniaturized FTIR-spectrometer based on optical MEMS translatory actuator,” in *MOEMS and miniaturized systems VI*, 2007, vol. 6466, p. 646602.

[170] E. R. Deutsch, D. Reyes, E. R. Schildkraut, and J. Kim, “High-resolution miniature FTIR spectrometer enabled by a large linear travel MEMS pop-up mirror,” in *Next-Generation Spectroscopic Technologies II*, 2009, vol. 7319, p. 73190J.

[171] T. Scharf, D. Briand, S. Bühler, O. Manzardo, H. P. Herzig, and N. F. De Rooij, “Gas detection with a micro FTIR spectrometer in the MIR region,” *Procedia Chem.*, vol. 1, no. 1, pp. 1379–1382, 2009.

[172] R. Legtenberg, A. W. Groeneveld, and M. Elwenspoek, “Comb-drive actuators for large displacements,” *J. Micromechanics Microengineering*, 1996.

[173] A. Fathy, Y. M. Sabry, S. Nazeer, T. Bourouina, and D. A. Khalil, “On-chip parallel Fourier transform spectrometer for broadband selective infrared spectral sensing,” *Microsystems Nanoeng.*, vol. 6, no. 1, pp. 1–9, 2020.

[174] D. A. Khalil, B. Mortada, M. Nabil, M. Medhat, and B. A. Saadany, “Compensated MEMS FTIR spectrometer architecture.” Google Patents, 2013.

[175] Y. M. Sabry, D. Khalil, B. Saadany, and T. Bourouina, “Curved silicon micromirror for linear displacement-to-angle conversion with uniform spot size,” *IEEE J. Sel. Top. Quantum Electron.*, vol. 21, no. 4, pp. 165–173, 2014.

[176] B. A. Saadany, A. N. Hafez, M. Medhat, and H. Haddara, “Technique to determine mirror position in optical interferometers.” Google Patents, 2014.

[177] P. R. Griffiths and J. A. De Haseth, *Fourier Transform Infrared Spectrometry: Second Edition*. 2006.

[178] P. Pellin and A. Broca, “A spectroscope of fixed deviation,” *Astrophys. J.*, vol. 10, p. 337, 1899.

[179] J. Browning, “On the use of compound prism spectroscopes,” *Mon. Not. R. Astron. Soc.*, vol. 31, p. 203, 1871.

[180] G. J. Zissis, “Dispersive prisms and gratings,” *Handb. Opt.*, vol. 2, pp. 1–5, 1995.

[181] C. W. Chen and E. W. Gossett, “Grism (grating-prism combination).” Google Patents, 1997.

[182] Y. Cheng, Z. Wu, S. Deng, M. Lu, and others, “Combined optical dispersion by prism and arrayed waveguide grating with multiple diffraction orders for Raman spectrometer,” *Opt. Spectrosc.*, vol. 117, no. 3, pp. 480–485, 2014.

[183] J. M. Lerner, “Imaging spectrometer fundamentals for researchers in the biosciences—a tutorial,” *Cytom. Part A J. Int. Soc. Anal. Cytol.*, vol. 69, no. 8, pp. 712–734, 2006.

[184] C. M. Sparrow, “On spectroscopic resolving power,” *Astrophys. J.*, vol. 44, p. 76, 1916.

[185] B. Bhushan, “Surface roughness analysis and measurement techniques,” in *Modern Tribology Handbook, Two Volume Set*, CRC press, 2000, pp. 79–150.

[186] A. Krywonos, J. E. Harvey, and N. Choi, “Linear systems formulation of scattering theory for rough surfaces with arbitrary incident and scattering angles,” *JOSA A*, vol. 28, no. 6, pp. 1121–1138, 2011.

[187] S. Schröder, A. Duparré, L. Coriand, A. Tünnermann, D. H. Penalver, and J. E. Harvey, “Modeling of light scattering in different regimes of surface roughness,” *Opt. Express*, vol. 19, no. 10, pp. 9820–9835, 2011.

[188] S. D. Lowther, K. C. Jones, X. Wang, J. D. Whyatt, O. Wild, and D. Booker, “Particulate matter measurement indoors: A review of metrics, sensors, needs, and

applications," *Environ. Sci. Technol.*, vol. 53, no. 20, pp. 11644–11656, 2019.

[189] B. Giechaskiel *et al.*, "Review of motor vehicle particulate emissions sampling and measurement: From smoke and filter mass to particle number," *J. Aerosol Sci.*, vol. 67, pp. 48–86, 2014.

[190] H. Burtscher, "Physical characterization of particulate emissions from diesel engines: a review," *J. Aerosol Sci.*, vol. 36, no. 7, pp. 896–932, 2005.

[191] J. Zhao and X. Yang, "Photocatalytic oxidation for indoor air purification: a literature review," *Build. Environ.*, vol. 38, no. 5, pp. 645–654, 2003.

[192] Q. Liao, Z. Zhang, X. Zhang, M. Mohr, Y. Zhang, and H.-J. Fecht, "Flexible piezoelectric nanogenerators based on a fiber/ZnO nanowires/paper hybrid structure for energy harvesting," *Nano Res.*, vol. 7, no. 6, pp. 917–928, 2014.

[193] K. S. Leschkies *et al.*, "Photosensitization of ZnO nanowires with CdSe quantum dots for photovoltaic devices," *Nano Lett.*, vol. 7, no. 6, pp. 1793–1798, 2007.

[194] K. Liu, M. Sakurai, and M. Aono, "ZnO-based ultraviolet photodetectors," *Sensors*, vol. 10, no. 9, pp. 8604–8634, 2010.

[195] H. Gong, J. Q. Hu, J. H. Wang, C. H. Ong, and F. R. Zhu, "Nano-crystalline Cu-doped ZnO thin film gas sensor for CO," *Sensors Actuators B Chem.*, vol. 115, no. 1, pp. 247–251, 2006.

[196] I. Azzouz *et al.*, "Zinc oxide nano-enabled microfluidic reactor for water purification and its applicability to volatile organic compounds," *Microsystems Nanoeng.*, vol. 4, p. 17093, 2018.

[197] T. Ma, M. Guo, M. Zhang, Y. Zhang, and X. Wang, "Density-controlled hydrothermal growth of well-aligned ZnO nanorod arrays," *Nanotechnology*, vol. 18, no. 3, p. 35605, 2007.

[198] W. L. Wolfe, *Introduction to radiometry*, vol. 29. SPIE Press, 1998.

[199] C. A. Lieber and A. Mahadevan-Jansen, "Automated method for subtraction of fluorescence from biological Raman spectra," *Appl. Spectrosc.*, vol. 57, no. 11, pp.

1363–1367, 2003.

[200] Z.-M. Zhang, S. Chen, and Y.-Z. Liang, “Baseline correction using adaptive iteratively reweighted penalized least squares,” *Analyst*, vol. 135, no. 5, pp. 1138–1146, 2010.

[201] L. Shao and P. R. Griffiths, “Automatic baseline correction by wavelet transform for quantitative open-path Fourier transform infrared spectroscopy,” *Environ. Sci. Technol.*, vol. 41, no. 20, pp. 7054–7059, 2007.

[202] G. Magnus, “Versuche über die Spannkräfte des Wasserdampfs,” *Ann. Phys.*, vol. 137, no. 2, pp. 225–247, 1844.

[203] P. R. Griffiths, L. Shao, and A. B. Leytem, “Completely automated open-path FT-IR spectrometry,” *Anal. Bioanal. Chem.*, vol. 393, no. 1, pp. 45–50, 2009.

[204] “SBIR Phase II: An Improved Open-Path FTIR Spectrometer for Remote Monitoring of Atmospheric Gases.” [Online]. Available: https://www.sbir.gov/sbirsearch/detail/392679.

[205] M. Capochichi-Gnambodoe, Y. G. Habba, and Y. Leprince-Wang, “A comparative study of the gas sensing properties of hierarchical ZnO nanostructures,” *Phys. status solidi*, vol. 13, no. 7–9, pp. 688–692, 2016.

[206] K. Zheng, C. Zheng, Y. Zhang, Y. Wang, and F. K. Tittel, “Review of Incoherent Broadband Cavity-Enhanced Absorption Spectroscopy (IBBCEAS) for Gas Sensing,” *Sensors*, vol. 18, no. 11, p. 3646, 2018.

[207] D. R. Herriott and H. J. Schulte, “Folded optical delay lines,” *Appl. Opt.*, vol. 4, no. 8, pp. 883–889, 1965.

[208] N. Daher *et al.*, “Multipass cells: 1D numerical model and investigation of spatio-spectral couplings at high nonlinearity,” *JOSA B*, vol. 37, no. 4, pp. 993–999, 2020.

[209] M. Kaumanns *et al.*, “Multipass spectral broadening of 18 mJ pulses compressible from 1.3 ps to 41 fs,” *Opt. Lett.*, vol. 43, no. 23, pp. 5877–5880, 2018.

[210] B. Cai, C. Hao, Z. Xie, and D. Sheng, “Applications of multipass cells in atomic

magnetometers and co-magnetometers.," *Bull. Am. Phys. Soc.*, vol. 64, 2019.

[211] J. U. White, "Long optical paths of large aperture," *JOSA*, vol. 32, no. 5, pp. 285–288, 1942.

[212] J. B. McManus, P. L. Kebabian, and M. S. Zahniser, "Astigmatic mirror multipass absorption cells for long-path-length spectroscopy," *Appl. Opt.*, vol. 34, no. 18, pp. 3336–3348, 1995.

[213] S. M. Chernin and E. G. Barskaya, "Optical multipass matrix systems," *Appl. Opt.*, vol. 30, no. 1, pp. 51–58, 1991.

[214] S. M. Chernin, "New generation of multipass systems in high resolution spectroscopy," *Spectrochim. Acta Part A Mol. Biomol. Spectrosc.*, vol. 52, no. 8, pp. 1009–1022, 1996.

[215] E. Hawe, C. Fitzpatrick, P. Chambers, and E. Lewis, "An investigation into the use of an integrating sphere as a gas absorption cell," *J. Opt. A Pure Appl. Opt.*, vol. 9, no. 6, p. S12, 2007.

[216] M. L. Thoma, R. Kaschow, and F. J. Hindelang, "A multiple-reflection cell suited for absorption measurements in shock tubes," *Shock Waves*, vol. 4, no. 1, pp. 51–53, 1994.

[217] A. Manninen, B. Tuzson, H. Looser, Y. Bonetti, and L. Emmenegger, "Versatile multipass cell for laser spectroscopic trace gas analysis," *Appl. Phys. B*, vol. 109, no. 3, pp. 461–466, 2012.

[218] B. Tuzson, M. Mangold, H. Looser, A. Manninen, and L. Emmenegger, "Compact multipass optical cell for laser spectroscopy," *Opt. Lett.*, vol. 38, no. 3, pp. 257–259, 2013.

[219] Z. Yang, M. Zou, and L. Sun, "Generalized optical design of the multiple-row circular multi-pass cell with dense spot pattern," *Opt. Express*, vol. 27, no. 23, pp. 32883–32891, 2019.

[220] J. M. Kriesel *et al.*, "Hollow core fiber optics for mid-wave and long-wave infrared spectroscopy," in *Chemical, Biological, Radiological, Nuclear, and Explosives*

(CBRNE) Sensing XII, 2011, vol. 8018, p. 80180V.

[221] Y. Matsuura and M. Miyagi, “Er: YAG, CO, and CO 2 laser delivery by ZnS-coated Ag hollow waveguides,” *Appl. Opt.*, vol. 32, no. 33, pp. 6598–6601, 1993.

[222] C. R. Young *et al.*, “Infrared hollow waveguide sensors for simultaneous gas phase detection of benzene, toluene, and xylenes in field environments,” *Anal. Chem.*, vol. 83, no. 16, pp. 6141–6147, 2011.

[223] J. F. da Silveira Petruci, A. Wilk, A. A. Cardoso, and B. Mizaikoff, “A hyphenated preconcentrator-infrared-hollow-waveguide sensor system for N 2 O Sensing,” *Sci. Rep.*, vol. 8, no. 1, pp. 1–6, 2018.

[224] R. Stach, J. Haas, E. Tütüncü, S. Daboss, C. Kranz, and B. Mizaikoff, “PolyHWG: 3D Printed Substrate-Integrated Hollow Waveguides for Mid-Infrared Gas Sensing,” *ACS sensors*, vol. 2, no. 11, pp. 1700–1705, 2017.

[225] M. Miyagi and S. Kawakami, “Design theory of dielectric-coated circular metallic waveguides for infrared transmission,” *J. Light. Technol.*, vol. 2, no. 2, pp. 116–126, 1984.

[226] Y. Fink, D. J. Ripin, S. Fan, C. Chen, J. D. Joannopoulos, and E. L. Thomas, “Guiding optical light in air using an all-dielectric structure,” *J. Light. Technol.*, vol. 17, no. 11, p. 2039, 1999.

[227] P. Yeh, A. Yariv, and E. Marom, “Theory of Bragg fiber,” *JOSA*, vol. 68, no. 9, pp. 1196–1201, 1978.

[228] Y. Zhou, V. Karagodsky, B. Pesala, F. G. Sedgwick, and C. J. Chang-Hasnain, “A novel ultra-low loss hollow-core waveguide using subwavelength high-contrast gratings,” *Opt. Express*, vol. 17, no. 3, pp. 1508–1517, 2009.

[229] J. A. Harrington, “A review of IR transmitting, hollow waveguides,” *Fiber Integr. Opt.*, vol. 19, no. 3, pp. 211–227, 2000.

[230] J. N. McMullin, R. Narendra, and C. R. James, “Hollow metallic waveguides in silicon V-grooves,” *IEEE photonics Technol. Lett.*, vol. 5, no. 9, pp. 1080–1082, 1993.

[231] A. Wilk *et al.*, "Substrate-integrated hollow waveguides: a new level of integration in mid-infrared gas sensing," *Anal. Chem.*, vol. 85, no. 23, pp. 11205–11210, 2013.

[232] J. J. R. Rohwedder, C. Pasquini, P. R. Fortes, I. M. Raimundo, A. Wilk, and B. Mizaikoff, "iHWG-\$μ\$NIR: a miniaturised near-infrared gas sensor based on substrate-integrated hollow waveguides coupled to a micro-NIR-spectrophotometer," *Analyst*, vol. 139, no. 14, pp. 3572–3576, 2014.

[233] S. E. Fiedler, A. Hese, and A. A. Ruth, "Incoherent broad-band cavity-enhanced absorption spectroscopy," *Chem. Phys. Lett.*, vol. 371, no. 3–4, pp. 284–294, 2003.

[234] Y. Guo and L. Sun, "Compact optical multipass matrix system design based on slicer mirrors," *Appl. Opt.*, vol. 57, no. 5, pp. 1174–1181, 2018.

[235] J. Ofner, H.-U. Krüger, and C. Zetzsch, "Circular multireflection cell for optical spectroscopy," *Appl. Opt.*, vol. 49, no. 26, pp. 5001–5004, 2010.

[236] P. Jouy *et al.*, "Mid-infrared spectroscopy for gases and liquids based on quantum cascade technologies," *Analyst*, vol. 139, no. 9, pp. 2039–2046, 2014.

[237] D. A. Knox, A. K. King, E. D. McNaghten, S. J. Brooks, P. A. Martin, and S. M. Pimblott, "Novel utilisation of a circular multi-reflection cell applied to materials ageing experiments," *Appl. Phys. B*, vol. 119, no. 1, pp. 55–64, 2015.

[238] M. Mangold, B. Tuzson, M. Hundt, J. Jágerská, H. Looser, and L. Emmenegger, "Circular paraboloid reflection cell for laser spectroscopic trace gas analysis," *JOSA A*, vol. 33, no. 5, pp. 913–919, 2016.

[239] M. Graf, H. Looser, L. Emmenegger, and B. Tuzson, "Beam folding analysis and optimization of mask-enhanced toroidal multipass cells," *Opt. Lett.*, vol. 42, no. 16, pp. 3137–3140, 2017.

[240] M. Graf, L. Emmenegger, and B. Tuzson, "Compact, circular, and optically stable multipass cell for mobile laser absorption spectroscopy," *Opt. Lett.*, vol. 43, no. 11, pp. 2434–2437, 2018.

[241] Y. M. Sabry, B. Saadany, D. Khalil, and T. Bourouina, "Silicon micromirrors with three-dimensional curvature enabling lensless efficient coupling of free-space light,"

Light Sci. Appl., vol. 2, no. 8, pp. e94--e94, 2013.

Abstract

Air pollution is a global issue that increasingly affects mankind. The effects of the pollution on health and on the environment, include global warming. The better our ability to monitor the pollution, the better we will be able to map its diffusion and mitigate for its consequence and even reduce it through information of decision makers. Towards collecting pollution data at large scale, MEMS FTIR spectrometer has the advantage of the real-time/continuous measurements besides being stable, compact and of low cost. Using it allows an effective and wide monitoring of multiple gas pollutant simultaneously with the same device. This motivates us for using the MEMS spectrometer in different gas sensing applications such as monitoring of volatile organic compounds with a lower limit of detection in parts per billion (ppb) concentration, open-path measurements and monitoring air purification. Trying to overcome the limited spectral resolution, the parallel spectrometer concept was introduced to measure gas with higher resolving power. Also, a novel differential spectrometer was developed. Since gas cells are key components in sensors where light interaction occurs, chip integrated gas cells including hollow waveguides and multi-pass cell were implemented. Integrating them with the MEMS spectrometer is an ultimate goal for having all the senor completely integrated on the same chip, leading to a more compact and lower cost sensor.

Résumé

La pollution de l'air constitue un enjeu sociétal qui affecte l'humanité toute entière. La pollution de l’air a de conséquences sanitaire et environnementale à échelle planétaire, incluant le réchauffement climatique. Plus il est possible de surveiller la pollution, plus nous serons en mesure de cartographier sa diffusion et en atténuer les conséquences, voire la réduire au travers d’outils d’aide à la décision. En vue de la collecte à large échelle de données sur la pollution, le spectromètre MEMS FTIR a l'avantage des mesures en temps réel / continu en plus d'être stable, compact et de faible coût. Son utilisation permet une surveillance de plusieurs polluants gazeux avec le même dispositif. Ceci nous a motivé pour tester le spectromètre MEMS dans différentes applications de détection de gaz telles que la surveillance des composés organiques volatils avec une limite de détection de l’ordre du ppb (part par milliards) en concentration, les mesures en circuit ouvert et une étude dur le monitoring de l’efficacité de la purification de l'air. Afin de palier à la résolution spectrale limitée du MEMS FTIR, le concept du spectromètre parallèle a été introduit pour mesurer le gaz avec un pouvoir de résolution plus élevé. En outre, un nouveau spectromètre différentiel a été introduit et testé. Enfin, étant donné que les cellules à gaz sont des composants clés dans les capteurs optiques, des cellules à gaz intégrées à la puce comprenant des guides d'ondes creux et une cellule à passes multiples ont été conçues réalisées et mises en œuvre. Leur intégration avec le spectromètre MEMS est un objectif ultime pour avoir des capteurs spectraux complètement intégrés sur la même puce, conduisant à un dispositif de mesure de gaz versatile plus compact et moins coûteux.